

# **Wireless Transceiver Design**

## For High Velocity Scenarios

**Tao Xu**

# 面向高速运动情景的 无线收发机设计

许涛

# Wireless Transceiver Design

## for High Velocity Scenarios

PROEFSCHRIFT

ter verkrijging van de graad van doctor  
aan de Technische Universiteit Delft,  
op gezag van de Rector Magnificus Prof. ir. K.C.A.M. Luyben,  
voorzitter van het College voor Promoties,  
in het openbaar te verdedigen op dinsdag 15 januari 2013  
om 12:30 uur  
door

Tao XU

Master of Science in Electronic Science and Technology  
geboren te Liaoning, China.

Dit proefschrift is goedgekeurd door de promotoren:

Prof. dr. ir. A.-J. van der Veen

Prof. dr. ir. G.J.T. Leus

Samenstelling promotiecommissie:

Rector Magnificus	voorzitter
Prof. dr. ir. A.-J. van der Veen	Technische Universiteit Delft, promotor
Prof. dr. ir. G.J.T. Leus	Technische Universiteit Delft, promotor
*Dr. ir. T.G.R.M. van Leuken	Technische Universiteit Delft
Prof. dr. O. Yaroyvi	Technische Universiteit Delft
Prof. dr. D.G. Simons	Technische Universiteit Delft
Dr. ir. H.S. Dol	TNO
Prof. dr. M. Stojanovic	Northeastern University, USA

\*Dr. ir. T.G.R.M. van Leuken heeft als begeleider in belangrijke mate aan de totstandkoming van het proefschrift bijgedragen.

Copyright © 2013 by Tao XU

All rights reserved. No part of the material protected by this copyright notice may be reproduced or utilized in any form or by any means, electronic or mechanical, including photocopying, recording or by any information storage and retrieval system, without the prior permission of the author.

ISBN 978-94-6186-094-1

*In memory of my grandparents  
and  
dedicated to my parents*



---

## Summary

This thesis is dedicated to transceiver designs for high data-rate wireless communication systems with rapidly moving terminals. The challenges are two-fold. On the one hand, more spectral bandwidth of the transmitted signals is required by future wireless systems to obtain higher transmission rates, which can result in the frequency selectivity of the communication channels. On the other hand, Doppler effects emerge when high mobile speeds are present, which can result in the time selectivity of the communication channels. Therefore, it is likely that future wireless communication systems operate in doubly-selective channels, which impose many difficulties on transceiver designs. In this thesis, we investigate these challenges in the following four scenarios, and propose a number of corresponding solutions.

### **OFDM over Narrowband Channels:**

Orthogonal frequency-division multiplexing (OFDM) is a typical multiple-carrier transmission technique. In a narrowband scenario, Doppler effects are well approximated as frequency shifts. In this manner, a narrowband doubly-selective channel for OFDM systems can be approximately characterized as a banded matrix especially when a basis expansion model (BEM) is exploited to model the channel. It thus allows to reduce the complexity of the channel equalization. However, there are various different BEM's available. We identify a particular BEM which leads to a more efficient hardware architecture than other choices, while still maintaining a high modeling accuracy.

---

**OFDM over Wideband Channels:**

The Doppler effect manifests itself as a distinct phenomenon in wideband channels compared to narrowband channels. Specifically, the wideband signal waveform is measurably dilated or compressed when Doppler is present rather than just frequency-shifted. This unique nature of wideband time-varying channels requires new designs for wideband OFDM systems. We first quantify the amount of interference resulting from wideband doubly-selective channels which follow the multi-scale/multi-lag (MSML) model. Then we discuss an equalization method for wideband channels either in the frequency domain or in the time domain. A novel optimum resampling procedure is also introduced, which is normally unnecessary in narrowband systems.

**Multi-Rate Transmissions over Wideband Channels:**

Traditional multi-carrier transmission schemes, e.g., OFDM, use a uniform data rate on each subcarrier, which is inherently mismatched with wideband time-varying channels. In fact, the time variation of wideband channels, i.e., the Doppler scales, imply a non-uniform sampling mechanism. To mitigate this, we propose a novel multi-rate transmission scheme by placing the information symbols at different non-overlapping sub-bands where each sub-band has a distinctive bandwidth. To combat the MSML effect of the channel, a filterbank is deployed at the receiver, where each branch of the filterbank samples the received signal at a corresponding rate. By selecting a proper transmit/receiver pulse, the effective input/output relationship can be captured by a block-diagonal channel, with each diagonal block being a banded matrix similarly as seen in narrowband OFDM systems. The benefit of this similarity is that existing low-complexity equalizers can be adopted for wideband communications.

**Robust Multi-band Transmissions over Wideband Channels:**

Accurate channel estimation for wideband doubly-selective channels is challenging and troublesome. Adaptive channel equalization is thus attractive since it does not require precise channel information and is robust to various prevailing environmental conditions. When the MSML effect emerges in wideband channels, it is not wise to adopt ex-



---

isting adaptive equalization designs that are previously used in other scenarios, e.g., narrowband channels. We adopt a multi-band frequency-division multiplexing (FDM) signal waveform at the transmitter to reduce the equalization complexity, while maintaining a high data rate. By carefully designing the transmit pulse, our proposed multi-layer turbo equalization, using a phase-locked loop (PLL) followed by a time-invariant finite impulse response (FIR) filter, is capable of equalizing such MSML channels.



---

## Glossary

### Mathematical Notation

$x$	scalar $x$
$\mathbf{x}$	vector $\mathbf{x}$
$\ \mathbf{x}\ $	Euclidean norm of vector $\mathbf{x}$
$\mathbf{X}$	matrix $\mathbf{X}$
$\mathbf{X}^T$	transpose of matrix $\mathbf{X}$
$\mathbf{X}^H$	Hermitian transpose of matrix $\mathbf{X}$
$\mathbf{X}^*$	complex conjugate of matrix $\mathbf{X}$
$\mathbf{X}^{-1}$	inverse of matrix $\mathbf{X}$
$\mathbf{X}^\dagger$	pseudoinverse of matrix $\mathbf{X}$
$\text{tr}\{\mathbf{X}\}$	trace of matrix $\mathbf{X}$
$\ \mathbf{X}\ $	Frobenius norm of matrix $\mathbf{X}$
$\text{diag}(\mathbf{x})$	square diagonal matrix with $\mathbf{x}$ as diagonal
$[\mathbf{X}]_{k,l}$	element on the $k$ th row and $l$ th column of matrix $\mathbf{X}$
$\mathbf{0}_{m \times n}$	$m \times n$ all-zero matrix
$\mathbf{1}_{m \times n}$	$m \times n$ all-one matrix
$\mathbf{e}_n$	unit vector with a one in the $n$ th entry
$\mathbf{I}_N$	identity matrix of size $N$
$\Re\{x\}$	real part of $x$
$\Im\{x\}$	imaginary part of $x$
$\hat{x}$	estimate of $x$
$\text{sgn}\{x\}$	the sign of $x \in \mathbb{R}$

---

$\lfloor x \rfloor$	largest integer smaller or equal to $x \in \mathbb{R}$
$\lceil x \rceil$	smallest integer larger or equal to $x \in \mathbb{R}$
$\langle x \rangle$	integer closest to $x \in \mathbb{R}$
$E\{x\}$	expectation of random variable $x$
$x_{\text{mod}/y}$	remainder after dividing $x \in \mathbb{R}$ by $y \in \mathbb{R}$
$\mathbb{R}$	the set of real numbers
$\mathbb{C}$	the set of complex numbers
$\times$	multiplication
$\otimes$	linear convolution
$\otimes$	Kronecker product
$\odot$	Hadamard (point-wise) product
$\delta_k$	a delta function which is equal to one only if $k = 0$ and zero otherwise

### Acronyms and Abbreviations

AWGN	Additive White Gaussian Noise
BEM	Basis Expansion Model
BER	Bit Error Rate
BPSK	Binary Phase Shift Keying
CE-BEM	Complex Exponential BEM
CCE-BEM	Critically-sampled CE-BEM
CDMA	Code Division Multiple Access
CE	Channel Estimator
CFO	Carrier Frequency Offset
CG	Conjugate Gradient
CP	Cyclic Prefix
CSI	Channel State Information
DFE	Decision Feedback Equalizer
DFT	Discrete Fourier Transformation
DKL-BEM	Discrete Karhuen-Loéve BEM
DPS-BEM	Discrete Prolate Spheroidal BEM
DSP	Digital Signal Processor
DSSS	Direct-Sequence Spread-Spectrum
DVB	Digital Video Broadcasting

EQ	Equalizer
FD	Frequency-Domain
FDM	Frequency-Division Multiplexing
FIR	Finite Impulse Response
FPGA	Field-Programmable Gate Array
GPS	Global Positioning System
IBI	Inter-Block Interference
ICI	Inter-Carrier Interference
IDFT	Inverse Discrete Fourier Transformation
ISI	Inter-Symbol Interference
I/O	Input-Output
LMMSE	Linear Minimum Mean Square Error
LS	Least Squares
LTE	Long Term Evolution
LTV	Linear Time Varying
MIMO	Multi-Input Multi-Output
MSE	Mean Squared Error
MSML	Multi-Scale Multi-Lag
NLMS	Normalized Least Mean Squares
NMSE	Normalized Mean Squared Error
OCE-BEM	Oversampled CE-BEM
OFDM	Orthogonal Frequency-Division Multiplexing
PDF	Probability Distribution Function
PLL	Phase-Locked Loop
P-BEM	Polynomial BEM
QPSK	Quadrature Phase Shift Keying
RLS	Recursive Least Squares
ROM	Read-Only Memory
SIMO	Single-Input Multi-Output
SINR	Signal-to-Interference-plus-Noise Ratio
SISO	Soft-Input Soft-Output
SNR	Signal-to-Noise Ratio
SSML	Single-Scale Multi-Lag
TD	Time-Domain

TI	Time-Invariant
T-F	Time-Frequency
UAC	Underwater Acoustic Communication
UMTS	Universal Mobile Telecommunications System
UWB	Ultra-wideband
WLAN	Wireless Local Area Network
WLTV	Wideband Linear Time Varying
ZF	Zero-Forcing
ZP	Zero-Padding

---

# Contents

<b>Glossary</b>	<b>v</b>
<b>1 Introduction</b>	<b>1</b>
1.1 Problem Statement and Research Objectives . . . . .	3
1.2 Contributions and Outline . . . . .	7
<b>2 Preliminaries</b>	<b>13</b>
2.1 Elements of Wireless Communications . . . . .	13
2.2 Wireless Fading Channels . . . . .	14
2.2.1 Parametric Channel Model . . . . .	15
2.2.2 Non-Parametric Channel Model . . . . .	24
2.3 Multi-Carrier Transmission . . . . .	26
<b>3 Narrowband OFDM Systems</b>	<b>31</b>
3.1 Introduction . . . . .	31
3.2 Narrowband Time-Varying OFDM System Model . . . . .	33
3.3 Algorithm Background Overview . . . . .	36
3.3.1 OFDM Carrier Arrangement . . . . .	37
3.3.2 LS Channel Estimation . . . . .	39
3.3.3 ZF Channel Equalization . . . . .	42
3.4 Parallel Implementation Architecture . . . . .	43
3.4.1 Channel Estimator . . . . .	43
3.4.2 Channel Equalizer . . . . .	49

3.5 Experiments . . . . .	52
3.6 Summary . . . . .	58
Appendix 3.A Detailed Derivation of (3.12) . . . . .	59
<b>4 Wideband OFDM Systems</b>	<b>63</b>
4.1 Introduction . . . . .	63
4.2 System Model Based on an MSML Channel . . . . .	65
4.2.1 Continuous Data Model . . . . .	65
4.2.2 Discrete Data Model . . . . .	67
4.3 Interference Analysis . . . . .	70
4.4 Channel Equalization Scheme . . . . .	73
4.4.1 Iterative Equalization . . . . .	74
4.4.2 Diagonal Preconditioning . . . . .	76
4.4.3 Optimal Resampling . . . . .	78
4.5 Frequency-Domain or Time-Domain Equalization? . . . . .	82
4.6 Numerical Results . . . . .	86
4.7 Summary . . . . .	90
Appendix 4.A Detailed Derivation of the Discrete Data Model . . . . .	91
Appendix 4.B System Model in the Time Domain and Time-domain Equalization . . . . .	92
Appendix 4.C Equalization using the Conjugate Gradient Algo- rithm . . . . .	95
Appendix 4.D Eigenvalue Locations . . . . .	96
<b>5 Multi-Layer Transceiver</b>	<b>97</b>
5.1 Introduction . . . . .	97
5.2 Wideband LTV Systems . . . . .	99
5.2.1 Parameterized Passband Data Model . . . . .	101
5.2.2 Related Works . . . . .	104
5.2.3 Parameterized Baseband Data Model . . . . .	107
5.3 Transmit Signal Design . . . . .	108
5.3.1 Single-Layer Signaling . . . . .	109
5.3.2 Pulse Design . . . . .	113
5.3.3 Multi-Layer Signaling . . . . .	116
5.4 Block-Wise Transceiver Design . . . . .	119



## Contents

---

5.5	Frequency-Domain Equalization . . . . .	121
5.6	Numerical Results . . . . .	123
5.6.1	Channel Model Validation . . . . .	124
5.6.2	Equalization Performance . . . . .	126
5.6.3	Single-Layer or Multi-Layer . . . . .	128
5.6.4	OFDM vs. Multi-Layer Block Transmission . . . . .	130
5.7	Summary . . . . .	132
	Appendix 5.A Proof of Theorem 5.1 . . . . .	134
	Appendix 5.B Proof of (5.29) . . . . .	135
	Appendix 5.C The Basic Scaling Factor of the Shannon Wavelet . . . . .	135
	Appendix 5.D Noise Statistics . . . . .	136
<b>6</b>	<b>Robust Semi-blind Transceiver</b>	<b>139</b>
6.1	Introduction . . . . .	139
6.2	System Model Based on an MSML Channel . . . . .	142
6.2.1	Transmit Signal . . . . .	142
6.2.2	Received Signal Resulting from an MSML Channel . . . . .	143
6.3	Receiver Design . . . . .	144
6.3.1	Multi-Branch Framework . . . . .	144
6.3.2	Soft Iterative Equalizer . . . . .	146
6.4	Experimental Results . . . . .	152
6.5	Summary . . . . .	159
	Appendix 6.A Proof of Proposition 6.1 . . . . .	160
	Appendix 6.B Proof of Proposition 6.2 . . . . .	164
<b>7</b>	<b>Conclusions and Future Work</b>	<b>167</b>
7.1	Conclusions . . . . .	167
7.2	Future Work . . . . .	170
	<b>Bibliography</b>	<b>173</b>
	<b>Samenvatting</b>	<b>181</b>
	<b>Acknowledgements</b>	<b>185</b>
	<b>Curriculum Vitae</b>	<b>187</b>

**List of Publications**

**189**

## Chapter 1

---

## Introduction

*Every day sees humanity more victorious in the struggle with space and time.*

Guglielmo Marconi

Since the successful demonstration of radio transmission made by Marconi in 1895, wireless communication has undergone many evolutions [1]. Today, wireless communication technology is, by any measure, one of the fastest growing segments of modern industry, and has become ubiquitous in our daily life. Examples that come to mind include mobile phones, radio-frequency identification (RFID) cards, wireless internet access, Bluetooth ear-phones, etc. However, one complication of these famous applications is that the communication terminals are relatively stationary or have a very low velocity compared to the speed of the communication medium. Another common feature of them is that only a low data transfer rate is usually employed. It is then natural to ask: what if users require a high data transfer rate while moving rapidly?

Let us consider the following two scenarios:

### **Vehicular communications:**

Fast moving vehicles in future intelligent transport systems will be able to “talk” to each other for information exchange. These vehicles could be cars running on the road, or airplanes approaching the airport, which may request a massive real-time data transfer.

### **Underwater acoustic communications:**

Underwater vehicles in future underwater communication networks can establish a continuous high-rate data communication link with a distant mother platform using acoustic waves. These vehicles can be



Example: Vehicular communications

Example: Underwater acoustic communications

**Figure 1.1:** Illustrations of communications between high-mobility terminals

remote detectors for offshore oil exploration, or submarines diving in shallow water environments.

These two examples, as depicted in Fig. 1.1, impose a common requirement on future wireless communication systems, which is a high data transfer rate between fast moving terminals.

In fact, in addition to the above examples, many other familiar communication systems manifest themselves with the same development trend, which is that they will not only require high data rates but also support rapidly moving users in the future. Let us consider the mobile phone system for instance. The first and second generation mobile phone systems, which emerged respectively in the 1980's and 1990's, were mainly developed for voice communications, which have low demands on the data rate. From the earliest years of this century, the third generation (3G) technology starts to be widely adopted, such as the Universal Mobile Telecommunications System (UMTS). Nowadays, 3G phone systems have been acting as digital mobile multimedia offering several wireless data services like video, graphics and other information besides voice. The basic requirement for these data services is high data transfer rate, which is beyond the capability of previous generation systems. Some examples that support advanced data services similarly as the 3G technology include wireless local area networks (WLANs) and digital video broadcasting (DVB). However, all these existing wireless systems are only able to provide low data rates (e.g., UMTS) or completely break down (e.g., DVB) at high speeds. Since 2004, the Long Term

Evolution (LTE) initiated by the 3rd Generation Partnership Project (3GPP) has been referred to as a major step towards fourth generation (4G) systems. One of the primary goals of the future 4G technology is to support rapidly moving users and even faster data transfers.

Increasing the data rate is always problematic as stated by Shannon's channel-capacity theorem, which states that the maximal achievable data rate is ultimately limited by the effective bandwidth, the available transmit power, and the interference energy (e.g., from the ambient noise). Solely increasing the transmit power is usually avoided because of the battery limitation on mobile devices. Hence the alternative is to increase the transmission bandwidth. In recent years, ultra-wideband (UWB) has been introduced to satisfy the high user data rate requirement. However, with the increased spectrum bandwidth, time dispersion of the transmitted symbols appears, inducing inter-symbol interference. When the mobility of the communication terminals is present, the performance of communication systems becomes even worse because the Doppler effect further deteriorates the conditioning of communication channels. An extreme example is the aforementioned underwater acoustic communications (UAC). On the one hand, acoustic communication is wideband in nature because its adopted transmission bandwidth is comparable to the central frequency. On the other hand, fast moving underwater vehicles usually introduce severe Doppler effects since the speed of sound propagation in water is very low compared to terrestrial radio. In this sense, UAC is acknowledged as one of the most challenging data communication applications today.

In summary, we claim that for providing a high data transfer rate for fast moving users, future communication systems will definitely have to combat a very adverse communication channel which imposes a big challenge on receiver designs.

## 1.1 Problem Statement and Research Objectives

When the bandwidth of the transmitted signal is larger than the coherence bandwidth of the communication channel, it gives rise to time dispersion of the transmitted symbols and frequency selectivity of the channel. The

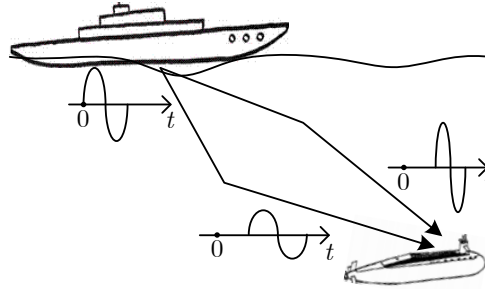


**Figure 1.2:** An illustration of the multiple-path propagation encountered in underwater acoustic communications.

time dispersion of the transmitted symbols induces intersymbol interference (ISI) when multipath propagation is present, and the frequency selectivity indicates that different frequency components exhibit distinct attenuations. Additionally, the Doppler effect caused by mobility gives rise to frequency dispersion of the transmitted symbols or time selectivity of the channel, especially when the channel coherence time is smaller than the symbol period. Consequently, it is likely that future wireless communication systems have to handle doubly-selective (i.e., frequency- and time-selective) channels.

The Doppler effect in combination with multipath propagation can cause severe interferences to a communication system in addition to the ambient noise, thus deteriorating its service quality. Many approaches to compensate for the Doppler effect and multipath attenuations have already been proposed in the literature during the past decades, e.g. [2–11]. To our knowledge, however, little attention is paid in these works to an efficient architecture for the hardware implementation of these proposed signal processing schemes. Another joint feature is that most of these methods adopt a relatively narrow bandwidth for wireless communications, i.e., they work in the narrowband regime. In other words, they all assume that the Doppler effect manifests itself by means of the well-known frequency shifts [12–16]. However, when the transmission bandwidth is comparable with the employed carrier frequency, or if the velocity of the wireless terminals is considerable relative to the speed of the communication medium, this narrowband assumption is violated and wideband communications are thus introduced. It

is noteworthy here that the concepts of “wideband” and “narrowband” may be different in various contexts. In this thesis, we adopt a definition that refers to the fractional bandwidth (i.e., the ratio of the baseband bandwidth divided by the center frequency), rather than the absolute bandwidth. For instance, one can define that when the fractional bandwidth is larger than 20%, the transmission is called wideband, otherwise narrowband. This definition is popularly used in acoustics and radar [17]. In this sense, an UAC system, which operates within a spectral bandwidth from 4 kHz to 8 kHz, is typically wideband. However, some broadband systems that have a small fractional bandwidth, e.g., in [18], would not qualify as wideband but is narrowband in this thesis. In a wideband scenario, the Doppler effect cannot be approximated by frequency shifts anymore as in the narrowband case but manifests itself by means of Doppler scales [15,19–24]. In this case, the transmitted signal is measurably compressed or dilated at the receiver because of the wideband time-varying channel. This phenomenon arises in a variety of wireless communication applications, such as underwater acoustic communication and wideband terrestrial radio frequency systems utilizing spread-spectrum or ultra-wideband signaling. Fig. 1.2 illustrates an UAC signal is transmitted along two distinct propagation paths, which are characterized by different Doppler effects and timing delays. In addition to the delays, the signal along each path experiences a different dilation or compression rather than the frequency shift that is well known in the narrowband case. In the following chapter, we will discuss more details about these different behaviors of the Doppler effect (i.e., in the wideband case and the narrowband case). Since the wideband channels exhibit key fundamental differences [15] relative to the more commonly considered narrowband channels, new transceiver designs for wideband time-varying systems are inevitable [25].

In this context, open research questions are:

- How should we design the receiver and/or the transmitter, when Doppler scales emerge in a wideband time-varying channel?
- For a wideband time-varying system, can we still adopt any knowledge from previous receiver designs that are used for narrowband time-varying channels?

Based on the questions above, we will address the following specific research questions:

- It is wise to review previous knowledge about transceiver design for narrowband time-varying channels, before studying wideband systems. Although many receiver design methods have been proposed to handle narrowband time-varying channels, an investigation from the aspect of the hardware implementation of an existing algorithm for such receivers lacks, and is interesting especially to circuit design engineers. How can it be implemented efficiently? Is there any algorithm simplification to reduce the hardware resource cost with only a minor performance influence? If a wideband receiver design can share similar structures with a narrowband receiver, these hardware implementation approaches can be used for both cases.
- When an adverse wideband time-varying channel is present, what are its effects on a traditional transmission scheme compared to those well-known effects in a narrowband case? How to reduce the complexity of the channel equalization then?
- Since existing transceiver designs are not suitable for wideband time-varying channels, can we intelligently design a new transmission scheme such that existing low-complexity equalizers, which are used for narrowband cases, can be adopted for wideband communications? In this case, existing hardware implementation of narrowband receivers may be adapted with minor changes for wideband systems.
- Another issue for wideband time-varying systems can be the challenge of obtaining precise channel information that is needed for the channel equalization. How to enhance the robustness of the equalization of a wideband time-varying channel, thus enhancing the detection of the transmitted data?

The answers to these questions will be important for the design of future wireless communication systems, which not only provide a high data transfer rate but also support fast moving users.



## 1.2 Contributions and Outline

The rest of the thesis is organized as follows.

In Chapter 2, we first give a schematic overview of wireless communication systems. Then, we introduce wireless channel models and describe their detailed expressions in two different scenarios, i.e., the narrowband and wideband regimes. The relations and differences of these two channel models are discussed. Additionally, multi-carrier transmission techniques are reviewed.

In Chapter 3, we consider an orthogonal frequency-division multiplexing (OFDM) transmission over a narrowband channel. The method of modeling the narrowband OFDM time-varying channels by a basis expansion model (BEM) is reviewed. Various architectures to implement the least-squares (LS) channel estimation and its corresponding zero-forcing (ZF) channel equalization are investigated by using different BEM's. The experimental results suggest that the OFDM receiver design tailored for a particular BEM model (i.e., the CCE-BEM) among these models is more appealing since it allows for a much more efficient hardware architecture while still maintaining a high detection accuracy.

The publications related to this chapter are the following:

- T. Xu; Z. Tang; H. Lu; R. van Leuken. Memory and Computation Reduction for Least-Square Channel Estimation of Mobile OFDM Systems. In *Proc. IEEE International Symposium on Circuits and Systems (ISCAS)*, pages 3556–3559, Seoul, Korea, May 2012.
- T. Xu, M. Qian, and R. van Leuken. Parallel Channel Equalizer for Mobile OFDM Systems. In *Proc. International Workshop on Circuits, Systems and Signal Processing (ProRISC)*, pages 200–203, Rotterdam, Netherlands, October 2012.

In Chapter 4, we are still interested in OFDM transmissions but over a wideband time-varying channel. We first seek to quantify the amount of interference resulting from wideband channels which are assumed to follow the multi-scale/multi-lag (MSML) model. To perform the channel equalization, we propose to use the conjugate gradient (CG) algorithm whose per-

formance is less sensitive to the channel condition than, e.g., a least-squares approach. The suitability of the preconditioning technique, which often accompanies the CG to accelerate the convergence, is also discussed. We show that in order for the diagonal preconditioner to function properly in the corresponding domain, optimal resampling is indispensable.

The publications related to this chapter are the following:

- T. Xu, Z. Tang, R. Remis, and G. Leus. Iterative Equalization for OFDM Systems over Wideband Multi-scale Multi-lag Channels. *EURASIP Journal on Wireless Communications and Networking*, DOI:10.1186/1687-1499-2012-280, August 2012.
- T. Xu, Z. Tang, G. Leus, and U. Mitra. Time- or Frequency-Domain Equalization for Wideband OFDM Channels?. In *Proc. International Conference on Acoustics, Speech, and Signal Processing (ICASSP)*, pages 3556–3559, Kyoto, Japan, March 2012.
- Z. Tang, R. Remis, T. Xu, G. Leus and M.L. Nordenvaad. Equalization for Multi-Scale Multi-Lag OFDM channels . In *Proc. Allerton Conference on Communication, Control, and Computing*, pages 654–661 , Monticello, IL, USA, September 2011.

In Chapter 5, we consider wideband time-varying channels which have the MSML nature, but propose new transmission schemes instead of OFDM. By carefully designing the transmit signal, we propose a simplified receiver scheme similarly as experienced by the narrowband OFDM transmissions. The benefit of this similarity is to make existing low-complexity equalizers, previously used in narrowband systems, still viable for wideband communications. Specifically, a new parameterized data model for wideband LTV channels is first proposed, where the continuous MSML channel is approximated by discrete channel coefficients. We argue that this parameterized data model is always subject to discretization errors in the baseband. However, by designing the transmit/receive pulse smartly and imposing a multi-branch structure on the receiver, we are able to eliminate the impact of the discretization errors on equalization. In addition, we propose a novel multi-layer transmit signaling scheme to enhance the bandwidth efficiency. It turns

out that the inter-layer interference, induced by the multi-layer transmitter, can also be minimized by the same design of the transmit/receive pulse. As a result, the effective channel experienced by the receiver can then be described by a block diagonal matrix, with each diagonal block being strictly banded similarly as observed by narrowband OFDM systems over narrowband time-varying channels.

The publications related to this chapter are the following:

- T. Xu, Z. Tang, G. Leus, and U. Mitra. Multi-Rate Block Transmissions over Wideband Multi-Scale Multi-Lag Channels. *IEEE Transactions on Signal Processing*, 2012.
- T. Xu, G. Leus, and U. Mitra. Orthogonal Wavelet Division Multiplexing for Wideband Time-Varying Channels. In *Proc. International Conference on Acoustics, Speech, and Signal Processing (ICASSP)*, pages 3556–3559, Prague, Czech, May 2011.
- G. Leus, T. Xu, and U. Mitra. Block Transmission over Multi-Scale Multi-Lag Wireless Channels. In *Proc. Asilomar Conference on Signals, Systems, and Computers*, pages 1050–1054, Pacific Grove, CA, USA, November 2010.

In Chapter 6, we focus on the robustness of wideband communications, and propose an adaptive multi-layer turbo equalization at the receiver. Different from the previous two chapters, herein we do not require perfect knowledge of the wideband channel information which is usually difficult to obtain. We use a multi-band transmitter which reduces the receiver complexity while still maintaining a high data rate. At the receiver, we propose a multi-branch framework, where each branch is aligned with the scale and delay of one path in the propagation channel. We show that by optimally designing the transmit and receive filter, the discrete signal at each branch can be characterized by a time-invariant finite impulse response (FIR) system subject to a carrier frequency offset (CFO). This enables a simpler equalizer design: a phase-locked loop (PLL), which aims to eliminate the CFO is followed by a time-invariant FIR filter. The updating of both the PLL and the filter taps is achieved by leveraging the soft-input soft-output (SISO) information yielded by a turbo decoder.

The publications related to this chapter are the following:

- T. Xu, Z. Tang, G. Leus, and U. Mitra. Adaptive Multi-Layer Turbo Equalization for Underwater Acoustic Communications. accepted by *MTS/IEEE OCEANS 2012*, Virginia, USA, October 2012.
- T. Xu, Z. Tang, G. Leus, and U. Mitra. Robust Transceiver Design with Multi-layer Adaptive Turbo Equalization for Doppler-Distorted Wideband Channels. *IEEE Transactions on Wireless Communications*, submitted. October 2012.

Besides the above works that are presented in this thesis, other contributions have been made in the following publications:

- H. Lu, T. Xu, H. Nikookar, and L.P. Ligthart. Performance Analysis of the Cooperative ZP-OFDM: Diversity, Capacity and Complexity. *International Journal on Wireless Personal Communications*, DOI:10.1007/s11277-011-0470-9, December 2011.
- H. Lu, T. Xu and H. Nikookar. Cooperative Communication over Multi-scale and Multi-lag Wireless Channels. In *Ultra Wideband*, ISBN:979-953-307-809-9, InTech, March 2012.
- H. Lu, H. Nikookar, and T. Xu. OFDM Communications with Cooperative relays. In *Communications and Networking*, ISBN:978-953-307-114-5, InTech, September 2010.
- H. Lu, T. Xu, M. Lakshmanan, and H. Nikookar. Cooperative Wavelet Communication for Multi-relay, Multi-scale and Multi-lag Wireless Channels. In *Proc. IEEE Vehicular Technology Conference (VTC)*, pages 1–5, Budapest, Hungary, May 2011.
- H. Lu, T. Xu, and H. Nikookar. Cooperative Scheme for ZP-OFDM with Multiple Carrier Frequency Offsets over Multipath Channel. In *Proc. IEEE Vehicular Technology Conference (VTC)*, pages 11–15, Budapest, Hungary, May 2011.

- 
- H. Lu, T. Xu, and H. Nikookar. Performance Analysis of the STFC for Cooperative ZP-OFDM Diversity, Capacity, and Complexity. In *Proc. International Symposium on Wireless Personal Multimedia Communications (WPMC)*, pages 11–14, Recife, Brazil, October 2010.
  - T. Xu, M. Qian, and R. van Leuken. Low-Complexity Channel Equalization for MIMO OFDM and its FPGA Implementation. In *Proc. International Workshop on Circuits, Systems and Signal Processing (ProRISC)*, pages 500–503, Veldhoven, Netherlands, November 2010.
  - T. Xu, H.L. Arriens, R. van Leuken and A. de Graaf. Precise SystemC-AMS Model for Charge-Pump Phase Lock Loop with Multiphase Outputs. In *Proc. IEEE International Conference on ASIC (ASICON)*, pages 50–53, Changsha, China, October 2009.
  - T. Xu, H.L. Arriens, R. van Leuken and A. de Graaf. A Precise SystemC-AMS model for charge pump phase lock loop verified by its CMOS circuit. In *Proc. International Workshop on Circuits, Systems and Signal Processing (ProRISC)*, pages 412–417, Veldhoven, Netherlands, November 2009.



## Chapter 2

---

## Preliminaries

*The wireless telegraph is not difficult to understand.  
The ordinary telegraph is like a very long cat. You pull  
the tail in New York, and it meows in Los Angeles.  
The wireless is exactly the same, only without the cat.*

Albert Einstein

Any communication system is in principle composed of three components, i.e., the transmitter, the communication channel and the receiver. Given a certain transmit waveform, the receiver design can be adapted to the type of communication channels. In this chapter, we first give a schematic overview of wireless communication systems. Then, we introduce wireless channel models and describe their detailed expressions for two different scenarios: narrowband and wideband. We here highlight again that the definition of “narrowband” and “wideband” in this thesis refers to the fractional bandwidth rather than the absolute bandwidth [17]. In narrowband systems, the Doppler effect manifests itself mainly as a frequency shift around the carrier frequency of the transmitted signals, while in wideband systems, the Doppler effect translates into a time scaling of the signal waveform. Finally, multi-carrier transmission techniques are reviewed.

### 2.1 Elements of Wireless Communications

Let us consider a wireless communication system, as depicted in Fig. 2.1. The source that contains information is first modulated at the transmitter to prepare for the propagation. The transmitted signal carrying the source information is then propagated over a wireless channel that can be a radio link or an acoustic environment. The received signal is demodulated at the receiver and the source information is finally recovered at the destination. In

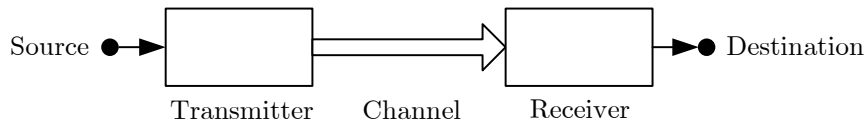


**Figure 2.1:** *Elements of a communication system*

practice, the transceiver (i.e., both the transmitter and the receiver) should be smartly designed according to the channel. Otherwise, on the one hand, a bulky communication system can be too expensive to be practical, and on the other hand, it may fail to establish a viable wireless link. Consequently, knowledge about the characteristics of the underlying channels is necessary for the transceiver design.

## 2.2 Wireless Fading Channels

Modeling the wireless signal propagation in general can be complex (e.g. using Maxwell's equations for electromagnetic wave propagation). Practical wireless channel modeling resorts to statistical methods, i.e., using a stochastic model with limited parameters to characterize the channel. An important parameter of a channel model is the fading effect, which refers to the changes in the received signal amplitude and phase over time and frequency. There are two types of channel fading: large-scale fading and small-scale fading. Large-scale fading statistically represents the average signal power attenuation as a function of propagating distance. It is generally assumed constant over time and independent of frequency. Small-scale fading describes random time-varying changes in signal amplitude and phase due to multipath propagation and relative movement between communication terminals. More detailed background information can be found, e.g., in [14, 26, 27]. In the remainder of this thesis, we will refer to the small-scale fading as 'fading' unless explicitly defined. Besides fading, if the channel coherence bandwidth is larger than the bandwidth of the transmitted signal, the time dispersion induces intersymbol interference (ISI). In addition, the Doppler effect causes channel temporal changes especially when the chan-



nel coherence time is smaller than the symbol period.

### 2.2.1 Parametric Channel Model

We consider a continuous-time linear time-varying (LTV) system model, where the embedded communication channel is perturbed by additive ambient noise, given by

$$\bar{r}(t) = \int_{-\infty}^{\infty} \bar{h}(t, \tau) \bar{s}(t - \tau) d\tau + \bar{w}(t), \quad (2.1)$$

where  $\bar{s}(t)$  and  $\bar{r}(t)$  are respectively the actual transmitted and received signal (normally in passband),  $\bar{h}(t, \tau)$  is the channel impulse response, and  $\bar{w}(t)$  is the noise.

When the above channel consists of resolvable propagation paths as usual, we can specify  $\bar{h}(t, \tau)$  as

$$\bar{h}(t, \tau) = \sum_{l=-\infty}^{\infty} \bar{h}_l \delta(\tau - \tau_l(t)), \quad (2.2)$$

where the  $l$ th path can mathematically be characterized by the path gain  $\bar{h}_l$  and the propagation delay  $\tau_l(t)$  that is dependent on time  $t$ . In this way, we can rewrite (2.1) as

$$\begin{aligned} \bar{r}(t) &= \int_{-\infty}^{\infty} \sum_{l=-\infty}^{\infty} \bar{h}_l \delta(\tau - \tau_l(t)) \bar{s}(t - \tau) d\tau + \bar{w}(t), \\ &= \sum_{l=-\infty}^{\infty} \bar{h}_l \bar{s}(t - \tau_l(t)) + \bar{w}(t), \end{aligned} \quad (2.3)$$

which indicates that the received signal is a sum of various copies of the transmitted signal, each of them distinctly delayed and attenuated.

To explicate each propagation delay component (i.e.,  $\tau_l(t)$ ), let us assume the  $l$ th path is related to a radial velocity  $v_l^{(T)}$  and  $v_l^{(R)}$  for the transmitter and the receiver, respectively. The time-varying delay component can be

expressed as [15, 19]

$$\tau_l(t) = \tau_l - \frac{(v_l^{(R)} - v_l^{(T)})(t - \tau_l)}{c + v_l^{(T)}},$$

where  $\tau_l$  is constant and uniquely determined by the initial delay of the  $l$ -th path,  $(v_l^{(R)} - v_l^{(T)})(t - \tau_l)$  reflects the length change of the  $l$ -th path along time, while  $(c + v_l^{(T)})$  is the effective signal propagation speed along the  $l$ -th path with  $c$  being the speed of the communication medium. To this end, let us introduce a time scaling factor as

$$\alpha_l = \frac{c + v_l^{(R)}}{c + v_l^{(T)}}$$

according to the Doppler effect, and thus adapt  $\tau_l(t)$  as

$$\tau_l(t) = \alpha_l \tau_l - (\alpha_l - 1)t. \quad (2.4)$$

Next, we substitute (2.4) into (2.3) and have

$$\bar{r}(t) = \sum_{l=-\infty}^{\infty} \bar{h}_l \sqrt{\alpha_l} \bar{s}(\alpha_l(t - \tau_l)) + \bar{w}(t), \quad (2.5)$$

where we also introduced a factor  $\sqrt{\alpha_l}$  which is an energy normalization factor as used in many literatures, e.g., [15, 20], although one may also combine it into the channel gain  $\bar{h}_l$ , e.g., in [28, 29]. Obviously, when the radial velocity  $v_l = v_l^{(R)} - v_l^{(T)} \equiv 0$ , i.e.,  $\alpha_l \equiv 1$ , for all paths, the channel embedded in (2.5) becomes time invariant. If  $\alpha_l \equiv \alpha_{l'}$  for any two paths for  $l \neq l'$  but  $\tau_l \neq \tau_{l'}$ , the channel is said to have a single-scale multi-lag (SSML) nature [28, 30]. However, in general, there are at least two paths for which  $\alpha_l \neq \alpha_{l'}$  and  $\tau_l \neq \tau_{l'}$ , and in this case the above system exhibits a multi-scale multi-lag (MSML) character [21, 22]. For a realistic channel, we can assume that  $\alpha_l \in [1, \alpha_{\max}]$  and  $\tau_l \in [0, \tau_{\max}]$ <sup>1</sup>, where  $\alpha_{\max} \geq 1$  and  $\tau_{\max} \geq 0$  determines the scale spread and delay spread, respectively.

<sup>1</sup>As a matter of fact, the case where  $\alpha_l < 1$  or  $\tau_l < 0$  can be converted to the current situation by means of proper resampling and timing at the receiver. This justifies us to simply consider a compressive and causal scenario, for the description ease in this thesis, without loss of generality.

The transmitted signal  $\bar{s}(t) = \Re\{s(t)e^{j2\pi f_c t}\}$  is normally located in pass-band, and is up-converted from the baseband signal  $s(t)$  with  $f_c$  being the central carrier frequency. In an analogous manner, the equivalent complex baseband received signal  $r(t)$  is related with the received passband signal  $\bar{r}(t)$  as  $\bar{r}(t) = \Re\{r(t)e^{j2\pi f'_c t}\}$ . Note that  $f'_c$  may not be equal to  $f_c$ . Therefore, the baseband system model corresponding to (2.5) can be given by (see for more details about the complex baseband equivalent derivation in [26,27])

$$\begin{aligned} r(t) &= e^{-j2\pi f'_c t} \sum_{l=-\infty}^{\infty} \bar{h}_l \sqrt{\alpha_l} s(\alpha_l(t - \tau_l)) e^{j2\pi \alpha_l f_c (t - \tau_l)} + w(t), \\ &= \sum_{l=-\infty}^{\infty} h_l \sqrt{\alpha_l} s(\alpha_l(t - \tau_l)) e^{j2\pi(\alpha_l f_c - f'_c)t} + w(t), \end{aligned} \quad (2.6)$$

with  $h_l = \bar{h}_l e^{-j2\pi \tau_l \alpha_l f_c}$ , and  $w(t)$  is the baseband version of  $\bar{w}(t) = \Re\{w(t)e^{j2\pi f'_c t}\}$ . When  $\alpha_l \neq 1$  exists, the embedded channel above is time varying. (2.6) also indicates that even when the transceiver adopts an identical central frequency, i.e.,  $f_c = f'_c$ , the baseband signal is still corrupted by carrier frequency offsets [c.f., the term  $(\alpha_l f_c - f'_c)$  in (2.6)].

It is noteworthy that the system descriptions in both (2.5) and (2.6) look different from more familiar LTV communication system models, e.g., described in [14]. Specifically, when people talk about the time variation of LTV channels, they normally refer to Doppler frequency shifts instead of the time-domain scales adopted in either (2.5) or (2.6). Moreover, it is also commonly assumed that the baseband signal should be free of the carrier frequency offset (CFO) when the receiver adopts the same central frequency as the transmitter. We will come back to these issues later on, showing that the above descriptions for LTV systems actually correspond to wideband communications and are the generalized version of the more familiar narrow-band system models given in [14].

## I. Wideband LTV Systems

*Continuous Channel Model:* Wideband LTV systems are often expressed as an integral, e.g., in [15, 20–22], given by

$$\bar{r}(t) = \int_0^{\tau_{\max}} \int_1^{\alpha_{\max}} \bar{h}(\alpha, \tau) \sqrt{\alpha} \bar{s}(\alpha(t - \tau)) d\alpha d\tau + \bar{w}(t), \quad (2.7)$$

which can be viewed as a generalization of (2.5) in an environment where a rich number of scatterers exists and the channel can thus be viewed as a collection of fast moving scatterers that are continuously distributed in range and velocity [20]. Here,  $\bar{h}(\alpha, \tau)$  is known as the *wideband spreading function* [20]. In the case of (2.5), we can explicate  $\bar{h}(\alpha, \tau) = \sum_{l=-\infty}^{\infty} \bar{h}_l \delta(\alpha - \alpha_l) \delta(\tau - \tau_l)$ . More detailed information about the wideband spreading function can be found, e.g., in [20, 23, 24, 31, 32].

To derive the equivalent baseband model, we can down-convert (2.7) using  $f'_c$  [c.f. (2.6)] and write

$$r(t) = \int_0^{\tau_{\max}} \int_1^{\alpha_{\max}} e^{j2\pi(\alpha f_c - f'_c)t} h(\alpha, \tau) \sqrt{\alpha} s(\alpha(t - \tau)) d\alpha d\tau + w(t), \quad (2.8)$$

where  $h(\alpha, \tau) = \bar{h}(\alpha, \tau) e^{-j2\pi\alpha\tau f_c}$ .

*Discrete Channel Model:* In order to facilitate the digital signal processing at the receiver, efforts to discretize the wideband channel embedded in (2.7) can be found, e.g., in [21, 22]. Herein, we cite the discrete scale-lag model provided by these works to approximate the wideband LTV systems in (2.7), whose noiseless expression is given by

$$\bar{r}^{\text{SL}}(t) = \sum_{r=0}^{R_\star} \sum_{l=0}^{\bar{L}_\star(r)} \bar{h}_{r,l} a_\star^{r/2} \bar{s}(a_\star^r(t - l\bar{T}_\star/a_\star^r)), \quad (2.9)$$

where we use <sup>SL</sup> in the superscript to emphasize that in this model both the scale and lag parameters are discretized. This model is known as the *scale-lag canonical model* in [21, 22, 33], where  $a_\star$  is referred to as the *basic scaling factor*

in [21] or *dilation spacing* in [22, 33], and  $\bar{T}_*$  is referred to as the *translation spacing* in [22, 33]. In practice, one approach [33] to seek a proper  $a_*$  and  $\bar{T}_*$  is linked to the wideband ambiguity function (WAF) of  $\bar{s}(t)$ , given by

$$\bar{\chi}(\alpha, \tau) = \int \bar{s}(t) \sqrt{\alpha} \bar{s}(\alpha(t - \tau)) dt, \quad (2.10)$$

such that  $a_*$  is defined as the first zero-crossing of  $\bar{\chi}(\alpha, 0)$  and  $\bar{T}_*$  as the first zero-crossing of  $\bar{\chi}(1, \tau)$ . An alternative approach [21] assumes that  $\bar{s}(t)$  has a single-sided bandwidth  $\bar{W}$  and Mellin support  $M$ . We note that the Mellin support is the scale analogy of the Doppler spread for narrowband LTV channels. Specifically, the Mellin support of a signal  $\bar{s}(t)$  is the support of the Mellin transform of  $\bar{s}(t)$  which is given by  $\int_0^\infty \bar{s}(t) t^{\varpi-1} dt$  with  $\varpi$  is the Mellin variable. More details about the Mellin transform can be found in [34, 35]. It is then well-known that in the Fourier domain Nyquist sampling theorem dictates that  $\bar{T}_* = 1/\bar{W}$  to ensure perfect signal reconstruction. Similarly we can apply an adapted Nyquist sampling result in the Mellin domain to obtain  $a_* = e^{1/M}$ . With the obtained  $a_*$  and  $\bar{T}_*$ , we follow [21] to define  $R_* = \lceil \ln \alpha_{\max} / \ln a_* \rceil$ , and  $\bar{L}_*(r) = \lceil a_*^r \tau_{\max} / \bar{T}_* \rceil$ . Under these conditions, the wideband spread function  $h(\alpha, \tau)$  is discretized as

$$\bar{h}_{r,l} = \bar{h}^{\text{SL}}(a_*^r, l\bar{T}_*/a_*^r), \quad (2.11)$$

where  $\bar{h}^{\text{SL}}(\alpha, \tau)$  is the scale-lag smoothed version of  $\bar{h}(\alpha, \tau)$  [21], which admits an expression as

$$\begin{aligned} \bar{h}^{\text{SL}}(\alpha, \tau) &= \int_1^{\alpha_{\max}} \int_0^{\tau_{\max}} \bar{h}(\alpha', \tau') \\ &\times \text{sinc}\left(\frac{\ln \alpha - \ln \alpha'}{\ln a_*}\right) \text{sinc}\left(\alpha \frac{\tau - \tau'}{\bar{T}_*}\right) d\tau' d\alpha'. \end{aligned} \quad (2.12)$$

The above has a slightly different definition than that in [22]: it implicitly assumes bandwidth and Mellin support limitations at the transmitter, while [22] assumes that the frequency support is limited at the transmitter while the Mellin support is limited at the receiver. However, they both achieve an identical description for these  $\bar{h}_{r,l}$ 's.

We note that we only provide a discrete system model in passband above. One may follow (2.9) to straightforwardly derive its complex baseband equiv-

alent as

$$r^{\text{SL}}(t) = \sum_{r=0}^{R_\star} \sum_{l=0}^{\bar{L}_\star(r)} h_{r,l} a_\star^{r/2} s(a_\star^r(t - l\bar{T}_\star/a_\star^r)) e^{j2\pi(a_\star^r f_c - f_c) t}, \quad (2.13)$$

where  $h_{r,l} = \bar{h}_{r,l} e^{-j2\pi l T_\star a_\star^r f_c}$ . However, we note that the derivation of a baseband model of a wideband system can be different from (2.13), and we refer readers to Chapter 4 for more details.

## II. Narrowband LTV Systems

*Continuous Channel Model:* Generally speaking, it is difficult to process the wideband received signal because, in addition to the reshaping of the wideband signal waveforms due to Doppler scales, the residual multiple CFOs in the basedband are cumbersome at the receiver. It is possible to simplify the channel models given by (2.8) and (2.13), but under a narrowband assumption. The narrowband assumption can be described concisely as follows:

1. The effective baseband bandwidth  $W$  is very small compared to the central frequency  $f_c$ , e.g.,  $W/f_c \ll 1$ .
2. The velocities,  $v$ , are very small compared to the speed of the communication medium  $c$ , e.g.,  $\max\{|2v/c|\} \ll 1$ .

For more detailed information about these narrowband assumptions, see [15, 16, 20]. When both of the above conditions are satisfied, the communication system can be called a narrowband system.

To derive the narrowband system model [12], let us start with the frequency-domain equivalent of (2.7), regardless of the ambient noise, given by

$$\begin{aligned} \bar{R}(f) &= \int_0^{\tau_{\max}} \int_1^{\alpha_{\max}} \bar{h}(\alpha, \tau) \sqrt{\alpha} \bar{S}\left(\frac{f}{\alpha}\right) e^{-j2\pi\tau f} d\alpha d\tau \\ &= \int_0^{\tau_{\max}} \int_0^{\alpha_{\max}^{-1}} \sqrt{1 + \beta} \bar{h}(1 + \beta, \tau) \bar{S}\left(\frac{f}{1 + \beta}\right) e^{-j2\pi\tau f} d\beta d\tau \end{aligned}$$

where  $\bar{R}(f)$  and  $\bar{S}(f)$  is the Fourier transform of  $\bar{r}(t)$  and  $\bar{s}(t)$ , respectively, and we have substituted  $\alpha = 1 + \beta$  in the second equation above. Since  $\alpha = \frac{c+v}{c-v}$  and  $\max\{|\frac{2v}{c}|\} \ll 1$ , we have

$$\beta = \alpha - 1 = \frac{2v}{c-v} \approx \frac{2v}{c},$$

which means  $|\beta| \ll 1$ . Therefore, by noticing

$$\frac{1}{1+\beta} = 1 - \beta + \beta^2 - \beta^3 + \dots \approx 1 - \beta,$$

we are allowed for the approximation given by

$$\bar{R}(f) \approx \int_0^{\tau_{\max}} \int_0^{\alpha_{\max}-1} \sqrt{1+\beta} \bar{h}(1+\beta, \tau) \bar{S}(f-\beta f) e^{-j2\pi\tau f} d\beta d\tau. \quad (2.14)$$

Moreover, since we assume that  $W/f_c \ll 1$  and the frequency component in  $\bar{S}(f)$  is limited by  $f \in [f_c - W/2, f_c + W/2]$ , we can further approximate (2.14) as

$$\begin{aligned} \bar{R}(f) &\approx \int_0^{\tau_{\max}} \int_0^{\alpha_{\max}-1} \sqrt{1+\beta} \bar{h}(1+\beta, \tau) \bar{S}(f-\beta f_c) e^{-j2\pi\tau f} d\beta d\tau \\ &= \int_0^{\tau_{\max}} \int_0^{\theta_{\max}} \bar{h}_N(\theta, \tau) \bar{S}(f-\theta) e^{-j2\pi\tau f} d\theta d\tau \end{aligned}$$

where we introduced a frequency shift

$$\theta = \beta f_c \approx \frac{2v}{c} f_c, \quad (2.15)$$

and the *narrowband spreading function*  $\bar{h}_N(\theta, \tau)$  is given by

$$\bar{h}_N(\theta, \tau) = \sqrt{\frac{f_c + \theta}{f_c}} \bar{h}\left(\frac{f_c + \theta}{f_c}, \tau\right).$$

Now, we convert  $\bar{R}(f)$  back to the time domain and obtain

$$\bar{r}(t) \approx \int_0^{\tau_{\max}} \int_0^{\theta_{\max}} \bar{h}_N(\theta, \tau) \bar{s}(t-\tau) e^{j2\pi\theta t} d\theta d\tau, \quad (2.16)$$

which indicates that a narrowband received signal can be represented by a superposition of the transmitted signal with time shifts  $\tau \in [0, \tau_{\max}]$  and frequency shifts  $\theta \in [0, \theta_{\max}]$  where  $\tau_{\max}$  and  $\theta_{\max} = (\alpha_{\max} - 1)f_c$  is the delay spread and Doppler shift spread, respectively. In other words, a Doppler frequency shift  $\theta$  is adopted to represent the time variation of the narrowband channel instead of a Doppler scale  $\alpha$ .

Similarly as in wideband scenarios, the complex baseband equivalent of the narrowband system in (2.16) can be given by

$$r(t) = e^{j2\pi(f_c - f'_c)t} \int_0^{\tau_{\max}} \int_0^{\theta_{\max}} h_N(\theta, \tau) s(t - \tau) e^{j2\pi\theta t} d\theta d\tau, \quad (2.17)$$

where  $f'_c$  is the central frequency adopted at the receiver, which may be different from  $f_c$ , and  $h_N(\theta, \tau) = \bar{h}_N(\theta, \tau) e^{-j2\pi\tau f_c}$ .

*Discrete Channel Model:* Discretizing the narrowband LTV channel embedded in (2.16) is thoroughly studied. One typical discretization approach is given by

$$\bar{r}^{\text{DL}}(t) = \sum_{q=0}^{Q_\star} \sum_{l=0}^{\bar{L}_\star} \bar{h}_{q,l} \bar{s}(t - l\bar{T}_\star) e^{j2\pi q\theta_\star t}, \quad (2.18)$$

which describes a well-known channel model in terms of sampled time delays and frequency shifts [36], called the *Doppler-shift-lag canonical model*, with  $T_\star$  and  $\theta_\star$  being the arithmetic time resolution and frequency shift resolution, respectively. Here we use <sup>DL</sup> in the superscript to emphasize that in this model both the Doppler-shift and lag parameters are discretized. Assuming  $\bar{s}(t)$  has an single-sided bandwidth of  $\bar{W}$  and a time period of  $\Omega$ , we have  $\bar{T}_\star = 1/\bar{W}$  and  $\theta_\star = 1/\Omega$  [36]. Hence,  $\bar{h}_{q,l} = \bar{h}^{\text{DL}}(q\theta_\star, l\bar{T}_\star)$  with

$$\begin{aligned} \bar{h}^{\text{DL}}(\theta, \tau) &= \frac{1}{\bar{T}_\star \theta_\star} \int_0^{\tau_{\max}} \int_0^{\theta_{\max}} \bar{h}_N(\theta', \tau') \\ &\quad \text{sinc}\left(\frac{\tau - \tau'}{\bar{T}_\star}\right) \text{sinc}\left(\frac{\theta - \theta'}{\theta_\star}\right) e^{-j2\pi\frac{\theta - \theta'}{\theta_\star}} d\theta' d\tau', \end{aligned} \quad (2.19)$$

where  $\bar{L}_\star = \lceil \tau_{\max}/\bar{T}_\star \rceil$  and  $Q_\star = \lceil \theta_{\max}/\theta_\star \rceil$  as defined in [36].



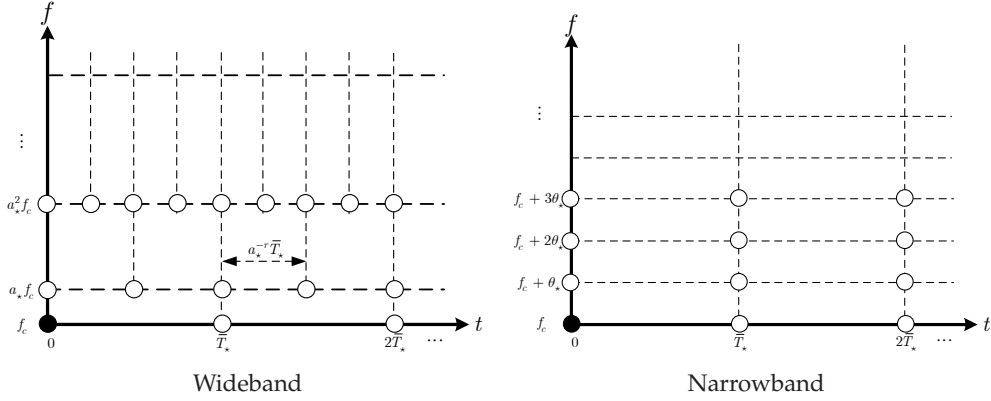


Figure 2.2:  $T$ - $F$  tile diagram of a discretized channel model

Following (2.18), the corresponding complex baseband equivalent is then given by

$$r^{\text{DL}}(t) = e^{j2\pi(f_c - f'_c)t} \sum_{q=0}^{Q_*} \sum_{l=0}^{\bar{L}_*} h_{q,l} s(t - l\bar{T}_*) e^{j2\pi q\theta_* t}, \quad (2.20)$$

where  $h_{q,l} = \bar{h}_{q,l} e^{-j2\pi l\bar{T}_* f_c}$ .

### III. Differences Between Wideband and Narrowband

From the above descriptions for wideband and narrowband channel models, their differences can be perceptually recognized. Firstly, narrowband LTV systems can be seen as an approximation of the corresponding wideband LTV systems; secondly, the narrowband transmitted signal waveform per se is not reshaped by scaling but only shifted in time and frequency; and thirdly, the received complex baseband signal equivalent in narrowband scenarios is free of the CFO if only  $f_c = f'_c$ . Hence generally speaking, it is usually much easier to handle a narrowband LTV channel than its wideband counterpart. More background information about the comparison between narrowband LTV systems and wideband LTV systems can be found, e.g., in [15, 20, 22, 24, 31]. Among their fundamental differences, we herein only want to emphasize one fact that the parameterized narrowband LTV channel is arithmetically uniform in both the lag (time) and frequency dimension

[c.f. (2.18)], while the parameterized wideband LTV channel is arithmetically uniform in the lag (time) dimension but geometrically uniform in the scale (frequency) dimension [c.f. (2.9)]. Therefore, they result in different time-frequency (T-F) tiling diagrams. In other words, a transmitted symbol will disperse differently over a narrowband LTV channel than over a wideband LTV channel. This fact is schematically depicted in Fig. 2.2, where the circles indicate the positions where the channel is sampled in the T-F plane. In the figure, we assume that a single symbol is transmitted at time 0 and carrier frequency  $f_c$ , whose location is represented by a dark circle, and the open circles show the locations of signal leakage. The symbol  $\theta_*$  in Fig. 2.2 denotes the arithmetically uniform frequency spacing used to sample the narrowband channel in the Doppler (frequency) dimension where  $Q_* = 3$  and  $\bar{L}_* = 2$  for illustration. Analogously,  $a_*$  in Fig. 2.2 denotes the geometrically uniform frequency spacing used to sample the wideband channel in the Doppler (frequency) dimension where  $R_* = 2$  and  $\bar{L}_*(0) = 2$  for illustration. From their comparison, we learn that a transmit signal will experience fundamentally different channel characteristics in wideband LTV systems than in narrowband LTV systems. Hence, distinct receiver designs are required for these two scenarios, respectively.

### 2.2.2 Non-Parametric Channel Model

In either wideband or narrowband systems, it is also common to consider the baseband channel as a LTV finite impulse response (FIR) filter. More specifically, assuming that the bandwidth of the channel is smaller than  $1/T$ , then let us sample  $r(t)$  at the symbol rate  $T$  based on the Nyquist criterion (otherwise, the sampling rate is increased). In this case, the  $n$ th sample of the received baseband signal is given by

$$\begin{aligned} r_n = r(nT) &= \sum_{l=-\infty}^{\infty} h_{n-l}^{(n)} s_l + w_n \\ &\doteq \sum_{l=0}^{L(n)} h_l^{(n)} s_{n-l} + w_n \end{aligned} \quad (2.21)$$

where  $s_n = s(nT)$  is the  $n$ th transmitted data symbol,  $w_n = w(nT)$  is the additive discrete noise. The superscript  $(n)$  in the FIR coefficients  $h_l^{(n)}$  stands for the time variation along consecutive symbol durations. In a realistic communication system, most of the channel power is concentrated within a limited time interval, implying that the channel has a limited time support, say  $L(n)T \geq \tau_{\max}$  where  $L(n)$  is generally dependent on time especially for wideband time-varying systems. In addition, if we take the causality of the transmission process into account, the channel can further be simplified to an FIR filter, with  $h_l^{(n)} = 0$  if  $l < 0$  or  $l > L(n)$  as expressed in the second equation of (2.21). The channel in (2.21) is typically “doubly-selective” (in both frequency and time), which is a generalization of various channel situations. For example, time-selective channels occur when  $h_l^{(n)} \equiv h_l^{(n)}$  with  $L(n) \equiv 0$ , indicating zero delay spread. For frequency-selective channels (2.21) degrades to  $h_l^{(n)} \equiv \sum_{m=1}^L h_l \delta_{l-m}$  with  $L(n) \equiv L$ , which is independent on the index  $n$ , implying zero Doppler spread. Herein,  $\delta_n$  denotes the Kronecker delta which equals one if  $n = 0$ , or zero otherwise. Finally, an AWGN channel is described by  $h_l^{(n)} \equiv h_l \delta_l$ , which is an idealized situation where both the delay and Doppler spread are zero.

Although the LTV FIR filter model provides a quite precise perception of a realistic channel, these time-varying FIR taps can be too cumbersome to utilize in practice in both the wideband and the narrowband case. To ease the processing procedure at the receiver, many existing works thus resort to a parsimonious channel model, such as the basis expansion model (BEM) [37]. The BEM is widely adopted for narrowband LTV channels, e.g., in [3–5, 8, 38–41].

To introduce how to use the BEM to model a narrowband time-varying channel, let us currently consider a block transmission with  $N$  symbols and  $L(n) \equiv L$  is constant during the concerned duration. Thus the channel in (2.21) is characterized in this narrowband regime by  $NL$  FIR taps:  $h_l^{(n)}$ , for  $l = \{0, 1, \dots, L\}$  and  $n = \{0, 1, \dots, N-1\}$ . If we denote  $\mathbf{h} = [\mathbf{h}_0^T, \dots, \mathbf{h}_{N-1}^T]^T$  stacking all the channel taps with  $\mathbf{h}_n = [h_0^{(n)}, h_1^{(n)}, \dots, h_L^{(n)}]^T$ , we can use the BEM to model the channel  $\mathbf{h}$  specified as [8]

$$\mathbf{h} \approx (\mathbf{Q} \otimes \mathbf{I}_{L+1}) \mathbf{c} \quad (2.22)$$

where  $\mathbf{Q} = [\mathbf{q}_{-Q}, \dots, \mathbf{q}_Q]$  is a  $N \times (2Q+1)$  matrix with  $\mathbf{q}_q$  being the  $q$ th basis

expansion function, and  $2Q$  is the BEM order. It is typical that these  $\mathbf{q}_q$ 's are designed to be orthonormal to each other, e.g.,

$$\mathbf{q}_q = [1, e^{j\frac{2\pi}{N}q}, \dots, e^{j\frac{2\pi(N-1)}{N}q}]^T$$

for the critically-sampled CE-BEM (CCE-BEM) [37]. Depending on the basis expansion function, various BEM designs are available, such as the discrete Karhuen-Loève BEM [42], the discrete prolate spheroidal BEM [39], etc. We further have  $\mathbf{c} = [\mathbf{c}_{-Q}^T, \dots, \mathbf{c}_Q^T]^T$  with  $\mathbf{c}_q = [c_{q,0}, c_{q,1}, \dots, c_{q,L}]^T$  being the  $q$ th BEM coefficient vector corresponding to  $\mathbf{q}_q$ . We highlight that when  $N > 2Q + 1$  as usual, BEM models allow to reduce the number of unknown channel parameters from  $NL$  (the  $h_l^{(n)}$ 's) to  $(2Q + 1)L$  (the  $c_{q,l}$ 's).

Besides the BEM approach, a Gauss-Markov process can also be found to model time-varying channels [43]. Other modeling methods using wavelet techniques can be found, e.g., in [44–46].

### 2.3 Multi-Carrier Transmission

Orthogonal frequency division multiplexing (OFDM), which is a spectrum efficient case of frequency-division multiplexing (FDM) where subcarriers overlap in the frequency domain while remaining orthogonal, is one of the most popular multicarrier techniques today [47]. In Fig. 2.3, the spectrum of a general FDM waveform is compared with OFDM.

With many desirable properties such as high spectral efficiency and inherent resilience to the multipath dispersions of frequency-selective channels [48], OFDM shows attractive features to many wireless communication applications, e.g., wireless local area networks (WLANs) and digital video broadcasting (DVB). Let us consider an OFDM waveform given by

$$s(t) = \frac{1}{\sqrt{KT}} \sum_{k=0}^{K-1} b_k e^{j2\pi f_k t}, \quad -T_{\text{pre}} < t \leq KT \quad (2.23)$$

where  $K$  is the number of orthogonal subcarriers, a data symbol  $b_k$  is modulated on the  $k$ -th subcarrier whose frequency is  $f_k = (k - K/2)\Delta f$ , for  $k = \{0, 1, \dots, K - 1\}$ , with  $\Delta f$  being the subcarrier frequency spacing,

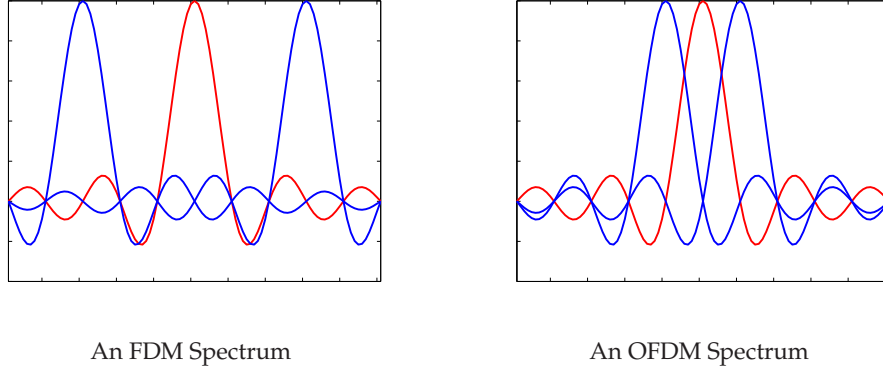


**Figure 2.3:** Signaling Spectrum Comparison, FDM v.s. OFDM

$KT = 1/\Delta f$  is the effective duration of an OFDM symbol, and  $\frac{1}{\sqrt{KT}}$  is a normalization factor. The length of the cyclic prefix is  $T_{\text{pre}}$ . It is well-known that the cyclic prefix is assumed to be longer than the delay spread to eliminate the inter-symbol interference (ISI) between successive OFDM symbols [48]. Though a cyclic extension is introduced above, the above expression can be changed to zero padding OFDM (ZP-OFDM) with minor modifications [48, 49]. Note that we consider a single OFDM symbol being transmitted for notational ease in (2.23), which is without loss of generality due to the use of cyclic extensions.

Stacking all the data within the OFDM symbol into a vector, as  $\mathbf{b} = [b_0, b_1, \dots, b_{K-1}]^T$ , we can equivalently describe (2.23) in a matrix-vector form given by

$$\mathbf{s}' = \mathbf{T}_{\text{CP}} \mathbf{s}$$

where  $\mathbf{T}_{\text{CP}}$  is a  $(K + K_{\text{pre}}) \times K$  matrix given by

$$\mathbf{T}_{\text{CP}} = \begin{bmatrix} \mathbf{0}_{K_{\text{pre}} \times (K - K_{\text{pre}})} & \mathbf{I}_{K_{\text{pre}}} \\ & \mathbf{I}_K \end{bmatrix},$$

with  $K_{\text{pre}} = \lceil T_{\text{pre}}/T \rceil$  and  $\mathbf{s} = [s_0, s_1, \dots, s_{K-1}]^T$  with  $s_n = s(nT)$ . More specifically,

$$\mathbf{s} = \mathbf{F}^H \mathbf{b}, \quad (2.24)$$

where  $\mathbf{F}$  stands for the  $K$  point unitary discrete Fourier transform (DFT) matrix specified by

$$[\mathbf{F}]_{m,k} = \frac{1}{\sqrt{K}} e^{-j2\pi \frac{mk}{K}}. \quad (2.25)$$

Suppose the above OFDM signal is transmitted over a frequency-selective channel as modeled in (2.21) with  $L(n) \equiv L$  and  $h_l^{(n)} \equiv \sum_{m=1}^L h_l \delta_{l-m}$ . Thus we can write the input/output (I/O) relation of this time-invariant OFDM system as [48, 49]

$$\begin{aligned} \mathbf{r}_T &= \mathbf{R}_{\text{CP}} \mathbf{H}'_T \mathbf{s}' + \mathbf{w}_T \\ &= \mathbf{R}_{\text{CP}} \mathbf{H}'_T \mathbf{T}_{\text{CP}} \mathbf{s} + \mathbf{w}_T \end{aligned} \quad (2.26)$$

$$= \mathbf{H}_T \mathbf{s} + \mathbf{w}_T \quad (2.27)$$

where  $\mathbf{r}_T = [r_0, r_1, \dots, r_{K-1}]^T$  stacks all the received signal samples in the time domain after discarding cyclic extensions,  $\mathbf{R}_{\text{CP}}$  is the  $K \times (K + K_{\text{pre}})$  cyclic-extension-removal matrix specified as

$$\mathbf{R}_{\text{CP}} = \begin{bmatrix} \mathbf{0}_{K \times K_{\text{pre}}} & \mathbf{I}_K \end{bmatrix},$$

and  $\mathbf{w}_T$  is similarly defined like  $\mathbf{r}_T$  as the discrete noise vector, while  $\mathbf{H}'_T$  is a  $(K + K_{\text{pre}}) \times (K + K_{\text{pre}})$  matrix representing the time-domain time-invariant channel given by

$$\mathbf{H}'_T = \begin{bmatrix} h_0 & & & & & & & & & & \\ \vdots & \ddots & & & & & & & & & \mathbf{0} \\ h_L & \vdots & h_0 & & & & & & & & \\ & \ddots & \vdots & \ddots & & & & & & & \\ & & & h_L & \vdots & \ddots & & & & & \\ & & & & \ddots & \vdots & \ddots & & & & \\ \mathbf{0} & & & & & \ddots & \vdots & \ddots & & & \\ & & & & & & h_L & \cdots & h_0 & & \end{bmatrix}$$

where  $h_l$  is the time-invariant channel coefficient. Here  $K_{\text{pre}} \geq L$ , which means that the prefix guard is longer than the maximal delay spread. The effective channel matrix in the time domain is then given by  $\mathbf{H}_T = \mathbf{R}_{\text{CP}} \mathbf{H}'_T \mathbf{T}_{\text{CP}}$ ,

which is specified as

$$\mathbf{H}_T = \begin{bmatrix} h_0 & & & h_L & \cdots & h_1 \\ \vdots & \ddots & & & \ddots & \vdots \\ h_L & \ddots & \ddots & \mathbf{0} & & h_L \\ & \ddots & \ddots & \ddots & & \\ & \mathbf{0} & \ddots & \ddots & \ddots & \\ & & & h_L & \cdots & h_0 \end{bmatrix}. \quad (2.28)$$

We highlight here that, when the channel is time invariant,  $\mathbf{H}_T$  is a circulant matrix as shown above.

If we describe the noiseless received OFDM signal in the frequency domain as [48,49]

$$\begin{aligned} \mathbf{r}_F &= \mathbf{F} \mathbf{r}_T \\ &= \mathbf{F} \mathbf{H}_T \mathbf{s} \\ &= \mathbf{F} \mathbf{H}_T \mathbf{F}^H \mathbf{b} \\ &= \mathbf{H}_F \mathbf{b}, \end{aligned} \quad (2.29)$$

where the frequency-domain channel matrix  $\mathbf{H}_F = \mathbf{F} \mathbf{H}_T \mathbf{F}^H$  is diagonal because  $\mathbf{H}_T$  is a circulant matrix [50]. It means that the time-invariant OFDM channel is characterized by a diagonal matrix in the frequency domain, indicating that the orthogonality among OFDM subcarriers is maintained at the receiver. However, when the Doppler effect is present,  $\mathbf{H}_F$  becomes full, thus introducing the inter-carrier interference (ICI). We refer readers to Chapter 3 and Chapter 4 for its more details in the narrowband case and the wideband case, respectively.

Besides the OFDM system mentioned above, other multi-carrier transmission techniques are available. For instance, instead of uniformly spacing subcarriers like in OFDM, we may also adopt wavelet techniques [51] to build a wavelet-OFDM scheme, which is popular in power line communications [52]. More multi-carrier transmissions using wavelet-based modulations can be found, e.g., in [53–58].





## Chapter 3

---

# Narrowband OFDM Systems

*Every truth has two sides; it is as well to look at both,  
before we commit ourselves to either.*

Aesop

In the last chapter, we have introduced the channel model in two scenarios: the narrowband and the wideband. OFDM was also introduced as a typical multi-carrier transmission technique. In this chapter, we first describe an OFDM transmission over a narrowband time-varying channel which is modeled by the basis expansion model (BEM). Afterwards, the least-squares (LS) channel estimation and its corresponding zero-forcing (ZF) channel equalization are investigated when different BEM models are used. The purpose herein is to identify a particular BEM model which allows a more efficient hardware architecture while still maintaining a high modeling accuracy.

### 3.1 Introduction

Future communication systems are required to support a high data transfer rate between fast moving terminals, e.g., vehicular communications depicted in Fig. 1.1. Orthogonal frequency division multiplexing (OFDM), as a bandwidth efficient multi-carrier transmission technique, shows attractive features to wireless radio applications [47]. It is well known that OFDM relies on the assumption that the channel stays constant within at least one OFDM symbol period to maintain the orthogonality among OFDM subcarriers. When temporal channel variation emerges due to the Doppler effect, this orthogonality is corrupted and non-negligible inter-carrier interference (ICI) is induced [59], severely deteriorating the system performance. In this case, channel equalization is necessary, for which we need accurate models

of narrowband time-varying channels. It is common to describe the channel taps statistically by their Doppler spectrum which may be bathtub-shaped [14]. Despite their accuracy, these models are generally cumbersome. Hence, many works resort to a parsimonious channel modeling approach such as a Gauss-Markov process [43] or the basis expansion model (BEM) [37] to describe the channel dynamics. The Gauss-Markov process is mainly adopted for time-domain sequential processing, while in this chapter we shall focus on the BEM which is often more convenient for block transmission schemes such as OFDM. The optimal BEM in terms of the mean square error (MSE) is the discrete Karhuen-Loève BEM (DKL-BEM) [42] which however requires the true channel statistics and thus is not always practical. The discrete prolate spheroidal BEM (DPS-BEM) [39] is derived based on the channel statistics approximated by a rectangular spectrum. Avoiding the dependence on the channel statistics, the critically-sampled complex-exponential BEM (CCE-BEM) [37] is proposed using complex exponentials as its basis functions. Due to its algebraic ease, the CCE-BEM is widely adopted, e.g., in [3, 5, 8, 37, 38, 40, 60, 61]. Additionally, the polynomial BEM (POL-BEM), which models each tap as a linear combination of a set of polynomials, has also gained attention for low Doppler spreads, e.g., in [62, 63]. The detailed comparison of the aforementioned BEMs can be found in [4, 39].

Research on OFDM systems from the aspect of the hardware implementations can also be found, e.g., on FPGA platforms [64] or using a specific digital signal processor (DSP) [65]. A complication of these works is assuming a time-invariant channel where the transceiver and significant scatterers are stationary or have a negligible velocity. Hence, the adopted OFDM systems are free of inter-carrier interference (ICI), and called “traditional OFDM” or time-invariant OFDM in this chapter. To our knowledge, little attention has been paid to an efficient hardware implementation of mobile OFDM, which refers to the OFDM systems over rapidly time-varying channels. In this chapter, we shall investigate efficient architectures corresponding to different BEM’s to implement the channel estimator and channel equalizer for mobile OFDM in the narrowband regime. Moreover, we then identify a particular model, among available BEM’s, which leads to the most efficient hardware architecture while still maintaining high modeling

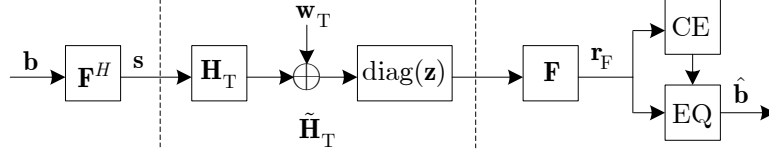


Figure 3.1: Transceiver block diagram.

accuracy.

### 3.2 Narrowband Time-Varying OFDM System Model

Let us consider an OFDM system with  $N$  subcarriers as described in (2.23) but over a narrowband time-varying channel modeled by (2.21) with  $L(n) \equiv L$  being constant during an OFDM duration. In this case, we adapt the OFDM system in (2.29) as [2, 3, 61]

$$\begin{aligned}
 \mathbf{r}_F &= \mathbf{FZ}\mathbf{H}_T\mathbf{F}^H\mathbf{b} + \mathbf{FZ}\mathbf{w}_T \\
 &= \mathbf{F}\tilde{\mathbf{H}}_T\mathbf{F}^H\mathbf{b} + \mathbf{FZ}\mathbf{w}_T \\
 &= \mathbf{H}_F\mathbf{b} + \mathbf{n}_F
 \end{aligned} \tag{3.1}$$

where  $\mathbf{r}_F$  is the received sample vector in the frequency domain and  $\mathbf{Z} = \text{diag}\{\mathbf{z}\}$  with its diagonal  $\mathbf{z} = [z_0, z_1, \dots, z_{N-1}]^T$  representing the time-domain windowing. We underscore that the time-domain windowing is normally not included in traditional OFDM systems [c.f., (2.29)], i.e.,  $\mathbf{Z} = \mathbf{I}_N$ . However such a time-domain windowing is required by a time-varying OFDM system (mobile OFDM) to suppress the ICI [2, 61]. Moreover,  $\mathbf{H}_T$  and  $\tilde{\mathbf{H}}_T = \mathbf{Z}\mathbf{H}_T$  represents the channel matrix in the time domain without and with windowing, respectively. With  $h_l^{(n)}$  denoting the  $l$ th channel tap at the  $n$ th time instant for  $l = \{0, 1, \dots, L\}$  with  $L$  finite (i.e.,  $h_l^{(n)} = 0$  for  $l < 0$  or  $l > L$ ),  $\mathbf{H}_T$

is specified a “pseudo-circulant” matrix given by

$$\mathbf{H}_T = \begin{bmatrix} h_0^{(0)} & & h_L^{(0)} & \cdots & h_1^{(0)} \\ \vdots & \ddots & & \ddots & \vdots \\ h_L^{(L)} & \ddots & \ddots & \mathbf{0} & h_L^{(L-1)} \\ & \ddots & \ddots & \ddots & \\ & \mathbf{0} & \ddots & \ddots & \\ & & h_L^{(N-1)} & \cdots & h_0^{(N-1)} \end{bmatrix}. \quad (3.2)$$

and  $\tilde{\mathbf{H}}_T$  thus has the same “pseudo-circulant” structure specified as

$$\tilde{\mathbf{H}}_T = \begin{bmatrix} \tilde{h}_0^{(0)} & & \tilde{h}_L^{(0)} & \cdots & \tilde{h}_1^{(0)} \\ \vdots & \ddots & & \ddots & \vdots \\ \tilde{h}_L^{(L)} & \ddots & \ddots & \mathbf{0} & \tilde{h}_L^{(L-1)} \\ & \ddots & \ddots & \ddots & \\ & \mathbf{0} & \ddots & \ddots & \\ & & \tilde{h}_L^{(N-1)} & \cdots & \tilde{h}_0^{(N-1)} \end{bmatrix} \quad (3.3)$$

where  $\tilde{h}_l^{(n)} = z_n h_l^{(n)}$ . Additionally,  $\mathbf{n}_F = \mathbf{F}\mathbf{Z}\mathbf{w}_T$  is the windowed frequency-domain noise, and  $\mathbf{H}_F = \mathbf{F}\tilde{\mathbf{H}}_T\mathbf{F}^H$  is the effective frequency-domain channel matrix that is not diagonal any more but full. Fig. 3.1 illustrates the data flow of this OFDM transmission over a narrowband time-varying channel by ignoring the introduction and the removal of the cyclic prefix.

Using the BEM to model the effective OFDM channel  $\tilde{\mathbf{H}}_T$  in the time domain, let us stack all the channel taps into a single vector  $\tilde{\mathbf{h}} = [\tilde{\mathbf{h}}_0^T, \dots, \tilde{\mathbf{h}}_{N-1}^T]^T$  with  $\tilde{\mathbf{h}}_n = [\tilde{h}_0^{(n)}, \tilde{h}_1^{(n)}, \dots, \tilde{h}_L^{(n)}]^T$ . Regardless of the modeling error, we follow (2.22) to first obtain [4, 37]

$$\tilde{\mathbf{h}} = (\mathbf{Q} \otimes \mathbf{I}_{L+1}) \mathbf{c} \quad (3.4)$$

where the  $(2Q+1)(L+1) \times 1$  vector

$$\mathbf{c} = [\mathbf{c}_{-Q}^T, \dots, \mathbf{c}_Q^T]^T$$

with

$$\mathbf{c}_q = [c_{q,0}, c_{q,1}, \dots, c_{q,L}]^T$$

being the  $q$ th BEM coefficient vector corresponding to the  $q$ th basis expansion function  $\mathbf{q}_q$ , and  $\mathbf{Q} = [\mathbf{q}_{-Q}, \dots, \mathbf{q}_Q]$  with  $2Q$  being the BEM order. (3.4) indicates that after introducing the BEM, one can estimate the BEM coefficients to perform channel estimation.

Using (3.4), we can describe  $\tilde{\mathbf{H}}_T$  in (3.3) alternatively as

$$\tilde{\mathbf{H}}_T = \sum_{q=-Q}^Q \text{diag}(\mathbf{q}_q) \mathbf{C}_q \quad (3.5)$$

where  $\mathbf{C}_q$  is an  $N \times N$  circulant matrix (assuming that  $N > L$  which is usually the case) given by

$$\mathbf{C}_q = \begin{bmatrix} c_{q,0} & & & c_{q,L} & \cdots & c_{q,1} \\ \vdots & \ddots & & & \ddots & \vdots \\ c_{q,L} & \ddots & \ddots & \mathbf{0} & & c_{q,L} \\ & \ddots & \ddots & \ddots & & \\ & \mathbf{0} & \ddots & \ddots & \ddots & \\ & & & c_{q,L} & \cdots & c_{q,0} \end{bmatrix}.$$

Now, we can describe OFDM systems in light of BEM by substituting (3.5) into (3.1) as [4]

$$\begin{aligned} \mathbf{r}_F &= \mathbf{F} \tilde{\mathbf{H}}_T \mathbf{F}^H \mathbf{b} + \mathbf{n}_F \\ &= \mathbf{F} \left( \sum_{q=-Q}^Q \text{diag}(\mathbf{q}_q) \mathbf{C}_q \right) \mathbf{F}^H \mathbf{b} + \hat{\mathbf{n}}_F \\ &= \sum_{q=-Q}^Q (\mathbf{F} \text{diag}(\mathbf{q}_q) \mathbf{F}^H) (\mathbf{F} \mathbf{C}_q \mathbf{F}^H) \mathbf{b} + \hat{\mathbf{n}}_F \\ &= \sum_{q=-Q}^Q \mathbf{D}_q \Delta_q \mathbf{b} + \hat{\mathbf{n}}_F \end{aligned} \quad (3.6)$$

where  $\mathbf{\Delta}_q = \mathbf{F}\mathbf{C}_q\mathbf{F}^H$  and

$$\mathbf{D}_q = \mathbf{F}\text{diag}(\mathbf{q}_q)\mathbf{F}^H \quad (3.7)$$

is a circulant matrix, while  $\hat{\mathbf{n}}_F$  combines  $\mathbf{n}_F$  and the BEM modeling error. Due to the circulant structure of  $\mathbf{C}_q$ , we also rewrite  $\mathbf{\Delta}_q$  as a diagonal matrix given by

$$\mathbf{\Delta}_q = \text{diag}(\mathbf{F}^{(L)}\mathbf{c}_q) \quad (3.8)$$

with  $\mathbf{F}^{(L)}$  representing the first  $L + 1$  columns of the Fourier matrix  $\sqrt{N}\mathbf{F}$ .

If we introduce

$$\hat{\mathbf{H}}_F = \sum_{q=-Q}^Q \mathbf{D}_q\mathbf{\Delta}_q \quad (3.9)$$

as the modeled channel matrix that approximates  $\mathbf{H}_F$ , we rewrite (3.6) as

$$\mathbf{r}_F = \hat{\mathbf{H}}_F\mathbf{b} + \hat{\mathbf{n}}_F \quad (3.10)$$

Now, let us have a look at the structure of  $\hat{\mathbf{H}}_F$ . We notice that  $\hat{\mathbf{H}}_F$  is a banded matrix approximately, as illustrated in Fig. 3.2. This is no surprise since  $\hat{\mathbf{H}}_F$  approximates the effective frequency-domain channel matrix  $\mathbf{H}_F$  and thus has a similar structure of  $\mathbf{H}_F$ . In practice,  $\mathbf{H}_F$  can always be approximated as a banded matrix [2], due to the limited Doppler shift spread of the channel and the use of a time-domain windowing  $\mathbf{Z}$ . Moreover, it is clear from (3.9) that since  $\mathbf{\Delta}_q$  is diagonal,  $\hat{\mathbf{H}}_F$  has a similar structure of  $\sum_q \mathbf{D}_q = \mathbf{F}\text{diag}(\sum_q \mathbf{q}_q)\mathbf{F}^H$ . In fact, the designs of the basis functions  $\mathbf{q}_q$ 's of a proper BEM family lead to a banded matrix  $\sum_q \mathbf{D}_q$  approximately (or exactly when the CCE-BEM is used) with a bandwidth of  $2Q + 1$  [4, 37]. In the following sections of this chapter, we will employ this feature of  $\hat{\mathbf{H}}_F$ .

### 3.3 Algorithm Background Overview

We underscore that there has been extensive research on the channel estimation and channel equalization for OFDM systems over narrowband linear time-varying (LTV) channels, e.g., for channel estimation in [4, 40, 63] and for channel equalization in [3, 5, 40, 41, 61, 66]. In this chapter, we do not

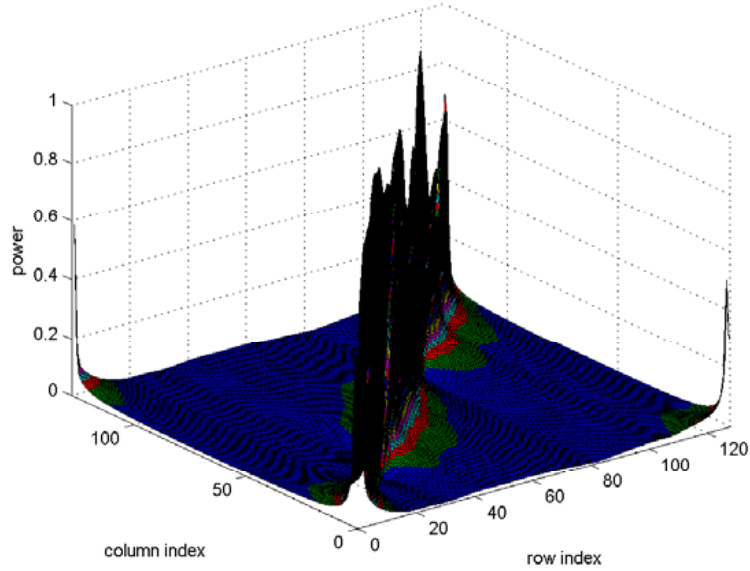


Figure 3.2: An example of the Power allocation of  $\hat{\mathbf{H}}_F$ .

attempt to summarize these efforts, but instead focus on the least-squares (LS) channel estimation and zero-forcing (ZF) equalization for narrowband OFDM LTV channels. In the following, we first clarify the arrangement of all OFDM subcarriers, and then describe the detailed descriptions for channel estimation and equalization respectively.

### 3.3.1 OFDM Carrier Arrangement

For time-varying OFDM systems, comb-type pilot subcarriers and guarded null subcarriers are usually required [4, 38]. Specifically, we assume that the  $N$  subcarriers of the OFDM symbol include  $N_P$  pilot subcarriers and  $(N - N_D - N_P)$  null subcarriers, and thus, out of  $N$  carriers, only  $N_D$  subcarriers carry information which are called data subcarriers. Let us specify an OFDM symbol vector  $\mathbf{b} = [b_0, b_1, \dots, b_{N-1}]^T$  which includes a pilot symbol set  $\mathbf{b}^{(p)} = [b_0^{(p)}, \dots, b_{N_P-1}^{(p)}]^T$ , and a data symbol set  $\mathbf{b}^{(d)} = [b_0^{(d)}, \dots, b_{N_D-1}^{(d)}]^T$  as well as zeros at null subcarriers. At the receiver, according to (3.10), the

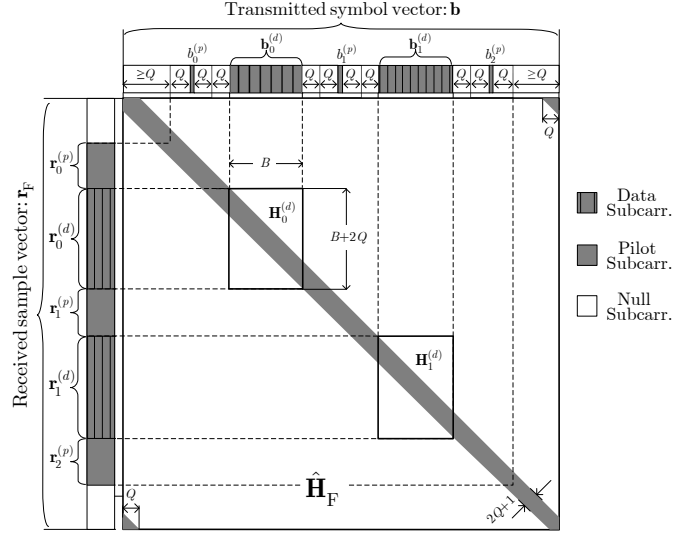


Figure 3.3: OFDM Subcarrier Allocation Illustration

noiseless received sample vector is modeled by  $\mathbf{r}_F = \hat{\mathbf{H}}_F \mathbf{b}$ , where  $\hat{\mathbf{H}}_F$  is (approximately) a banded matrix with a bandwidth of  $2Q + 1$ . Illustratively, as depicted in Fig. 3.3. between  $\mathbf{b}$  and  $\mathbf{r}_F$ , the banded channel matrix  $\hat{\mathbf{H}}_F$  is placed whose bandwidth is  $2Q + 1$ . Moreover, the gray part of  $\hat{\mathbf{H}}_F$  in Fig. 3.3 stands for significant non-zero entries, while its blank part represents the trivial entries (which will be zeros if the CCE-BEM is used).

In order to combat a narrowband time-varying OFDM channel modelled by  $\hat{\mathbf{H}}_F$ , it is crucial to carefully allocate these subcarriers and their corresponding observations [4, 38]. We follow [4] to arrange OFDM subcarriers. These  $N_P$  pilots are distributed into the OFDM symbol, and every transmitted pilot is guarded by  $2Q$  null subcarriers to diminish mutual influences with adjacent data subcarriers in the present of Doppler frequency shifts. The rest of null subcarriers are placed on edge positions, and we require that the number of edge null subcarriers is sufficiently large (i.e.,  $\geq Q$ ) [3, 5, 40, 61], whose reason will be evident later on. In such a manner, the  $N_D$  data subcarriers are separated into several isolated clusters. If we assume that each data cluster has the same length  $B$  for simplicity reasons, the



$m$ th isolated transmitted data subcarrier cluster is denoted by a  $B \times 1$  vector  $\mathbf{b}_m^{(d)} = [b_0^{(d,m)}, \dots, b_{B-1}^{(d,m)}]^T \subset \mathbf{b}^{(d)}$ , for  $m \in \{0, 1, \dots, N_B - 1\}$  with

$$N_B = N_D/B.$$

Illustratively, such an arrangement of the OFDM subcarriers is depicted in Fig. 3.3, with  $N_P = 3$ . From there, it is clear that within the transmitted OFDM symbol  $\mathbf{b}$ , the guarded pilots  $b_k^{(p)}$  and null edge subcarriers separate the  $N_D$  data subcarriers into  $N_P - 1$  clusters.

At the receiver, corresponding to this  $m$ th transmitted data cluster  $\mathbf{b}^{(d,m)}$ , we build an observation window denoted by a  $(B + 2Q) \times 1$  vector  $\mathbf{r}_m^{(d)} = [r_{-Q}^{(d,m)}, \dots, r_0^{(d,m)}, \dots, r_{B-1}^{(d,m)}, \dots, r_{B-1+Q}^{(d,m)}]^T \subset \mathbf{r}_F$ . Likewise, corresponding to the  $k$ th transmitted pilot  $b_k^{(p)}$ , for  $k \in \{0, 1, \dots, N_P - 1\}$ , its observation window is denoted as a  $(2Q+1) \times 1$  vector  $\mathbf{r}_k^{(p)} = [r_{-Q}^{(p,k)}, \dots, r_0^{(p,k)}, \dots, r_Q^{(p,k)}]^T \subset \mathbf{r}_F$ . In Fig 3.3, the locations of these observation windows is also illustrated. We note that other options for the observation window are available [4], but the method adopted here is the optimal choice for LS channel estimation [4].

### 3.3.2 LS Channel Estimation

Pilots and their observations at the receiver are used to estimate time-varying channels. We recall the  $N_P \times 1$  vector  $\mathbf{b}^{(p)} = [b_0^{(p)}, \dots, b_{N_P-1}^{(p)}]^T$  which stacks all pilot symbols, and let the  $(2Q+1)N_P \times 1$  vector  $\mathbf{r}^{(p)} = [\mathbf{r}_0^{(p)T}, \dots, \mathbf{r}_{N_P-1}^{(p)T}]^T$  represent all the received samples within the pilot observation windows embedded in  $\mathbf{r}_F$ . Then from (3.6), we obtain

$$\mathbf{r}^{(p)} = \sum_{q=-Q}^Q \mathbf{D}_q^{(p)} \mathbf{\Delta}_q^{(p)} \mathbf{b}^{(p)} + \hat{\mathbf{n}}^{(p)} \quad (3.11)$$

where  $\mathbf{D}_q^{(p)}$  is a submatrix obtained from  $\mathbf{D}_q$  by only selecting the rows (columns) corresponding to  $\mathbf{r}^{(p)}$  in  $\mathbf{r}_F$  ( $\mathbf{b}^{(p)}$  in  $\mathbf{b}$ );  $\mathbf{\Delta}_q^{(p)}$  is obtained from  $\mathbf{\Delta}_q$  by selecting the rows of  $\mathbf{b}^{(p)}$  in  $\mathbf{b}$ , while  $\hat{\mathbf{n}}^{(p)}$  not only contains the noise obtained from  $\hat{\mathbf{n}}_F$  in a similar manner but also includes crosstalk components from different positions of the data subcarriers (see [4] for details). We note that in this chapter the statistics of  $\hat{\mathbf{n}}^{(p)}$  is irrelevant since we focus on an LS channel estimation.

In order to estimate the BEM coefficients in  $\mathbf{c}$ , we now convert (3.11) (see Appendix 3.A for the detailed derivations) into

$$\mathbf{r}^{(p)} = \mathbf{A}^{(p)} \mathbf{c} + \hat{\mathbf{n}}^{(p)}, \quad (3.12)$$

where the  $(2Q + 1)N_P \times (2Q + 1)(L + 1)$  matrix  $\mathbf{A}^{(p)}$  is specified as

$$\mathbf{A}^{(p)} = \mathbf{D}^{(p)} \left( \mathbf{I}_{2Q+1} \otimes \left( \text{diag}\{\mathbf{b}^{(p)}\} \mathbf{F}^{(L,p)} \right) \right) \quad (3.13)$$

and

$$\mathbf{D}^{(p)} = [\mathbf{D}_{-Q}^{(p)}, \dots, \mathbf{D}_Q^{(p)}],$$

while  $\mathbf{F}^{(L,p)}$  collects the rows of  $\mathbf{F}^{(L)}$  corresponding to the positions of  $\mathbf{b}^{(p)}$  in  $\mathbf{b}$ . It is noteworthy that  $\mathbf{A}^{(p)}$  is only related to the pilot symbols  $\mathbf{b}^{(p)}$ , the BEM basis functions  $\mathbf{q}_q$ 's [c.f. (3.7)] and the normalized Fourier matrix  $\mathbf{F}$ , all of which are perfectly known at the receiver. In other words,  $\mathbf{A}^{(p)}$  can be pre-computed when designing the channel estimator (CE).

Based on the LS criterion, we obtain the estimate of the BEM coefficient vector from (3.12) given by

$$\hat{\mathbf{c}} = \left( \mathbf{A}^{(p)H} \mathbf{A}^{(p)} \right)^{-1} \mathbf{A}^{(p)H} \mathbf{r}^{(p)}, \quad (3.14)$$

which has less entries than the channel gain vector  $\tilde{\mathbf{h}}$  [cf. (3.4)] when  $N > (2Q + 1)$  as usually the case. It also explains the benefit of introducing the BEM since it allows for reducing the number of the estimated parameters. If we rewrite

$$\hat{\mathbf{c}} = [\hat{\mathbf{c}}_{-Q}^T, \dots, \hat{\mathbf{c}}_Q^T]^T$$

it is clear that  $\hat{\mathbf{c}}_q$  estimates the  $q$ th BEM coefficient vector  $\mathbf{c}_q$ . Here it is noteworthy that  $N_P > L$  is assumed in this chapter so that  $\mathbf{A}^{(p)H} \mathbf{A}^{(p)}$  is invertible (otherwise, pilots from multiple OFDM symbols are needed to be jointly considered to perform the channel estimation [67], which is not included in this thesis).

However, the final purpose of the estimator is not these BEM coefficients, but the channel between the transmitted data subcarriers and their corresponding observations at the receiver [5, 40], e.g.,  $\mathbf{H}_m^{(d)}$  in Fig. 3.3. It shall be equalized by the channel equalizer (EQ) to recover the transmitted data

symbols that carry information. As illustrated in Fig. 3.3, the data subcarriers and their observation windows are divided into isolated clusters. Instead of handling the whole OFDM symbol jointly, we can parallelize the estimation for each cluster. Specifically, we explicitly write the  $m$ th observation vector  $\mathbf{r}_m^{(d)}$  that corresponds to  $\mathbf{b}_m^{(d)}$  for  $m \in \{0, 1, \dots, N_B - 1\}$ , regardless of noise, as

$$\begin{aligned} \mathbf{r}_m^{(d)} &= \sum_{q=-Q}^Q \mathbf{D}_{q,m}^{(d)} \mathbf{\Delta}_{q,m}^{(d)} \mathbf{b}_m^{(d)} \\ &= \sum_{q=-Q}^Q \mathbf{D}_{q,m}^{(d)} \text{diag}(\mathbf{F}_m^{(L,d)} \mathbf{c}_q) \mathbf{b}_m^{(d)} \end{aligned} \quad (3.15)$$

$$= \mathbf{H}_m^{(d)} \mathbf{b}_m^{(d)}, \quad (3.16)$$

where  $\mathbf{D}_{q,m}^{(d)}$  is a  $(B + 2Q) \times B$  submatrix obtained from  $\mathbf{D}_q$  by selecting rows (columns) corresponding to  $\mathbf{r}_m^{(d)}$  in  $\mathbf{r}_F$  ( $\mathbf{b}_m^{(d)}$  in  $\mathbf{b}$ );  $\mathbf{F}_m^{(L,d)}$  is obtained from  $\mathbf{F}^{(L)}$  by selecting the rows of  $\mathbf{b}_m^{(d)}$  in  $\mathbf{b}$ , and  $\mathbf{\Delta}_{q,m}^{(d)} = \text{diag}(\mathbf{F}_m^{(L,d)} \mathbf{c}_q)$  is obtained from  $\mathbf{\Delta}_q$  similarly, while the  $(B + 2Q) \times B$  sub-channel matrix

$$\mathbf{H}_m^{(d)} = \sum_{q=-Q}^Q \mathbf{D}_{q,m}^{(d)} \text{diag}(\mathbf{F}_m^{(L,d)} \mathbf{c}_q). \quad (3.17)$$

By replacing  $\mathbf{c}_q$  in (3.17) with  $\hat{\mathbf{c}}_q$  from (3.14), we obtain

$$\begin{aligned} \hat{\mathbf{H}}_m^{(d)} &= \sum_{q=-Q}^Q \mathbf{D}_{q,m}^{(d)} \text{diag}(\mathbf{F}_m^{(L,d)} \hat{\mathbf{c}}_q) \\ &= \sum_{q=-Q}^Q \hat{\mathbf{H}}_{q,m}^{(d)}, \end{aligned} \quad (3.18)$$

where  $\hat{\mathbf{H}}_{q,m}^{(d)}$  is the  $q$ th component of  $\hat{\mathbf{H}}_m^{(d)}$ , which is specified as  $\hat{\mathbf{H}}_{q,m}^{(d)} = \mathbf{D}_{q,m}^{(d)} \text{diag}(\mathbf{F}_m^{(L,d)} \hat{\mathbf{c}}_q)$ .

### 3.3.3 ZF Channel Equalization

After obtaining each  $\hat{\mathbf{H}}_m^{(d)}$ , a ZF equalization is carried out accordingly given by

$$\hat{\mathbf{b}}_m^{(d)} = \left( \hat{\mathbf{H}}_m^{(d)H} \hat{\mathbf{H}}_m^{(d)} \right)^{-1} \hat{\mathbf{H}}_m^{(d)H} \mathbf{r}_m^{(d)}, \quad (3.19)$$

where  $\hat{\mathbf{b}}_m^{(d)}$  is a  $B \times 1$  vector as an estimate of  $\mathbf{b}_m^{(d)}$ . We perform (3.19) for  $m = \{0, 1, \dots, N_B\}$  and thus all the transmitted data symbols are recovered.

It is known that the inversion of a  $B \times B$  matrix  $\hat{\mathbf{H}}_m^{(d)H} \hat{\mathbf{H}}_m^{(d)}$  is costly when it is considered as a full matrix [50]. As mentioned before,  $\hat{\mathbf{H}}_F$  is a banded matrix approximately (or exactly when the CCE-BEM is used) and the matrix bandwidth is  $(2Q + 1)$  that is usually much less than the matrix size. Therefore, we are allowed to reduce the computational complexity of inverting  $\hat{\mathbf{H}}_m^{(d)H} \hat{\mathbf{H}}_m^{(d)}$ , if the trivial entries (or zeros when the CCE-BEM is used) outside the matrix bandwidth are removed from  $\hat{\mathbf{H}}_F$  (equiv. from  $\hat{\mathbf{H}}_m^{(d)}$ ) [c.f. Fig. 3.3]). Such operation is well motivated by the fact that the energy of these trivial entries is reasonably negligible as indicated by Fig. 3.2, thus allowing for a significant reduction of the equalization complexity at the price of an acceptable performance loss [2,3,5,40,61]. We will discuss this in more details in Section 3.4.2. Inspired by these works [2,3,5,40,61], we first introduce a  $(B + 2Q) \times B$  selecting matrix which only has ones within a  $2Q + 1$  bandwidth or zeros otherwise, as depicted by

$$\mathbf{\Theta} = \begin{bmatrix} 1 & & \mathbf{0} \\ \vdots & \ddots & \\ 1 & \mathbf{1} & 1 \\ & \ddots & \vdots \\ \mathbf{0} & & 1 \end{bmatrix}.$$

Then, instead of  $\hat{\mathbf{H}}_m^{(d)}$  defined in (3.18), we shall actually substitute into (3.19) its adapted version after removing trivial entries. Specifically, we adapt

(3.18), by introducing  $\Theta$ , as

$$\begin{aligned}\hat{\mathbf{H}}_m^{(d)} &= \Theta \odot \sum_{q=-Q}^Q \mathbf{D}_{q,m}^{(d)} \text{diag}(\mathbf{F}_m^{(L,d)} \hat{\mathbf{c}}_q) \\ &= \sum_{q=-Q}^Q \left( \Theta \odot \mathbf{D}_{q,m}^{(d)} \right) \text{diag}(\mathbf{F}_m^{(L,d)} \hat{\mathbf{c}}_q)\end{aligned}\quad (3.20)$$

$$= \sum_{q=-Q}^Q \hat{\mathbf{H}}_{q,m}^{(d)}, \quad (3.21)$$

where  $\odot$  stands for the Hadamard (element-wise) product, and

$$\hat{\mathbf{H}}_{q,m}^{(d)} = \Theta \odot \mathbf{D}_{q,m}^{(d)} \text{diag}(\mathbf{F}_m^{(L,d)} \hat{\mathbf{c}}_q).$$

Here, we note that we keep the same notations (i.e.,  $\hat{\mathbf{H}}_m^{(d)}$  and  $\hat{\mathbf{H}}_{q,m}^{(d)}$ ) as in (3.18) for notation ease. To avoid any confusion, in the remainder of this chapter, we will refer to (3.21) as the definition of  $\hat{\mathbf{H}}_m^{(d)}$  unless explicitly defined.

## 3.4 Parallel Implementation Architecture

After reviewing the background of LS channel estimation and ZF equalization for narrowband OFDM time-varying channels, we shall in this section describe efficient architectures for their implementation.

### 3.4.1 Channel Estimator

As mentioned in Section 3.3.3, we understand that the channel estimator yields  $\hat{\mathbf{H}}_m^{(d)}$ 's as defined in (3.21), for  $m \in \{0, 1, \dots, N_B - 1\}$ , which shall be used by the channel equalizer in practice.

**General LS estimator** To efficiently implement the LS estimator, we first combine (3.14) and (3.20) to avoid the unnecessary computations on known matrices (i.e.,  $\mathbf{A}^{(p)}$  and  $\mathbf{F}_m^{(L,d)}$ 's).

Let us first introduce a  $(2Q + 1)B \times (2Q + 1)N_P$  matrix

$$\mathbf{M}_m = \left( \mathbf{I}_{2Q+1} \otimes \mathbf{F}_m^{(L,d)} \right) \left( \mathbf{A}^{(p)H} \mathbf{A}^{(p)} \right)^{-1} \mathbf{A}^{(p)H},$$

and then obtain a  $B \times (2Q + 1)N_P$  submatrix  $\mathbf{M}_{q,m}$  that is embedded in  $\mathbf{M}_m$  at the rows corresponding to  $\hat{\mathbf{c}}_q$  in  $\hat{\mathbf{c}}$  [c.f. (3.14)]. In this way, we can obtain an equation [c.f. (3.14)] given by

$$\mathbf{F}_m^{(L,d)} \hat{\mathbf{c}}_q = \mathbf{M}_{q,m} \mathbf{r}^{(p)}.$$

Now, we rewrite (3.20), for  $m \in \{0, \dots, N_B - 1\}$ , as

$$\begin{aligned} \hat{\mathbf{H}}_m^{(d)} &= \sum_{q=-Q}^Q \left( \Theta \odot \mathbf{D}_{q,m}^{(d)} \right) \text{diag}(\mathbf{F}_m^{(L,d)} \hat{\mathbf{c}}_q) \\ &= \sum_{q=-Q}^Q \left( \Theta \odot \mathbf{D}_{q,m}^{(d)} \right) \text{diag}(\mathbf{M}_{q,m} \mathbf{r}^{(p)}) \end{aligned} \quad (3.22)$$

$$= \sum_{q=-Q}^Q \hat{\mathbf{H}}_{q,m}^{(d)}, \quad (3.23)$$

where we rewrite  $\hat{\mathbf{H}}_{q,m}^{(d)}$  in (3.21) as  $\hat{\mathbf{H}}_{q,m}^{(d)} = \left( \Theta \odot \mathbf{D}_{q,m}^{(d)} \right) \text{diag}(\mathbf{M}_{q,m} \mathbf{r}^{(p)})$ .

Next, we reduce memory utilization by exploiting special matrix structures. We observe that  $\Theta \odot \mathbf{D}_{q,m}^{(d)}$  is a banded Toeplitz matrix with a bandwidth of  $(2Q + 1)$ , which is obtained from the circulant matrix  $\mathbf{D}_q$  [c.f. (3.7)] corresponding to the position of  $\hat{\mathbf{H}}_m^{(d)}$  in  $\hat{\mathbf{H}}_F$ . It indicates that we only need the first  $2Q + 1$  entries in the first column of this circulant matrix  $\mathbf{D}_q$  to represent all  $\Theta \odot \mathbf{D}_{q,m}^{(d)}$ 's for  $m \in \{0, \dots, N_B - 1\}$ . We denote a vector  $\mathbf{d}_q$  to stack these  $2Q + 1$  entries. Moreover,  $\hat{\mathbf{H}}_m^{(d)}$  is a banded matrix with a bandwidth of  $(2Q + 1)$  [c.f. (3.22)], and hence a memory efficient storage, called the DIA format [68], is adopted in this chapter. Fig. 3.4 illustrates how  $\hat{\mathbf{H}}_m^{(d)}$  is represented by its DIA format  $\bar{\mathbf{H}}_m^{(d)}$ , where  $Q = 1$  is used and  $\bar{\mathbf{h}}_{q,m}^{(d)T}$  stands for the  $(Q + q)$ th row in  $\bar{\mathbf{H}}_m^{(d)}$ . Likewise, we denote  $\bar{\mathbf{H}}_{q,m}^{(d)}$  as the DIA format of  $\hat{\mathbf{H}}_{q,m}^{(d)}$  in (3.23).

Finally, we describe the steps to efficiently implement (3.22) as Algorithm 1, which is suitable for any BEM model, and the only difference lies in



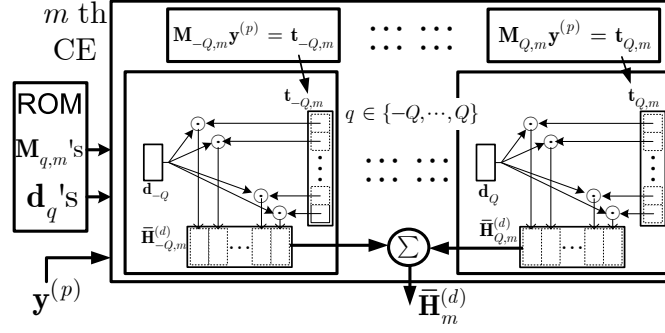
Figure 3.5: Schematic of the  $m$ th General LS estimator

Table 3.1: Computation Complexity Analysis for Channel Estimator

Complex Operations	Estimator Architecture	
	Simplified (for CCE-BEM)	General
CMs	$(2Q + 1)N_P B$	$(2Q + 1)(N_P + N_B)B$
CAs	$(2Q + 1)(N_P - 1)B$	$((2Q + 1)(2Q + N_P) - 1)B$

complex adders (CAs) for the  $m$ th estimator, for  $m \in \{0, \dots, N_B - 1\}$ . Its implementation schematic is depicted in Fig. 3.5. To maximize the processing concurrency, the parallelism for  $m \in \{0, \dots, N_B - 1\}$  can be adopted.

**Simplified LS estimator using CCE-BEM** Although we have investigated an efficient implementation above, it still has a fairly high complexity and thus one may hope to further simplify it. Among various (windowed) BEM's, we observe that the basis functions of the CCE-BEM yield shifted identity matrices, i.e.,  $\mathbf{D}_q = \mathbf{F} \text{diag} \{\mathbf{q}_q\} \mathbf{F}^H = \mathbf{I}^{(q)}$  according to (3.7) since  $\mathbf{q}_q = [1, e^{j\frac{2\pi}{N}q}, \dots, e^{j\frac{2\pi(N-1)}{N}q}]^T$  for the CCE-BEM; and  $\mathbf{I}^{(q)}$  only contains 1's on the  $q$ th (sub- or super-) diagonal but 0's otherwise, and  $\mathbf{I}^{(0)} = \mathbf{I}_N$  is an identity matrix. It also yields  $\Theta \odot \mathbf{D}_{q,m}^{(d)} = \mathbf{D}_{q,m}^{(d)}$  in (3.20).

If we exploit this property (i.e.,  $\mathbf{D}_q = \mathbf{I}^{(q)}$ ) in (3.13),  $\mathbf{A}^{(p)}$  is then yielded with the special sparse structure as shown in the left part of Fig. 3.6, where the blank area stands for zero entries. Moreover, if we introduce a permuta-



tion matrix  $\mathbf{P}$  which only contains 1's in the positions

$$\left\{ \left( i + 1, \lfloor i/N_P \rfloor + (2Q + 1)i_{\text{mod}/N_P} + 1 \right) \right\}_{i=0}^{N_P-1}$$

but 0's elsewhere, then since

$$\mathbf{P}\mathbf{D}^{(p)} = \mathbf{I}_{(2Q+1)N_P},$$

we obtain that [c.f. (3.13)]

$$\mathbf{P}\mathbf{A}^{(p)} = \mathbf{I}_{2Q+1} \otimes \left( \text{diag}(\mathbf{b}^{(p)})\mathbf{F}^{(L,p)} \right)$$

is a block diagonal matrix as shown in the right part of Fig. 3.6 with every sub-block at the diagonal of  $\mathbf{P}\mathbf{A}^{(p)}$  being the same sub-matrix given by

$$\bar{\mathbf{A}}^{(p)} = \text{diag} \left( \mathbf{b}^{(p)} \right) \mathbf{F}^{(L,p)}.$$

Consequently, denoting  $\bar{\mathbf{r}}^{(p)} = \mathbf{P}\mathbf{r}^{(p)} = [\bar{\mathbf{r}}_{-Q}^{(p)T}, \dots, \bar{\mathbf{r}}_Q^{(p)T}]^T$ , we can split (3.14) in parallel for  $q \in \{-Q, \dots, Q\}$  into

$$\hat{\mathbf{c}}_q = \left( \bar{\mathbf{A}}^{(p)H} \bar{\mathbf{A}}^{(p)} \right)^{-1} \bar{\mathbf{A}}^{(p)H} \bar{\mathbf{r}}_q^{(p)}, \quad (3.24)$$

Note that the permutation operation by  $\mathbf{P}$  does not cost additional resources or processing latency, since it only refers to different access addresses into the memories in the hardware design.

Further observations based on  $\mathbf{D}_q = \mathbf{I}^{(q)}$  suggest that the multiplication between  $\Theta \odot \mathbf{D}_{q,m}^{(d)} = \mathbf{D}_{q,m}^{(d)}$  and  $\text{diag}(\mathbf{F}_m^{(L,d)}\hat{\mathbf{c}}_q)$  in (3.20) only acts as placing the vector  $\mathbf{F}_m^{(L,d)}\hat{\mathbf{c}}_q$  onto the  $(Q+q)$ th diagonal line of the Toeplitz-like matrix  $\hat{\mathbf{H}}_m^{(d)}$ , for  $q \in \{-Q, \dots, Q\}$ . Let us use Fig. 3.4 for an illustration. When the CCE-BEM is used, the entries within the framed diagonal line in  $\hat{\mathbf{H}}_m^{(d)}$  in Fig. 3.4 is actually equal to  $\mathbf{F}_m^{(L,d)}\hat{\mathbf{c}}_q$  with  $q = -1$ . It is equivalent to say that in its DIA format  $\bar{\mathbf{H}}_m^{(d)}$ , the corresponding row  $\bar{\mathbf{h}}_{q,m}^{(d)T}$  is actually composed by  $\mathbf{F}_m^{(L,d)}\hat{\mathbf{c}}_q$ , i.e.,  $\bar{\mathbf{h}}_{q,m}^{(d)} = \mathbf{F}_m^{(L,d)}\hat{\mathbf{c}}_q$ . Therefore, if we jointly consider the fact that the estimator will yield a DIA format  $\bar{\mathbf{H}}_m^{(d)}$  instead of  $\hat{\mathbf{H}}_m^{(d)}$ , the operation in (3.20) acts equally as placing  $\mathbf{F}_{L,m}^{(d)}\hat{\mathbf{h}}_q$ 's onto the corresponding rows in  $\bar{\mathbf{H}}_m^{(d)}$ , for  $q \in \{-Q, \dots, Q\}$ , when the CCE-BEM is used.

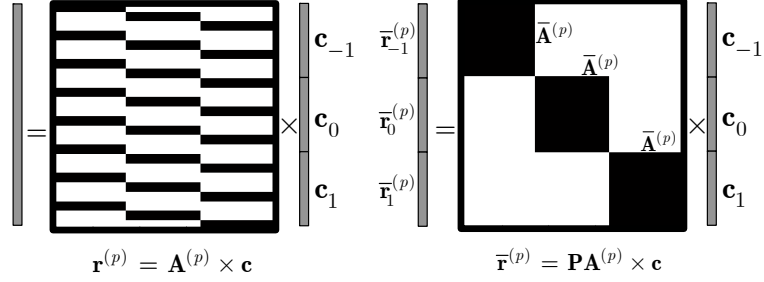


**Figure 3.6:** Special Matrix Structure with CCE-BEM, where  $Q = 1$  and  $N_P = 8$  for instance, and  $\mathbf{P}$  is a permutation matrix.

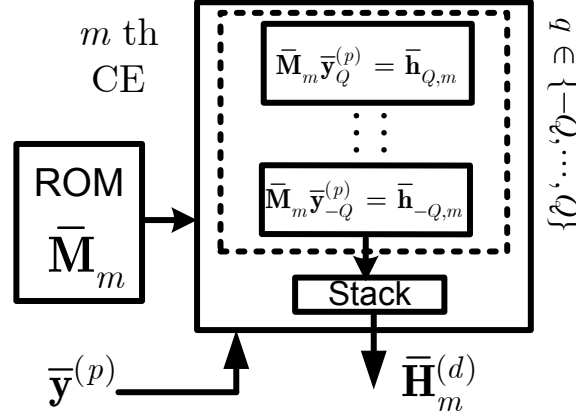


**Figure 3.7:** Schematic of the  $m$ th Simplified LS estimator

Now, we are allowed to describe the LS estimation tailored to the CCE-BEM, for  $q \in \{-Q, \dots, Q\}$  and  $m \in \{0, \dots, N_B - 1\}$ , as

$$\bar{\mathbf{h}}_{q,m}^{(d)T} = \mathbf{F}_m^{(L,d)} \hat{\mathbf{c}}_q \quad (3.25)$$

and then, by substituting (3.24) into (3.25), we obtain

$$\bar{\mathbf{h}}_{q,m}^{(d)T} = \bar{\mathbf{M}}_m \bar{\mathbf{r}}_q^{(p)} \quad (3.26)$$

where the  $B \times N_P$  matrix  $\bar{\mathbf{M}}_m$  is given by

$$\bar{\mathbf{M}}_m = \mathbf{F}_m^{(L,d)} \left( \bar{\mathbf{A}}^{(p)H} \bar{\mathbf{A}}^{(p)} \right)^{-1} \bar{\mathbf{A}}^{(p)H}$$

which is also perfectly known at the receiver.

Finally, the yielded DIA format of each  $\hat{\mathbf{H}}_m^{(d)}$  is stacked as

$$\bar{\mathbf{H}}_m^{(d)} = [\bar{\mathbf{h}}_{-Q,m}^{(d)}, \dots, \bar{\mathbf{h}}_{Q,m}^{(d)}]^T.$$

We call this implementation method as the ‘‘Simplified LS Estimator’’, which is particularly tailored for the CCE-BEM. Its detailed implementation is described as Algorithm 2. Its computational complexity is listed in Table 3.1 for comparison with the previous method. It is clear that this simplified LS estimator is more economic and memory efficient than the previous general LS estimator. The schematic of the simplified LS estimator is de-

---

**Algorithm 2** *Simplified LS estimator (for CCE-BEM)*

---

0. Pre-compute the matrix all  $\bar{\mathbf{M}}_m$ 's for  $m = \{0, \dots, N_B - 1\}$ ; Totally  $N_D N_P$  elements are stored for ROM;
  1. Carefully collect  $\bar{\mathbf{r}}_q^{(p)}$ 's and perform (3.26) to attain  $\bar{\mathbf{h}}_{q,m}^{(d)}$  for  $q = \{-Q, \dots, Q\}$ , which is stacked into a  $(2Q + 1) \times B$  matrix  $\bar{\mathbf{H}}_m^{(d)}$ , the DIA format of  $\hat{\mathbf{H}}_m^{(d)}$ .
- 

picted in Fig. 3.7. To maximize the concurrency, the processing parallelism for both  $q \in \{-Q, \dots, Q\}$  and  $m \in \{0, \dots, N_B - 1\}$  can be exploited. It is noteworthy that, when  $Q = 0$ , (3.26) degrades to the channel estimation for the traditional OFDM systems which operate in the time-invariant channels. In other words, our simplified estimator tailored for the CCE-BEM can be considered as an extension of the channel estimator design for the time-invariant OFDM systems. One may argue that the CCE-BEM is inferior to other BEM models [4, 39] in terms of the modeling accuracy. We shall show that the CCE-BEM still yields a good performance of channel estimation in the presence of a realistic mobility velocity.

### 3.4.2 Channel Equalizer

To recover the  $m$ th data cluster denoted by a  $B \times 1$  vector  $\mathbf{b}_m^{(d)}$ , a ZF equalization is introduced in (3.19), where a matrix inversion is required. For a traditional OFDM over a time-invariant channel,  $Q = 0$  is efficient and thus  $\hat{\mathbf{H}}_m^{(d)}$

**Table 3.2:** Complexity Analysis for the Estimator and Equalizer

Complex Operations	Mobile OFDM		TI OFDM	
	Simplified CE	EQ	CE	EQ
CMs	$(2Q + 1)N_P B$	$(4Q^2 + 12Q + 2)B$	$N_P B$	0
CAs	$(2Q + 1)(N_P - 1)B$	$(4Q^2 + 8Q + 3)B$	$(N_P - 1)B$	0
CDs	0	$(2Q + 1)B$	0	$B$

is a diagonal matrix. In this case, the equalization (3.19) has only a computational complexity linear to the vector size  $B$ . However, when the channel is time varying,  $\hat{\mathbf{H}}_m^{(d)}$  is in principle a full matrix, and thus the equalization complexity using its direct matrix inversion is too high (i.e.,  $\mathcal{O}(B^3)$  [50]) to be practical. An important feature is that each  $\hat{\mathbf{H}}_m^{(d)}$  is a banded matrix with a bandwidth of  $2Q + 1$  [c.f. (3.21)], and thus  $\hat{\mathbf{H}}_m^{(d)H} \hat{\mathbf{H}}_m^{(d)}$  is a banded positive definite Hermitian matrix. Based on this property, we can adapt the LDL<sup>H</sup> factorization [50] to realize the inversion more efficiently, yielding a low-complexity equalization as specified in Algorithm 3. This equalization has a computational complexity  $\mathcal{O}(Q^2 B)$ , which is usually much less than  $\mathcal{O}(B^3)$  because  $Q$  is typically small (e.g.,  $Q = 1$ ) [3]. Note that the above algorithm requires a strictly banded matrix  $\hat{\mathbf{H}}_m^{(d)}$  [3], which also explains  $\Theta$  in (3.20). We also need to note that the above process is correct, for  $m = \{0, \dots, N_B - 1\}$ , only if the number of null subcarriers at either edge is larger than the half bandwidth of  $\hat{\mathbf{H}}_m^{(d)}$ , i.e.,  $\geq Q$  [c.f. Fig. 3.3]. Such a condition is widely considered in the literature in, e.g., [3, 5, 40, 61], and it can be satisfied in many existing OFDM standards, e.g., a multiple-band UWB standard [69]. Table 3.2 specifies the complexity of the equalizer for the  $m$ th data cluster in complex operations, i.e. CAs, CMs, and complex dividers (CDs). In the same table, we also quote the complexity of our channel estimator tailored for the CCE-BEM from Table 3.1.

To implement the channel equalizer efficiently, we first recall that the DIA format  $\hat{\mathbf{H}}_m^{(d)}$  is obtained by the channel estimator as described in the previous section, instead of its original matrix  $\hat{\mathbf{H}}_m^{(d)}$ . Here, prior to the equalizer implementation, we describe how to efficiently store the matrices used in Algorithm 3 (i.e.,  $\mathbf{W}_m = \hat{\mathbf{H}}_m^{(d)H} \hat{\mathbf{H}}_m^{(d)}$ , while  $\mathbf{L}$  and  $\mathbf{D}$  are obtained from

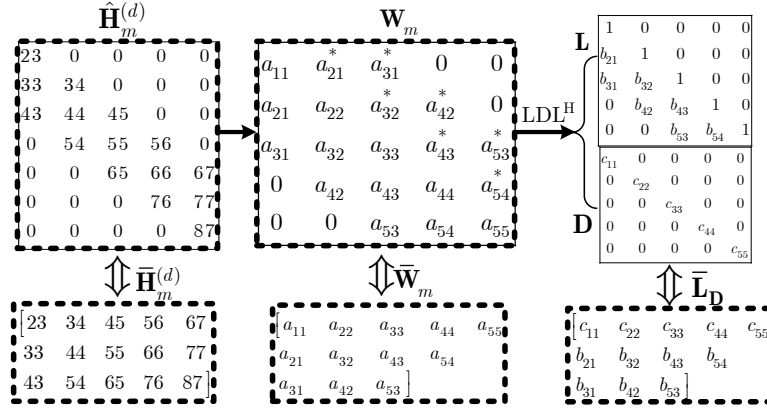


Figure 3.8: Efficient Storage Format of Matrices for the equalizer

$$\begin{aligned}
 \hat{\mathbf{H}}_m^{(d)}[i, j] &= \bar{\mathbf{H}}_m^{(d)}[(i-j)B + j] & , j \leq i \leq j + Q \\
 \mathbf{D}[j, j] &= \bar{\mathbf{L}}_D[j] \\
 \mathbf{L}[i, j] &= \bar{\mathbf{L}}_D \left[ (i-j)B - \frac{(i-j)(i-j-1)}{2} + j \right] & , j < i \leq \min(B, j + 2Q) \\
 \mathbf{W}_m[i, j] &= \bar{\mathbf{W}}_m \left[ (i-j)B - \frac{(i-j)(i-j-1)}{2} + j \right] & , j \leq i \leq \min(B, j + 2Q)
 \end{aligned}$$

Figure 3.9: Index Mapping between Matrices and their DIA format

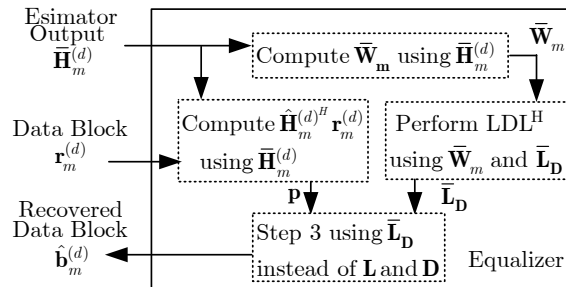


Figure 3.10: The Schematic for the equalizer.

$\mathbf{W}_m = \mathbf{L}\mathbf{D}\mathbf{L}^H$ ). Due to the special structures of these matrices, the DIA format is adapted herein. We plot Fig. 3.8 to illustrate the storage of these matrices, where  $\bar{\mathbf{W}}_m$  is the adapted DIA format to store  $\mathbf{W}_m$ , while  $\bar{\mathbf{L}}_D$  represents two matrices  $\mathbf{L}$  and  $\mathbf{D}$  jointly since the diagonal of  $\mathbf{L}$  always equals to one and  $\mathbf{D}$  is diagonal with the same size of  $\mathbf{L}$ . The index mapping from these DIA formats to the original matrices are given in Fig. 3.9, where we deliberately consider the DIA format only accessed in one-dimension addresses to represent the physical memories. Using the index mapping, each matrix computation in Algorithm 3 can thus be identically carried out using their DIA formats, and the only difference lies in exploiting different indices for each non-zero value. It is noteworthy that such index mapping does not introduce additional operations since it only refers to different memory addresses. Fig. 3.10 depicts the schematic of the equalizer for the  $m$ th data cluster  $\mathbf{b}_m^{(d)}$ , for  $m \in \{0, \dots, N_B - 1\}$ .

From the above, we know that the  $m$ th channel estimator yields a DIA format  $\bar{\mathbf{H}}_m^{(d)}$  of  $\hat{\mathbf{H}}_m^{(d)}$ , which are used directly by the  $m$ th equalizer as an input. It indicates that the aforementioned channel estimator shares the same interfaces to communicate with our channel equalizer herein. Fig. 3.11 describes the parallel connection between each pair of channel estimator (CE) and equalizer (EQ), and also illustrates the testbench environment used in this chapter.

### 3.5 Experiments

For the OFDM setup, we consider the cases listed in Table 3.3. It is known that using a larger  $Q$ , a higher system performance with regards to the symbol detection accuracy can be obtained [3–5, 40, 61]. But its paid price is a higher hardware cost for implementation, which is evident later. Each pilot is guarded by  $2Q$  null subcarriers on its either side. In addition to these guarded null subcarriers, the number of the null edge subcarriers placed at either edge is needed to be larger than  $Q$ . For all the cases, QPSK symbols are modulated on the data and pilot subcarriers; To represent the time-varying channels, the Jakes' model [14] with a maximal normalized Doppler factor (i.e., the Doppler shift divided by the OFDM subcarrier interval) of 0.02 is

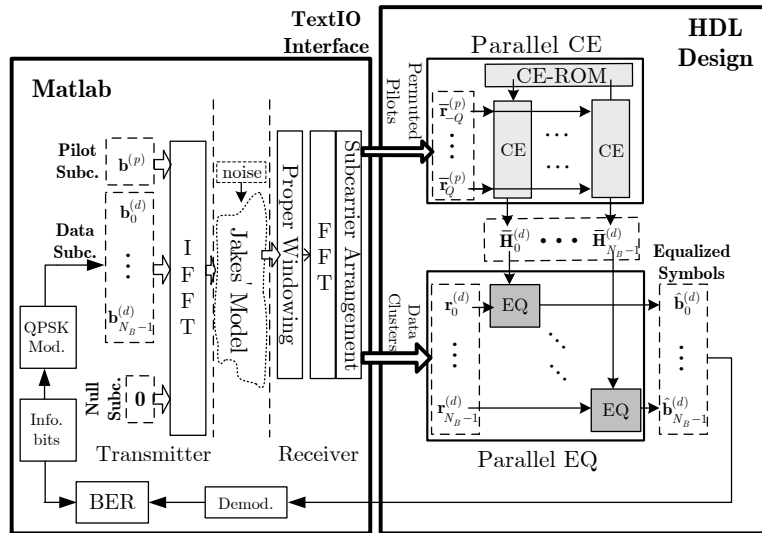


Figure 3.11: Testbench of Mobile OFDM Baseband Receiver

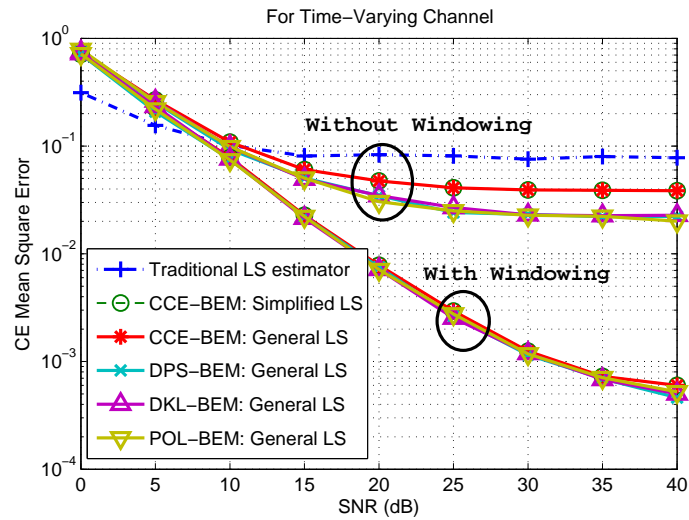


Figure 3.12: Channel Estimation Accuracy

**Table 3.3:** Testing Setups for OFDM System

Setup	$Q$	$N$	$N_P$	$N_B$	$B$	$N_D$	Edge Guard*	
O	0	256	8	7	35	245	1	2
I	1	256	8	7	30	210	3	3
II	2	256	8	7	25	175	4	5
III	3	256	8	7	20	140	6	6

\* referring to the edge null subcarriers. The number of the null subcarrier at either edge must be larger than  $Q$ . For simplicity reasons, we never place separated data subcarriers but only place them as  $N_B$  clusters, and thus abundant edge null subcarriers may exist.

adopted. Physically, if we consider that the OFDM baseband bandwidth is  $W = 20$  MHz and the central radio frequency is  $f_c = 10$  GHz, this maximal normalized Doppler factor corresponds to the highest velocity of  $v = 84.38$  km/h (computed by  $\frac{f_c \times 2v/c}{W/N} = 0.02$ , where  $c = 1.08 \times 10^9$  km/h). Moreover, the delay tap number of the channel is taken less than  $N_P$ , which means a delay spread of 0.4ms if the baseband bandwidth of  $W = 20$  MHz, such that  $N_P > L$  is satisfied [c.f. (3.14)]. One can check that this OFDM system satisfies our narrowband assumption according to Chapter 2, because the moving velocity is negligible compared to the propagation speed of terrestrial ratio  $v \ll c$ , and also the bandwidth is very small compared to the central frequency  $W \ll f_c$ . The time-varying channel is windowed by a time-domain windowing from [61]. According to the testbench environment as illustrated in Fig. 3.11, we randomly generate the received OFDM symbols for our LS channel estimator and ZF equalizer, and then examine the performances of the channel estimation and equalization.

Let us currently focus on the Setup O and Setup I for the OFDM system. Fig. 3.12 illustrates the mean-square-error (MSE) performances of the LS channel estimator using various BEM's for the Setup I, with different signal-to-noise ratio (SNR) conditions. The traditional LS estimator for the time-invariant (TI) OFDM channels is realized using our simplified LS estimator corresponding to  $Q = 0$  as previously mentioned. The MSE is defined as

$$\text{MSE} = \frac{1}{N_B} \sum_{m=0}^{N_B-1} \left\| \mathbf{H}_{F,m}^{(d)} - \hat{\mathbf{H}}_m^{(d)} \right\|^2 / \left\| \mathbf{H}_{F,m}^{(d)} \right\|^2, \quad (3.27)$$



where  $\mathbf{H}_{F,m}^{(d)}$  is carved from  $\mathbf{H}_F$  in (3.1) at the same positions corresponding to  $\hat{\mathbf{H}}_m^{(d)}$  in  $\hat{\mathbf{H}}_F$ . From Fig. 3.12, it is clear that the traditional estimator designed for TI channels can not combat a time-varying channel, while the performances of our LS estimators without a time windowing are still not good. With a proper windowing design, our LS estimators all perform well for time-varying channels, no matter which BEM is adopted. It is noteworthy that although the estimation accuracy of a simplified LS estimator using the CCE-BEM is indeed inferior to other BEM models, the drop of the estimation accuracy is slight especially in presence of the time-domain windowing. Additionally, it is certain that the estimation accuracies obtained by using different implementation methods (i.e., general LS estimator or simplified LS estimator) are identical when the CCE-BEM is adopted to model the channel.

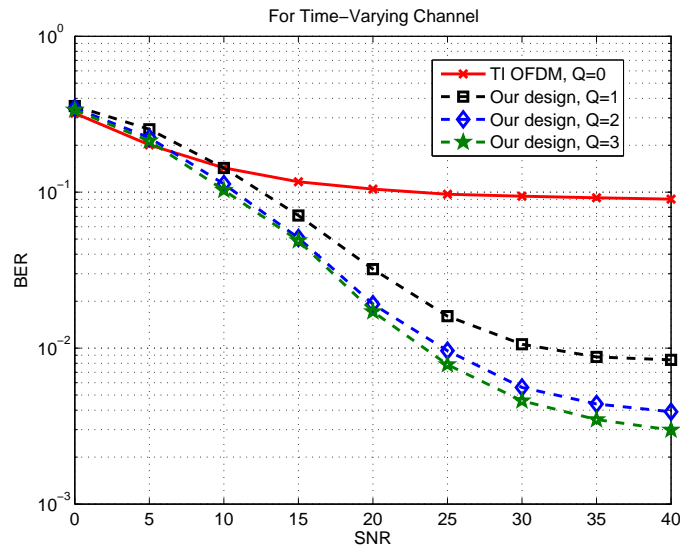
At the same time, we compare the hardware resource utilizations of the aforementioned two approaches of implementing the channel estimation (i.e., general LS estimator and simplified LS estimator). Setup I is tested. Specifically, using a similar methodology as [70], we first realize an LS estimator for one data cluster (e.g., the  $m$ th data cluster), and then duplicate it to generate other pairs with  $Q = 1$ , resulting a concurrency for  $m = \{0, \dots, N_B - 1\}$ . Table 3.4 lists the values of their synthesis results in a 90nm technology. It shows that our simplified LS estimator brings a roughly 57% cut for the ASIC core area (excluding the ROM), a 88% savage for the ROM size and a 55% reduction of the processing latency compared to the general LS estimator. Jointly considering their estimation performances shown in Fig. 3.12 and their hardware costs herein, it suggests that the it is more appealing to design time-varying OFDM systems using the CCE-BEM than using other BEM options.

Now, we select the simplified LS estimator tailored to the CCE-BEM and then combine it with the ZF channel equalizer. Fig. 3.13 compares the bit-error ratio (BER) performance of our design using OFDM Setup I, II and III (i.e., with  $Q = 1, 2$  and  $3$ ) for a narrowband time-varying channel. Additionally, we also build a TI OFDM receiver corresponds to OFDM Setup O using  $Q = 0$  and without any time-domain windowing. We note that these BER performances are obtained without any channel coding. It is clear that since the TI OFDM receiver fails to combat the time variation of the channel,

**Table 3.4: Synthesis Results of Channel Estimator**

		ASIC Core Area <sup>*</sup> ( $10^3 \mu m^2$ )	ROM Area <sup>*</sup> ( $10^3 \mu m^2$ )	Latency <sup>*</sup> (cycle)
Method	Simplified CE	487.46	25.24	159
	General CE	1129.84	213.36	353

<sup>\*</sup> 90nm ASIC technology with 100MHz clock and 20 (40) bits are adopted for a real (complex) number; Here  $Q = 1$ .

**Figure 3.13: BER Performance**

it hardly recover the transmitted data information correctly. However the receiver using our estimator and equalizer significantly improves the BER performance especially at a higher SNR. In addition, the use of a larger  $Q$  parameter indeed brings a performance improvement with regards to the symbol detection accuracy, as noticed by [3, 5, 40, 61].

To investigate the hardware resource utilization of our designs, we implement the designs with these setups (i.e., with  $Q = 0, 1, 2$  and  $3$ ). Similar for the channel estimator, we first realize a ZF equalizer in combina-

**Table 3.5: Comparison of FPGA Implementations**

		Mobile OFDM			TI OFDM
		$Q = 3$	$Q = 2$	$Q = 1$	$Q = 0$
Latency (cycle)		2759	2451	1758	706
Resource *	acc. Inst.	128720	96966	69808	20163
	LUTs	40.02%	35.69%	27.14%	6.88%
	CLBs	40.05%	35.71%	27.18%	6.94%
	DFFs	3.70%	3.22%	2.32%	0.98%
	DSP48Es	28.52%	25.43%	18.24%	4.16%
	RAMS	65.77%	58.73%	42.25%	8.94%

\* 20 (40) bits for a real (complex) number on Xilinx 6VLX240TFF1156 Device with a 100MHz clock; The RAMS stands for the block RAM components, which are mainly used to store matrices during the channel estimation and equalization.

tion with a simplified LS estimator, and then duplicate their combination for  $m = \{0, \dots, N_B - 1\}$ . Their synthesis results on a Xilinx 6VLX240TFF1156 device are listed in Table 3.5, where the processing latency is counted by the clock cycles and the FPGA resource utilization report is quoted. It is no surprise that a time-varying OFDM receiver (or a mobile OFDM receiver) based on the BEM requires more hardware efforts to support high-mobility users since we remarkably extend a TI OFDM system. In other words, the BER improvement of time-varying OFDM systems is earned at the price of more complicated hardware design, compared to a TI OFDM receiver. Moreover, we observe that for the time-varying OFDM system from  $Q = 1$  to  $Q = 3$ , the hardware resource utilization (e.g., by considering “acc. Inst.” as an overall utilization of hardware resource), as well as the processing latency, increases roughly linearly along  $Q$ . Jointly considering the BER performance as illustrated in Fig. 3.13, an excessively large  $Q$  (e.g.,  $Q = 3$ ) is not desirable since a remarkable increased hardware cost only brings a slight improvement of the BER performance. For instance, a roughly 0.1dB BER improvement from  $Q = 2$  to  $Q = 3$  is obtained, but at a price of 1.32 times resource utilization. It indicates that a small  $Q$  is sufficient (e.g.,  $Q = 2$ ) to provide an accurate symbol detection without introducing too high hardware utilization.

### 3.6 Summary

The narrowband OFDM system model in light of BEM was introduced. Two efficient implementations for the least-squares estimator of OFDM time-varying channels were discussed. The first one is the general estimator which supports estimation methods using various BEM models. The second one, the simplified estimator particularly tailored for the CCE-BEM, leads to a more efficient hardware architecture, while still maintains a high estimation accuracy. Hence, the CCE-BEM is more appealing to time-varying OFDM systems than other BEM's. The efficient implementation of the parallel equalizer was presented afterwards. Our design for OFDM receivers with a small BEM order is capable of combatting the narrowband time-varying OFDM channel. For comparison, a traditional time-invariant OFDM receiver design which only works for time-invariant channels fails in a time-varying channel.

### Appendix 3.A Detailed Derivation of (3.12)

Let us start from the noiseless version of (3.11) as

$$\mathbf{r}^{(p)} = \sum_{q=-Q}^Q \mathbf{D}_q^{(p)} \Delta_q^{(p)} \mathbf{b}^{(p)}$$

where  $\mathbf{D}_q^{(p)}$  is a submatrix obtained from  $\mathbf{D}_q$  by only selecting rows (columns) corresponding to  $\mathbf{r}^{(p)}$  in  $\mathbf{r}_F$  ( $\mathbf{b}^{(p)}$  in  $\mathbf{b}$ ), and  $\Delta_q^{(p)}$  is obtained from  $\Delta_q$  by selecting the rows of  $\mathbf{b}^{(p)}$  in  $\mathbf{b}$ .

We first notice that  $\Delta_q = \text{diag}(\mathbf{F}^{(L)} \mathbf{c}_q)$  as specified in (3.8), and thus we can specify  $\Delta_q^{(p)}$  as

$$\Delta_q^{(p)} = \text{diag}(\mathbf{F}^{(L,p)} \mathbf{c}_q),$$

where  $\mathbf{F}^{(L,p)}$  collects the rows of  $\mathbf{F}^{(L)}$  corresponding to the positions of  $\mathbf{b}^{(p)}$  in  $\mathbf{b}$ .

To this end, it is clear that

$$\begin{aligned} \Delta_q^{(p)} \mathbf{b}^{(p)} &= \text{diag}(\mathbf{F}^{(L,p)} \mathbf{c}_q) \mathbf{b}^{(p)} \\ &= \text{diag}(\mathbf{b}^{(p)}) \mathbf{F}^{(L,p)} \mathbf{c}_q. \end{aligned} \quad (3.28)$$

Substituting (3.28) into  $\mathbf{r}^{(p)}$ , we obtain

$$\begin{aligned} \mathbf{r}^{(p)} &= \sum_{q=-Q}^Q \mathbf{D}_q^{(p)} \left( \text{diag}(\mathbf{b}^{(p)}) \mathbf{F}^{(L,p)} \right) \mathbf{c}_q \\ &= [\mathbf{D}_{-Q}^{(p)}, \dots, \mathbf{D}_Q^{(p)}] \\ &\quad \times \mathbf{I}_{2Q+1} \otimes \left( \text{diag}(\mathbf{b}^{(p)}) \mathbf{F}^{(L,p)} \right) \\ &\quad \times [\mathbf{c}_{-Q}^T, \dots, \mathbf{c}_Q^T]^T \\ &= \mathbf{D}^{(p)} \left( \mathbf{I}_{2Q+1} \otimes \left( \text{diag}(\mathbf{b}^{(p)}) \mathbf{F}^{(L,p)} \right) \right) \mathbf{c} \end{aligned} \quad (3.29)$$

where  $\otimes$  stands for the Kronecker product,  $\mathbf{D}^{(p)} = [\mathbf{D}_{-Q}^{(p)}, \dots, \mathbf{D}_Q^{(p)}]$  and  $\mathbf{c} = [\mathbf{c}_{-Q}^T, \dots, \mathbf{c}_Q^T]^T$ .

Consequently, if we denote

$$\mathbf{A}^{(p)} = \mathbf{D}^{(p)} \left( \mathbf{I}_{2Q+1} \otimes \left( \text{diag}(\mathbf{b}^{(p)}) \mathbf{F}^{(L,p)} \right) \right)$$

as defined in (3.13), we obtain

$$\mathbf{r}^{(p)} = \mathbf{A}^{(p)} \mathbf{c}$$

which is the noiseless version of (3.12).

**Algorithm 3** *Low-Complexity equalization algorithm*

1. Compute the matrix  $\mathbf{W}_m = \hat{\mathbf{H}}_m^{(d)H} \hat{\mathbf{H}}_m^{(d)}$  and also  $\mathbf{p} = \hat{\mathbf{H}}_m^{(d)H} \mathbf{r}_m^{(d)}$ ;
2. Perform the banded-LDL<sup>H</sup> factorization as  $\mathbf{W}_m = \mathbf{L}\mathbf{D}\mathbf{L}^H$ , where  $\mathbf{D}$  is a diagonal matrix, and  $\mathbf{L}$  is a lower triangular matrix whose diagonal are ones and whose lower bandwidth is  $2Q$ ; Such LDL<sup>H</sup> factorization can be implemented in pseudo-code as:

```

 $\mathbf{D}[0, 0] = \mathbf{W}_m[0, 0];$ 
for( $i = 1; i < B; i = i + 1$ )
   $u = \max(0, i - 2Q);$ 
  for( $j = u; j < i; j = j + 1$ )
     $\mathbf{L}[i, j] = \frac{1}{\mathbf{D}[j, j]} \left( \mathbf{W}_m[i, j] - \sum_{k=u}^{j-1} \mathbf{L}^*[j, k] \mathbf{L}[i, k] \mathbf{D}[k, k] \right);$ 
  end
   $\mathbf{D}[i, i] = \mathbf{W}_m[i, i] - \sum_{k=u}^{i-1} |\mathbf{L}[i, k]|^2 \mathbf{D}[k, k];$ 
end

```

3. Solve  $\mathbf{W}_m \hat{\mathbf{b}}_m^{(d)} = \mathbf{p}$  by solving firstly the triangular system  $\mathbf{L}\mathbf{f} = \mathbf{p}$  and the diagonal system  $\mathbf{D}\mathbf{g} = \mathbf{f}$ , and then another triangular system  $\mathbf{L}^H \hat{\mathbf{b}}_m^{(d)} = \mathbf{g}$  to recover  $\hat{\mathbf{b}}_m^{(d)}$ . This step can be specified in pseudo-code as:

```

for( $i = 0; i < B; i = i + 1$ )
   $u = \max(0, i - 2Q);$ 
   $\mathbf{f}[i] = \mathbf{p}[i] - \sum_{k=u}^{i-1} \mathbf{L}[i, k] \mathbf{f}[k];$   $\mathbf{g}[i] = \mathbf{f}[i] / \mathbf{D}[i, i];$ 
end
for( $i = B - 1; i \geq 0; i = i - 1$ )
   $v = \min(B - 1, i + 2Q);$ 
   $\hat{\mathbf{b}}_m^{(d)}[i] = \mathbf{g}[i] - \sum_{k=i+1}^v \mathbf{L}^*[k, i] \hat{\mathbf{b}}_m^{(d)}[k];$ 
end

```





## Chapter 4

---

# Wideband OFDM Systems

*Give people a little bit more bandwidth and they'll find something for which that bandwidth is not nearly enough.*

Paul Green

In Chapter 2, the fundamental differences between the narrowband channels and the wideband channels have already been clarified. In Chapter 3, OFDM over narrowband channels was discussed. This chapter describes OFDM transmissions over a wideband channel and seeks to quantify the amount of interference resulting from the time variation of wideband channels which generally follow the multi-scale/multi-lag (MSML) model. It is shown that a more complicated receiver scheme is inevitable for wideband OFDM time-varying channels compared to the narrowband case.

### 4.1 Introduction

For the narrowband communication systems considered in the last chapter, the Doppler effect manifests itself primarily as frequency shifts [15, 16]. In this case, it is reasonable to assume that each OFDM subcarrier experiences statistically identical frequency offsets [59] and the effective channel matrix of a narrowband OFDM system is approximately banded [2] in the presence of Doppler. Many researches on narrowband OFDM LTV systems are based on this banded approximation [2, 3, 5, 40, 40, 41, 61, 66] and we have also exploited this banded structure in the last chapter to propose an efficient implementation architecture for narrowband OFDM receiver designs.

In a *wideband* system, where the relative signal bandwidth is large, the Doppler effect should be more appropriately modeled as scalings of the signal waveform [15, 16]. Wideband systems arise in, e.g., underwater acoustic

communication (UAC) systems or wideband terrestrial radio frequency systems such as ultra wideband (UWB). Due to multipath, a wideband linear time-varying (LTV) channel can be more accurately described by a multi-scale multi-lag (MSML) model [15, 21]. Many signaling schemes have been studied for wideband systems. For instance, [33, 71] consider direct-sequence spread spectrum (DSSS). Recently, the use of OFDM for UAC or UWB has received considerable attention. To counteract the scaling effect due to Doppler, [72] proposes a multi-band OFDM system such that within each band, the narrowband assumption can still be valid. More commonly, many works assume a single-scale multi-lag (SSML) model for the wideband LTV channel. Based on the SSML assumption, after a resampling operation the channel can be approximated by a time-invariant channel but subject to a carrier frequency offset (CFO) [28, 30]. However, since the channel should be more accurately described by an MSML model, determining the optimal resampling rate is not trivial [29].

In this chapter, we consider OFDM transmission over on an MSML model. The resulting channel, which is a full matrix in the presence of Doppler, will be equalized by means of the conjugate gradient (CG) algorithm [50, 73], whose performance is less sensitive to the condition of the channel matrix than, e.g., a least-squares approach. On the other hand, the convergence rate of CG is inversely proportional to the channel matrix condition number. This is especially of significance if a truncated CG is to be used in practice, which halts the algorithm after a limited number of iterations in order to reduce the overall complexity. Therefore, it is desired that the channel matrix is well-conditioned to ensure a fast convergence. To this end, preconditioning techniques can be invoked to enforce the eigenvalues of the channel matrix to cluster around one [74]. To achieve a balance between performance and complexity, we restrict the preconditioner to be a diagonal matrix, whose diagonal entries can be designed by following the steps given in [75]. We notice that a circulant preconditioner in the time domain was introduced in [41], which is equivalent to a diagonal preconditioner in the frequency domain. This preconditioner is introduced based on a basis expansion model (BEM), which is often used to approximate the channel's time-variation for a narrowband system. For a wideband system as considered in this chapter,

it can be shown that this preconditioner in the frequency domain is equal to the inverse of the diagonal entries of the frequency-domain channel matrix.

What is not considered in [41, 75] is the resampling operation at the receiver, which is an indispensable and crucial step for wideband LTV channels. Different from the trivial resampling scheme for SSML channel models, an optimum resampling method is proposed in [29] for MSML channels, which aims at minimizing the average error of approximating the MSML channel by an SSML model. This chapter studies the resampling from a preconditioning point of view. It is observed that if the major channel energy is located on the off-diagonals of the channel matrix, a diagonal preconditioner will deteriorate the channel matrix condition rather than improve it, thereby reducing the convergence rate of CG instead of increasing it as opposed to the claim of [75]. The energy distribution of the channel matrix is governed by the resampling. Different from [29], which only considers rescaling the received signal, and [76], which considers both rescaling and frequency synchronization, this chapter will show that for OFDM systems, all these three resampling parameters can have a significant impact on the system performance (i.e., rescaling, frequency synchronization and time synchronization). More specifically, we will extend the results of [76] and [77] by jointly optimizing these three resampling parameters both in the frequency domain and the time domain.

## 4.2 System Model Based on an MSML Channel

### 4.2.1 Continuous Data Model

Suppose that the baseband transmit signal  $s(t)$  consists of  $K$  subcarriers, we adapt (2.23) to describe this OFDM signal with a minor change given by

$$s(t) = \frac{1}{\sqrt{KT}} \sum_{k=0}^{K-1} b_k e^{j2\pi f_k t} u(t), \quad -T_{\text{pre}} < t \leq KT + T_{\text{post}} \quad (4.1)$$

where the data symbol  $b_k$  is modulated on the  $k$ th subcarrier  $f_k = k\Delta f$ , for  $k = 0, 1, \dots, K-1$ , with  $\Delta f$  being the OFDM subcarrier spacing. With  $T = 1/(K\Delta f)$ ,  $KT$  is the effective duration of an OFDM symbol. The cyclic

prefix is given as  $T_{\text{pre}}$  which is assumed to be longer than the delay spread. Different from (2.23), we introduce a cyclic postfix  $T_{\text{post}}$ , which is assumed long enough to ensure signal completeness in case of scaling and will be defined later on. Additionally, the rectangular pulse  $u(t)$  is defined to be 1 within  $t \in [-T_{\text{pre}}, KT + T_{\text{post}}]$  and 0 otherwise. Prior to transmission,  $s(t)$  is up-converted to passband, yielding  $\bar{s}(t) = \Re\{s(t)e^{j2\pi f_c t}\}$  where  $f_c$  denotes the carrier frequency. With sufficient cyclic extensions, the interference from adjacent OFDM symbols can be neglected and hence we are allowed to consider an isolated OFDM symbol in this chapter without loss of generality. Although this chapter discusses the scenario when cyclic extensions are used, the analysis can be directly applied to zero padding OFDM (ZP-OFDM) with minor modifications.

The considered signal is transmitted over a wideband LTV channel, which is assumed to comprise multiple resolvable paths as mentioned in (2.5) but with a finite path number of  $L + 1$ . With a collection of these  $L + 1$  paths, the actual received signal  $\bar{r}(t)$  is given by

$$\bar{r}(t) = \sum_{l=0}^L \bar{h}_l \sqrt{\alpha_l} \bar{s}(\alpha_l(t - \tau_l)) + \bar{w}(t), \quad (4.2)$$

and, if  $f_c = f'_c$  in (2.6), we obtain its corresponding complex baseband equivalent given by

$$r(t) = \sum_{l=0}^L h_l \sqrt{\alpha_l} s(\alpha_l(t - \tau_l)) e^{j2\pi(\alpha_l - 1)f_c t} + w(t) \quad (4.3)$$

where  $\bar{r}(t) = \Re\{r(t)e^{j2\pi f_c t}\}$  and  $\bar{w}(t) = \Re\{w(t)e^{j2\pi f_c t}\}$ , while  $h_l = \bar{h}_l e^{-j2\pi\tau_l\alpha_l f_c}$ .

By substituting (4.1) into (4.3), we can rewrite  $r(t)$  as

$$\begin{aligned} r(t) &= \sum_{l=0}^L h_l \sqrt{\alpha_l} \left( \frac{1}{\sqrt{KT}} \sum_{k=0}^{K-1} b_k e^{j2\pi f_k \alpha_l (t - \tau_l)} u(\alpha_l(t - \tau_l)) \right) e^{j2\pi(\alpha_l - 1)f_c t} + w(t) \\ &= \frac{1}{\sqrt{KT}} \sum_{k=0}^{K-1} b_k h_k(t) e^{j2\pi f_k t} + w(t), \end{aligned} \quad (4.4)$$

where

$$h_k(t) = \sum_{l=0}^L h_l \sqrt{\alpha_l} e^{-j2\pi f_k \alpha_l \tau_l} e^{j2\pi(\alpha_l - 1)(f_c + f_k)t} u(\alpha_l t - \alpha_l \tau_l), \quad (4.5)$$

which stands for the time-varying channel frequency response seen by the  $k$ th subcarrier. From the definition of  $h_k(t)$ , we notice that the  $k$ th subcarrier experiences a frequency offset of  $(\alpha_l - 1)(f_c + f_k)$  over the  $l$ th path.

*Remark 4.1.* The cyclic prefix is assumed to be longer than the delay spread and the cyclic postfix has a duration long enough to ensure signal continuity in the observation window for  $t \in [0, KT]$ . Specifically, it is required that  $u(\alpha_l t - \alpha_l \tau_l) = 1$  within this window for all paths. In other words, because  $u(\alpha_l t - \alpha_l \tau_l)$  gives a time support on  $t \in \left[ \frac{-T_{\text{pre}} + \alpha_l \tau_l}{\alpha_l}, \frac{KT + T_{\text{post}} + \alpha_l \tau_l}{\alpha_l} \right]$ , we should then always satisfy  $\frac{-T_{\text{pre}} + \alpha_l \tau_l}{\alpha_l} \leq 0$  and also  $\frac{KT + T_{\text{post}} + \alpha_l \tau_l}{\alpha_l} \geq KT$  for any  $l \in \{0, 1, \dots, L\}$ . This leads to

$$T_{\text{pre}} \geq \alpha_{\text{max}} \tau_{\text{max}}, \quad (4.6)$$

$$T_{\text{post}} \geq (\alpha_{\text{max}} - 1)KT. \quad (4.7)$$

■

When the above conditions are satisfied, we are allowed to drop the notation of the rectangular pulse  $u(t)$  embedded in  $h_k(t)$  in the sequel for the sake of notational ease.

### 4.2.2 Discrete Data Model

For MSML channels, discretizing the received signal and achieving time-frequency synchronization is not trivial [29, 30]. We illustrate such difficulty in Fig. 4.1, where we assume the transmit signal propagates via three paths. Since the received symbol is the summation of these three paths, it invites the following questions:

1. Which point should we consider as the starting point of the OFDM symbol (time synchronization)?
2. What sampling rate should we adopt to discretize the received signal over MSML channels (rescaling)?

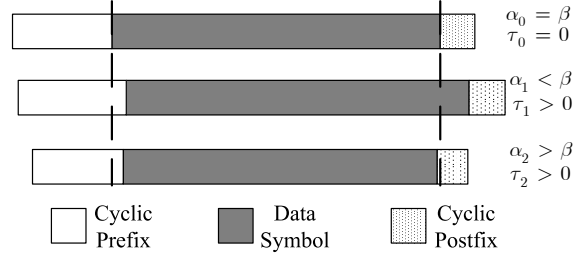


**Figure 4.1:** Illustration of the synchronization and resampling problem;  $\alpha_l$  stands for the scaling factor due to the  $l$ th path, and  $\beta$  for the rescaling factor adopted by the receiver during resampling.

3. What frequency shift should we apply to remove the residual carrier frequency offset (frequency synchronization)?

These problems can mathematically be described by determining  $\beta$ ,  $\phi$  and  $\sigma$  in the following expression

$$r^{(\beta, \phi, \sigma)}(t) = \sqrt{\frac{1}{\beta}} r\left(\frac{t}{\beta} - \sigma T\right) e^{j2\pi f_c \phi t / \beta}, \quad (4.8)$$

where  $\beta$  is a positive number within  $[1, \alpha_{\max}]$  and  $\beta T$  represents the sampling rate at the receiver;  $\sigma$  is the time shift factor, which is used to represent time synchronization; and likewise,  $\phi$  is the phase shift factor used for frequency synchronization.  $\sqrt{\frac{1}{\beta}}$  is a normalization factor. Later on, we will show that a different choice of  $(\beta, \phi, \sigma)$  can influence the energy distribution of the channel matrix significantly. For the moment, we leave the values of these parameters open to allow for a general treatment of the problems. It is clear that when  $(\beta, \phi, \sigma) = (1, 0, 0)$ , there is no resampling operation carried out.

After resampling, the noiseless sample obtained at the  $n$ th time instance in the time domain is given by (see Appendix 4.A for the detailed derivation)

$$\begin{aligned} r_n^{(\beta, \phi, \sigma)} &= r^{(\beta, \phi, \sigma)}(nT) \\ &= \sum_{l=0}^L h_l^{(\beta, \sigma)} e^{j2\pi \omega \frac{(\alpha_l - 1 + \phi)}{\beta} \frac{n}{K}} \times \left( \sum_{k=0}^{K-1} b_k e^{j2\pi \frac{\alpha_l}{\beta} \frac{nk}{K}} \right) e^{-j2\pi \alpha_l (\lambda_l + \sigma) \frac{k}{K}}, \quad (4.9) \end{aligned}$$

where we use

$$\omega = \frac{f_c}{\Delta f}$$

to denote the normalized carrier frequency and

$$\lambda_l = \frac{\tau_l}{T}$$

to denote the normalized delay of the  $l$ th path; and the discrete channel coefficient is given by

$$h_l^{(\beta, \sigma)} = \sqrt{\frac{\alpha_l}{\beta K T}} \bar{h}_l e^{-j2\pi f_c (\alpha_l \tau_l + (\alpha_l - 1) \sigma T)}.$$

In (4.9), the term  $e^{j2\pi\omega \frac{(\alpha_l - 1 + \phi)}{\beta} \frac{n}{K}}$  corresponds to the residual CFO related with the  $l$ th path after resampling; the term  $e^{-j2\pi f \alpha_l (\lambda_l + \sigma) \frac{k}{K}}$  corresponds to the phase changes due to the time shift along the  $l$ th path; and the summation  $\sum_{k=0}^{K-1} b_k e^{j2\pi \frac{\alpha_l}{\beta} \frac{nk}{K}}$  is the adapted version of the transmitted OFDM signal due to the channel time variation in the  $l$ th path.

Let us now stack the received samples  $r_n^{(\beta, \phi, \sigma)}$ , for  $n = 0, \dots, K-1$ , into a vector  $\mathbf{r}_T^{(\beta, \phi, \sigma)} = [r_0^{(\beta, \phi, \sigma)}, \dots, r_{K-1}^{(\beta, \phi, \sigma)}]^T$ , and similarly let  $\mathbf{b} = [b_0, \dots, b_{K-1}]^T$ . In the noiseless case, it follows that

$$\mathbf{r}_T^{(\beta, \phi, \sigma)} = \sum_{l=0}^L h_l^{(\beta, \sigma)} \mathbf{D}_l^{(\beta, \phi)} \mathbf{F}_{\alpha_l/\beta}^H \mathbf{\Lambda}_l^{(\sigma)} \mathbf{b}, \quad (4.10)$$

where  $\mathbf{F}_\alpha$  denotes a fractional normalized discrete Fourier transform (DFT) matrix, whose  $(m, k)$ th entry is defined as

$$[\mathbf{F}_\alpha^H]_{m,k} = \frac{1}{\sqrt{K}} e^{j2\pi\alpha \frac{mk}{K}}. \quad (4.11)$$

Obviously,  $\mathbf{F}_1$  reduces to a regular normalized DFT matrix. In addition,

$$\mathbf{\Lambda}_l^{(\sigma)} = \text{diag}([1, e^{j2\pi\alpha_l(\lambda_l + \sigma)\frac{1}{K}}, \dots, e^{j2\pi\alpha_l(\lambda_l + \sigma)\frac{K-1}{K}}]^T), \quad (4.12)$$

and

$$\mathbf{D}_l^{(\beta, \phi)} = \text{diag}([1, e^{j2\pi\omega \frac{\alpha_l - 1 + \phi}{\beta} \frac{1}{K}}, \dots, e^{j2\pi\omega \frac{\alpha_l - 1 + \phi}{\beta} \frac{K-1}{K}}]^T), \quad (4.13)$$

where the superscript  $(\beta, \phi)$  in  $\mathbf{D}_l^{(\beta, \phi)}$  and  $(\sigma)$  in  $\mathbf{\Lambda}_l^{(\sigma)}$  reflects the dependence on the specific resampling parameters. This convention will hold throughout this chapter.

### 4.3 Interference Analysis

Normally speaking, equalization of an OFDM channel is implemented in the frequency domain. To this end, the received signal  $\mathbf{r}_T^{(\beta,\phi,\sigma)}$  is first transformed into the frequency domain by means of the DFT, which in the absence of noise yields

$$\mathbf{r}_F^{(\beta,\phi,\sigma)} = \mathbf{F}_1 \mathbf{r}_T^{(\beta,\phi,\sigma)} = \mathbf{H}_F^{(\beta,\phi,\sigma)} \mathbf{b}, \quad (4.14)$$

where  $\mathbf{H}_F^{(\beta,\phi,\sigma)}$  stands for the frequency-domain (FD) channel matrix, which is defined as

$$\begin{aligned} \mathbf{H}_F^{(\beta,\phi,\sigma)} &= \sum_{l=0}^L h_l^{(\beta,\sigma)} \mathbf{F}_1 \mathbf{D}_{\alpha_l}^{(\beta,\phi)} \mathbf{F}_{\alpha_l/\beta}^H \mathbf{\Lambda}_{\lambda_l}^{(\sigma)} \\ &= \sum_{l=0}^L h_l^{(\beta,\sigma)} \mathbf{H}_{F,l}^{(\beta,\phi)} \mathbf{\Lambda}_{\lambda_l}^{(\sigma)}, \end{aligned} \quad (4.15)$$

with  $\mathbf{H}_{F,l}^{(\beta,\phi)} = \mathbf{F}_1 \mathbf{D}_{\lambda_l}^{(\beta,\phi)} \mathbf{F}_{\alpha_l/\beta}^H$  being its  $l$ th component, whose  $(m, k)$ th entry is specified as

$$\begin{aligned} \left[ \mathbf{H}_{F,l}^{(\beta,\phi)} \right]_{m,k} &= \frac{1}{K} \sum_{n=0}^{K-1} e^{-j2\pi \frac{mn}{K}} e^{j2\pi \omega \frac{\alpha_l - 1 + \phi}{\beta} \frac{n}{K}} e^{j2\pi \frac{\alpha_l}{\beta} \frac{nk}{K}} \\ &= \frac{1}{K} \sum_{n=0}^{K-1} e^{-jn \frac{2\pi}{K} ((m-k) - (\xi_{l,F1} k + \xi_{l,F2}))} \\ &= e^{-j \frac{(K-1)\pi}{K} ((m-k) - (\xi_{l,F1} k + \xi_{l,F2}))} \times \\ &\quad \frac{\text{sinc}((m-k) - (\xi_{l,F1} k + \xi_{l,F2}))}{\text{sinc}(\frac{1}{K} ((m-k) - (\xi_{l,F1} k + \xi_{l,F2})))}, \end{aligned} \quad (4.16)$$

where  $\xi_{l,F1} = \frac{\alpha_l - \beta}{\beta}$  and  $\xi_{l,F2} = \frac{\alpha_l - 1 + \phi}{\beta} \omega$  with  $\text{sinc}(t) = \frac{\sin(\pi t)}{\pi t}$ .

It is obvious from (4.16) that in the absence of Doppler effects, i.e.,  $\alpha_l = 1$  for  $l = 0, 1, \dots, L$ , no rescaling and frequency synchronization is necessary, hence  $\beta = 1$  and  $\phi = 0$ , which leads to a diagonal  $\mathbf{H}_{F,l}^{(1,0)}$  with  $\left[ \mathbf{H}_{F,l}^{(\beta,\phi)} \right]_{m,k} = \delta_{m-k}$ . In another special case where  $\alpha_l \equiv \alpha$  for  $l = 0, 1, \dots, L$ , we can also enforce a diagonal  $\mathbf{H}_{F,l}^{(\beta,\phi)}$  by letting  $\beta = \alpha$  and  $\phi = 1 - \alpha$ , a scenario considered



in, e.g., [28]. For a realistic wideband LTV channel, however, the channel energy distribution in  $\mathbf{H}_{F,l}^{(\beta,\phi)}$  is governed by a Dirichlet kernel, where the center of this Dirichlet kernel is offset by

$$\Delta_{F,l}^{(\beta,\phi)}(k) = \xi_{l,F1}k + \xi_{l,F2}. \quad (4.17)$$

Clearly, such an offset is not only dependent on the Doppler spread  $\alpha$  and the carrier frequency  $f_c$ , but also on the subcarrier frequency  $f_k = k\Delta f$ . The dependence of the signal energy offset on the subcarrier index is unique to wideband channels, and is also referred to as nonuniform Doppler shifts in [28]. In contrast, the frequency offset for narrowband channels is statistically identical for all the subcarriers [59].

The Dirichlet kernel in (4.16) also suggests that the signal energy is mostly concentrated in subcarrier  $k + \Delta_{F,l}^{(\beta,\phi)}(k)$  and its nearby subcarriers, and decays fast in subcarriers farther away. To appreciate how fast the signal energy decays, let us introduce  $B_{F,l}^{(\beta,\phi)}(k)$  to quantify the number of subcarriers where most of the energy of  $b_k$  is located, which can thus be viewed as the bandwidth of  $\mathbf{H}_{F,l}^{(\beta,\phi)}$  along its  $k$ th column.  $B_{F,l}^{(\beta,\phi)}(k)$  is obtained as the smallest  $B$  for which

$$\begin{aligned} & \sum_{m=k+\Delta_{F,l}^{(\beta,\phi)}(k)-B}^{k+\Delta_{F,l}^{(\beta,\phi)}(k)+B} \left| [\mathbf{H}_{F,l}^{(\beta,\phi)}]_{m,k} \right|^2 > \gamma \sum_{m=0}^{K-1} \left| [\mathbf{H}_{F,l}^{(\beta,\phi)}]_{m,k} \right|^2 \\ \Leftrightarrow & \sum_{m=k+\Delta_{F,l}^{(\beta,\phi)}(k)-B}^{k+\Delta_{F,l}^{(\beta,\phi)}(k)+B} \left| \frac{\text{sinc}(\pi((m-k) - (\xi_{l,F1}k + \xi_{l,F2})))}{\text{sinc}(\frac{\pi}{K}((m-k) - (\xi_{l,F1}k + \xi_{l,F2})))} \right|^2 \\ & > \gamma \sum_{m=0}^{K-1} \left| \frac{\text{sinc}(\pi((m-k) - (\xi_{l,F1}k + \xi_{l,F2})))}{\text{sinc}(\frac{\pi}{K}((m-k) - (\xi_{l,F1}k + \xi_{l,F2})))} \right|^2, \end{aligned} \quad (4.18)$$

where  $\gamma$  is a positive threshold no larger than 1. In the left plot of Fig. 4.2, the relationship between  $\max_k B_{F,l}^{(\beta,\phi)}(k)$  and  $\gamma$  for the case  $\beta = 1$  and  $\alpha = 0$  (no resampling and frequency synchronization) is plotted. It is clear that most of the signal energy of  $b_k$  is captured within a limited bandwidth. For example, with a bandwidth  $\max_k B_{F,l}^{(1,0)}(k) = 5$ , roughly 98% of the signal energy of  $b_k$  is captured. Notably, this bandwidth is almost independent of  $\xi_{l,F1}$  and  $\xi_{l,F2}$  as suggested by the left plot of Fig. 4.2.

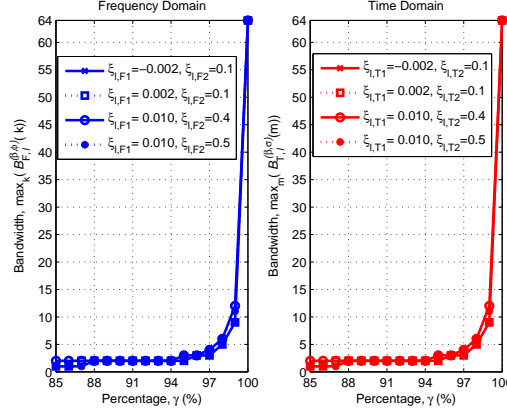


Figure 4.2: Bandwidth of  $\mathbf{H}_{F,l}^{(\beta,\phi)}$  and  $\mathbf{H}_{T,l}^{(\beta,\sigma)}$

Since each  $\mathbf{H}_{F,l}^{(\beta,\phi)}$  is roughly banded, it is therefore reasonable to approximate  $\mathbf{H}_F^{(\beta,\phi,\sigma)}$ , which is a weighted sum of different  $\mathbf{H}_{F,l}^{(\beta,\phi)}$  matrices, also as banded. As an example, we plot in Fig. 4.3 the structure of  $\mathbf{H}_F^{(\beta,\phi)}$ , where we assume that there are in total two paths. Obviously, the approximate bandwidth of  $\mathbf{H}_F^{(\beta,\phi,\sigma)}$  at the  $k$ th column, denoted as  $B_F^{(\beta,\phi)}(k)$ , is

$$\begin{aligned}
 B_F^{(\beta,\phi)}(k) &= \\
 &\max_l \left( k + \Delta_{F,l}^{(\beta,\phi)}(k) + B_{F,l}^{(\beta,\phi)}(k) \right) - \min_l \left( k + \Delta_{F,l}^{(\beta,\phi)}(k) - B_{F,l}^{(\beta,\phi)}(k) \right) \\
 &\approx \max_l \left( \Delta_{F,l}^{(\beta,\phi)}(k) \right) - \min_l \left( \Delta_{F,l}^{(\beta,\phi)}(k) \right) + 2\max_l \left( B_{F,l}^{(\beta,\phi)}(k) \right), \quad (4.19)
 \end{aligned}$$

which is independent of  $\sigma$ . We refer the reader to Fig. 4.3 for the physical meaning of the notations. It is important to underscore that since the bandwidth  $B_F^{(\beta,\phi)}(k)$  is dependent on the subcarrier index  $k$ , the boundaries of the band are not parallel to each other as in the narrowband case. A banded approximation of the channel matrix is crucial to many low-complexity equalizers, e.g., [2,3,5,41]. The equalizer considered in this chapter will also adopt this approximation to reduce the complexity. More specifically, we first define a matrix  $\mathbf{B}_F^{(\beta,\phi)}$ , whose  $(m, k)$ th entry is equal to 1 if  $\min_l \left( k + \Delta_{F,l}^{(\beta,\phi)}(k) - B_{F,l}^{(\beta,\phi)}(k) \right) \leq$

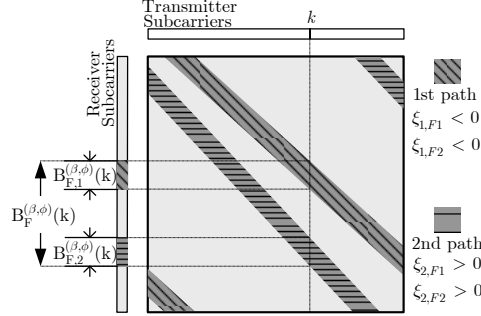


Figure 4.3: Illustration of the FD matrix  $\mathbf{H}_F^{(\beta, \phi, \sigma)}$  for two paths

$m \leq \max_l \left( k + \Delta_{F,l}^{(\beta, \phi)}(k) + B_{F,l}^{(\beta, \phi)}(k) \right)$ , and 0 otherwise, and we then consider the matrix

$$\bar{\mathbf{H}}_F^{(\beta, \phi, \sigma)} = \mathbf{B}_F^{(\beta, \phi)} \odot \mathbf{H}_F^{(\beta, \phi, \sigma)} \quad (4.20)$$

as the banded approximation of  $\mathbf{H}_F^{(\beta, \phi, \sigma)}$ .

With the banded approximation, let us rewrite (4.14) as

$$\mathbf{r}_F^{(\beta, \phi, \sigma)} = \bar{\mathbf{H}}_F^{(\beta, \phi, \sigma)} \mathbf{b} + \bar{\mathbf{v}}_F^{(\beta, \phi, \sigma)}, \quad (4.21)$$

where  $\bar{\mathbf{v}}_F^{(\beta, \phi, \sigma)} = \left( \mathbf{H}_F^{(\beta, \phi, \sigma)} - \bar{\mathbf{H}}_F^{(\beta, \phi, \sigma)} \right) \mathbf{b}$ .

The above analysis can also be applied in the time domain in an analogous manner. See Appendix 4.B for the details. Here we only want to highlight that, different from the energy distribution in the FD channel matrix which is influenced by the rescaling factor  $\beta$  and the phase-shift factor  $\phi$  [c.f.  $\xi_{l,F1}$  and  $\xi_{l,F2}$  in (4.16)], the energy distribution in the TD channel matrix is affected by the rescaling factor  $\beta$  and the time-shift factor  $\sigma$  [c.f.  $\xi_{l,T1}$  and  $\xi_{l,T2}$  in (4.39)]. However, similarly as the FD channel matrix, we can also understand from the right subplot of Fig. 4.2 that  $\mathbf{H}_{T,l}^{(\beta, \sigma)}$  is roughly banded along the  $l$ th path in the time domain, and so is the overall time-domain channel matrix  $\mathbf{H}_T^{(\beta, \phi, \sigma)}$ .

## 4.4 Channel Equalization Scheme

Let us now focus on the channel frequency-domain equalization, which is

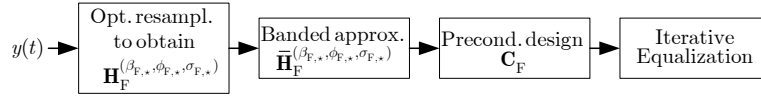


**Figure 4.4:** Illustration of our equalization scheme.

depicted in Fig. 4.4. In this figure, it is clear that, prior to the equalization, we propose an optimum resampling operation to achieve  $(\beta, \phi, \sigma) = (\beta_{F,*}, \phi_{F,*}, \sigma_{F,*})$ , which is different from [29, 76] as mentioned previously. Specifically, the resampling method proposed in [29] only considers the rescaling parameter  $\beta$  while [76] ignores the time-shift parameter  $\sigma$ . Afterwards, the banded matrix  $\bar{\mathbf{H}}_F^{(\beta_{F,*}, \phi_{F,*}, \sigma_{F,*})}$  is adopted to approximate  $\mathbf{H}_F^{(\beta_{F,*}, \phi_{F,*}, \sigma_{F,*})}$  according to the approach mentioned in the last section. Our banded method induces a non-parallel bandwidth structure which is different from the banded approach used in narrowband OFDM systems [2, 3, 5, 66]. In order to speed up the convergence of the iterative equalization, we then design a diagonal preconditioner to improve the condition of this banded matrix. It is noteworthy here that our preconditioner design is adapted from [41, 75] to enhance its suitability for our MSML scenario. Finally, iterative equalization is proposed on the preconditioned channel matrix. Although we choose the CG method in this chapter, other iterative methods can also be applied, such as the LSQR algorithm [78].

Additionally, we would like to highlight that just as a single-carrier channel can be equalized in the frequency domain, it is also possible to equalize an OFDM channel in the time domain. Due to the similarity, we again refer the reader to Appendix 4.B for a detailed mathematical derivation of the time-domain method. The question in which domain the wideband channel should be equalized, shall be addressed in the next section.

#### 4.4.1 Iterative Equalization

To better motivate the other components of our equalization scheme, we first introduce the channel equalization method itself. A zero-forcing equalizer in

the frequency domain is considered, given by

$$\hat{\mathbf{b}} = \left( \bar{\mathbf{H}}_{\mathbf{F}}^{(\beta, \phi, \sigma)H} \bar{\mathbf{H}}_{\mathbf{F}}^{(\beta, \phi, \sigma)} \right)^{-1} \bar{\mathbf{H}}_{\mathbf{F}}^{(\beta, \phi, \sigma)H} \mathbf{r}_{\mathbf{F}}^{(\beta, \phi, \sigma)}, \quad (4.22)$$

where  $\hat{\mathbf{b}}$  is the obtained estimate of  $\mathbf{b}$ . Because the original channel matrix  $\mathbf{H}_{\mathbf{F}}^{(\beta, \phi, \sigma)}$  is a full matrix, its inversion inflicts a complexity of  $\mathcal{O}(K^3)$  and is thus not desired for a practical system. To lower the complexity,  $\mathbf{H}_{\mathbf{F}}^{(\beta, \phi, \sigma)}$  has been replaced by the banded approximation  $\bar{\mathbf{H}}_{\mathbf{F}}^{(\beta, \phi, \sigma)}$  in (4.22).

Besides, the matrix inversion in (4.22) will be implemented iteratively using the CG algorithm. An advantage of using CG rather than inverting the matrix directly is that the resulting data estimates yielded by CG are always constrained in the Krylov subspace, making its performance less susceptible to the spectral distribution of  $\bar{\mathbf{H}}_{\mathbf{F}}^{(\beta, \phi, \sigma)}$ . In practice, a truncated CG, which halts the algorithm after a limited number of iterations, is desired to further reduce the complexity. It is well-known that the convergence of the CG algorithm can be accelerated by applying preconditioning on  $\bar{\mathbf{H}}_{\mathbf{F}}^{(\beta, \phi, \sigma)}$  [74, 75, 79]. With  $\mathbf{C}_{\mathbf{F}}$  denoting such a preconditioner, the I/O relationship given in (4.21) in the noiseless case can be rewritten as

$$\begin{aligned} \mathbf{r}_{\mathbf{F}}^{(\beta, \phi, \sigma)} &= \left( \bar{\mathbf{H}}_{\mathbf{F}}^{(\beta, \phi, \sigma)} \mathbf{C}_{\mathbf{F}} \right) (\mathbf{C}_{\mathbf{F}}^{-1} \mathbf{b}) \\ &= \bar{\mathbf{H}}_{\mathbf{F}\mathbf{C}}^{(\beta, \phi, \sigma)} \mathbf{b}_{\mathbf{C}} \end{aligned} \quad (4.23)$$

from which an estimate of  $\mathbf{b}_{\mathbf{C}} = \mathbf{C}_{\mathbf{F}}^{-1} \mathbf{b}$  is first obtained by applying CG on the preconditioned matrix  $\bar{\mathbf{H}}_{\mathbf{F}\mathbf{C}}^{(\beta, \phi, \sigma)} = \bar{\mathbf{H}}_{\mathbf{F}}^{(\beta, \phi, \sigma)} \mathbf{C}_{\mathbf{F}}$ . Afterwards,  $\hat{\mathbf{b}} = \mathbf{C}_{\mathbf{F}} \hat{\mathbf{b}}_{\mathbf{C}}$  is computed to obtain the final data estimates. For details about our CG equalization, see Appendix 4.C.

The optimal design of  $\mathbf{C}_{\mathbf{F}}$  can be exhaustive [79]. Inspired by [75], we find our preconditioner by minimizing a cost function based on the Frobenius norm, which clusters most of the eigenvalues of  $\bar{\mathbf{H}}_{\mathbf{F}}^{(\beta, \phi, \sigma)} \mathbf{C}_{\mathbf{F}}$  around 1 with the exception of a few outliers. Further, observing that the design of  $\mathbf{C}_{\mathbf{F}}$  itself, as well as the operation of  $\bar{\mathbf{H}}_{\mathbf{F}}^{(\beta, \phi, \sigma)} \mathbf{C}_{\mathbf{F}}$ , inflicts an additional complexity, a common approach is to impose a sparse structure on  $\mathbf{C}_{\mathbf{F}}$ , e.g., diagonal [75] as

$$\mathbf{C}_{\mathbf{F}} = \text{diag}\{[c_{\mathbf{F},0}, c_{\mathbf{F},1} \cdots, c_{\mathbf{F},K-1}]^T\}. \quad (4.24)$$

#### 4.4.2 Diagonal Preconditioning

In this subsection, we will show that the normal approach to design the diagonal preconditioner as described in [75] will not necessarily cluster eigenvalues around one. To realize this, let us consider the diagonal preconditioner  $\mathbf{C}_{F,\star}$  that minimizes the cost function in the Frobenius norm [75] given by

$$\mathbf{C}_{F,\star} = \arg \min_{\mathbf{C}_F} \left\| \bar{\mathbf{H}}_F^{(\beta,\phi,\sigma)} \mathbf{C}_F - \mathbf{I}_{K \times K} \right\|_{\text{Fro}}^2$$

which leads to

$$\begin{aligned} c_{F,k,\star} &= \arg \min_{c_{F,k}} \left\| \bar{\mathbf{H}}_F^{(\beta,\phi,\sigma)} c_{F,k} \mathbf{e}_k - \mathbf{e}_k \right\|_2^2, \\ &= \frac{[\bar{\mathbf{H}}_F^{(\beta,\phi,\sigma)}]_{k,k}^*}{\left\| \bar{\mathbf{H}}_F^{(\beta,\phi,\sigma)} \mathbf{e}_k \right\|_2^2}, \end{aligned} \quad (4.25)$$

where  $\mathbf{e}_k$  is the  $k$ th column of the identity matrix.

One problem of the above diagonal preconditioner designed by (4.25) is that the eigenvalues may, in some situations, tend to cluster around zero instead of one, with the consequence that the condition number of the preconditioned channel matrix increases considerably. To understand this, assume there exists a  $\epsilon_1 > 0$  such that

$$\left\| \bar{\mathbf{H}}_F^{(\beta,\phi,\sigma)} \mathbf{e}_{k C_{F,k}} - \mathbf{e}_k \right\|_2^2 \leq \epsilon_1^2, \quad (4.26)$$

for  $k = \{0, 1, \dots, K-1\}$ . At the same time, assume there exists a  $\epsilon_0 > 0$  such that

$$\left\| \bar{\mathbf{H}}_F^{(\beta,\phi,\sigma)} \mathbf{e}_{k C_{F,k}} \right\|_2^2 \leq \epsilon_0^2 \quad (4.27)$$

for  $k \in \{0, \dots, K-1\}$ .

If we denote the  $k$ th eigenvalue of the preconditioned channel matrix  $\bar{\mathbf{H}}_F^{(\beta,\phi,\sigma)} \mathbf{C}_F$  as  $\mu_k$ , (4.27) indicates that (for details see Appendix 4.D)

$$\sum_{k=0}^{K-1} |\mu_k|^2 \leq K \epsilon_0^2$$

which means that all  $\mu_k$ 's lie inside a disk of radius  $\sqrt{K}\epsilon_0$  centered around zero. Similarly, from (4.26) we have

$$\sum_{k=0}^{K-1} |\mu_k - 1|^2 \leq K\epsilon_1^2$$

which implies that all  $\mu_k$ 's at the same time lie inside a disk of  $\sqrt{K}\epsilon_1$  centered around one. It is clear that if  $\epsilon_0 < \epsilon_1$ , then minimizing  $\left\| \bar{\mathbf{H}}_{\mathbf{F}}^{(\beta, \phi, \sigma)} \mathbf{C}_{\mathbf{F}} - \mathbf{I}_{K \times K} \right\|_{\text{Fro}}^2$  will at the same time minimize the Frobenius norm  $\left\| \bar{\mathbf{H}}_{\mathbf{F}}^{(\beta, \phi, \sigma)} \mathbf{C}_{\mathbf{F}} \right\|_{\text{Fro}}^2$  itself, making the eigenvalues more clustered around zero rather than one.

With  $c_{\mathbf{F}, k, \star}$  defined in (4.25), we can show that

$$\epsilon_1 = \max_k \frac{\sum_{m=0}^{K-1} |[\bar{\mathbf{H}}_{\mathbf{F}}^{(\beta, \phi, \sigma)}]_{m,k}|^2 - |[\bar{\mathbf{H}}_{\mathbf{F}}^{(\beta, \phi, \sigma)}]_{k,k}|^2}{\sum_{m=0}^{K-1} |[\bar{\mathbf{H}}_{\mathbf{F}}^{(\beta, \phi, \sigma)}]_{m,k}|^2}, \quad (4.28)$$

and

$$\epsilon_0 = \max_k \frac{|[\bar{\mathbf{H}}_{\mathbf{F}}^{(\beta, \phi, \sigma)}]_{k,k}|^2}{\sum_{m=0}^{K-1} |[\bar{\mathbf{H}}_{\mathbf{F}}^{(\beta, \phi, \sigma)}]_{m,k}|^2}. \quad (4.29)$$

Obviously, if  $|[\bar{\mathbf{H}}_{\mathbf{F}}^{(\beta, \phi, \sigma)}]_{k,k}|^2 < \sum_{m=0}^{K-1} |[\bar{\mathbf{H}}_{\mathbf{F}}^{(\beta, \phi, \sigma)}]_{m,k}|^2$ , for  $k = 0, \dots, K-1$ , then the optimal diagonal preconditioner will cluster the eigenvalues in a "wrong" area. This case arises when the sum of the off-diagonal power in each column is higher than the power on the diagonal. Such a situation could occur in multi-scale channels where significant channel power is located on off-diagonal entries as we argued in the previous section (see Fig. 4.3 for instance). In the upper-left plot of Fig. 4.5, the eigenvalues of such a matrix, with and without preconditioning, are displayed on a complex plane. It can be seen that diagonal preconditioning indeed clusters the eigenvalues around zero rather than one.

To evaluate the impact of such a preconditioner on the convergence of CG, we compute the mean squared error (MSE) as

$$\text{MSE} = \frac{\|\mathbf{b} - \hat{\mathbf{b}}^{(i)}\|^2}{\|\hat{\mathbf{b}}\|^2}, \quad (4.30)$$

with  $\hat{\mathbf{b}}^{(i)}$  being the result obtained at the  $i$ th iteration of our CG equalization as mentioned in Appendix 4.C. In the top-right plot of Fig. 4.5, it is clear

that the CG convergence with such a diagonal preconditioner is even worse than without any preconditioning. This illustrates that the diagonal preconditioning defined in (4.25) may not always yield a better performance than without preconditioning, as opposed to what is claimed in [41, 75]. Using a more complex structured preconditioner can avoid this, which is, however, not desired due to complexity and implementation considerations.

To alleviate this problem, we adapt the diagonal preconditioner in (4.24) and (4.25) as follows

$$c_{F,k,\star} = \begin{cases} \frac{[\bar{\mathbf{H}}_F^{(\beta,\phi,\sigma)}]_{k,k}^*}{\|\bar{\mathbf{H}}_F^{(\beta,\phi,\sigma)} \mathbf{e}_k\|_2}, & \text{if } \zeta_{\text{FC}}^{(\beta,\phi,\sigma)}(k) \geq 1 \\ 1, & \text{otherwise} \end{cases} \quad (4.31)$$

where

$$\zeta_{\text{FC}}^{(\beta,\phi,\sigma)}(k) = \frac{\left| [\bar{\mathbf{H}}_F^{(\beta,\phi,\sigma)}]_{k,k} \right|^2}{\sum_{m=0, m \neq k}^{K-1} \left| [\bar{\mathbf{H}}_F^{(\beta,\phi,\sigma)}]_{m,k} \right|^2}. \quad (4.32)$$

In Section 4.4.3, we will show how to enhance (4.32) with a higher probability by means of optimal resampling.

### 4.4.3 Optimal Resampling

From the previous subsections, we understand that the effectiveness of a diagonal preconditioner depends on the energy distribution of the channel matrix. It is desired that the channel matrix should have most of its energy concentrated on the main diagonal. The analysis in Section 4.2.2 learns that the resampling operation  $(\beta, \phi, \sigma)$  plays an important role in governing the energy distribution of the channel matrix, and so far we have left  $(\beta, \phi, \sigma)$  open for choice. Recall that resampling is a standard step taken in many wideband LTV communication systems to compensate for the Doppler effect. For example, optimizing  $\beta$  is considered in [29], while  $\beta$  and  $\phi$  are jointly optimized in [66]. In this sense, the optimal resampling proposed in this chapter can be considered as a generalization of [29, 66].



Next, we shall discuss how to jointly optimize the resampling parameters  $(\beta, \phi, \sigma)$ . Focusing on the FD matrix  $\mathbf{H}_F^{(\beta, \phi, \sigma)}$ , we desire  $\left| \left[ \mathbf{H}_F^{(\beta, \phi, \sigma)} \right]_{k,k} \right|^2 > \sum_{m \neq k} \left| \left[ \mathbf{H}_F^{(\beta, \phi, \sigma)} \right]_{m,k} \right|^2$  for all  $k \in \{0, 1, \dots, K-1\}$ . However, satisfying the above condition for each index  $k$  individually is expensive. As a relaxation, we practically seek  $\sum_k \left| \left[ \bar{\mathbf{H}}_F^{(\beta, \phi, \sigma)} \right]_{k,k} \right|^2 > \sum_k \sum_{m \neq k} \left| \left[ \bar{\mathbf{H}}_F^{(\beta, \phi, \sigma)} \right]_{m,k} \right|^2$ .

To this end, let us denote the diagonal energy ratio as

$$\rho_F^{(\beta, \phi, \sigma)} = \frac{\sum_{k=0}^{K-1} \left| \left[ \mathbf{H}_F^{(\beta, \phi, \sigma)} \right]_{k,k} \right|^2}{\sum_{k=0}^{K-1} \sum_{m=0}^{K-1} \left| \left[ \mathbf{H}_F^{(\beta, \phi, \sigma)} \right]_{m,k} \right|^2}, \quad (4.33)$$

and define our resampling operation by solving

$$(\beta_{F,*}, \phi_{F,*}, \sigma_{F,*}) = \arg \max_{\beta, \phi, \sigma} \rho_F^{(\beta, \phi, \sigma)}, \quad (4.34)$$

which leads to the maximal ratio  $\rho_F^{(\beta_{F,*}, \phi_{F,*}, \sigma_{F,*})}$ . One can also explain this resampling as minimizing the total amount of ICI in the frequency domain.

Since the energy governing mechanism is determined by the sinc function as indicated in (4.16), we can equivalently rewrite (4.34) by only maximizing the diagonal energy of  $\mathbf{H}_F^{(\beta, \phi, \sigma)}$  as

$$\begin{aligned} (\beta_{F,*}, \phi_{F,*}, \sigma_{F,*}) &= \arg \max_{\beta, \phi, \sigma} \sum_{k=0}^{K-1} \left| \left[ \mathbf{H}_F^{(\beta, \phi, \sigma)} \right]_{k,k} \right|^2 \\ &= \arg \max_{\beta, \phi, \sigma} \sum_{k=0}^{K-1} \left| \sum_{l=0}^L h_l^{(\beta, \sigma)} e^{-j \frac{(K-1)\pi}{K} (\xi_{l,F1} k + \xi_{l,F2})} \times \right. \\ &\quad \left. \frac{\text{sinc}(\xi_{l,F1} k + \xi_{l,F2})}{\text{sinc}(\frac{1}{K} (\xi_{l,F1} k + \xi_{l,F2}))} \times e^{j2\pi(\lambda_l + \sigma) \frac{k}{K}} \right|^2, \end{aligned} \quad (4.35)$$

where again  $\xi_{l,F1} = \frac{\alpha_l - \beta}{\beta}$  and  $\xi_{l,F2} = \frac{\alpha_l - 1 + \phi}{\beta} \omega$ . It is noteworthy that all three parameters,  $\beta$ ,  $\phi$  and  $\sigma$ , play a role in (4.35), indicating that separately considering one or two parameters as in [29, 66] might lead to a local maximum.

**Table 4.1:** Channel I: Frequency-Domain Approach

Channel I ( $T = 0.2\text{ms}$ $\omega = 256$ $K = 128$ )	path	scale $\alpha_l$	delay $\lambda_l$	path gain $\bar{h}_l$
	$l = 0$	1.0150	0.00	0 dB
	$l = 1$	1.0154	10.15	-3 dB
	$l = 2$	1.0201	20.40	-5 dB
Resampl. Para.	Orig. $(\beta, \phi, \sigma)$	$(1, 0, 0)$		
	$(\beta_{F,*}, \phi_{F,*}, \sigma_{F,*})$	$(1.0150, -0.0150, -15.00)$		
Cond. Num. for FD	Orig. / no precondition.	$4.26 \times 10^5$		
	Orig. / with precondition.	$1.19 \times 10^6$		
	Resampl. / no precondition.	23.36		
	Resampl. / with precondition.	7.17		
FD Ratio	Orig.	$\rho_F^{(1,0,0)} = 0.0021$		
	Resampl.	$\rho_F^{(\beta_{F,*}, \phi_{F,*}, \sigma_{F,*})} = 0.9279$		

To illustrate our resampling approach in the frequency domain, we consider the channel example specified in Table 4.1, where we also compare the properties of the resampled FD channel (i.e., the condition number and diagonal power ratio of the channel matrix) with the original MSML FD channel. A geometric interpretation may help to understand our resampling operation since  $\beta$  rotates the FD matrix through  $\xi_{l,F1} = \frac{\alpha_l - \beta}{\beta}$ ,  $\phi$  shifts the FD matrix through  $\xi_{l,F2} = \frac{\alpha_l - 1 + \phi}{\beta} \omega$  in (4.16), and  $\sigma$  influences the phase of each element in (4.35). The joint effect of these actions maximizes the matrix diagonal energy. The yielded resampling  $(\beta_{F,*}, \phi_{F,*}, \sigma_{F,*}) = (1.015, -0.015, -15.00)$  corresponds to a maximal diagonal power ratio  $\rho_F^{(\beta_{F,*}, \phi_{F,*}, \sigma_{F,*})} = 0.9279$ . We underscore that the condition number is already significantly reduced, solely by the optimum resampling, from  $4.26 \times 10^5$  to 23.36. In comparison, the resampling method proposed in [29] yields  $(\beta, \phi, \sigma) = (1.016, 0, 0)$  and  $\rho_F^{(1.016, 0, 0)} = 0.3623$ . Its corresponding condition number is 432.78, which is larger than our condition number after resampling. This is not surprising since the criterion adopted in [29] focuses only on minimizing the aggregate errors between the multi-scale channel and its single-scale approximation, which is different from our criterion.

In the lower plots of Fig. 4.5, we show the effectiveness of diagonal pre-

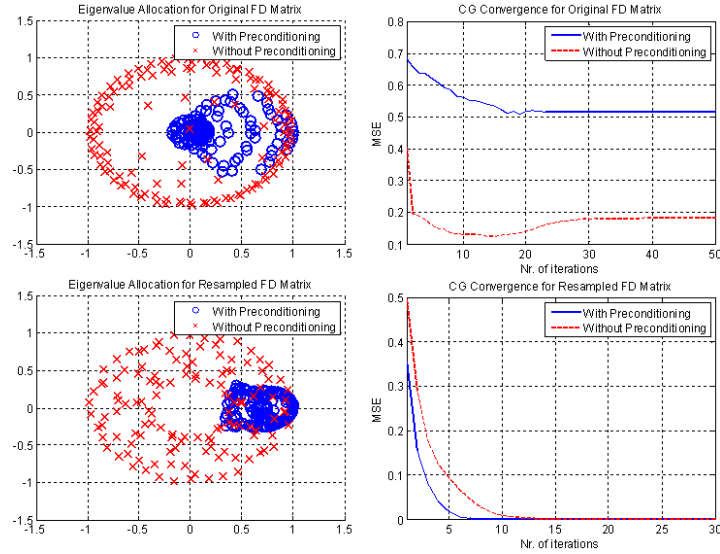


**Figure 4.5:** Left plots: eigenvalues with and without preconditioning; Right plots: convergence performance with and without preconditioning; FD matrix for top two plots corresponds to the original channel, FD matrix for bottom two plots is obtained after our optimum resampling; The MSML channel is set according to Table 4.1.

conditioning applied to the resampled channel in Table 4.1. It is clear that, after our resampling procedure, the diagonal preconditioner clusters the eigenvalues of the preconditioned FD channel matrix closer to one than without preconditioning, which further reduces the condition number from 23.36 to 7.17. In contrast, without optimal resampling, the preconditioner “wrongly” pushes the eigenvalues closer to zero. In this case, the matrix condition number increases from  $4.26 \times 10^5$  to  $1.19 \times 10^6$ , and hence the CG equalizer performs even worse than without preconditioning as shown in the top two plots of Fig. 4.5.

Similarly, we can show that optimal resampling can also improve the performance of the CG in the time domain, for which we just provide Table 4.2 and Fig. 4.6 here due to space limitations. From them, we can make the same observations as from Table 4.1 and Fig. 4.5 for the frequency domain case.

**Table 4.2: Channel II: Time-Domain Approach**

Channel II ( $T = 0.2\text{ms}$ $\omega = 640$ $K = 128$ )	path	scale $\alpha_l$	delay $\lambda_l$	path gain $\bar{h}_l$
	$l = 0$	1.0161	1.00	0 dB
	$l = 1$	1.0180	0.80	-3 dB
	$l = 2$	1.0244	3.00	-5 dB
Resampl. Para.	Orig. $(\beta, \phi, \sigma)$ $(\beta_{T,*}, \phi_{T,*}, \sigma_{T,*})$	$(1, 0, 0)$ $(1.0160, -0.0210, -1.00)$		
Cond. Num. for TD	Orig. / no precondition.	$2.54 \times 10^4$		
	Orig. / with precondition.	$7.37 \times 10^4$		
	Resampl. / no precondition.	50.78		
	Resampl. / with precondition.	15.03		
TD Ratio	Orig.	$\rho_F^{(1,0,0)} = 0.0021$		
	Resampl.	$\rho_F^{(\beta_{F,*}, \phi_{F,*}, \sigma_{F,*})} = 0.9168$		

## 4.5 Frequency-Domain or Time-Domain Equalization?

In the previous sections, we showed that the equalization of an OFDM channel can be implemented in either the frequency or the time domain. With the CG algorithm specified in Appendix 4.C, it is clear that the cost of equalization in the frequency domain will be upper-bounded by  $\mathcal{O}(B_F^{(\beta,\phi)} K)$  with  $B_F^{(\beta,\phi)} = \max_k B_F^{(\beta,\phi)}(k)$  for each CG iteration. Likewise, the cost of equalization in the time domain will be upper-bounded by  $\mathcal{O}(B_T^{(\beta,\sigma)} K)$  with  $B_T^{(\beta,\sigma)} = \max_m B_T^{(\beta,\sigma)}(m)$ . By assuming that the number of CG iterations is predetermined and identical in both domains, we can use the ratio  $B_F^{(\beta,\phi)} / B_T^{(\beta,\sigma)}$  as a criterion to choose in which domain the equalization will be realized in order to minimize the complexity.

However, the evaluation of  $B_F^{(\beta,\phi)} / B_T^{(\beta,\sigma)}$  is cumbersome and lacks the insight of the channel physics. For simplicity reasons, we equivalently consider the proportion given by

$$\epsilon = \frac{B_F^{(\beta,\phi)} - 2B_{\text{rul}}}{B_T^{(\beta,\sigma)} - 2B_{\text{rul}}} = \frac{\max_k \left( \max_l (\Delta_{F,l}^{(\beta,\phi)}(k)) - \min_l (\Delta_{F,l}^{(\beta,\phi)}(k)) \right)}{\max_m \left( \max_l (\Delta_{T,l}^{(\beta,\sigma)}(m)) - \min_l (\Delta_{T,l}^{(\beta,\sigma)}(m)) \right)}, \quad (4.36)$$

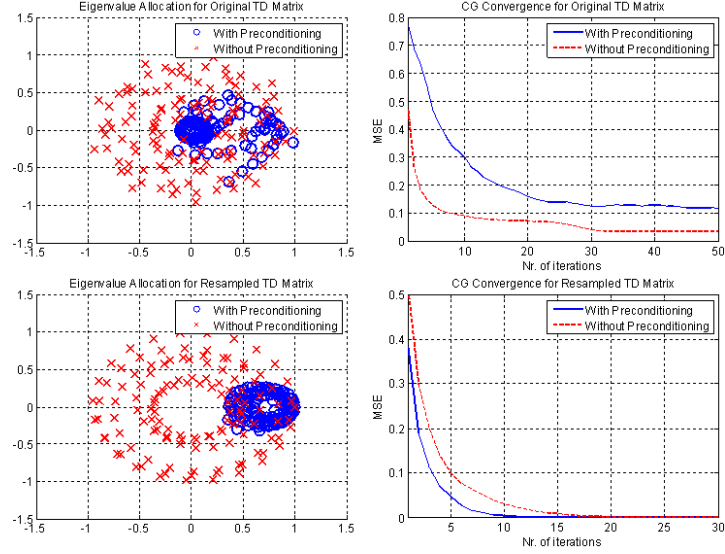


**Figure 4.6:** Left plots: eigenvalues with and without preconditioning; Right plots: convergence performance with and without preconditioning; TD matrix for top two plots corresponds to the original channel, TD matrix for bottom two plots is obtained after our optimum resampling; The MSML channel is set according to Table 4.2.

where we reasonably assume  $B_{\text{ru1}} = \max_{l,k} B_{F,l}(k) \approx \max_{l,m} B_{T,l}(m)$  [see Fig. 4.2]. One may argue that the above evaluation is still cumbersome. However, if a realistic channel allows us to assume, for all  $l \in \{1, 2, \dots, L\}$ , that

$$\begin{aligned} |\alpha_l - \beta_{F,\star}|/\beta_{F,\star} &\ll 1/(K-1), \\ |\alpha_l - \beta_{T,\star}|/\beta_{T,\star} &\ll 1/(K-1), \end{aligned}$$

which indicates that the Doppler scale spread is well-limited, it follows that  $\max_{l,k} (|\xi_{l,F1}|k) \ll 1$  and  $\max_{l,m} (|\xi_{l,T1}|m) \ll 1$ . In other words,  $\Delta_{F,l}^{(\beta_{F,\star}, \phi_{F,\star})}(k) \approx \langle \xi_{l,F2} \rangle$  and  $\Delta_{T,l}^{(\beta_{T,\star}, \sigma_{T,\star})}(m) \approx \langle \xi_{l,T2} \rangle$ , both of which are independent of the

symbol index. With these assumptions,  $\epsilon$  can further be simplified as

$$\begin{aligned} \epsilon &\approx \frac{\max_l(\langle \xi_{l,F2} \rangle) - \min_l(\langle \xi_{l,F2} \rangle)}{\max_l(\langle \xi_{l,T2} \rangle) - \min_l(\langle \xi_{l,T2} \rangle)} \\ &= \frac{\left\langle (\max_l(\alpha_l) - 1 + \phi_{F,*}) \frac{\omega}{\beta_{F,*}} \right\rangle - \left\langle (\min_l(\alpha_l) - 1 + \phi_{F,*}) \frac{\omega}{\beta_{F,*}} \right\rangle}{\left\langle \max_l(\alpha_l(\lambda_l + \sigma_{T,*})) \right\rangle - \left\langle \min_l(\alpha_l(\lambda_l + \sigma_{T,*})) \right\rangle} \end{aligned}$$

which suggests that if the maximum difference between the Doppler shifts of each path (i.e.,  $\frac{\alpha_l - 1}{\beta} \omega$ ) is smaller than the maximum difference between the time shifts of each path (i.e.,  $\alpha_l \lambda_l$ ), then equalization should be realized in the frequency domain; otherwise, a time-domain approach will be preferred. A similar conclusion has been made for narrowband systems [80], though its extension to wideband systems is not straightforward as shown above.

To illustrate the above idea, we again use the channel examples specified in Table 4.1 and Table 4.2 respectively. We use  $B_{\text{rul}} = 5$  to roughly capture  $\gamma = 98\%$  of the channel energy in both domains where  $\gamma$  is introduced in (4.18). In this way, we have  $\epsilon \approx 0.10 < 1$  for the channel in Table 4.1, while for the channel in Table 4.2, we have  $\epsilon \approx 2.00 > 1$ .

For both channels, we compare the equalization performance in different domains. OFDM with  $K = 128$  subcarriers using QPSK is transmitted and the receiver is assumed to have perfect channel knowledge. We examine the bit error rate (BER) results of our CG equalization with a fixed CG iteration number (e.g.,  $i_{F,\max} = i_{T,\max} = 100$ ). We use different bandwidths for the banded approximation  $\bar{\mathbf{H}}_F^{(\beta_{F,*}, \phi_{F,*}, \sigma_{F,*})}$  and  $\bar{\mathbf{H}}_T^{(\beta_{T,*}, \phi_{T,*}, \sigma_{T,*})}$  during the equalization and the values for  $(\beta_{F,*}, \phi_{F,*}, \sigma_{F,*})$  and  $(\beta_{T,*}, \phi_{T,*}, \sigma_{T,*})$  have also been given in Table 4.1 and Table 4.2, respectively. After our optimal resampling in either domain, the CG equalization is carried out using the appropriate preconditioner design.

The left subplot of Fig. 4.7 plots the BER performance as a function of signal-to-noise ratio (SNR) for Channel I. Note that

$$(\beta_{F,*}, \phi_{F,*}, \sigma_{F,*}) = (1.015, -0.015, -15)$$

and

$$(\beta_{T,*}, \phi_{T,*}, \sigma_{T,*}) = (1.015, -0.016, 0.00)$$

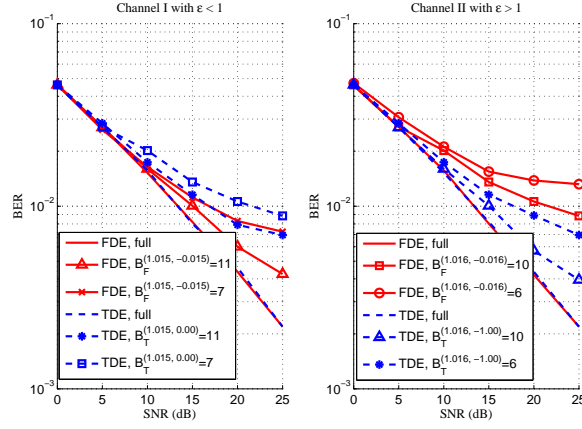


Figure 4.7: BER vs. SNR for the two channels given in Table 4.1 and Table 4.2

for this channel. It can be seen that the performance of the FD equalizer (FDE) based on  $\bar{\mathbf{H}}_F^{(\beta_{F,*}, \phi_{F,*}, \sigma_{F,*})}$  outperforms the TD equalizer (TDE) based on  $\bar{\mathbf{H}}_T^{(\beta_{T,*}, \phi_{T,*}, \sigma_{T,*})}$  using the same bandwidth  $B_F^{(\beta_{F,*}, \phi_{F,*})} = B_T^{(\beta_{T,*}, \sigma_{T,*})}$ . In other words, FDE is more attractive than TDE in this case.

The BER performance for Channel II is illustrated in the right subplot of Fig. 4.7, where the optimal resampling parameters are

$$(\beta_{T,*}, \phi_{T,*}, \sigma_{T,*}) = (1.016, -0.021, -1)$$

and

$$(\beta_{F,*}, \phi_{F,*}, \sigma_{F,*}) = (1.016, -0.016, -3).$$

In this case, it is evident that the TD equalizer is more appealing.

These observations made for the channels in Table 4.1 and Table 4.2 confirm our metric  $\epsilon$  for determining which domain is more suitable for channel equalization. Additionally, we like to point out that, in either domain, with a larger bandwidth the BER performance of our CG equalization will be increased.

**Table 4.3: Channel parameters**

Case 1: $\epsilon < 1$			Case 2: $\epsilon > 1$		
$K = 128, \omega = 256$			$K = 128, \omega = 640$		
$L$	$\alpha_{\max}$	$\tau_{\max}/T$	$L$	$\alpha_{\max}$	$\tau_{\max}/T$
5	1.008	30.00	5	1.010	4.00

## 4.6 Numerical Results

In this section, we randomly generate two different types of wideband channels as specified in Table 4.3:  $\epsilon < 1$  (Case I) represents wideband LTV channels where the Doppler differences among the multipath are more pronounced than the delay differences; and  $\epsilon > 1$  (Case II) is the case where the Doppler differences among the multipath are less pronounced than the delay differences. For all simulations, OFDM with  $K = 128$  subcarriers is considered with QPSK. The wideband channels are assumed to have  $L = 5$  paths, whose channel gains (i.e.,  $\bar{h}_l$ 's) are modeled to be identically and independently distributed. The path delay ( $\tau_l$ ) is chosen as a random variable that has a uniform distribution within the range  $[0, \tau_{\max}]$ . Likewise, the path scale ( $\alpha_l$ ) is chosen as a random variable that obeys a uniform distribution within the range  $[1, 1 + \alpha_{\max}]$ . For both cases, the receiver is assumed to have perfect channel knowledge and the cyclic extensions at the transmitter are  $T_{\text{pre}} = 32T$  and  $T_{\text{post}} = 10T$  which satisfy (4.6) and (4.7). In all simulations, a banded approximation of the channel matrix is adopted in both domains with the same bandwidth (e.g.,  $B_{\text{F}}^{(\beta_{\text{F}}, \star, \phi_{\text{F}}, \star)} = B_{\text{T}}^{(\beta_{\text{T}}, \star, \sigma_{\text{T}}, \star)} = 11$ ).

In Fig. 4.8, the convergence of the CG equalization is plotted in terms of the bit error rate (BER) against the number of iterations at SNR = 30dB for Case I. Since  $\epsilon < 1$ , frequency-domain equalization (FDE) is carried out. It is clear that the receiver, which simply adopts a diagonal preconditioner in (4.25) without resampling, performs worst. The performance is already considerably improved if optimal resampling is applied. Moreover the use of our preconditioner given by (4.31) boosts the performance even further.

The proposed resampling and preconditioning method can also benefit from other Krylov-based algorithms. For instance, the LSQR algorithm exploiting a full channel matrix is studied in [41]. Note that [41] focuses on



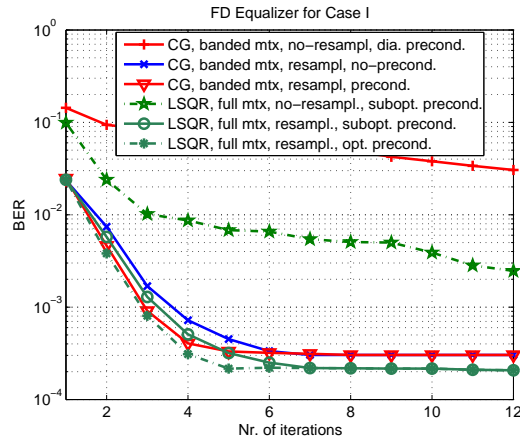


Figure 4.8: BER vs. number of iterations for Case I channels at SNR = 30dB

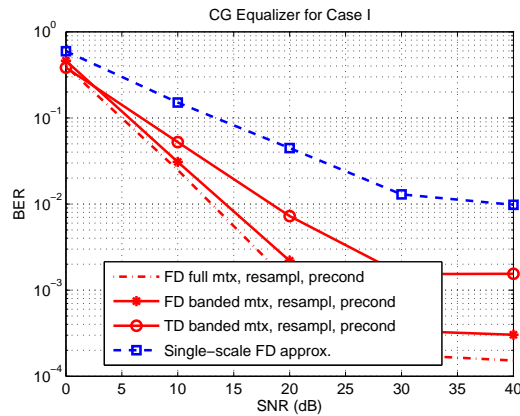


Figure 4.9: BER vs. SNR for Case I channels

a narrowband LTV system where no resampling is required. Further, the preconditioner given in [41] is based on a truncated basis expansion model (BEM) which is usually used for the approximation of a narrowband time-varying channel. Because it is not clear whether such a truncated BEM is still suitable for a wideband LTV channel, in order to emulate a similar approach

as in [41] for constructing the preconditioner, we utilize a (trivial) full-order critically-sampled complex exponential BEM (the CCE-BEM [37]) in the simulation. The preconditioner in [41] then boils down to the inverse of the diagonal of the frequency-domain channel matrix, which is obviously sub-optimal in the Frobenius norm sense. Consequently, it is no surprise that directly applying the equalizer of [41] to wideband LTV channels yields a bad performance as shown in Fig. 4.8. In comparison, the LSQR algorithm benefiting from the optimal resampling and our preconditioner renders the fastest convergence rate and lowest BER amongst all the equalization schemes. Of course, such an improved BER performance is achieved by leveraging the full channel matrix at the cost of a higher complexity, compared to our proposed method using banded matrices.

Fig. 4.9 exhibits the BER versus SNR for the CG-based equalization schemes, where a truncated CG is used which halts at the 5th iteration. It can be seen in the figure that the equalizer leveraging the full channel matrix gives the best BER performance but inflicts more complexity. When using a banded channel matrix approximation, the frequency-domain approach performs much better than the time-domain approach because we have  $\epsilon < 1$  for this type of channel. Additionally, the equalization approach in [29] is carried out and its performance is also shown in Fig. 4.9. As we discussed earlier, the resampling operation in [29] is solely focused on the rescaling parameter ignoring the impact of frequency and time synchronization, which is therefore sub-optimal. Besides, the equalizer in [29] approximates the channel matrix to be diagonal (i.e., using a bandwidth of one for the banded matrices), and thus its performance becomes inferior in the presence of higher scale differences among the multipath as in the tested channel here.

The performance of the equalizers for Case II is depicted in Fig. 4.10, where the significance of optimal resampling and our adapted preconditioner is again illustrated just like in Fig. 4.8. Similarly, we can see that the LSQR algorithm in [41] also works well for this type of channel if optimal resampling and preconditioning are included.

Different from Case I, the channels of Case II are subject to a larger delay spread than a Doppler spread (i.e.,  $\epsilon > 1$ ). In this case, a time-domain equalizer will be more effective than its frequency-domain counterpart as

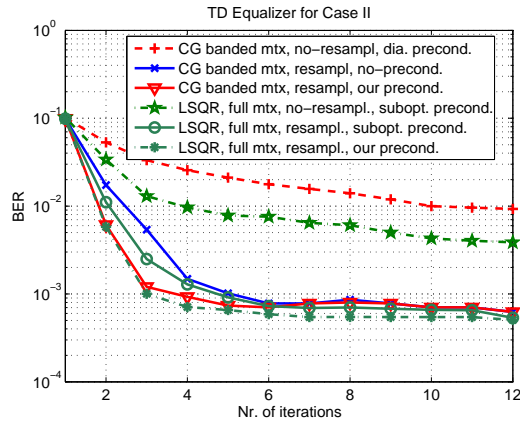


Figure 4.10: BER vs. number of iterations for Case II Channels at SNR = 30dB.

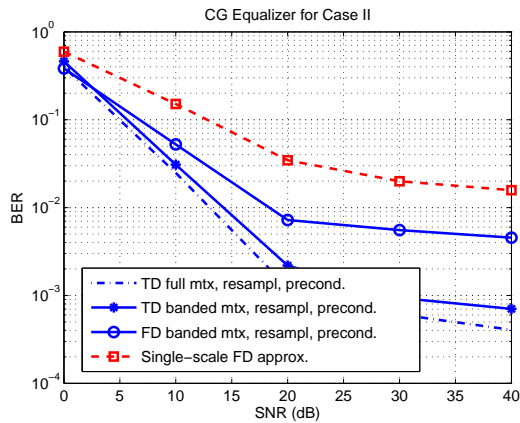


Figure 4.11: BER vs. SNR for Case II channels

validated in Fig. 4.11. The equalizer in [29] yields a much worse performance than ours since the Doppler scale spread differences in this case are even higher than for Case I.

## 4.7 Summary

In this chapter, we have discussed iterative equalization of wideband channels using the conjugate gradient (CG) algorithm for OFDM systems. The channel follows a multi-scale multi-lag (MSML) model, and suffers therefore from interferences in both the frequency domain and time domain. To lower the equalization complexity, the channel matrices are approximated to be banded in both domains. A novel method of optimal resampling is proposed, which is indispensable for wideband communications. A diagonal preconditioning technique, that accompanies the CG method to accelerate the convergence, has also been adapted to enhance its suitability. Experimental results have shown that our equalization scheme allows for a superior performance to those schemes based on a single-scale resampling method, without any resampling operation, or using a traditional preconditioning procedure. In addition, we gave a simple criterion to determine whether to use a frequency-domain or time-domain equalizer, depending on the channel situation, to obtain the best BER performance with the same complexity. Such a criterion is also validated by experiments.

## Appendix 4.A Detailed Derivation of the Discrete Data Model

Here we give the derivation of (4.9), assuming no noise is present. We start from (4.8) given by

$$\begin{aligned} r_n^{(\beta, \phi, \sigma)} &= r^{(\beta, \phi, \sigma)}(nT) \\ &= \frac{1}{\sqrt{\beta KT}} \sum_{k=0}^{K-1} b_k h_k \left( \frac{nT}{\beta} - \sigma T \right) e^{j2\pi(\phi f_c + f_k) \frac{nT}{\beta}} e^{-j2\pi f_k \sigma T} \end{aligned}$$

where  $h_k(t)$  is defined in (4.5) and the embedded  $u(t)$  in  $h_k(t)$  is considered to be one for the concerned observation window as clarified in Remark 4.1.

Now, we substitute  $h_k(t)$  to obtain

$$\begin{aligned} r_n^{(\beta, \phi, \sigma)} &= \frac{1}{\sqrt{\beta KT}} \sum_{k=0}^{K-1} b_k \sum_{l=0}^L \bar{h}_l \sqrt{\alpha_l} e^{-j2\pi(f_c + f_k) \alpha_l \tau_l} e^{j2\pi(\alpha_l - 1)(f_c + f_k) \left( \frac{nT}{\beta} - \sigma T \right)} \\ &\quad \times e^{j2\pi(\phi f_c + f_k) \frac{nT}{\beta}} e^{-j2\pi f_k \sigma T} \\ &= \frac{1}{\sqrt{\beta KT}} \sum_{k=0}^{K-1} b_k \times \sum_{l=0}^L \bar{h}_l \sqrt{\alpha_l} \\ &\quad \times \left( e^{-j2\pi f_c \alpha_l \tau_l} e^{j2\pi(\alpha_l - 1) f_c \left( \frac{nT}{\beta} - \sigma T \right)} e^{j2\pi \phi f_c \frac{nT}{\beta}} \right) \\ &\quad \times \left( e^{-j2\pi f_k \alpha_l \tau_l} e^{j2\pi(\alpha_l - 1) f_k \left( \frac{nT}{\beta} - \sigma T \right)} e^{j2\pi f_k \frac{nT}{\beta}} e^{-j2\pi f_k \sigma T} \right) \\ &= \sum_{l=0}^L \left( \sqrt{\frac{\alpha_l}{\beta KT}} \bar{h}_l e^{-j2\pi f_c (\alpha_l \tau_l + (\alpha_l - 1) \sigma T)} \right) e^{j2\pi f_c \frac{(\alpha_l - 1 + \phi) nT}{\beta}} \\ &\quad \times \left( \sum_{k=0}^{K-1} b_k e^{j2\pi f_k \frac{\alpha_l nT}{\beta}} \right) e^{-j2\pi f_k \alpha_l (\tau_l + \sigma T)} \\ &= \sum_{l=0}^L h_l^{(\beta, \sigma)} e^{j2\pi f_c \frac{(\alpha_l - 1 + \phi) nT}{\beta}} \times \left( \sum_{k=0}^{K-1} b_k e^{j2\pi f_k \frac{\alpha_l nT}{\beta}} \right) e^{-j2\pi f_k \alpha_l (\tau_l + \sigma T)}, \end{aligned}$$

where the channel coefficient is given by

$$h_l^{(\beta, \sigma)} = \sqrt{\frac{\alpha_l}{\beta KT}} \bar{h}_l e^{-j2\pi f_c (\alpha_l \tau_l + (\alpha_l - 1) \sigma T)}$$

Now, if we denote

$$\omega = \frac{f_c}{\Delta f}$$

for the normalized carrier frequency and

$$\lambda_l = \frac{\tau_l}{T}$$

for the normalized delay of the  $l$ th path, we have

$$r_n^{(\beta, \phi, \sigma)} = \sum_{l=0}^L h_l^{(\beta, \sigma)} e^{j2\pi\omega \frac{(\alpha_l - 1 + \phi)}{\beta} \frac{n}{K}} \times \left( \sum_{k=0}^{K-1} b_k e^{j2\pi \frac{\alpha_l}{\beta} \frac{nk}{K}} \right) e^{-j2\pi\alpha_l(\lambda_l + \sigma) \frac{k}{K}}$$

which gives (4.9).

## Appendix 4.B System Model in the Time Domain and Time-domain Equalization

To derive the time-domain model, let us rewrite (4.10) as

$$\mathbf{r}_T^{(\beta, \phi, \sigma)} = \mathbf{H}_T^{(\beta, \phi, \sigma)} \mathbf{s}, \quad (4.37)$$

where  $\mathbf{s} = \mathbf{F}_1^{-1} \mathbf{b}$ , and  $\mathbf{H}_T^{(\beta, \phi, \sigma)}$  stands for the time-domain (TD) channel matrix

$$\mathbf{H}_T^{(\beta, \phi, \sigma)} = \sum_{l=0}^L h_l^{(\beta, \sigma)} \mathbf{D}_{\alpha_l}^{(\beta, \phi)} \mathbf{H}_{T,l}^{(\beta, \sigma)} \quad (4.38)$$

with  $\mathbf{H}_{T,l}^{(\beta, \sigma)} = \mathbf{F}_{\alpha_l/\beta}^H \mathbf{\Lambda}_{\lambda_l}^{(\sigma)} \mathbf{F}_1$  being its  $l$ th component. The  $(m, k)$ th entry of  $\mathbf{H}_{T,l}^{(\beta, \sigma)}$  is given by

$$\begin{aligned} \left[ \mathbf{H}_{T,l}^{(\beta, \sigma)} \right]_{m,k} &= \frac{1}{K} \sum_{n=0}^{K-1} e^{j2\pi \frac{\alpha_l}{\beta} \frac{mn}{K}} e^{j2\pi\alpha_l(\lambda_l + \sigma) \frac{n}{K}} e^{-j2\pi \frac{nk}{K}} \\ &= e^{-j \frac{(K-1)\pi}{K} ((k-m) - (\xi_{l,T1}m + \xi_{l,T2}))} \times \\ &\quad \frac{\text{sinc}(\pi ((k-m) - (\xi_{l,T1}m + \xi_{l,T2})))}{\text{sinc}(\frac{\pi}{K} ((k-m) - (\xi_{l,T1}m + \xi_{l,T2})))}, \end{aligned} \quad (4.39)$$

where  $\xi_{l,T1} = \frac{\alpha_l - \beta}{\beta}$  and  $\xi_{l,T2} = \alpha_l(\lambda_l + \sigma)$ .

Observing the analogy between (4.16) and (4.39), a similar interference analysis can be made on  $\mathbf{H}_T$ . By defining

$$\Delta_{T,l}^{(\beta,\sigma)}(m) = \langle \xi_{l,T1}m + \xi_{l,T2} \rangle, \quad (4.40)$$

we can introduce the symbol  $B_{T,l}^{(\beta,\sigma)}(m)$  defined as [c.f. (4.18)]

$$\begin{aligned} B_{T,l}^{(\beta,\sigma)}(m) &= \min\{B\}, \\ \text{s.t.} \quad & \sum_{k=m+\Delta_{T,l}^{(\beta,\sigma)}(m)-B}^{m+\Delta_{T,l}^{(\beta,\phi)}(m)+B} \left| \frac{\text{sinc}(\pi((k-m) - (\xi_{l,T1}m + \xi_{l,T2})))}{\text{sinc}(\frac{\pi}{K}((k-m) - (\xi_{l,T1}m + \xi_{l,T2})))} \right|^2 \\ & > \gamma \sum_{k=0}^{K-1} \left| \frac{\text{sinc}(\pi((k-m) - (\xi_{l,T1}m + \xi_{l,T2})))}{\text{sinc}(\frac{\pi}{K}((k-m) - (\xi_{l,T1}m + \xi_{l,T2})))} \right|^2, \end{aligned} \quad (4.41)$$

which determines the index set of the data symbols that contribute the most to the  $m$ th received signal  $[\mathbf{r}_T^{(\beta,\phi,\sigma)}]_m$  via the  $l$ th path. Note that  $B_{F,l}^{(\beta,\phi)}(k)$  in (4.18) depends on the resampling factor  $\beta$  and the frequency shift factor  $\phi$ , whereas  $B_{T,l}^{(\beta,\sigma)}(m)$  in (4.41) depends on the resampling factor  $\beta$  and the time shift factor  $\sigma$ .

Similarly as in the frequency domain, we obtain a banded approximation of  $\mathbf{H}_T^{(\beta,\phi,\sigma)}$  by introducing

$$B_T^{(\beta,\sigma)}(m) \approx \max_l \left( \Delta_{T,l}^{(\beta,\sigma)}(m) \right) - \min_l \left( \Delta_{T,l}^{(\beta,\sigma)}(m) \right) + 2 \max_l \left( B_{T,l}^{(\beta,\sigma)}(m) \right) \quad (4.42)$$

and a selection matrix  $\mathbf{B}_T^{(\beta,\sigma)}$ , whose  $(m, k)$ th entry is equal to 1 if

$$\min_l \left( m + \Delta_{T,l}^{(\beta,\sigma)}(m) - B_{T,l}^{(\beta,\sigma)}(m) \right) \leq k \leq \max_l \left( m + \Delta_{T,l}^{(\beta,\sigma)}(m) + B_{T,l}^{(\beta,\sigma)}(m) \right),$$

and 0 otherwise. Then the banded approximation of  $\mathbf{H}_T^{(\beta,\phi,\sigma)}$  is obtained by

$$\bar{\mathbf{H}}_T^{(\beta,\phi,\sigma)} = \mathbf{B}_T^{(\beta,\sigma)} \odot \mathbf{H}_T^{(\beta,\phi,\sigma)}. \quad (4.43)$$

We can then rewrite (4.37) as

$$\mathbf{r}_T^{(\beta,\phi,\sigma)} = \bar{\mathbf{H}}_T^{(\beta,\phi,\sigma)} \mathbf{s} + \bar{\mathbf{v}}_T^{(\beta,\phi,\sigma)}, \quad (4.44)$$

where  $\bar{\mathbf{v}}_T^{(\beta,\phi,\sigma)} = \left( \mathbf{H}_T^{(\beta,\phi,\sigma)} - \bar{\mathbf{H}}_T^{(\beta,\phi,\sigma)} \right) \mathbf{s}$ .

The time-domain equalization can be presented in an analogous manner as in the frequency domain. Similar to its FD counterpart in (4.23), we here rewrite the noiseless case for (4.44) as

$$\begin{aligned} \mathbf{r}_{\text{TC}}^{(\beta,\phi,\sigma)} &= \mathbf{C}_T \mathbf{r}_T^{(\beta,\phi,\sigma)} = \left( \mathbf{C}_T \bar{\mathbf{H}}_T^{(\beta,\phi,\sigma)} \right) \mathbf{s} \\ &= \bar{\mathbf{H}}_{\text{TC}}^{(\beta,\phi,\sigma)} \mathbf{s} = \bar{\mathbf{H}}_{\text{TC}}^{(\beta,\phi,\sigma)} \mathbf{F}_1^H \mathbf{b} \end{aligned} \quad (4.45)$$

where  $\mathbf{s} = \mathbf{F}_1^H \mathbf{b}$ ,  $\mathbf{C}_T$  is the preconditioner applied in the time domain and  $\bar{\mathbf{H}}_{\text{TC}}^{(\beta,\phi,\sigma)} = \mathbf{C}_T \bar{\mathbf{H}}_T^{(\beta,\phi,\sigma)}$ . We first estimate  $\mathbf{s}$  by applying the CG algorithm on  $\mathbf{r}_{\text{TC}}^{(\beta,\phi,\sigma)}$  to invert  $\bar{\mathbf{H}}_{\text{TC}}^{(\beta,\phi,\sigma)}$  iteratively, and afterwards we obtain  $\hat{\mathbf{b}} = \mathbf{F}_1^H \hat{\mathbf{s}}$ .

We highlight that the adopted diagonal preconditioner

$$\mathbf{C}_{T,\star} = \text{diag}\{[c_{T,0,\star}, c_{T,1,\star}, \dots, c_{T,K-1,\star}]^T\}$$

is defined in a similar manner as in the frequency domain. Specifically, we use

$$c_{T,m,\star} = \begin{cases} \frac{[\mathbf{H}_T^{(\beta,\phi,\sigma)}]_{m,m}^*}{\|\mathbf{e}_m^T \mathbf{H}_T^{(\beta,\phi,\sigma)}\|_2^2}, & \text{if } \zeta_{\text{TC}}^{(\beta,\phi,\sigma)}(m) \geq 1 \\ 1, & \text{otherwise} \end{cases} \quad (4.46)$$

where

$$\zeta_{\text{TC}}^{(\beta,\phi,\sigma)}(m) = \frac{\left| [\mathbf{H}_T^{(\beta,\phi,\sigma)}]_{m,m} \right|^2}{\sum_{k=0, k \neq m}^{K-1} \left| [\mathbf{H}_T^{(\beta,\phi,\sigma)}]_{m,k} \right|^2}. \quad (4.47)$$

To enhance the suitability of the preconditioner, the optimal resampling operation is needed as given by

$$\begin{aligned} (\beta_{T,\star}, \phi_{T,\star}, \sigma_{T,\star}) &= \arg \max_{\beta,\phi,\sigma} \sum_{m=0}^{K-1} \left| \sum_{l=0}^L h_l^{(\beta,\sigma)} e^{j2\pi\omega \frac{\alpha_l - 1 + \phi}{\beta} \frac{m}{K}} \times \right. \\ &\quad \left. e^{-j \frac{(K-1)\pi}{K} (\xi_{l,T1} m + \xi_{l,T2})} \times \frac{\text{sinc}(\xi_{l,T1} k + \xi_{l,T2})}{\text{sinc}(\frac{1}{K} (\xi_{l,T1} m + \xi_{l,T2}))} \right|^2. \end{aligned} \quad (4.48)$$



## Appendix 4.C Equalization using the Conjugate Gradient Algorithm

If we consider to solve the preconditioned system in (4.23) in a similar manner as (4.22), we have

$$\hat{\mathbf{b}}_C = \bar{\mathbf{M}}_{FC}^{(\beta, \phi, \sigma)^{-1}} \bar{\mathbf{H}}_{FC}^{(\beta, \phi, \sigma)^H} \mathbf{r}_F^{(\beta, \phi, \sigma)}$$

where  $\bar{\mathbf{M}}_{FC}^{(\beta, \phi, \sigma)} = \bar{\mathbf{H}}_{FC}^{(\beta, \phi, \sigma)^H} \bar{\mathbf{H}}_{FC}^{(\beta, \phi, \sigma)}$ , and  $\hat{\mathbf{b}}_C$  is the estimate of  $\mathbf{b}_C = \mathbf{C}_F^{-1} \mathbf{b}$ .

Its implementation using CG is described in the frequency domain as follows

1. Define  $\mathbf{d}_F = \bar{\mathbf{H}}_F^{(\beta, \phi, \sigma)^H} \mathbf{r}_F^{(\beta, \phi, \sigma)}$  and  $i = 0$ ;
2. Define  $\mathbf{a}^{(0)} = \mathbf{g}^{(0)} = \mathbf{d}_F$ ,  $u^{(0)} = \frac{\|\mathbf{d}_F\|^2}{\mathbf{d}_F^H \bar{\mathbf{M}}_{FC}^{(\beta, \phi, \sigma)} \mathbf{d}_F}$  and  $\hat{\mathbf{b}}_C^{(0)} = u^{(0)} \mathbf{d}_F$ .
3. Perform the following iterations:

Loop

$$\begin{aligned} \mathbf{g}^{(i)} &= \mathbf{d}_F - \bar{\mathbf{M}}_{FC}^{(\beta, \phi, \sigma)} \hat{\mathbf{b}}_C^{(i)}, \\ \mathbf{a}^{(i)} &= \frac{\|\mathbf{g}^{(i)}\|_{\text{Fro}}^2}{\|\mathbf{g}^{(i-1)}\|_{\text{Fro}}^2} \mathbf{a}^{(i-1)} + \mathbf{g}^{(i)}, \\ u^{(i)} &= \frac{\|\mathbf{g}^{(i)}\|_{\text{Fro}}^2}{\mathbf{a}^{(i)H} \bar{\mathbf{M}}_{FC}^{(\beta, \phi, \sigma)} \mathbf{a}^{(i)}}, \\ \hat{\mathbf{b}}_C^{(i)} &= \hat{\mathbf{b}}_C^{(i-1)} + u^{(i)} \mathbf{a}^{(i)} \end{aligned} \tag{4.49}$$

End Loop;

4. Perform  $\hat{\mathbf{b}}^{(i)} = \mathbf{C}_F \hat{\mathbf{b}}_C^{(i)}$ , which is the  $i$ th output of the equalization process, and the index  $i$  is incremental from 0 to  $i_{\max}$  where  $i_{\max}$  is the iteration number when the stopping criterion of the CG is satisfied.

Notably, the optimal stopping criterion for CG can be case dependent, e.g., as discussed in [73, 79], and is not included in this chapter. When our CG iterations stop, we finally have  $\hat{\mathbf{b}} = \hat{\mathbf{b}}^{(i_{\max})}$ , which is the data estimate.

It is worthy to note that the computational complexity of each CG iteration above is determined by the complex multiplication (CM) of  $\bar{\mathbf{M}}_{FC}^{(\beta, \phi, \sigma)}$

with a vector (e.g.  $\hat{\mathbf{b}}_C^{(i)}$  or  $\mathbf{a}^{(i)}$ ), e.g., as in (4.49). When  $\mathbf{C}_F^{(\beta, \phi, \sigma)}$  is a diagonal preconditioner as considered in this chapter, the bandwidth of the preconditioned  $\bar{\mathbf{H}}_{FC}^{(\beta, \phi, \sigma)}$  equals that of  $\bar{\mathbf{H}}_C^{(\beta, \phi, \sigma)}$ , and consequently  $\bar{\mathbf{M}}_{FC}^{(\beta, \phi, \sigma)}$  is banded with a bandwidth  $2B_F^{(\beta, \phi)}$  where  $B_F^{(\beta, \phi)} = \max_k B_F^{(\beta, \phi)}(k)$  with  $B_F^{(\beta, \phi)}(k)$  defined in (4.19). In this case, the computational complexity of each iteration is upper-bounded by  $\mathcal{O}(B_F^{(\beta, \phi)} K)$  which is linear in the vector size  $K$ .

One can also repeat the above derivations using the TD notations for the TD CG equalization.

## Appendix 4.D Eigenvalue Locations

We consider the diagonal matrix  $\mathbf{C}_F = \text{diag}\{[c_{F,0}, c_{F,1}, \dots, c_{F,K-1}]^T\}$ , and denote the eigenvalues of  $\bar{\mathbf{H}}_{FC}^{(\beta, \phi, \sigma)} = \bar{\mathbf{H}}_F^{(\beta, \phi, \sigma)} \mathbf{C}_F$  as  $\{\mu_1, \mu_2, \dots, \mu_{K-1}\}$ .

Let  $\mathbf{U}\mathbf{W}\mathbf{U}$  be a Schur decomposition of  $\bar{\mathbf{H}}_{FC}^{(\beta, \phi, \sigma)}$  such that  $\mathbf{U}\mathbf{U}^H = \mathbf{I}_{K \times K}$  and the diagonal elements of  $\mathbf{W}$  equal  $\{\mu_1, \mu_2, \dots, \mu_{K-1}\}$ . Then

$$\begin{aligned} \sum_{k=0}^{K-1} |\mu_k|^2 &= \|\text{diag}\{\mathbf{W}\}\|_2^2 \leq \|\mathbf{W}\|_{\text{Fro}}^2 \\ &= \|\bar{\mathbf{H}}_{FC}^{(\beta, \phi, \sigma)}\|_{\text{Fro}}^2 = \|\bar{\mathbf{H}}_F^{(\beta, \phi, \sigma)} \mathbf{C}_F\|_{\text{Fro}}^2. \end{aligned}$$

Note that  $\bar{\mathbf{H}}_F^{(\beta, \phi, \sigma)} \mathbf{e}_{kC_F, k} = \bar{\mathbf{H}}_F^{(\beta, \phi, \sigma)} \mathbf{C}_F \mathbf{e}_k$ , where  $\mathbf{e}_k$  stands for an all-zero vector except for its  $k$ th entry which equals 1, as defined in (4.25) for  $k = 0, 1, \dots, K$ . We then recall (4.27), which holds for any  $k \in \{0, 1, \dots, K-1\}$ , and thus upper-bounds the above expressions as

$$\sum_{k=0}^{K-1} |\mu_k|^2 \leq K \|\bar{\mathbf{H}}_F^{(\beta, \phi, \sigma)} \mathbf{e}_{kC_F, k}\|_{\text{Fro}}^2 \leq K \epsilon_0^2.$$

Similarly, we can also prove that  $\sum_{k=0}^{K-1} |\mu_k - 1|^2 \leq K \epsilon_1^2$  associated with (4.26).

## Chapter 5

---

# Multi-Layer Transceiver

*The aim of exact science is to reduce the problems of nature to the determination of quantities by operations with numbers.*

James C. Maxwell

Chapter 4 described an OFDM system design over wideband time-varying channels. It indicated the increased complexity of the receiver design compared to a narrowband OFDM system which was the focus of Chapter 3. In this chapter, we propose new transmission schemes instead of OFDM with the purpose of obtaining a simplified receiver scheme similarly as experienced by the narrowband OFDM transmissions. The benefit of this similarity is to make existing low-complexity equalizers, previously used in narrowband systems, still viable for wideband communications.

### 5.1 Introduction

As shown in the previous chapters, wideband linear time-varying (LTV) channels exhibit some key fundamental differences [15] relative to the more commonly considered narrowband channels. Though a standard signaling scheme is proposed for wideband channels based on orthogonal frequency division multiplexing (OFDM) in the last chapter, the intercarrier interference (ICI) of OFDM systems due to wideband time-variation is generally cumbersome. It is thus expected that certain novel transceiver scheme can be designed such that low-complexity equalizers widely adopted for narrowband LTV systems (e.g., as considered in Chapter 3) can still be allowed for wideband LTV communications.

The success of OFDM over narrowband channels is that its transmission admits a uniform sampling in the lag and Doppler shift domain, which

aligns with the uniform time-frequency (T-F) lattice of narrowband time-varying channels. In contrast, the wideband channel is characterized by a non-uniform T-F lattice [22, 28, 30]. To counteract this mismatch, a multi-band OFDM scheme is proposed in [72], wherein the wideband LTV channel is split into sub-channels with a sufficiently small bandwidth such that each of the sub-channels can be modeled as a narrowband LTV channel. Other often adopted approaches are based on a *single-scale multi-lag* (SSML) assumption for wideband LTV channels (see e.g., [28, 30, 81]). Such a SSML channel can be converted to a narrowband channel subject to a single carrier frequency offset (CFO) by means of resampling. However, we observe that this assumption is suboptimal in the presence of multiple scales [29, 76]. In this chapter, we consider MSML models appropriate for wideband LTV channels, signaling tailored to this model, and equalizers for this joint design of a channel model and signaling scheme.

The concept of an MSML model has been previously presented in [21, 22, 33]. These works exploit the transmission of a *single pulse/symbol in isolation*, develop the MSML model, and typically consider the associated matched-filter for the demodulation of this single pulse/symbol. In particular, in [21], information symbols are modulated onto a single-scale orthogonal wavelet-based pulse at the transmitter, and the channel is mathematically described by a discretized time-scale model based on the characteristics of the adopted wavelet. A crucial assumption adopted in [21] is that the time-scale channel model should not corrupt the scale-orthogonality of the transmit pulse, but it is not clear under which conditions this assumption remains valid. As an improvement, [33] combines direct-sequence spread-spectrum (DSSS) modulation with a wavelet-based pulse to enforce the scale-orthogonality of the transmit pulse. Common to these works is that both channel modeling and signaling is assumed to occur in baseband, but on the other hand, a special (wavelet-based) pulse is employed that has a bandpass property. In our own work [82], we consider a much more general system, where we use a low-pass pulse, which is up-converted to a carrier frequency before transmission over an MSML channel. The challenge is that, at the receiver the passband to baseband conversion must be carefully treated in MSML channels.

A unique feature of the MSML channel is that one can increase the spec-

tral efficiency by communicating simultaneously over multiple scales ([21, 22, 33, 82] employ single-scale signaling); for clarity, we shall refer to such signaling as multi-layered. In fact, multi-layered signaling for narrowband channels has been considered in [53] with variants of such orthogonal wavelet division multiplexing provided in [56, 58, 83, 84], and it is already known [58, 84] that such a multi-layered transmission scheme based on a wavelet modulation can achieve the same spectral efficiency as that of a traditional method, *e.g.*, OFDM. A challenge with these signaling schemes is that wavelet orthogonality is not maintained after transmission over the MSML channel. In [85], we designed a multi-layer signal for MSML channels. The resulting channel was banded in nature, allowing for the use of low-complexity equalizers for banded narrowband channels [2, 3, 5]. However, it is not clear how to adapt the all-baseband processing scheme in [85] to a passband transmission. In the current work, we endeavor to fill this gap.

The main contributions of this work are 1) a novel parameterization of the continuous MSML passband channel; we show that the associated discrete baseband data model is subject to inter-scale interference without proper transmit signal design; 2) proposing a transmit and receive pulse design which aims to eliminate this inter-scale interference and induces a multi-branch receiver structure which can leverage channel diversity; 3) a multi-layer signal design matched to the parameterized channel model which increases spectral efficiency; 4) a new block transmission scheme with a novel guard interval to eliminate inter-block interference, enabling the use of low-complexity equalizers due to the resulting signal structure.

## 5.2 Wideband LTV Systems

Let us consider a wideband LTV system in (2.7) as

$$\bar{r}(t) = \int_0^{\tau_{\max}} \int_1^{\alpha_{\max}} \bar{h}(\alpha, \tau) \sqrt{\alpha} \bar{s}(\alpha(t - \tau)) d\alpha d\tau + \bar{w}(t), \quad (5.1)$$

where  $\bar{s}(t)$  and  $\bar{r}(t)$  are respectively the actual transmitted and received signal (normally in passband),  $\bar{h}(\alpha, \tau)$  is known as the wideband spreading function [20]  $\bar{w}(t)$  stands for the additive noise, which is assumed to be a

white Gaussian process with mean zero and variance  $\sigma^2$ . Additionally, we assume that  $\tau$  and  $\alpha$  are limited to  $\tau \in [0, \tau_{\max}]$  and  $\alpha \in [1, \alpha_{\max}]$  due to physical restrictions, where the parameters  $\tau_{\max} > 0$  and  $\alpha_{\max} > 1$ <sup>1</sup> represent the *maximal delay spread* and *maximal scale spread*, respectively. Further, the transmitted signal considered in this chapter is assumed to be a passband signal with carrier frequency  $f_c$  and effective bandwidth  $W_*$ , and therefore

$$\bar{s}(t) = \Re\{s(t)e^{j2\pi f_c t}\}, \quad (5.2)$$

where  $s(t)$  denotes the baseband counterpart of  $\bar{s}(t)$ , which is hence band-limited within  $[-\frac{W_*}{2}, \frac{W_*}{2}]$ . We note that in this chapter, we will use the notations with and without “-” for the signal in the passband and in the baseband, respectively, unless explicitly defined. For instance,  $\bar{r}(t)$  and  $\bar{s}(t)$  are always referred to the transmitted and received signal in passband, respectively, while  $r(t)$  and  $s(t)$  are their corresponding complex baseband equivalent.

In the remainder of the section, we will first seek a parameterized representation for the I/O relationship in (5.1) in passband, and then try to derive a discrete data model in baseband. To derive a discrete baseband data model, one may follow from (2.9) to (2.13) in Chapter 2 (see [21, 22] for more details of this method), which is performed based on a single central frequency at the receiver. However, such a baseband discrete data model is always subject to multiple central frequency offsets (CFO) [c.f. (2.13)], which is different to handle. In fact, due to the scaling effect, the original signal can have several differently scaled versions simultaneously at the receiver, each having a disparate effective carrier frequency deviating from  $f_c$  as well as a distinct bandwidth. In this chapter, we shall propose a novel method for deriving its parameterized data model by taking the passband nature of the transmitted signal into account when discretizing the channel as follows.

---

<sup>1</sup>As a matter of fact, the case of dilation with  $\alpha_{\max} < 1$  can be converted to a case of compression by means of proper resampling at the receiver. This justifies us to simply consider a compressive scenario without loss of generality.

### 5.2.1 Parameterized Passband Data Model

Our first step is to parameterize the continuous channel  $\bar{h}(\alpha, \tau)$  in (5.1) along the scale dimension. This can be achieved by employing the results of [21], giving rise to the following approximation

$$\bar{r}(t) \approx \bar{r}^S(t) = \sum_{r=0}^{R_\star} \int_0^{\tau_{\max}} \bar{h}_r(\tau) a_\star^{r/2} \bar{s}(a_\star^r(t - \tau)) d\tau, \quad (5.3)$$

where  $a_\star$  is referred to as the *basic scaling factor* in [21], or *dilation spacing* in [22, 33], whose physical interpretation will be discussed in detail in the Remark 5.1; in particular, according to [21],  $R_\star = \lceil \ln \alpha_{\max} / \ln a_\star \rceil$  and

$$\bar{h}_r(\tau) = \int_{-\infty}^{\infty} \bar{h}(\alpha', \tau) \text{sinc} \left( \frac{\ln a_\star^r - \ln \alpha'}{\ln a_\star} \right) d\alpha', \quad (5.4)$$

represents the scale-smoothed version of  $\bar{h}(\alpha, \tau)$  that is evaluated at the scale  $a_\star^r$ .

Note that in (5.3), we have used a superscript “S” to underscore that so far only the scale parameter is discretized (later, the superscript “L” will refer to lag discretization, and superscript “SL” for joint scale and lag discretization). In light of the finite summation in (5.3), we can interpret  $\bar{r}^S(t)$  resulting from a *time-invariant* multiple-input single-output (MISO) system, where the signal transmitted via the  $r$ th virtual channel is  $a_\star^{r/2} \bar{s}(a_\star^r t)$ ; the effective associated channel is  $\bar{h}_r(t)$ , and the  $r$ th component of the received signal can be denoted as

$$\bar{r}_r^S(t) = \int_0^{\tau_{\max}} \bar{h}_r(\tau) a_\star^{r/2} \bar{s}(a_\star^r(t - \tau)) d\tau. \quad (5.5)$$

Equation (5.3) represents a passband data signal, and our objective is eventually to establish a baseband model. Towards this end, we first find an expression for the  $r$ th component of the signal in terms of its baseband counterpart of the transmit signal  $a_\star^{r/2} \bar{s}(a_\star^r t) = \Re\{a_\star^{r/2} s(a_\star^r t) e^{j2\pi a_\star^r f_c t}\}$ . It is clear from this expression that the baseband signal  $a_\star^{r/2} s(a_\star^r t)$  is up-converted to an effective carrier frequency  $a_\star^r f_c$  and has an effective bandwidth  $a_\star^r W_\star$ . Accordingly, we can also obtain the baseband version for  $\bar{r}_r^S(t)$  by observing

that

$$\begin{aligned}
\bar{r}_r^S(t) &= \int_0^{\tau_{\max}} \bar{h}_r(\tau) a_\star^{r/2} \Re \left\{ s(a_\star^r(t - \tau)) e^{j2\pi f_c a_\star^r(t - \tau)} \right\} d\tau, \\
&= \Re \left\{ e^{j2\pi f_c a_\star^r t} \int_0^{\tau_{\max}} \left( \bar{h}_r(\tau) e^{-j2\pi f_c a_\star^r \tau} \right) a_\star^{r/2} s(a_\star^r(t - \tau)) d\tau \right\}, \\
&= \Re \left\{ e^{j2\pi f_c a_\star^r t} \int_0^{\tau_{\max}} h_r(\tau) a_\star^{r/2} s(a_\star^r(t - \tau)) d\tau \right\}, \tag{5.6}
\end{aligned}$$

where we have introduced the notation  $h_r(t)$  in the last equality to represent

$$h_r(t) = \bar{h}_r(t) e^{-j2\pi f_c a_\star^r t}, \tag{5.7}$$

which can be interpreted as the continuous baseband channel for the  $r$ th component signal. Let  $r_r^S(t)$  represent the baseband counterpart of  $\bar{r}_r^S(t)$ , i.e.,

$$\bar{r}_r^S(t) = \Re \{ r_r^S(t) e^{j2\pi f_c a_\star^r t} \}.$$

From (5.6), it then follows that

$$r_r^S(t) = \int_0^{\tau_{\max}} h_r(\tau) a_\star^{r/2} s(a_\star^r(t - \tau)) d\tau. \tag{5.8}$$

Now, we are able to exploit the results of [21] again to seek a discrete approximation of  $h_r(t)$  in (5.7). Due to the fact that the  $r$ th scaled version  $s(a_\star^r t)$  is band-limited to  $a_\star^r W_\star$ , we can approximate (5.8) as

$$r_r^S(t) \approx r_r^{\text{SL}}(t) = \sum_{l=0}^{L_\star(r)} h_{r,l} a_\star^{r/2} s(a_\star^r t - lT_\star), \tag{5.9}$$

where  $T_\star$  is referred to as the *translation spacing* in [22, 33], and  $L_\star(r) = \lceil a_\star^r \tau_{\max} / T_\star \rceil$  denotes the number of channel taps, which is clearly dependent on the component index  $r$ ; further,

$$h_{r,l} = h_r^L(lT_\star / a_\star^r), \tag{5.10}$$

with  $h_r^L(\tau)$  being the lag-smoothed version of  $h_r(\tau)$ :

$$h_r^L(\tau) = \int_0^{\tau_{\max}} h_r(\tau') \text{sinc} \left( a_\star^r \frac{\tau - \tau'}{T_\star} \right) d\tau'. \tag{5.11}$$



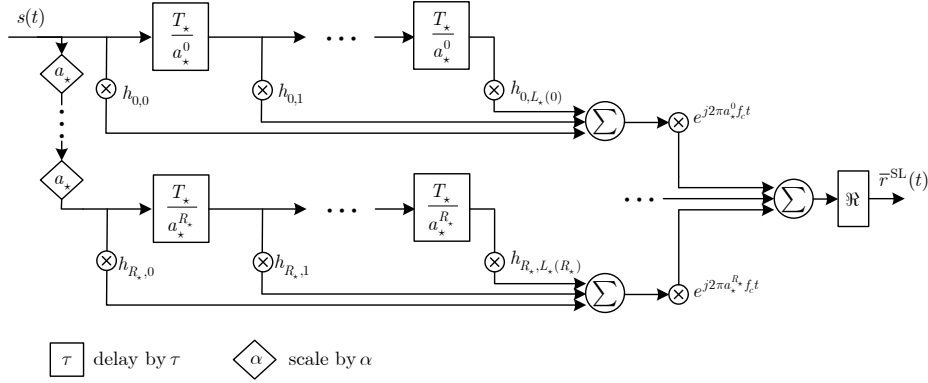


**Figure 5.1:** A parameterized passband data model

Substituting (5.9) into (5.3) yields

$$\begin{aligned} \bar{r}^{SL}(t) &= \Re \left\{ \sum_{r=0}^{R_*} e^{j2\pi f_c a_*^r t} r_r^{SL}(t) \right\} \\ &= \Re \left\{ \sum_{r=0}^{R_*} e^{j2\pi f_c a_*^r t} \sum_{l=0}^{L_*(r)} h_{r,l} a_*^{r/2} s(a_*^r t - lT_*) \right\}, \end{aligned} \quad (5.12)$$

where the continuous channel  $\bar{h}(\alpha, \tau)$  in passband is expressed in terms of the baseband channel parameters  $h_{r,l}$  that are discretized in both the scale and lag dimension. Combining (5.4) and (5.11), we obtain

$$h_{r,l} = \int_0^{\tau_{\max}} \int_1^{\alpha_{\max}} \bar{h}(\alpha, \tau) e^{-j2\pi f_c a_*^r \tau} \operatorname{sinc} \left( r - \frac{\ln \alpha}{\ln a_*} \right) \operatorname{sinc} \left( l - \frac{a_*^r \tau}{T_*} \right) d\alpha d\tau. \quad (5.13)$$

A schematic overview of the passband model in (5.12) is given in Fig. 5.1.

*Remark 5.1.* In the above data model, the continuous channel is approximated by a finite number of discrete channel coefficients, which inevitably induces an approximation error. To enable a good fit, it is desired that the scale and lag resolution should be as high as possible. These resolutions are determined, respectively, by the *dilation spacing*  $a_*$  and the *translation spacing*  $T_*$ . On the other hand, too high of a resolution will give rise to a channel

model with a large order, which is undesirable from a receiver design point of view.

In practice, one approach to seek a proper  $a_*$  is linked to the wideband ambiguity function (WAF) of  $\bar{s}(t)$  in the passband [22,33]:

$$\bar{\chi}(\alpha, \tau) = \int \bar{s}(t) \sqrt{\alpha} \bar{s}(\alpha(t - \tau)) dt; \quad (5.14)$$

similarly,  $T_*$  is linked to the WAF of  $s(t)$  in baseband

$$\chi(\alpha, \tau) = \int s(t) \sqrt{\alpha} s(\alpha(t - \tau)) dt. \quad (5.15)$$

Under the assumption that  $\bar{\chi}(\alpha, \tau)$  decays rapidly in the scale dimension,  $a_*$  is defined as the first zero-crossing of  $\bar{\chi}(\alpha, 0)$ . Likewise, under the assumption that  $\chi(\alpha, \tau)$  decays rapidly in the lag dimension,  $T_*$  is defined as the first zero-crossing of  $\chi(1, \tau)$ . An alternative approach [21] assumes that  $\bar{s}(t)$  has a limited effective bandwidth  $W_*$  and Mellin support  $M_*^2$ . It is well-known that in the Fourier domain the Nyquist sampling theorem dictates that  $T_* = 1/W_*$  to ensure perfect signal reconstruction. We can apply an adapted Nyquist sampling result in the Mellin domain to obtain  $a_* = e^{1/M_*}$ .

That these two approaches render a good approximation is derived and motivated in [22,33] and [21], respectively. We will show, in a subsequent numerical example, that these two approaches produce similar values of  $T_*$  and  $a_*$ . The first approach is easier to use, but relies on the rapid decay assumption of the WAFs. In this sense, the second approach is more robust.

## 5.2.2 Related Works

A comparison between the parameterization of wideband LTV channels and that of narrowband LTV channels (see for the latter e.g., [10,36]) has been thoroughly treated in [21,22] and also discussed in Chapter 2. Here, we

---

<sup>2</sup>The Mellin support is the scale analogy of the Doppler spread for narrowband LTV channels. Specifically, the Mellin support of a signal  $\bar{s}(t)$  is the support of the Mellin transform of  $\bar{s}(t)$  which is given by  $\int_0^\infty \bar{s}(t) t^{x-1} dt$ . More details about the Mellin transform can be found in [34,35], and we will give in Appendix 5.C a numerical example to show how the Mellin transform can be implemented.

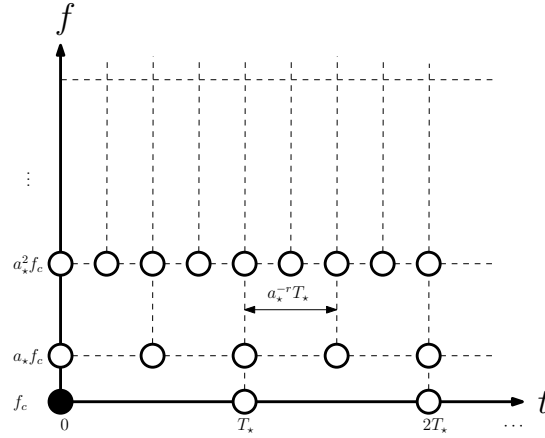
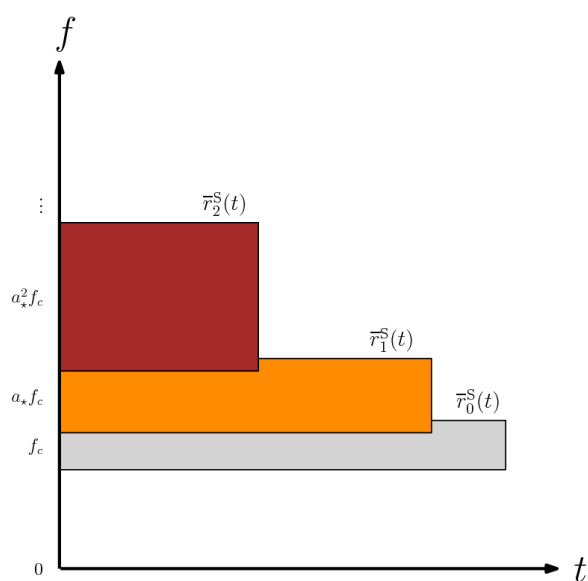


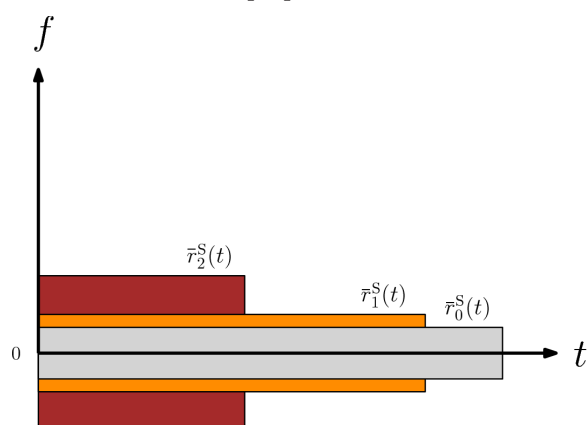
**Figure 5.2:** Time-frequency (T-F) tile diagram of the proposed discretized channel model for Wideband LTV channels

just recall the fact that the parameterized narrowband LTV channel is arithmetically uniform in both the lag (time) and frequency dimension, while the parameterized wideband LTV channel is arithmetically uniform in the lag (time) dimension but geometrically uniform in the scale (frequency) dimension, resulting in a different T-F tiling diagram.

Compared to the wideband scale-lag canonical models in [21, 22, 33], in the derivation towards our channel model, we first parameterize the channel in the scale dimension in passband, and then convert the channel to baseband where it is further parameterized in the lag dimension. Such a conversion between passband and baseband is not taken into account by [21, 22, 33] in the parameterization process. We use Fig. 5.2 to describe our parameterization process. The circles in this figure indicate the positions where the channel is sampled in the time-frequency (T-F) plane. In the figure, we assume a single symbol is transmitted at time 0 and carrier frequency  $f_c$ , whose location is represented by a dark circle, while the open circles show the locations of signal leakage. It is clear that the lags are parameterized using the baseband parameter  $T_*$ . For comparison, the method used in [21, 22, 33] does not consider a passband-to-baseband conversion, and thus leads to the T-F plane as shown in Fig. 2.2, where a passband parameter  $\bar{T}_*$  is adopted. Although these two figures show a minor difference with regards to the lags,



In the proposed model



In the model of [21]

**Figure 5.3:** *Decomposition of the received signal*

their detailed derivations are fundamentally different as described above. More important, our model also indicates that the wideband LTV channel has a distinct behavior with regards to the parameterization process compared with its narrowband counterpart. Specifically, the parameterized nar-

rowband LTV channel is arithmetically uniform in both the lag (time) and frequency dimension, while the parameterized wideband LTV channel is arithmetically uniform in the lag (time) dimension but geometrically uniform in the scale (frequency) dimension [c.f. Fig. 5.2 vs. Fig. 2.2].

The key of the parameterization process for the channel lies in the choice of the transmit (and receive) pulse denoted as  $p(t)$ . This chapter follows the convention of most communication systems by assuming a general low-pass waveform for  $p(t)$ . To make it suitable for transmission,  $p(t)$  is converted to passband by multiplying it with  $e^{j2\pi f_c t}$  prior to transmission. In comparison, [21] uses a Haar wavelet and [33] uses a second-order derivative passband Gaussian chip (a Ricker wavelet) for  $p(t)$ , which are bandpass signals in nature. The pulse  $p(t)$  can therefore be directly transmitted without an extra step of conversion to passband. The transmit pulse and the data model in this chapter will have a more general application than those in [21, 33].

In light of our MISO view, each component of the received signal in our model, denoted as  $\bar{r}_r^S(t)$  in (5.3), can be represented in the T-F plane by a block centered around a distinctive carrier frequency  $a_*^r f_c$  as illustrated in Fig. 5.3. Because there lacks an explicit conversion between passband and baseband, the data models in [21, 33] are, strictly speaking, derived in baseband for a general definition of  $p(t)$ . Therefore, the T-F representation of the received signal in [21, 33] is depicted by Fig. 5.3, where each component,  $\bar{r}_r^S(t)$ , is represented by a block around DC in a nested manner.

### 5.2.3 Parameterized Baseband Data Model

The passband signal model (5.12) clearly establishes the challenges of deriving a baseband signal representation. As shown in Fig. 5.3, each component of the received signal,  $\bar{r}_r^S(t)$ , is characterized by a unique carrier frequency  $a_*^r f_c$ . There exists no universal carrier frequency for down-conversion of all the components. Similarly, since each component of the received signal has a distinct bandwidth  $a_*^r W_*$ , which is dependent on the component index  $r$ , this invites the question of which sampling rate we should adopt to discretize the received signal<sup>3</sup>.

<sup>3</sup>We notice that a similar problem (finding an optimal single sampling rate) is considered in [29].

In particular, suppose we let the receiver be synchronized with the  $k$ th component of the received signal. After down-conversion, the resulting baseband signal can be expressed as

$$\begin{aligned} z_k^{\text{SL}}(t) &= \bar{r}^{\text{SL}}(t) e^{-j2\pi f_c a_*^k t} \\ &= \sum_{l=0}^{L_*(k)} h_{k,l} a_*^{k/2} s(a_*^k t - lT_*) \\ &\quad + \sum_{r=0, r \neq k}^{R_*} e^{j2\pi f_c (a_*^r - a_*^k) t} \sum_{l=0}^{L_*(r)} h_{r,l} a_*^{r/2} s(a_*^r t - lT_*). \end{aligned} \quad (5.16)$$

For this baseband signal, if we choose a sampling period  $T_*/a_*^k$  for discretization, it is only optimal for the  $k$ th component (the first summand above). In addition, the other channel coefficients  $h_{r,l}$ , for  $r \neq k$ , are obtained by sampling the channel in the lag domain with  $T_*/a_*^r$  rather than  $T_*/a_*^k$  [c.f. (5.13)]. This means that once the signal in (5.16) is discretized, the resulting discrete baseband model will be subject to a nuisance embedded in the second term on its right-hand side, which will inevitably give rise to a performance penalty on a practical receiver.

In this chapter, we will tackle the above problem through the design of the transmit and receive pulse. As will become evident soon, if the transmit and receive pulse can smartly be designed, we are able to annihilate the nuisance from the discrete baseband model.

### 5.3 Transmit Signal Design

Prior to proceeding, we first assume that there exists a real pulse  $p(t)$  of unit energy that is strictly band-limited with baseband bandwidth  $W_*$ . In other words, if  $P(f)$  denotes the Fourier transform of  $p(t)$ , then  $P(f)$  has non-zero elements only within  $[-W_*/2, W_*/2]$ .

For a pulse  $p(t)$ , we denote its scaled version as

$$p_{k'}(t) = a^{k'/2} p(a^{k'} t), \quad (5.17)$$

where  $a$  is referred to as the *base scale*. The effective bandwidth of  $p_{k'}(t)$  equals  $a^{k'} W_*$ . If we use  $p_{k'}(t)$  as a transmit pulse to modulate symbols  $s_{k',n}$ ,

then the baseband transmit signal  $s_{k'}(t)$  can be written as

$$s_{k'}(t) = \sum_n s_{k',n} p_{k'}(t - nT/a^{k'}), \quad (5.18)$$

where  $T$  is referred to as the *base lag*. The above expression suggests that  $s_{k'}(t)$  has symbol period  $T/a^{k'}$ . The value of  $a$  and  $T$  will be soon determined in Section 5.3.1.

For the sake of clarity, we first derive a *single-layer* signaling scheme, where a single-rate pulse  $p_{k'}(t)$  is used to modulate the transmit symbols, and then generalize it to a *multi-layer* signaling scheme.

### 5.3.1 Single-Layer Signaling

In the *single-layer* signaling scheme, the transmit signal is  $s_{k'}(t)$ , which is next up-converted to the carrier frequency  $a^{k'} f_c$  resulting in the passband signal

$$\bar{s}_{k'}(t) = \Re\{s_{k'}(t)e^{j2\pi a^{k'} f_c t}\}.$$

A critical element of our design is the assumption that we can properly match the scales and delays of our signaling to that of the channel. This boils down to matching the parameters as follows:

$$a = a_*, \text{ and } T = a^{k'} T_*, \quad (5.19)$$

which corresponds to a Nyquist sampling scheme using  $a$  and  $T$  in the Mellin domain and in the Fourier domain, respectively, for the received signal on the  $k'$ th layer (see [21] for more details). Note that the above requirements are not always easy to satisfy because  $a_*$  and  $T_*$  themselves are in turn determined by  $p_{k'}(t)$ . We will return to this issue in Section 5.3.2, but for now assume that (5.19) is perfectly achieved.

At the receiver, we down-convert the received signal using a center frequency  $a^k f_c$  (note that  $k$  is not necessarily equal to  $k'$ ). After down-conversion,

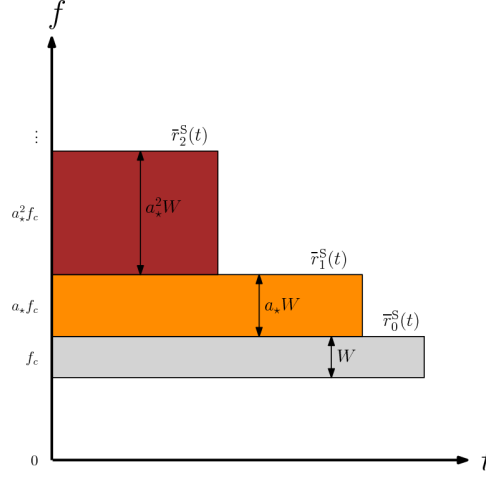


**Figure 5.4:** Components of the received signal are non-overlapping in the frequency domain thanks to Theorem 5.1

the baseband representation given by (5.16) can be rewritten as

$$\begin{aligned}
 z_{k,k'}^{\text{SL}}(t) &= \sum_{r=0}^{R_{k'}} e^{j2\pi f_c(a^{k'+r}-a^k)t} \sum_{l=0}^{L_{k'}(r)} h_{r,l}^{(k')} a^{r/2} s_{k'}(a^r t - lT/a^{k'}) \\
 &= \sum_{r=0}^{R_{k'}} \delta_{k-r-k'} \sum_{l=0}^{L(k'+r)} h_{r,l}^{(k')} a^{r/2} s_{k'}(a^r t - lT/a^{k'}) \\
 &+ \underbrace{\sum_{r=0, r \neq k-k'}^{R_{k'}} e^{j2\pi f_c(a^{k'+r}-a^k)t} \sum_{l=0}^{L(k'+r)} h_{r,l}^{(k')} a^{r/2} s_{k'}(a^r t - lT/a^{k'})}_{C_{r+k'}(t): \text{CROSSTALK}}. \quad (5.20)
 \end{aligned}$$

Comparing (5.20) to (5.16), we have added  $k'$  in the subscript of  $z_{k,k'}^{\text{SL}}(t)$  to emphasize the dependence of this signal on the specific carrier frequency,  $a^{k'} f_c$ , used for up-conversion. Later, we will see that in a multi-layer signaling scheme,  $k'$  represents the  $k'$ th transmission layer. In (5.20), the number of scales  $R_{k'}$  is equal to

$$R_{k'} = \lceil \ln \alpha_{\max} / \ln a \rceil \equiv R. \quad (5.21)$$



Because  $R_{k'}$  is independent of  $k'$ , we will drop this subscript in the sequel for the sake of notational ease. The number of lags  $L_{k'}(r)$  in (5.20) is determined by

$$L_{k'}(r) = \lceil a^{r+k'} \tau_{max}/T \rceil = L(r + k'), \quad (5.22)$$

with  $L(r) = \lceil a^r \tau_{max}/T \rceil$ ;  $h_{r,l}^{(k')}$  is similarly defined as in (5.13), but taking (5.19) into account:

$$\begin{aligned} h_{r,l}^{(k')} &= \int_0^{\tau_{max}} \int_1^{\alpha_{max}} \bar{h}(\alpha, \tau) e^{-j2\pi f_c a^{k'+r} \tau} \\ &\quad \times \text{sinc} \left( r - \frac{\ln \alpha}{\ln a} \right) \text{sinc} \left( l - \frac{a^{k'+r} \tau}{T} \right) d\alpha d\tau. \end{aligned} \quad (5.23)$$

We next seek to nullify the crosstalk term in (5.20) by taking the following steps. We first deploy a receive filter  $p_k(t)$  on  $z_{k,k'}^{SL}(t)$ , and then discretize the resulting signal by sampling at rate  $T/a^k$ . The resulting sample obtained at the  $m$ th sampling instant, denoted as  $y_{k,k',m}$ , can be expressed as

$$\begin{aligned} y_{k,k',m} &= p_k^*(-t) \otimes z_{k,k'}^{SL}(t)|_{t=mT/a^k} \\ &= \int p_k \left( t - \frac{mT}{a^k} \right) z_{k,k'}^{SL}(t) dt \end{aligned} \quad (5.24)$$

$$\begin{aligned} &= \int p_k \left( t - \frac{mT}{a^k} \right) \sum_{r=0}^R \delta_{k-r-k'} \sum_{l=0}^{L(k)} h_{r,l}^{(k-r)} a^{r/2} s_{k-r}(a^r t - lT_{k-r}) dt \\ &+ \int p_k \left( t - \frac{mT}{a^k} \right) \sum_{r=0, r \neq k-k'}^R C_{r+k'}(t) dt. \end{aligned} \quad (5.25)$$

The following theorem will be useful to the ensuing derivations (see Appendix 5.A for a proof).

*Theorem 5.1.* If the base scale  $a$  satisfies both (5.19) and

$$a \geq \frac{2f_c + W_\star}{2f_c - W_\star}, \quad (5.26)$$

then

$$\int_{-\infty}^{\infty} \sqrt{a^k a^{k'}} p(a^k t - mT) e^{j2\pi f_c a^{k'} t} p(a^{k'} t - nT) e^{-j2\pi f_c a^{k'} t} dt = \delta_{k-k'} g_{n-m}, \quad (5.27)$$

where

$$g_n = \int p(t)p(t - nT)dt. \quad (5.28)$$

With the aid of Theorem 5.1, we are able to eliminate the crosstalk term in (5.20) since (see Appendix 5.B for a proof)

$$\int p_k \left( t - \frac{mT}{a^k} \right) \sum_{r=0, r \neq k-k'}^R C_{r+k'}(t) dt = 0. \quad (5.29)$$

As a result of (5.29), we can simplify (5.25) to

$$\begin{aligned} y_{k,k',m} &= \sum_{r=0}^R \delta_{k-r-k'} \int p_k \left( t - \frac{mT}{a^k} \right) \sum_n s_{k-r,n} \sum_{l=0}^{L(k)} h_{r,l}^{(k-r)} a^{k/2} p \left( a^k t - (n+l)T \right) dt \\ &= \sum_{r=0}^R \delta_{k-r-k'} \sum_n s_{k-r,n} \sum_{l=0}^{L(k)} h_{r,l}^{(k-r)} \int a^k p \left( a^k t - (n+l)T \right) p(a^k t - mT) dt \\ &= \sum_{r=0}^R \delta_{k-r-k'} \sum_n s_{k-r,n} \sum_{l=0}^{L(k)} h_{r,l}^{(k-r)} g_{m-n-l} \end{aligned} \quad (5.30)$$

where  $g_{m-n-l}$  in the last equality is defined in (5.28).

To avoid information loss, we will repeat the above operations for  $k = 0, \dots, K-1$  with  $K \geq R+1$  in the single-layer transmission. This means that a multi-branch structure is imposed on the receiver, where each branch is aimed at processing one component of the received signal. Such a receiver structure is schematically depicted in Fig. 5.5. In Section 5.4, we will show how to combine the results from each branch optimally to estimate the data symbols.

*Remark 5.2.* As mentioned earlier, corresponding to the parameterized channel model, we have effectively decomposed the received signal into several components, each one occupying a different position in the frequency domain. As a matter of fact, Theorem 5.1 ensures that these components will not be overlapping with each other. This idea is suggested by Fig. 5.4, where the equality in (5.27) is assumed. Accordingly, the receive filter  $p_k(t)$  serves as a low-pass filter eliminating the crosstalk term.

In comparison, the components of the received signal in [21,33] are nested within each other in the frequency domain [see Fig. 5.3]. To eliminate the

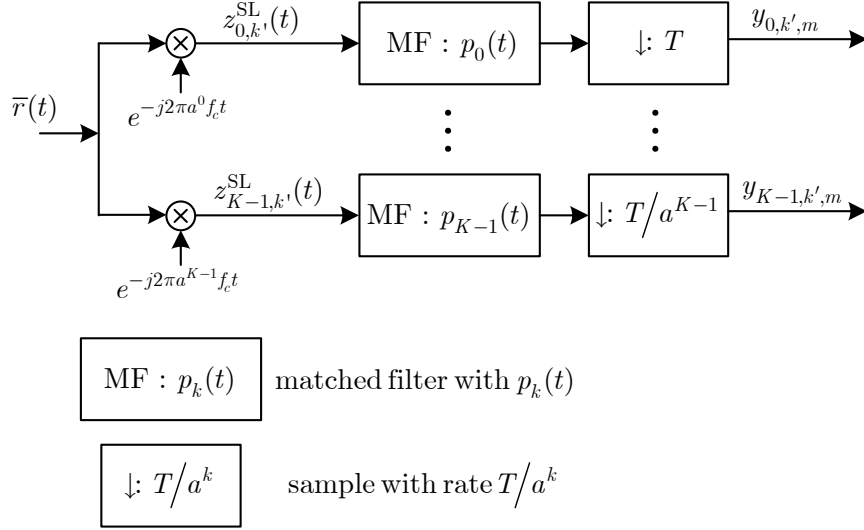


Figure 5.5: The proposed receiver architecture with  $K$  receive branches

crosstalk term, [21, 33] resort to the scale-orthogonality of the transmit waveform, i.e.,

$$\int p_k(t)p_{k'}(t)dt = \delta_{k-k'}. \quad (5.31)$$

It is not specified by [21] how to guarantee the above equality. A more solid treatment is given by [33], which, however, relies on a particular direct-sequence spread-spectrum construction of the signal.

### 5.3.2 Pulse Design

In this subsection, we give a heuristic illustration of the design of the pulse  $p(t)$ . Without loss of generality, we consider the case of  $k' = 0$ , for which the transmit pulse in passband admits an expression of  $p(t)e^{j2\pi f_c t}$ . Usually, the carrier frequency  $f_c$  is a system parameter, and therefore our design freedom is the pulse type and its effective bandwidth  $W_\star$ .

For a given pulse type, once we have chosen a certain bandwidth  $W_\star$  for the baseband pulse  $p(t)$ , resulting in its passband pulse  $\Re\{p(t)e^{j2\pi f_c t}\}$ , the *dilation spacing*  $a_\star$  and *translation spacing*  $T_\star$  are accordingly determined (see

Remark 5.1 for more details). Then, matching these parameters with the *base scale*  $a$  and *base lag*  $T$  of the transmit signal means that  $a = a_*$  and  $T = T_*$  [c.f. (5.19)]. We next determine whether the resulting  $a$  satisfies (5.26) in Theorem 5.1. If so, the design is complete. Otherwise, one should select a different bandwidth for the pulse or even a different pulse type to repeat the above steps.

Here, we give a specific example of  $p(t)$ , which is a sinc function defined as

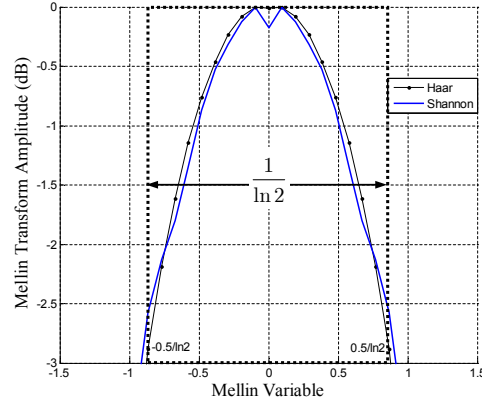
$$p(t) = W^{1/2} \text{sinc}(Wt), \quad (5.32)$$

whose effective bandwidth is exactly  $W_* = W$ . It is known that  $\Re\{p(t)e^{j2\pi f_c t}\}$  belongs to the Shannon wavelets [86] if we choose  $W = \frac{2}{3}f_c$  in (5.32), and in this case a *dilation spacing* of  $a_* = 2$  is yielded. This is corroborated by Fig. 5.6 and Fig. 5.6, which depicts the results based on a Mellin approach and a WAF approach, respectively. Additionally, the corresponding *translation spacing* is given by  $T_* = 1/W_* = 1/W$ . For the parameter matching, we have  $a = a_*$  and  $T = T_*$ . In this case,  $a = 2$  and  $W_* = W = \frac{2}{3}f_c$  satisfy the equality of (5.26). In this manner, this specific example is a suitable pulse design.

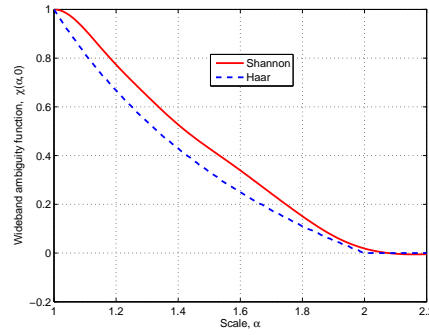
As a comparison, we note that the Haar wavelet used in [21] as the pass-band pulse, for which  $p(t)$  corresponds to a rectangular function, is not a suitable pulse design for our purposes. Although it gives the same  $a_* = 2$  as shown in Fig. 5.6, it has a much larger effective bandwidth than the Shannon wavelet due to the spectrum leakage as shown in Fig. 5.7. As a result, after parameter matching, the (in)equality in (5.26) cannot hold, which implies that the cross-talk in (5.20) is non-negligible. This effect is further studied in more details in Section 5.6.

Another interesting consequence of using a Shannon wavelet is that the resulting sampled correlation function  $g_n$  defined in (5.28) is

$$g_n = W_* \int \text{sinc}(W_* t) \text{sinc}(W_* t - n) dt = \text{sinc}(n) = \delta_n. \quad (5.33)$$



Mellin support



Wideband ambiguity function

**Figure 5.6:** Two approaches for solving  $a$ 

As a result, we are able to simplify (5.30) further to

$$\begin{aligned}
 y_{k,k',m} &= \sum_{r=0}^R \delta_{k-r-k'} \sum_n s_{k-r,n} \sum_{l=0}^{L(k)} h_{r,l}^{(k-r)} \delta(m-n-l) \\
 &= \sum_{r=0}^R \delta_{k-r-k'} \sum_{l=0}^{L(k)} h_{r,l}^{(k-r)} s_{k-r,m-l},
 \end{aligned} \tag{5.34}$$

which enables the design of a low-complexity equalizer in the sequel.

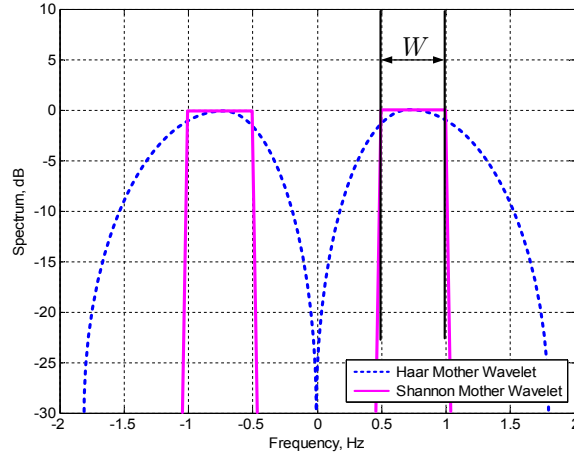


Figure 5.7: Spectrum of the Haar and Shannon mother wavelets

### 5.3.3 Multi-Layer Signaling

Recall that in OFDM, the maximum spectral efficiency can be achieved by partitioning the available bandwidth into several orthogonal sub-bands. Analogously, we can also design a multi-layer transmission scheme, where in the  $k'$ th layer, the transmit data symbols are modulated by a different pulse  $p_{k'}(t)$ , and up-converted to a carrier frequency  $a^{k'} f_c$  for  $k' = 0, \dots, K' - 1$ . Thanks to Theorem 5.1, the sub-bands occupied by each layer will not overlap with each other. When the (in)equality in (5.26) holds, these sub-bands will be contiguous, resulting in a maximum spectral efficiency. In contrast to OFDM, the sub-bands have unequal bandwidth. The proof of the above ideas is rather trivial by straightforwardly applying Theorem 5.1. Here, we can just reuse Fig. 5.4 to illustrate the idea schematically.

With multiple layers, the actually transmitted signal  $\bar{x}(t)$  in passband can

be expressed as

$$\begin{aligned}\bar{x}(t) &= \sum_{k'=0}^{K'-1} \bar{x}_{k'}(t) \\ &= \sum_{k'=0}^{K'-1} \sum_n \Re\{a^{k'/2} s_{k',n} p(a^{k'}t - nT) e^{j2\pi f_c a^{k'}t}\}. \end{aligned} \quad (5.35)$$

Accordingly, at the  $k$ th receive branch, the resulting sample obtained at the  $m$ th time-instant, denoted as  $y_{k,m}$ , is just a superposition of  $y_{k,k',m}$  derived in (5.34) for  $k' = 0, \dots, K' - 1$ , i.e.,

$$\begin{aligned}y_{k,m} &= \sum_{k'=0}^{K'-1} y_{k,k',m} \\ &= \sum_{k'=0}^{K'-1} \sum_{r=0}^R \delta_{k-r-k'} \sum_{l=0}^{L(k)} h_{r,l}^{(k-r)} s_{k-r,m-l} \\ &= \sum_{r=0}^R \sum_{l=0}^{L(k)} h_{r,l}^{(k-r)} s_{k-r,m-l}. \end{aligned} \quad (5.36)$$

The above indicates that the received signal at each branch is subject to both inter-symbol interference (ISI) and inter-layer interference (ILI) as a consequence of the MSML channel model.

We conclude this subsection with the following remark.

*Remark 5.3.* With  $W_\star$  and  $a$  obtained as indicated in the previous subsection, we can impose an upper-bound on the number of transmit layers  $K'$ . Like the base frequency  $f_c$ , usually the total available transmission bandwidth of a communication system  $B$  is fixed, and therefore

$$B \geq \sum_{k'=0}^{K'-1} a^{k'} W_\star, \quad (5.37)$$

from which an upper-bound for  $K'$  can be attained.

*Remark 5.4.* The T-F tiling diagram of the proposed multi-layer transmission scheme is shown in Fig. 5.8, where each black circle indicates the T-F position

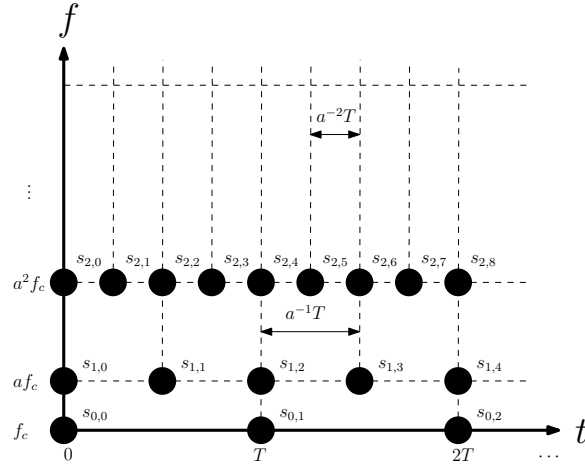


**Figure 5.8:** *T-F tiling diagram of a multi-layer transmission signaling scheme*

where one transmit data symbol is located. One can immediately observe the resemblance to the T-F tiling diagram of the parameterized channel plotted in Fig. 5.2. By this means, we match the transmit signal to the channel in the T-F plane.

*Remark 5.5.* The transmit signal described in (5.35) belongs to the multi-scale wavelet modulation (MSWM) family proposed in [58, 84] if  $\Re\{p(t)e^{j\pi f_c t}\}$  is an orthogonal wavelet. One difference between this chapter and [58, 84] is that the latter works only examine a wavelet signal over a flat fading channel, while we tailor our signal by intelligently designing the pulse to the MSML channel model. Despite this difference, one can still use the same arguments in [58, 84] to show that the transmit signal given in (5.35) will have the same spectral efficiency<sup>4</sup> as traditional transmission schemes such as OFDM if the equality in (5.26) is satisfied (we refer readers to [58, 84] for a detailed proof). If only the inequality in (5.26) is satisfied, there will be some frequency gap between adjacent transmit layers, and the bandwidth efficiency will be reduced. Similarly, such a frequency gap can also emerge in practical multi-carrier systems, where spectrum gaps are introduced to

<sup>4</sup>Spectral efficiency refers to the available information rate for a given transmission bandwidth [27].



reduce the inter-carrier interference induced by Doppler, e.g., in [10, 87, 88].

## 5.4 Block-Wise Transceiver Design

For the sake of clarity, let us recap the results in (5.36) here as

$$y_{k,m} = \sum_{r=0}^R \sum_{l=0}^{L(k)} h_{r,l}^{(k-r)} s_{k-r,m-l} + v_{k,m}, \quad (5.38)$$

where we have also added the noise term  $v_{k,m}$ , whose expression can be obtained by

$$v_{k,m} = \int_{-\infty}^{+\infty} a^{k/2} \bar{w}(t) e^{-j2\pi f_c a^k t} p(mT - a^k t) dt, \quad (5.39)$$

where the continuous time noise  $\bar{w}(t)$  is introduced in (5.1). Equation (5.38) shows that the discrete samples at the  $k$ th receiver branch are related to the transmitted information symbols via a 2-D time-varying discrete finite impulse response (FIR) filter. This feature will be exploited by considering a block-wise transmission, where the transmitted symbols on each layer are partitioned into successive blocks, each containing  $N + Z$  data symbols. The data symbols contained in such a block from all the  $K'$  layers can be collectively expressed as

$$\sum_{k'=0}^{K'-1} \sum_{n=0}^{N+Z-1} \Re\{a^{k'/2} s_{k',n} p(a^{k'} t - nT) e^{j2\pi f_c a^{k'} t}\}. \quad (5.40)$$

To avoid inter-block interference (IBI), we introduce a cyclic prefix (CP) of a length of  $Z$  symbols along each layer, such that

$$s_{k',n} = \begin{cases} b_{k',n-Z}, & \text{for } Z \leq n < N + Z \\ b_{k',N+n-Z}, & \text{for } 0 \leq n < Z \end{cases}, \quad (5.41)$$

where  $b_{k',n}$  stands for the  $n$ th information symbol transmitted at the  $k'$ th transmit layer.

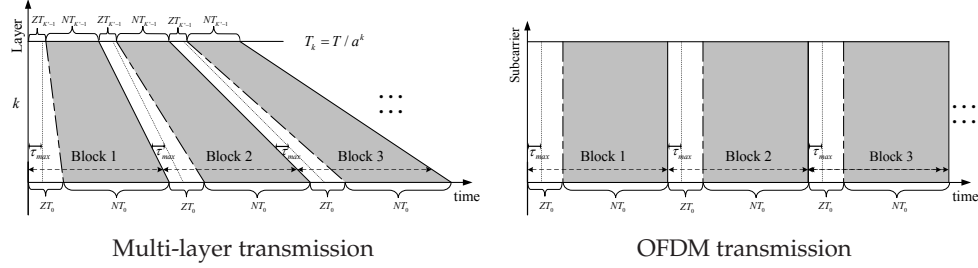


**Figure 5.9:** Structure of transmitted data blocks in the T-F plane

At the receiver, we will consider a filter bank with  $K = R + K' - 1$  branches, whose structure is depicted in Fig. 5.5, with the received samples on the  $k$ th branch given by (5.38). Obviously, IBI can be completely annihilated if  $Z \geq L(k)$  for all  $k \in \{0, 1, \dots, R + K' - 1\}$ , or in other words,

$$Z \geq \lceil a^{R+K'-1} \tau_{\max} / T \rceil = \lceil a^{R+K'-1} L(0) \rceil. \quad (5.42)$$

All the data blocks are treated in this way. Here, it is interesting to note that because of the disparate scale at each transmit layer, the representations of the different blocks in the T-F plane are not parallel to each other as for OFDM. This effect is schematically illustrated in Fig. 5.9, where the shaded area indicates the area in the T-F plane where information symbols reside, and the blank area represents that of the CPs. It is noteworthy that the use of these CP symbols is another difference distinguishing our work from that of [58, 84], where it is not clear how to add a guard interval to the MSWM signal. We show that adding these CPs is not trivial as shown in Fig. 5.9. For comparison, the case of OFDM block transmission is also sketched in Fig. 5.9.

To design a block equalizer, we stack the information symbols sent through the  $k'$ th transmission layer in a vector  $\mathbf{b}_{k'} = [b_{k',0}, \dots, b_{k',N-1}]^T$ , and  $\mathbf{b}_k = \mathbf{0}$  if  $k < 0$  or  $k > K' - 1$ . Likewise, we stack the received samples from the  $k$ th receiver branch, with CP stripped off, in a vector  $\mathbf{y}_k = [y_{k,Z}, \dots, y_{k,Z+N-1}]^T$ . It follows from (5.38) that

$$\mathbf{y}_k = \sum_{r=0}^R \mathbf{H}_r^{(k-r)} \mathbf{b}_{k-r} + \mathbf{v}_k, \quad (5.43)$$

where  $\mathbf{v}_k$  is similarly defined as  $\mathbf{y}_k$ , and  $\mathbf{H}_r^{(k-r)}$  denotes an  $N \times N$  circulant matrix with first column  $[h_{r,0}^{(k-r)}, h_{r,1}^{(k-r)}, \dots, h_{r,L(k)}^{(k-r)}, 0, \dots, 0]^T$ . If we next stack the  $\mathbf{b}_{k'}$ 's from all the transmit layers into one vector  $\mathbf{b} = [\mathbf{b}_0^T, \dots, \mathbf{b}_{K'-1}^T]^T$ , and the  $\mathbf{y}_k$ 's from all receive branches into one vector  $\mathbf{y} = [\mathbf{y}_0^T, \dots, \mathbf{y}_{K'+R-1}^T]^T$ , it then follows from (5.43) that

$$\mathbf{y} = \mathbf{H}\mathbf{b} + \mathbf{v} \quad (5.44)$$

where  $\mathbf{v}$  is similarly defined as  $\mathbf{y}$ , and  $\mathbf{H}$  stands for the  $(K' + R - 1)N \times K'N$  matrix specified as

$$\mathbf{H} = \begin{bmatrix} \mathbf{H}_0^{(0)} & & & \mathbf{0} \\ \vdots & \ddots & & \\ \mathbf{H}_R^{(0)} & & \ddots & \\ & \ddots & & \mathbf{H}_0^{(K'-1)} \\ & & \ddots & \vdots \\ \mathbf{0} & & & \mathbf{H}_R^{(K'-1)} \end{bmatrix} \quad (5.45)$$

We conclude this section with the following remarks.

*Remark 5.6.* The 2-D FIR filter structure is clearly revealed in (5.45), where the block element  $\mathbf{H}_r^{(k)}$  can be viewed as the block tap of a time-varying outer FIR filter (note the varying superscript). Each  $\mathbf{H}_r^{(k)}$  yields an FIR filter with scalar tap  $h_{r,l}^k$ , which is time-invariant inducing the circulant structure of  $\mathbf{H}_r^k$ .

*Remark 5.7.* With  $K' = 1$ , the proposed transceiver scheme reduces to a single-layer approach. We can then interpret the I/O relationship in (5.44) as a SIMO-OFDM system with  $R + 1$  receive antennas. Further, if the Doppler effect is absent with  $R = 0$ , then the I/O relationship in (5.44) can be interpreted as a multi-band OFDM system [72] with  $K' - 1$  bands.

## 5.5 Frequency-Domain Equalization

The circulant structure of  $\mathbf{H}_r^{(k)}$  suggests that it is possible to equalize the channel in the frequency domain, as in traditional OFDM systems for narrowband time-invariant channels, to lower the equalization complexity. This is achieved in two steps.

In the first step, let us transform the received signal to the frequency domain by  $\tilde{\mathbf{y}} = (\mathbf{I}_{K'+R-1} \otimes \mathbf{F})\mathbf{y}$ , where  $[\mathbf{F}]_{n,m} = \frac{1}{\sqrt{N}}e^{-j2\pi\frac{nm}{N}}$  denotes the normalized discrete Fourier transform (DFT) matrix. The frequency-domain expression of (5.44) can then be expressed as

$$\tilde{\mathbf{y}} = \tilde{\mathbf{H}}\tilde{\mathbf{b}} + \tilde{\mathbf{v}}, \quad (5.46)$$

where  $\tilde{\mathbf{b}} = (\mathbf{I}_{K'} \otimes \mathbf{F})\mathbf{b}$ , and  $\tilde{\mathbf{v}}$  is similarly defined as  $\tilde{\mathbf{b}}$ . Furthermore,

$$\tilde{\mathbf{H}} = \begin{bmatrix} \tilde{\mathbf{H}}_0^{(0)} & & & \mathbf{0} \\ \vdots & \ddots & & \\ \tilde{\mathbf{H}}_R^{(0)} & & \ddots & \\ & \ddots & & \tilde{\mathbf{H}}_0^{(K'-1)} \\ & & \ddots & \vdots \\ \mathbf{0} & & & \tilde{\mathbf{H}}_R^{(K'-1)} \end{bmatrix} \quad (5.47)$$

where  $\tilde{\mathbf{H}}_r^{(k)} = \mathbf{F}\mathbf{H}_r^{(k)}\mathbf{F}^{-1}$  denotes an  $N \times N$  diagonal matrix whose  $n$ th diagonal is

$$\tilde{h}_{r,n}^{(k)} = \sum_{l=0}^{L(k)} h_{r,l}^{(k)} e^{j\frac{2\pi}{N}nl}. \quad (5.48)$$

Observe that  $\tilde{\mathbf{H}}$  has a banded structure on the block level with each block entry being a diagonal matrix. There exists a  $(K' + R - 1)N \times (K' + R - 1)N$  permutation matrix  $\mathbf{P}_{K'+R-1}$  and a  $K'N \times K'N$  permutation matrix  $\mathbf{P}_{K'}$  matrix<sup>5</sup>, such that we can permute (5.46) to

$$\tilde{\mathbf{y}} = \check{\mathbf{H}}\check{\mathbf{b}} + \check{\mathbf{v}}, \quad (5.49)$$

where  $\check{\mathbf{y}} = \mathbf{P}_{K'+R-1}\tilde{\mathbf{y}}$ ;  $\check{\mathbf{b}} = \mathbf{P}_{K'}\tilde{\mathbf{b}}$ ;  $\check{\mathbf{v}} = \mathbf{P}_{K'+R-1}\tilde{\mathbf{v}}$ , and  $\check{\mathbf{H}} = \mathbf{P}_{K'+R-1}\tilde{\mathbf{H}}\mathbf{P}_{K'}^T$ . It is straightforward to show that  $\check{\mathbf{H}}$  is a *block diagonal* matrix, where each diagonal block is a  $(K' + R - 1) \times K'$  strictly banded matrix with a bandwidth of  $R + 1$ . The structure of  $\check{\mathbf{H}}$  is illustrated in Fig. 5.10. Denoting the  $k$ th

<sup>5</sup>We use  $\mathbf{P}_K$  to represent a permutation matrix of a proper dimension with depth  $K$ . Specifically, consider a vector  $\mathbf{a} = [a_0, a_1, \dots, a_{NK-1}]^T$ , then  $\mathbf{P}_K\mathbf{a} = [\mathbf{a}_0^T, \mathbf{a}_1^T, \dots, \mathbf{a}_{K-1}^T]^T$  with  $\mathbf{a}_k = [a_k, a_{K+k}, a_{2K+k}, \dots, a_{(N-1)K+k}]^T$  for  $k = 0, 1, \dots, K - 1$ .

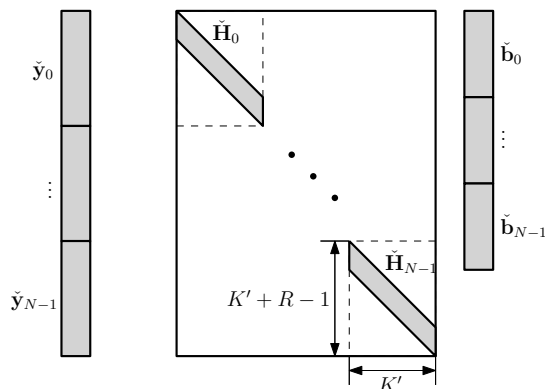


Figure 5.10: Illustration of the matrix-vector form for (5.49)

diagonal block as  $\check{\mathbf{H}}_n$ , for  $n \in \{0, \dots, N-1\}$ , we can split  $\check{\mathbf{y}}$  into  $N$  subvectors, where the  $n$ th subvector  $\check{\mathbf{y}}_n$ , which is comprised of the  $nK'$ th through  $[(n+1)K' - 1]$ st entries of  $\check{\mathbf{y}}$ , is given by

$$\check{\mathbf{y}}_n = \check{\mathbf{H}}_n \check{\mathbf{b}}_n + \check{\mathbf{v}}_n, \quad (5.50)$$

where  $\check{\mathbf{b}}_n$  and  $\check{\mathbf{v}}_n$  are defined similarly to  $\check{\mathbf{y}}_n$ . The strictly banded structure of  $\check{\mathbf{H}}_n$  enables us to employ the low-complexity LMMSE equalizer designed in [3] or the low-complexity turbo equalizer in [5] to equalize each  $\check{\mathbf{H}}_n$ , one by one.

*Remark 5.8.* The derivations throughout the chapter do not exploit any assumption about the noise statistics of  $v_{k,m}$ . For the low-complexity LMMSE equalizer of [3] or the low-complexity turbo equalizer of [5], it is desirable that the noise should be zero mean and uncorrelated. In Appendix 5.D, we show that this is guaranteed if the continuous-time noise  $\bar{w}(t)$  is white and zero mean, and if an ideal pulse  $p(t)$  can be designed as in Section 5.3.2.

## 5.6 Numerical Results

In this section, we provide some simulation results to demonstrate the performance of the proposed wideband system. We will use a discrete path

model to emulate the real wideband LTV channel

$$\bar{h}(\alpha, \tau) = \sum_{p=0}^P \bar{h}_p \delta(\alpha - \alpha_p) \delta(\tau - \tau_p), \quad (5.51)$$

with  $P = 10$ ;  $\bar{h}_p$  is modeled as an i.i.d. Gaussian variable with zero mean and unit variance. Without loss of generality, we assume that  $\tau_p$  is equal to 0 if  $p = 0$ ; otherwise it is modeled to have a uniform distribution over  $[0, \tau_{\max})$ . Likewise, we assume that  $\alpha_p$  is equal to 1 if  $p = 0$ ; otherwise it is modeled to have a uniform distribution over  $[1, \alpha_{\max})$ . Although the values of  $\bar{h}_p$ ,  $\tau_p$  and  $\alpha_p$  are assumed to stay constant during several transmitted blocks, they result in a wideband channel whose channel response varies with time. Consequently, the I/O relationship in (5.1) can be written as

$$\bar{r}(t) = \sum_{p=0}^P \bar{h}_p \sqrt{\alpha_p} \bar{s}(\alpha_p(t - \tau_p)), \quad (5.52)$$

For the transmission, we use

$$p(t) = \text{sinc}(t/T) / \sqrt{T}, \quad (5.53)$$

as the transmission waveform with the *base lag*  $T$  equal to  $10^{-3}$ s ( $W = 1$ kHz). The carrier frequency  $f_c$  is chosen to be 1.5kHz. As a result, the *base scale*  $a$  of  $p(t)e^{j2\pi f_c t}$  is equal to 2. Refer to Section 5.3.2 for more details about these parameters.

### 5.6.1 Channel Model Validation

To examine the accuracy of the proposed channel model, we follow a similar channel sounding approach as used in [21]: we send a single information symbol  $s_{0,0}$  modulated on  $p(t)$  in order to examine the channel in terms of the impulse response function. The normalized mean squared-error (NMSE) between  $\bar{r}(t)$  in (5.52) and  $\bar{r}^{\text{SL}}(t)$  evaluated at the output of the receiver branches is computed as

$$\text{NMSE}_{\text{MSML}} = \frac{\sum_{k=0}^R \sum_{l=0}^{L(k)} \left| \int p_k(t - \frac{lT}{a^k}) (\bar{r}(t) - \bar{r}^{\text{SL}}(t)) e^{-j2\pi f_c a^k t} dt \right|^2}{\sum_{r=0}^R \sum_{l=0}^{L(k)} \left| \int p_k(t - \frac{lT}{a^k}) \bar{r}(t) e^{-j2\pi f_c a^k t} dt \right|^2}. \quad (5.54)$$

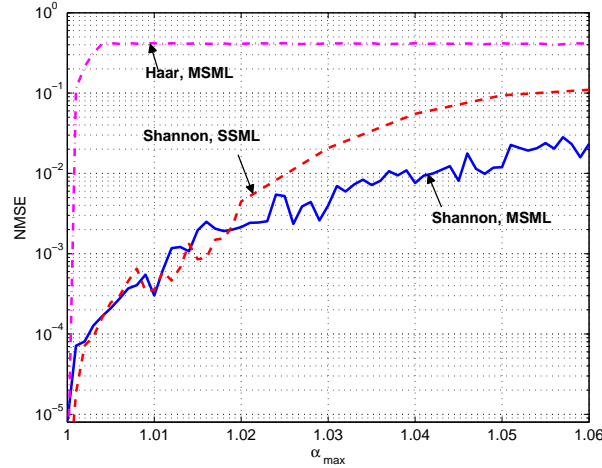


**Figure 5.11:** Channel modeling performance. The solid line corresponds to the NMSE of the proposed model; the dash-dotted line to the NMSE of the channel model in [21], and the dashed line to the NMSE of the channel model based on an SSML assumption.

We now compare three NMSEs in Fig. 5.11, corresponding to the following situations: a MSML model using a pulse design with parameter matching (“Shannon, MSML”), a MSML model using a pulse design without parameter matching (“Haar, MSML”), and a SSML model (“Shannon, SSML”). We underscore that, using the transmit pulse given in (5.53) satisfies the equality in Theorem 5.1 (“Shannon, MSML”). The second curve (“Haar, MSML”) corresponds to the case where a Haar wavelet is used as the transmit pulse, which is characterized by the same parameters  $T$ ,  $a$  and  $f_c$ . We derive a channel model following the approach of [21], and calculate the NMSE of this channel model in the same way as (5.54). Note that because the Haar wavelet has a considerable power leakage outside the considered bandwidth [see Fig. 5.7], Theorem 5.1 is violated, implying that the crosstalk in (5.16) cannot be entirely eliminated. The resulting cross-talk, which can be viewed as a modeling error, results in the performance degradation seen in Fig. 5.11 (“Haar, MSML”). The third NMSE curve (“Shannon, SSML”) is motivated by the fact that the wideband LTV channel is often modeled using an SSML as-

sumption [28,30,81], or assuming a single rate to sample the channel [29,76]. In these works, a single-scale signal, denoted as  $\bar{r}_{\text{single}}(t)$ , is coined to approximate the received signal. This signal  $\bar{r}_{\text{single}}(t)$  can be expressed as

$$\bar{r}_{\text{single}}(t) = \sum_{p=0}^P \bar{h}_p \sqrt{a_{\text{single}} \bar{s}} (a_{\text{single}}(t - \tau_p)), \quad (5.55)$$

where  $a_{\text{single}}$  can be found by e.g., [29]

$$a_{\text{single}} = \arg \min_{\alpha} \left| \bar{r}(t) - \sum_{p=0}^P \bar{h}_p \sqrt{\alpha \bar{s}} (\alpha(t - \tau_p)) \right|^2. \quad (5.56)$$

The corresponding channel modeling error is computed by adapting (5.54) as

$$\text{NMSE}_{\text{SSML}} = \frac{\sum_{l=0}^{L(k)} \left| \int p_{\text{single}}(t - \frac{lT}{\alpha_{\text{single}}}) (\bar{r}(t) - \bar{r}_{\text{single}}(t)) e^{-j2\pi f_c \alpha_{\text{single}} t} dt \right|^2}{\sum_{l=0}^{L(k)} \left| \int p_{\text{single}}(t - \frac{lT}{\alpha_{\text{single}}}) \bar{r}(t) e^{-j2\pi f_c \alpha_{\text{single}} t} dt \right|^2}, \quad (5.57)$$

where  $p_{\text{single}}(t) = a_{\text{single}}^{1/2} p(a_{\text{single}} t)$ . It can be seen that the modeling performance yielded by the SSML channel model is similar to the proposed MSML model for a low-to-moderate Doppler spread  $\alpha_{\text{max}}$ , but deteriorates fast when the Doppler spread gets higher.

### 5.6.2 Equalization Performance

Supported by the results in Fig. 5.11, we will assume in the ensuing simulations that our model (5.12) has negligible errors and therefore,  $\bar{r}^{\text{SL}}(t) \approx \bar{r}(t)$ . For equalization, three types of channels are tested, whose channel parameters are specified in Table 5.1. A multi-layer transmission is deployed with  $K' = 3$  transmit layers. Accordingly,  $K = R + K' - 1$  receiver branches are employed at the receiver. Each transmit block contains  $N = 128$  binary phase shift keying (BPSK) symbols, and is preceded by a CP of length  $Z = 16$ .

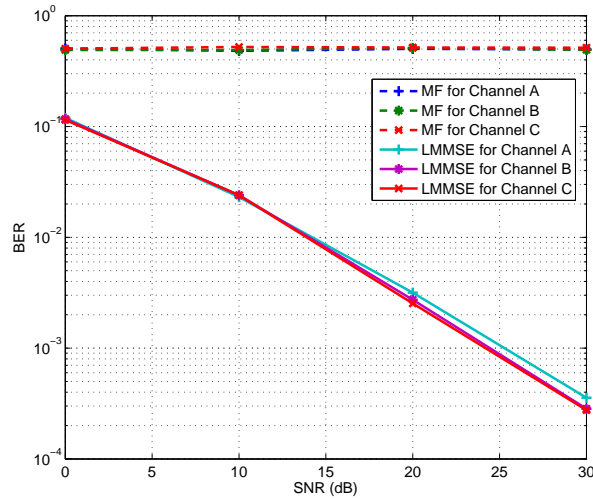
Fig. 5.12 shows the bit-error-rate (BER) performance of the proposed transceiver architecture using an LMMSE equalizer. As can be seen, the LMMSE equal-



**Table 5.1:** Parameters for the adopted wideband channels

Channel	$\tau_{max}$	$\alpha_{max}$	$L(0)$	$R$	the maximal data rate of a single-layer transmission *	the data rate of our multi-layer transmission *
A	0.6 ms	1.00	1	0	$3.76 \times 10^3$ bps	$6.59 \times 10^3$ bps
B	1.2 ms	1.02	2	1	$3.76 \times 10^3$ bps	$6.59 \times 10^3$ bps
C	1.8 ms	1.04	2	1	$3.76 \times 10^3$ bps	$6.59 \times 10^3$ bps

\* using BPSK,  $N = 128$ ,  $K = 3$ ,  $Z = 16$  and  $T = 1.0$ ms. The data rate is given by  $\frac{1}{L(0)T}$  for the work of [21],  $\frac{N}{N+Z} \frac{a^K - 1}{T}$  for a single-layer transmission, and  $\frac{N}{N+Z} \frac{a^K - 1}{(a-1)T}$  for a multi-layer transmission, where  $a = 2$ .

**Figure 5.12:** BER performance using an LMMSE equalizer

izer renders a similar performance irrespective of the channel spread in delay and scale. As a comparison, we have also provided the performance of a matched-filter (MF) equalizer, which is used in [21], which is inferior due to a high modeling error and indicates the necessity of channel equalization in the presence of inter-symbol/inter-scale interference.

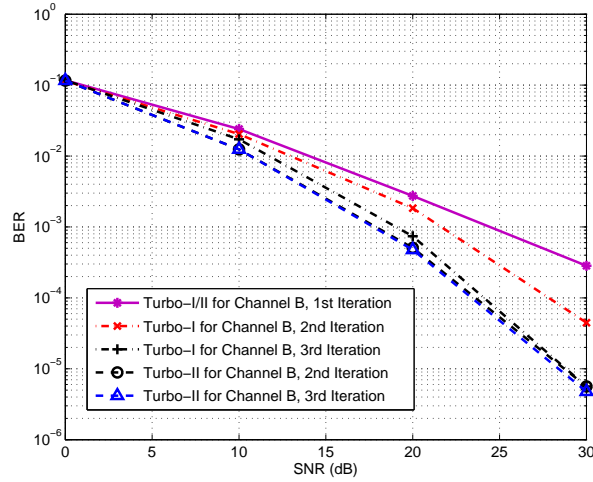
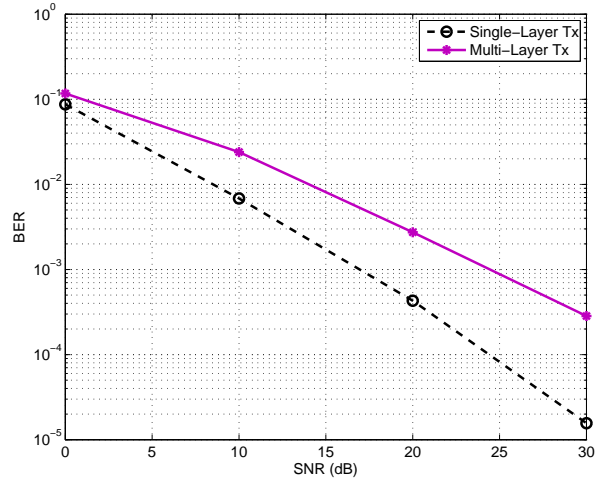


Figure 5.13: BER performance using a banded turbo equalizer [5]

As mentioned before, since the proposed transceiver architecture results in a banded channel matrix (see (5.49)), many techniques designed for narrowband systems, with suitable adaptation, can be employed for our transmission scheme over wideband MSML channels. For instance, the matrix inversion required for the LMMSE equalizer can be achieved using the low-complexity algorithm given in [3]. Further, we can employ the banded turbo equalizers proposed in [5], which rely also on the banded structure of the channel matrix, to improve the BER performance even further along more equalization iterations. The results of the banded turbo equalizers for channel B are illustrated in Fig. 5.13. These simulation results indicate the suitability of these low-complexity algorithms designed in [3,5] for narrowband systems.

### 5.6.3 Single-Layer or Multi-Layer

In this subsection, we compare the multi-layer transmission scheme with respect to the single-layer transmission scheme, where we use the parameters of Channel C that are summarized in Table 5.1, and the multi-layer trans-



**Figure 5.14:** BER comparison between the multi-layer transmission and the single-layer transmission

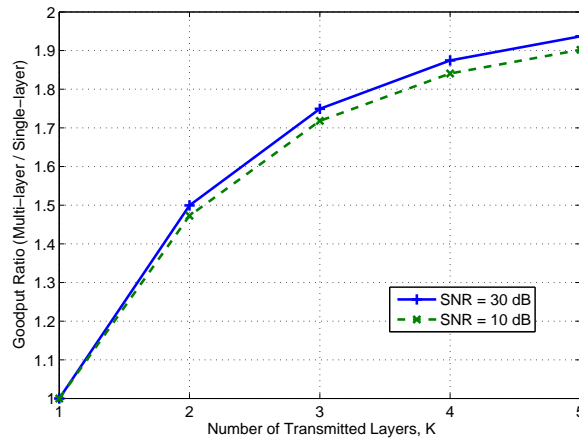


**Figure 5.15:** Goodput ratio between the multi-layer transmission and the single-layer transmission

mitter consists of  $K' = 3$  layers. The BER performance is compared with

the results given in Fig. 5.14. One can see that the single-layer transmission results in a better equalization performance. This is not a surprise, since the receiver for the multi-layer transmission has the more demanding task of resolving the interference among the different layers sent from the transmitter. On the other hand, the multi-layer transmitter results in a much higher spectral efficiency. To make a more fair comparison, we utilize the “goodput ratio” as a criterion, which is defined as

$$\text{Goodput Ratio} = \frac{(1 - \text{BER}_M)\beta_M}{(1 - \text{BER}_S)\beta_S},$$

where  $\beta_M$  and  $\beta_S$  denote the maximal data rate of the multi-layer transmission and the single-layer transmission, respectively, and  $\text{BER}_M$  and  $\text{BER}_S$  denote the BER of the multi-layer transmission and the single-layer transmission, respectively. The goodput gives an index of the effective throughput of a system. The goodput ratio is plotted in Fig. 5.15, where we observe that the multi-layer transmission always has a larger goodput than the single-layer transmission, and this advantage is even more pronounced when the number of layers increases.

#### 5.6.4 OFDM vs. Multi-Layer Block Transmission

In this subsection, we compare the performance of the multi-layer block transmission (MLBT) scheme with respect to the traditional OFDM transmission scheme over a wideband channel (i.e., Channel C in Table 5.1). The multi-layer scheme consists of  $K = 3$  layers, with the blocks on each layer containing  $N = 128$  symbols. Accordingly, we let the OFDM scheme employ 224 subcarriers, within a duration of 128ms, to fill the same effective transmission bandwidth as our multi-layer scheme. In order to allow for a fair uncoded performance comparison, we precode OFDM with a discrete Fourier transform at the transmitter, and use BSPK modulation as in our MLBT scheme. In addition, both schemes are equipped with the same guard interval of 16ms (i.e.,  $Z = 16$  for our MLBT or 28 samples for OFDM), such that the spectral efficiencies are identical (i.e.,  $\frac{16}{128+16} \approx 0.89$ ). To equalize such an OFDM channel, we follow the widely used approach in practical OFDM systems, by first obtaining a uniform sampling rate [29] and then

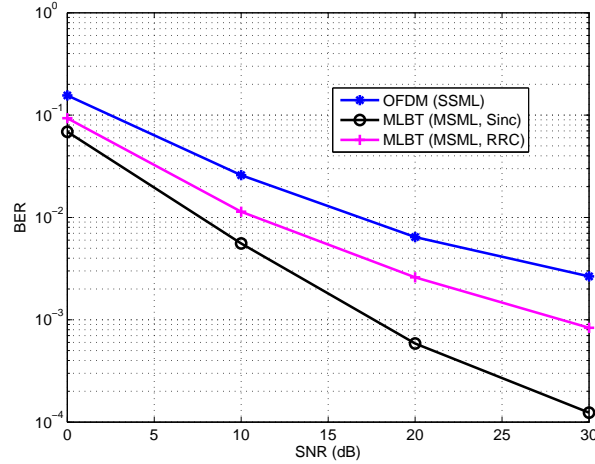


Figure 5.16: BER comparison between the multi-layer transmission and OFDM

performing a banded channel equalization [3,5,72] in the frequency domain. The adopted matrix bandwidth here is 3. Note that, in this manner, the equalization of the OFDM channel has the same complexity as the frequency-domain equalization of our MLBT scheme, since they both induce a banded channel matrix with the same bandwidth. As shown in Fig. 5.16, the MLBT schemes yield a better performance than OFDM, because the transmit signal in the MLBT schemes is specially designed for MSML channels while the OFDM transmit signal is only optimized for SSML channels. By assuming an SSML model to approximate the actual MSML channel, a large channel modeling error is inevitable in the presence of a profound Doppler scale spread as shown in Fig. 5.11. Note that in Fig. 5.16, we have depicted the performance of the multi-layer scheme based on two pulses for  $p(t)$ : one is the sinc function as given in (5.32) that has been used so far, and the other is the root-raised cosine (RRC) function given by

$$p(t) = \frac{\sin(\pi(1 - \beta)Wt) + 4\beta Wt \cos(\pi(1 + \beta)Wt)}{\pi\sqrt{W}t(1 - (4\beta Wt)^2)}$$

with  $\beta = 0.25$  being the roll-off factor. For both pulses, the same *base scale*  $a = 2$  and *base lag*  $T = 1\text{ms}$  is applied. We have argued in Section 5.3.2 that these parameters are chosen to match the *dilation spacing*  $a_*$  and *translation spacing*  $T_*$  of the sinc function. For the RRC function, it can be computed that the corresponding  $a_*$  is larger than 2 and the corresponding  $T_*$  is less than 1ms (because its effective bandwidth  $(1 + \beta)W$  is more than  $W = 1\text{kHz}$ ). It indicates that the use of  $a = 2$  and  $T = 1\text{ms}$  does not match the channel parameters tightly, which inflicts a performance penalty on the multi-layer scheme based on the RRC pulse.

## 5.7 Summary

Multi-scale multi-lag (MSML) channel models are appropriate for a variety of wideband time-varying channels such as underwater acoustic systems or terrestrial ultra-wideband radio systems. In this work, we have provided a novel parameterization of the continuous time multi-scale multi-lag (MSML) channel by taking the passband nature of the propagating signal explicitly into account. The associated baseband signal is evaluated and shown to result in inter-scale and inter-symbol interference. We have proposed a novel multi-layer transceiver for such MSML channels. At the transmitter, the information symbols are placed at different non-overlapping sub-bands to enhance the spectral efficiency, where each sub-band has a distinctive bandwidth, and therefore, the transmission in each sub-band is characterized by a different data rate. Our multi-layer transmission is a special case of the known multi-scale wavelet modulation (MSWM), and can thus achieve the same spectral efficiency as traditional transmissions, e.g., OFDM. Different from a traditional MSWM signal, we have built a block transmission scheme and introduced a guard interval to eliminate inter-block interference. To combat the multi-scale multi-lag effect of the channel, a filterbank is deployed at the receiver, where each branch of the filterbank will resample the received signal in a different way. By selecting a proper transmitter pulse, we have shown that the effective I/O relationship in the discrete domain can be captured by a block-diagonal channel, with each diagonal block being a banded matrix. As a result, the low-complexity equalizers that have been

---

intensively used for narrowband systems become also applicable here. For a comparison, without a proper pulse design, the multi-layer transmission is subject to inter-layer interference and performance loss is thus inevitable. We have argued that the key to the success of the proposed scheme lies in a proper choice of the transmit pulse such that the channel parameters will have a tight match with the parameters of the transmit pulse. Optimal transmit pulse design remains an interesting topic for future work.

## Appendix 5.A Proof of Theorem 5.1

Let

$$\begin{aligned} a(t) &= \sqrt{\frac{a^k}{T}} p(a^k t - mT) e^{j2\pi f_c a^k t}, \\ b(t) &= \sqrt{\frac{a^{k'}}{T}} p(a^{k'} t - nT) e^{j2\pi f_c a^{k'} t}, \end{aligned}$$

whose Fourier transform is denoted as  $\mathcal{A}(f)$  and  $\mathcal{B}(f)$ , respectively. With these notations, the left-hand side of (5.27) can be rewritten as

$$\begin{aligned} & \int_{-\infty}^{\infty} \frac{\sqrt{a^k a^{k'}}}{T} p(a^k t - mT) e^{j2\pi f_c a^k t} p(a^{k'} t - nT) e^{-j2\pi f_c a^{k'} t} dt \\ &= \int_{-\infty}^{\infty} a(t) b^*(t) dt = \int_{-\infty}^{\infty} \mathcal{A}(f) \mathcal{B}^*(f) df, \end{aligned}$$

where the last equality holds due to Parseval's theorem. We understand that  $\mathcal{A}(f)$  is defined within the range

$$\mathcal{S}_a = [a^k f_c - a^k \frac{W}{2}, a^k f_c + a^k \frac{W}{2}] \cup [-a^k f_c - a^k \frac{W^*}{2}, -a^k f_c + a^k \frac{W^*}{2}],$$

and  $\mathcal{B}(f)$  is defined within the range

$$\mathcal{S}_b = [a^{k'} f_c - a^{k'} \frac{W^*}{2}, a^{k'} f_c + a^{k'} \frac{W^*}{2}] \cup [-a^{k'} f_c - a^{k'} \frac{W^*}{2}, -a^{k'} f_c + a^{k'} \frac{W^*}{2}]. \quad (5.58)$$

With  $a$  chosen as in (5.26),  $\mathcal{S}_a \cap \mathcal{S}_b = \emptyset$  if  $k \neq k'$ . When  $k = k'$ , we have

$$g_{n-m} = \int a^k p(a^k t - mT) p^*(a^k t - nT) dt, \quad (5.59)$$

$$= \int p(t) p^*(t - (n-m)T) dt. \quad (5.60)$$

Because  $p(t)$  is real, we obtain (5.28).



## Appendix 5.B Proof of (5.29)

The crosstalk term in (5.25) can be fully written as

$$\begin{aligned}
& \int p_k\left(t - \frac{mT}{a^k}\right) \sum_{r=0, r \neq k-k'}^R C_{r+k'}(t) dt \\
&= \int p_k\left(t - \frac{mT}{a^k}\right) \sum_{r=0, r \neq k-k'}^R e^{j2\pi f_c(a^{r+k'} - a^k)t} \sum_{l=0}^{L(k'+r)} h_{r,l}^{(k')} a^{r/2} s_{k'}(a^r t - lT) dt \\
&= \sum_{r=0, r \neq k-k'}^R \sum_{l=0}^{L(k'+r)} \sum_n h_{r,l}^{(k')} s_{k',n} T \\
&\quad \times \int \frac{\sqrt{a^k a^{r+k'}}}{T} e^{j2\pi f_c(a^{r+k'} - a^k)t} p\left(t - \frac{mT}{a^k}\right) p\left(a^{k+r}t - \frac{(l+n)T}{a^{k'}}\right) dt.
\end{aligned}$$

It is then sufficient to prove that

$$\int \frac{\sqrt{a^k a^{r+k'}}}{T} e^{j2\pi f_c(a^{r+k'} - a^k)t} p_k\left(t - \frac{mT}{a^k}\right) p\left(a^r t - \frac{(l+n)T}{a^{k'}}\right) dt = 0, \quad (5.61)$$

for  $r \neq k - k'$ . Note that  $p_k\left(t - \frac{mT}{a^k}\right) = a^{k/2} p(a^k t - mT)$ . This enables us to rewrite (5.61) as

$$\begin{aligned}
& \int \frac{\sqrt{a^k a^{r+k'}}}{T} e^{j2\pi f_c(a^{r+k'} - a^k)t} p_k\left(t - \frac{mT}{a^k}\right) p\left(a^r t - (l+n)T_{k'}\right) dt \\
&= \int \left(\sqrt{\frac{a^k}{T}} p(a^k t - mT) e^{j2\pi f_c a^k t}\right)^* \sqrt{\frac{a^{r+k'}}{T}} p(a^{r+k'} t - (l+n)T) e^{j2\pi f_c a^{r+k'} t} dt, \\
&= \delta_{r+k'-k, g_{k,m-l-n}},
\end{aligned}$$

where the last equality is due to Theorem 5.1. This concludes the proof.

## Appendix 5.C The Basic Scaling Factor of the Shannon Wavelet

Here, we examine the signal  $\bar{p}(t) = \sqrt{W} \text{sinc}(Wt) e^{j2\pi f_c t}$ , which yields a Shannon wavelet with  $f_c = 1.5W$ . We resort to two approaches to determine

the *basic scaling factor* of the Shannon wavelet. The first approach, which is adopted in [21], utilizes the Mellin transform, while the second approach, which is adopted in [33], utilizes the wideband ambiguity function.

For the first approach, we use a general Mellin variable  $\varpi = c - j2\pi\beta$ , where  $c$  is a real constant and  $\beta$  is a real variable. It can be derived that the Mellin transform of  $\bar{p}(t)$  can be expressed as

$$\begin{aligned}\mathcal{M}(\beta) &= \int_0^\infty \bar{p}(t)t^{\varpi-1} dt = \int_0^\infty t^{c-j2\pi\beta} \bar{p}(t) \frac{dt}{t}, \\ &= \int_0^\infty \bar{p}(t)e^{c \ln(t)} e^{-j2\pi\beta \ln(t)} \frac{dt}{t}.\end{aligned}$$

If we take a geometrically time-warped version of  $\bar{p}(t)$ , i.e.,  $\bar{x}(t) := \bar{p}(e^t)e^{ct}$ , we can rewrite the above equation as

$$\mathcal{M}(\beta) = \int_{-\infty}^\infty \bar{x}(u)e^{-j2\pi\beta u} du,$$

which actually shows that the Mellin transform is inherently a logarithmic-time Fourier transform. Consequently, the discrete (inverse) Mellin transform can also be implemented by an inverse discrete Fourier transform (IDFT) but in the geometric sampling domain, which is obtained by interpolating the uniform domain [89]. In this chapter, we follow the scale-representation [35] for the Mellin transform and use  $c = 1/2$  instead of  $c = 1$ . The latter is used for the discrete Mellin transform in [34]. Therefore, we can adopt the DFT on the geometric samples to examine the Mellin bandwidth of  $\bar{p}(t)$ , which is shown in Fig. 5.6, indicating that  $M_\star \approx \ln(1/2)$ , and thus  $a_\star \approx 2$ .

For the second approach, we use the wideband ambiguity function  $\bar{\chi}_{\bar{p}}(\alpha, \tau) = \int \bar{p}(t)\sqrt{\alpha}\bar{p}(\alpha(t - \tau))dt$  and select  $a_\star$  according to  $a_\star = \min|\alpha|$  subject to  $\bar{\chi}(\alpha, 0) = 0$ . This yields also  $a_\star = 2$  as suggested by Fig. 5.6.

## Appendix 5.D Noise Statistics

From (5.39), it is easy to show that  $\mathcal{E}(v_{k,m}) = 0$  if  $\mathcal{E}(\bar{w}(t)) = 0$ .

For the second-order moment of  $v_{k,m}$ , it follows that

$$\begin{aligned} & \mathcal{E} (v_{k,m} v_{k',m'}) \\ &= \mathcal{E} \left( \int a^{k/2} \bar{w}(t) e^{-j2\pi f_c a^k t} p(a^k t - mT) dt \int a^{k'/2} \bar{w}^*(t) e^{j2\pi f_c a^{k'} t} p(a^{k'} t - m'T) dt \right) \\ &= T \int \int \mathcal{E} (\bar{w}(t) \bar{w}^*(t')) \frac{\sqrt{a^k a^{k'}}}{T} e^{-j2\pi f_c a^k t} p(a^k t - mT) e^{j2\pi f_c a^{k'} t'} p(a^{k'} t' - m'T) dt dt'. \end{aligned}$$

With the assumption that  $\mathcal{E} (\bar{w}(t) \bar{w}^*(t')) = \sigma^2 \delta(t-t')$ , the above can be further simplified as

$$\begin{aligned} & \mathcal{E} (v_{k,m} v_{k',m'}) \\ &= \sigma^2 T \int \frac{\sqrt{a^k a^{k'}}}{T} e^{-j2\pi f_c a^k t} p(a^k t - mT) e^{j2\pi f_c a^{k'} t} p(a^{k'} t - m'T) dt \\ &\stackrel{a}{=} \sigma^2 T \delta_{k-k'} g_{k,m-m'} \\ &\stackrel{b}{=} \sigma^2 T \delta_{k-k'} \delta_{m-m'}, \end{aligned}$$

where  $\stackrel{a}{=}$  holds per Theorem 5.1, and  $\stackrel{b}{=}$  holds due to (5.33).



## Chapter 6

---

# Robust Semi-blind Transceiver

*Intelligence is the ability to adapt to change.*

Stephen W. Hawking

Chapter 4 and Chapter 5 both describes the wireless transmissions over wideband time-varying channels although the transmit schemes were different. They were common in assuming a perfect knowledge of the wideband channel coefficients at the receiver, which however is normally difficult to achieve. This chapter describes the adaptive multi-layer turbo equalization at the receiver, where the channel estimation is bypassed. Its adaptive ability to track the channel changes gives the robustness to the receiver design for various prevailing environmental conditions.

### 6.1 Introduction

As mentioned in last two chapters, a wideband time-varying channel is often represented by a multi-scale multi-lag (MSML) model [15, 20–22, 32, 33], which corresponds to the multipath nature of a wideband communication channel: the time-of-arrival differences among the propagation paths give rise to multi-lag while the angle-of-arrival differences, and thereby the different Doppler effects from each path give rise to multi-scale.

The receiver design based on such an MSML channel model is challenging, and has only been reported in limited literature such as [21, 33]. A more common practice is to assume that the Doppler effect is uniform to all the propagation paths, which equivalently amounts to a single-scale multi-lag (SSML) assumption [28, 30, 81]. It is well-known that an SSML channel can be turned into a narrowband channel subject to a single carrier frequency offset (CFO) by means of resampling, after which many existing equalization

methods can be applied. Although an SSML model greatly simplifies the receiver design, the performance of the receiver is, to a great extent, hampered by the corresponding modeling error with respect to the actual MSML nature of the channel. In this sense, an optimal resampler plays an extremely important role [29,76]. In addition, an optimal multiple-rate resampling structure is proposed in [90] instead of a single-rate resampling rate used in the previous works. However, it is worth mentioning that both the SSML-based receiver and these optimal resampling methods require perfect knowledge of the WLTV channel, which is very difficult to attain in practice.

For narrowband systems, it has been shown that if the transmit/receiver pulse is properly designed, the receiver can be made more robust against the channel dispersion, thereby reducing the complexity of the receiver design. The importance of pulse design for wideband systems has recently also been recognized in [21,82,85]. Especially in the latter two works, it is shown that if the pulse shape and bandwidth satisfy certain orthogonality conditions, then the continuous MSML channel in the passband, can be parameterized in such a way that the corresponding discrete baseband channel can be represented by a time-invariant finite impulse response (FIR) filter.

Inspired by the results in [85], we will use a root raised-cosine pulse at the transmitter, which is commonly used in existing communication systems. This root raised-cosine pulse is designed to have a very small bandwidth for two reasons: 1) the orthogonality condition that is essential to parameterizing the channel can be satisfied; 2) an underwater acoustic channel usually has a very long delay spread. By letting the transmit pulse assume a small bandwidth, we are able to reduce the number of FIR taps in the effective discrete channel model.

There are two major differences between this chapter and [85] in the transceiver design. Firstly, although both works has a multi-band transmitter structure to fill up the available bandwidth, the subbands in [85] are contiguous to each other and have a different bandwidth. Due to the inter-band interference resulting from the Doppler effect, the corresponding baseband channel becomes a 2D FIR, requiring a more complex equalizer structure. In comparison, the subbands in this work have equal bandwidth, and are sufficiently separated from each other such that the inter-band interference can

be avoided. This facilitates a simpler equalizer design, but the bandwidth efficiency is obviously sacrificed.

Secondly, the parameterization of the channel in [85] is transparent to the channel conditions: the sampling of the channel always starts from 0 in the time plane and from  $f_c$ , the carrier frequency of the transmitted signal, in the frequency plane. In this work, we allow for a multitude of different channel parameterization schemes. In each scheme, the beginning of the sampling positions is aligned with the lag and scale of one certain path by starting from  $\tau_q$  in the time plane and from  $\alpha_q f_c$  in the frequency plane, where  $\tau_q$  and  $\alpha_q$  stand for the lag and scale of the  $q$ th path, respectively. Suppose that there are  $Q$  resolvable propagation paths. We can therefore generate  $Q$  discrete versions of the received (continuous) signal, each related with a distinctive channel model. This means that a single-input multiple-output (SIMO) system is actually established, for which we can call for a multi-branch framework at the receiver. By this means, we are able to achieve a more accurate discrete representation of the MSML channel while at the same time leverage the channel diversity. Interestingly, we notice a similar “multichannel” receiver structure in [91], where  $Q$  asynchronous CDMA users are present: the signal generated at the  $q$ th sub-channel is a differently delayed version of the received signal, which aligns with the  $q$ th CDMA user. If we view each path in the MSML channel as an asynchronous “user”, then our receiver structure is in this sense a generalization of that in [91] in both the time and frequency domain.

Despite a different sampling grid of the channel in the time-frequency plane than that in [85], we can show that for each receiver branch, the corresponding discrete channel can still be modeled by a time-invariant FIR. This allows us to impose a time-invariant FIR structure for the equalizer on each receiver branch. The equalizer taps will be obtained adaptively in this work using a recursive least-squares (RLS) filter. In addition, a phase-locked loop (PLL) is combined with the RLS filter to combat the residual CFO. The latter results from a synchronization error because when we sample the channel in the frequency direction, the starting position might not be perfectly aligned with the actual scale of the path in practice. We notice that such a receiver scheme is just identical to that in [92], but the underlying mechanism is com-

pletely different: the multi-channel framework in [92] corresponds to the multiple antennas deployed at the receiver; further, the time-invariant FIR equalizer structure in [92] is based on the assumption that the channel impulse response stays constant during a short interval of time, while in our work this structure is viable thanks to an optimally designed pulse shape, and does not rely on the constant channel assumption.

## 6.2 System Model Based on an MSML Channel

### 6.2.1 Transmit Signal

For the reasons mentioned in the introduction, we employ a multi-band transmission scheme, where the transmit signal  $\bar{s}(t)$  is comprised of  $K$  signals, each transmitted over a different carrier frequency:

$$\bar{s}(t) = \sum_{k=0}^{K-1} \sum_n s_k(t) e^{j2\pi f_k t}, \quad (6.1)$$

where  $f_k$  stands for the carrier frequency for the the  $k$ th subband around a central frequency  $f_c$  as  $f_k = f_c + (k - \frac{K-1}{2})\Delta_f$ . Here,  $\Delta_f$  denotes the distance between the center frequencies of two adjacent subbands. Additionally,

$$s_k(t) = s_{k,n} p(t - nT), \quad (6.2)$$

where  $s_{k,n}$  stands for the  $n$ th data symbol transmitted in the  $k$ th subband, and  $p(t)$  for the transmit pulse, for which we use a root raised cosine function in this chapter given by

$$p(t) = C \cdot \text{sinc}(t/T) \frac{\cos(\pi\kappa t/T)}{1 - 4\kappa^2 t^2/T^2}, \quad (6.3)$$

with  $\kappa$  being the rolloff in the range  $[0, 1]$ ;  $T$  the symbol period, and  $C$  is a constant such that  $p(t)$  has unit energy. As a result, the bandwidth occupied by each subband is  $B = (1 + \kappa)/T$ . In order to reduce the interference between the subbands, we insert an adequately wide guard band between the subbands such that  $\Delta_f > B$ , and therefore, the overall bandwidth of  $s(t)$  equals  $B + (K - 1)\Delta_f$ .



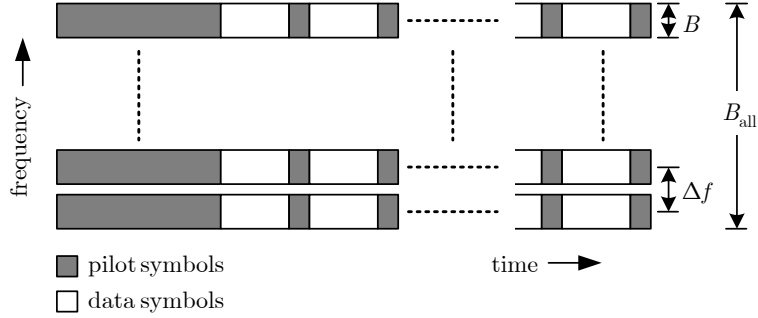


**Figure 6.1:** An example of the proposed multi-band transmission scheme

We assume that the data symbols are transmitted in blocks, and inter-block interference (IBI) has already been eliminated by means of, e.g., zero padding such that it is sufficient to just focus on individual transmit blocks. Let us use  $\mathbf{s}_k = [s_{k,0}, s_{k,1}, \dots, s_{k,N-1}]^T$  to denote the data symbols that are gathered in one such transmit block through the  $k$ th subband. It is assumed to consist of  $N_P$  pilot symbols and  $N_D$  information-carrying symbols, whose positions are given by  $\mathcal{N}_P$  and  $\mathcal{N}_D$ , respectively. In this work, we consider only time-multiplexed pilots and  $\mathcal{N}_D \cup \mathcal{N}_P = \{0, 1, \dots, N-1\}$ .

An example of the transmission scheme as described above is given by Fig. 6.1.

## 6.2.2 Received Signal Resulting from an MSML Channel

We consider a wideband linear time-varying channel as mentioned in (2.5) but with a finite path number of  $Q$ . Its noiseless case can be formulated as

$$\bar{r}(t) = \sum_{q=0}^{Q-1} \bar{h}_q \sqrt{\alpha_q} \bar{s}(\alpha_q(t - \tau_q)), \quad (6.4)$$

where  $\bar{s}(t)$  and  $\bar{r}(t)$  are respectively the actual transmitted and received signal (normally in passband).

## 6.3 Receiver Design

### 6.3.1 Multi-Branch Framework

Corresponding to the MSML feature of the channel, we design a multi-branch receiver, where each branch is obtained based on the parameters of one path of the channel. For the  $q$ th branch in particular, let us define the receive filter as

$$p_q(t) = \alpha_q^{1/2} p(\alpha_q t) \quad (6.5)$$

which is obviously a low-pass filter with bandwidth  $B_q = \alpha_q B$  [c.f. (6.3)].

Before applying this filter, we first down-convert the received signal such that the component of the  $k$ th subband is located at baseband. After the receive filter, the output can be expressed as

$$y_k^{(q)}(t) = \int p_q^*(t-t') \bar{r}(t' + \frac{\tau_q}{\alpha_q}) e^{-j2\pi\alpha_q f_k t'} dt, \quad (6.6)$$

which, after discretization, renders the following signal

$$y_k^{(q)}[n] = y_k^{(q)}(n \frac{T}{\alpha_q}), \quad (6.7)$$

for  $n = 0, \dots, N-1$ . In the above expressions, the parameters  $\alpha_q$  and  $\tau_q$  stem from the scale and delay of the  $q$ th propagation path.

At this stage, we introduce the following proposition (see Appendix 6.A for a proof), which will be crucial to our equalizer design.

*Proposition 6.1.* Let  $a_*$  denote the *basic scaling factor* of  $p(t)e^{j2\pi f_k t}$ , whose meaning will be clear in Appendix 6.A. For channels with realistic scales ( $|\alpha_{\max} - 1| \ll 1$ ), if

$$a_* \geq \frac{2f_k + B}{2f_k - B}, \quad (6.8)$$

then we have

$$y_k^{(q)}[n] \approx \sum_{l=0}^{L_q} g_{k,l}^{(q)} s_{k,n-l}. \quad (6.9)$$

where  $g_{k,l}^{(q)}$  defines the taps of a time-invariant FIR filter of order  $L_q$ .

Proposition 6.1 suggests that if the transmit and receiver filter are designed properly (such that the inequality in (6.8) is satisfied), the discrete baseband I/O relationship can be described by a time-invariant FIR system. To leverage sufficient statistics, we can apply Proposition 6.1 for all the paths present in the channel with the resulting signal  $y_k^{(q)}[n]$  for  $q \in \{0, \dots, Q\}$  forming the output of one branch of the receiver. By this means, we effectively create a single-input multiple-output (SIMO) system. The multi-branch operation is schematically depicted in Fig. 6.2.

Now that we are dealing with a multi-branch framework, and for each branch the effective channel embedded in (6.9) is a time-invariant FIR, this enables in theory a time-invariant FIR equalizer on each branch such that the effective (composite) channel can be perfectly inverted. To establish the taps of such a time-invariant FIR requires, however, the knowledge of  $g_{k,l}^{(q)}$ , which is in turn determined by the path coefficients  $h_q$ ,  $\alpha_q$  and  $\tau_q$ . In practice, estimating these path coefficients can be very challenging, especially for  $h_q$ . Besides, all significant paths of the channel must be estimated, which can inflict a high computational burden in many situations. In this work, we avoid the necessity of estimating all the channel coefficients, but train the equalizer taps adaptively by means of a recursive least-squares filter (RLS). An apparent advantage is that for an individual branch, we only need to estimate the scale and delay of a single path. Another advantage is that we can leverage channel diversity by exploiting the multi-branch structure. Note though that the number of branches is allowed to be smaller than the actual number of paths in the channel.

The delay and scale estimates can be obtained by using a preamble sequence together with a matched-filter bank at the receiver, which should have a good resolution in both scale and time. See e.g., [33] for such a sequence design and the filter bank design. In reality, a mismatch in the scale estimate is more serious than a mismatch in the delay estimate.

*Proposition 6.2.* When the estimation error  $\gamma_q = \alpha_q - \hat{\alpha}_q$  is sufficiently small, we can easily incorporate this estimation error in the discrete model of (6.9), and adapt it to (see Appendix 6.B for a proof)

$$y_k^{(q)}[n] \approx e^{j2\pi f_k n T \gamma_q / \alpha_q} \sum_{l=0}^{L_q} g_{k,l}^{(q)} s_{k,n-l}, \quad (6.10)$$

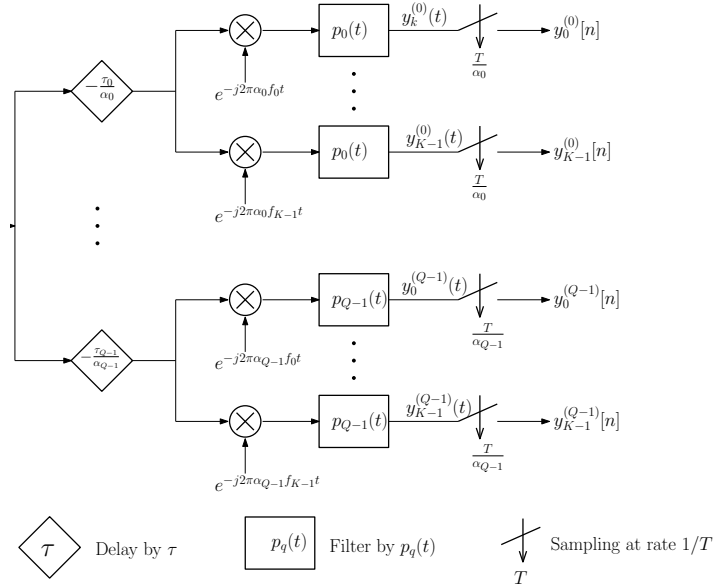


Figure 6.2: A multi-branch block scheme

which suggests that  $y_k^{(q)}[n]$  will be subject to a carrier frequency offset (CFO).

### 6.3.2 Soft Iterative Equalizer

Corresponding to the multi-band transmission scheme and the multi-branch framework at the receiver, we apply for each subband and each branch of the receiver a distinctive equalizer, whose taps will be attained adaptively by means of an RLS scheme. Compared to the ordinary approach, there are two differences in the RLS scheme used in this work: 1) a phase shift is first applied to the received signal to correct the inherent CFO due to the scale mismatch in (6.10); 2) the RLS filter sweeps the received signal forward and backward for several times. This step is especially useful for an underwater environment, where the channel conditions can sometimes be extremely volatile, and as a result, the channel model given in (6.4) is only valid for a very limited duration. To enable robust communication, it is typical that messages are transmitted in short bursts, which imposes a huge pressure on

the convergence rate of the RLS filter. An effective countermeasure is to let the equalizer run over the same received sequence several times until convergence [93, 94].

To describe the above mathematically, let us introduce the vector

$$\mathbf{y}_{k,n}^{(q)} = \begin{bmatrix} y_k^{(q)} \left[ n - \frac{(L_{\text{tap}}-1)}{2} \right] \\ y_k^{(q)} \left[ n - \frac{(L_{\text{tap}}-3)}{2} \right] \\ \vdots \\ y_k^{(q)} \left[ n + \frac{(L_{\text{tap}}-3)}{2} \right] \\ y_k^{(q)} \left[ n + \frac{(L_{\text{tap}}-1)}{2} \right] \end{bmatrix} \quad (6.11)$$

to denote the input at the  $n$ th time interval to the equalizer for the  $k$ th subband and  $q$ th branch, where  $L_{\text{tap}}$  stands for the number of equalizer taps. Then the output of the  $q$ th equalizer obtained during the forward sweep is computed as

$$\hat{s}_{k,n,p}^{(q)} = \mathbf{c}_{k,n-1,p}^{(q)H} \mathbf{y}_{k,n}^{(q)} e^{-j\theta_{k,n-1,p}^{(q)}}, \quad (6.12)$$

where  $\hat{s}_{k,n,p}^{(q)}$  stands for the estimate of the  $n$ -th symbol transmitted over the  $k$ th subband obtained at the  $q$ th branch during the  $p$ -th sweep; likewise,  $\mathbf{c}_{k,n,p}^{(q)}$  stacks the corresponding equalizer taps, and  $\theta_{k,n,p}^{(q)}$  denotes the phase shift applied to the signal  $\mathbf{y}_{k,n}^{(q)}$ . We assume that the sweep index  $p$  is even for a forward sweep, during which the symbol index  $n$  increases from 0 to  $N-1$  when  $p=0$  and from 1 to  $N-1$  in the subsequent forward sweeps. In the backward sweep (with an odd sweep index  $p$ ), the output of the  $q$ th equalizer is computed as

$$\hat{s}_{k,n,p}^{(q)} = \mathbf{c}_{k,n+1,p}^{(q)H} \mathbf{y}_{k,n}^{(q)} e^{-j\theta_{k,n+1,p}^{(q)}}, \quad (6.13)$$

where the symbol index  $n$  decreases from  $N-2$  to 0. For the sake of simplicity, we borrow the notation from [94], and combine the operations in (6.12) and (6.13) in one expression as

$$\hat{s}_{k,n,p}^{(q)} = \mathbf{c}_{k,n\pm 1,p}^{(q)H} \mathbf{y}_{k,n}^{(q)} e^{-j\theta_{k,n\pm 1,p}^{(q)}}, \quad (6.14)$$

where  $+$  is selected in  $\pm$  for the forward sweep, and  $-$  is selected for the backward sweep. Finally, the estimate of  $s_{k,n}$  attained at the  $p$ th sweep is

obtained as the average of the outputs of all the branches as

$$\hat{s}_{k,n,p} = \sum_{q=0}^{Q-1} \hat{s}_{k,n,p}^{(q)}. \quad (6.15)$$

In the sequel, we will describe the steps to update  $\mathbf{c}_{k,n,p}^{(q)H}$  and  $\theta_{k,n,p}^{(q)}$ . This is achieved with the aid of a soft-input soft-output (SISO) decoder [95], where the equalizer provides not only the hard information, i.e., the symbol estimates, but also the soft information, i.e., the *a posteriori* log-likelihood ratios (LLR) to the decoder. For binary phase-shift keying (BPSK) symbols<sup>1</sup>, the *a priori* LLR is computed as

$$\text{LLR}_{k,n,p}^{(\text{in})} = \ln \left( \frac{e^{-(\text{Re}[\hat{s}_{k,n,p}] - \mu)^2 / 2\sigma^2}}{e^{-(\text{Re}[\hat{s}_{k,n,p}] + \mu)^2 / 2\sigma^2}} \right), \quad (6.16)$$

where  $\mu$  and  $\sigma^2$  are obtained by exploiting knowledge of the pilot BPSK symbols as

$$\mu = \frac{1}{N_p} \sum_{n \in \mathcal{N}_p} \sum_{k=0}^{K-1} \text{Re}[\hat{s}_{k,n,p}] s_{k,n}, \quad (6.17)$$

and

$$\sigma^2 = \frac{1}{N_p - 1} \sum_{n \in \mathcal{N}_p} \sum_{k=0}^{K-1} |\text{Re}[\hat{s}_{k,n,p}] - \mu s_{k,n}|^2. \quad (6.18)$$

In deriving the above, we have assumed that the symbol estimates during the  $p$ th sweep have a normal distribution with mean  $\pm\mu$  and variance  $\sigma^2$  on the real axis. Such an assumption is made not only for the sake of convenience but also due to the fact that the distribution of random variables at the output of a linear Wiener filter are known to be quite close to Gaussian [96]. In addition, due to the time-invariance FIR assumption on the effective channel (see Proposition 6.1), we have assumed that such statistics obtained at the positions of the pilot symbols will hold for the whole signal sequence, which is approximately true when a sufficient number of pilots are distributed over the signal.

<sup>1</sup>The extension to a higher-order constellation is straightforward, and will not be repeated here due to space restrictions.

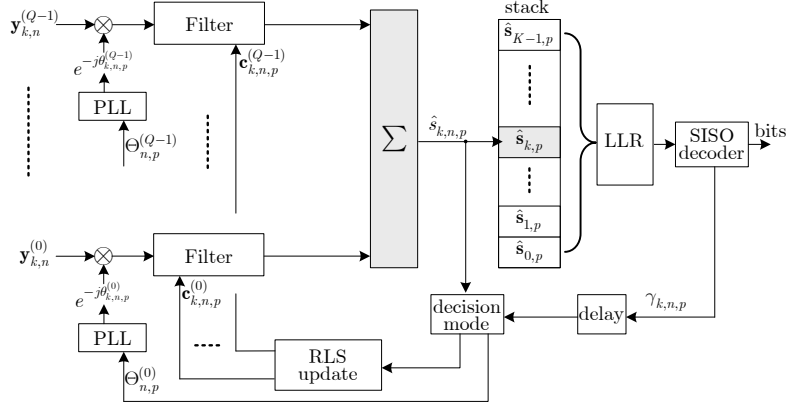


Figure 6.3: The block scheme of the adaptive turbo equalizer

In turn, the SISO decoder will generate, besides decoded bits, soft information in the form of an *a posteriori* LLR, which is fed back to the equalizer to derive the probabilities of  $\hat{s}_{k,n,p}$  belonging to 0 or 1, respectively given by  $\gamma_{k,n,p}(0)$  and  $\gamma_{k,n,p}(1)$ , with

$$\gamma_{k,n,p}(0) = \frac{e^{\text{LLR}_{k,n,p}^{(\text{out})}}}{1 + e^{\text{LLR}_{k,n,p}^{(\text{out})}}}, \quad (6.19)$$

and

$$\gamma_{k,n,p}(1) = 1 - \gamma_{k,n,p}(0). \quad (6.20)$$

Note that  $\gamma_{k,n,p}(0)$  and  $\gamma_{k,n,p}(1)$  indicate the reliability of the estimate  $\hat{s}_{k,n,p}$ .

The block scheme of the proposed equalizer design is depicted in Fig. 6.3.

**Adaptive RLS Filtering** Since we have converted the WLTV channel into a branch of time-invariant FIR channels, an ordinary RLS filtering, which takes a possible CFO at each receiver branch into account, can be applied. A difference in this chapter is that in the decision-directed mode, the updating only takes place if the reference symbols, which will be defined soon, are sufficiently reliable. This is achieved by comparing the soft information  $\gamma_{k,n,p-1}$  provided by the SISO decoder during the previous sweep with a predefined

threshold  $\Gamma$ . With the following definitions

$$\begin{aligned}\bar{\mathbf{c}}_{k,n,p} &= [\mathbf{c}_{k,n,p}^{(0)T}, \dots, \mathbf{c}_{k,n,p}^{(Q-1)T}]^T, \\ \mathbf{x}_{k,n,p}^{(q)} &= \mathbf{y}_{k,n}^{(q)} e^{-j\theta_{k,n\pm 1,p}^{(q)}}, \\ \bar{\mathbf{x}}_{k,n,p} &= [\mathbf{x}_{k,n,p}^{(0)T}, \dots, \mathbf{x}_{k,n,p}^{(Q-1)T}]^T,\end{aligned}\quad (6.21)$$

the updating process is described in Table 6.1.

<p>IF <math>n \in \mathcal{N}_P</math> or <math>\gamma_{k,n,p-1} &gt; \Gamma</math></p> $\bar{\mathbf{g}}_{k,n,p} = \frac{\bar{\mathbf{P}}_{k,n\pm 1,p} \bar{\mathbf{x}}_{k,n,p}^*}{\lambda + \bar{\mathbf{x}}_{k,n,p}^T \bar{\mathbf{P}}_{k,n\pm 1,p} \bar{\mathbf{x}}_{k,n,p}^*},$ $\bar{\mathbf{P}}_{k,n,p} = \lambda^{-1} \left[ \bar{\mathbf{P}}_{k,n\pm 1,p} - \bar{\mathbf{g}}_{k,n,p} \bar{\mathbf{x}}_{k,n,p}^T \bar{\mathbf{P}}_{k,n\pm 1,p} \right],$ $\bar{\mathbf{c}}_{k,n,p} = \bar{\mathbf{c}}_{k,n\pm 1,p} + \epsilon_{k,n,p} \bar{\mathbf{g}}_{k,n,p}$ <p>ELSE</p> $\bar{\mathbf{g}}_{k,n,p} = \bar{\mathbf{g}}_{k,n\pm 1,p},$ $\bar{\mathbf{P}}_{k,n,p} = \bar{\mathbf{P}}_{k,n\pm 1,p},$ $\bar{\mathbf{c}}_{k,n,p} = \bar{\mathbf{c}}_{k,n\pm 1,p}$ <p>END</p>
---

**Table 6.1:** The ordinary RLS algorithm

In Table 6.1,  $\lambda$  denotes the common RLS forgetting factor;  $\bar{\mathbf{g}}_{k,n,p}$  is the Kalman gain vector;  $\bar{\mathbf{P}}_{k,n,p}$  is the error covariance matrix and the error signal is given by

$$\epsilon_{k,n,p} = \hat{s}_{k,n,p} - s_{k,n,p,\text{ref}}, \quad (6.22)$$

where in the training mode,  $n \in \mathcal{N}_P$ , the reference symbols are given by the pilots

$$s_{k,n,p,\text{ref}} = s_{k,n}; \quad (6.23)$$

while in the decision-directed mode,  $n \in \mathcal{N}_P$ , the reference symbols are given by

$$s_{k,n,p,\text{ref}} = \begin{cases} -1 & \text{if } \gamma_{k,n,p-1}(1) > \Gamma, \\ +1 & \text{if } \gamma_{k,n,p-1}(0) > \Gamma, \\ \text{sgn}\{\text{Re}[\hat{s}_{k,n,p}]\} & \text{otherwise.} \end{cases} \quad (6.24)$$



The adaptive filter is initialized with  $\bar{\mathbf{c}}_{k,0,0} = [1, \mathbf{0}_{1 \times (QL_{\text{tap}}-1)}]^T$  and  $\bar{\mathbf{P}}_{k,0,0} = \mathbf{I}_{QL_{\text{tap}}}$ . At the signal boundaries of consecutive forward and backward sweeps, the following convention is adopted as  $\bar{\mathbf{c}}_{k,N,p} = \bar{\mathbf{c}}_{k,N,p-1}$  and  $\bar{\mathbf{P}}_{k,N,p} = \bar{\mathbf{P}}_{k,N,p-1}$  for odd  $p$  (from forward sweep to backward sweep), otherwise  $\bar{\mathbf{c}}_{k,1,p} = \bar{\mathbf{c}}_{k,1,p-1}$  and  $\bar{\mathbf{P}}_{k,1,p} = \bar{\mathbf{P}}_{k,1,p-1}$ .

As we mentioned before, short-burst messaging is typical to underwater communications, which imposes a huge pressure on the convergence rate of the RLS filter. To accelerate the convergence, let us approximate that the effective channel from each branch is uncorrelated. Accordingly, we can enforce a block diagonal structure on the error covariance matrix as

$$\bar{\mathbf{P}}_{k,n,p} = \begin{bmatrix} \mathbf{P}_{k,n,p}^{(0)} & & \\ & \ddots & \\ & & \mathbf{P}_{k,n,p}^{(Q-1)} \end{bmatrix} \quad (6.25)$$

where  $\mathbf{P}_{k,n,p}^{(q)}$  is an  $L_{\text{tap}} \times L_{\text{tap}}$  matrix with  $\mathbf{P}_{k,0,0}^{(q)} = \mathbf{I}_{L_{\text{tap}}}$ . It is then easy to simplify the ordinary RLS algorithm as in Table 6.2.

IF $n \in \mathcal{N}_P$ or $\gamma_{k,n,p-1} > \Gamma$
$\mathbf{g}_{k,n,p}^{(q)} = \frac{\mathbf{P}_{k,n\pm 1,p}^{(q)} \mathbf{x}_{k,n,p}^{(q)*}}{\lambda + \sum_{q'=0}^{Q-1} \mathbf{x}_{k,n,p}^{(q')T} \mathbf{P}_{k,n\pm 1,p}^{(q')} \mathbf{x}_{k,n,p}^{(q')*}}$ $\mathbf{P}_{k,n,p}^{(q)} = \lambda^{-1} \left[ \mathbf{P}_{k,n\pm 1,p}^{(q)} - \mathbf{g}_{k,n,p}^{(q)} \mathbf{x}_{k,n,p}^{(q)T} \mathbf{P}_{k,n\pm 1,p}^{(q)} \right]$ $\mathbf{c}_{k,n,p}^{(q)} = \mathbf{c}_{k,n\pm 1,p}^{(q)} + \epsilon_{k,n,p} \mathbf{g}_{k,n,p}^{(q)}$
ELSE
$\mathbf{g}_{k,n,p}^{(q)} = \mathbf{g}_{k,n\pm 1,p}^{(q)}$ $\mathbf{P}_{k,n,p}^{(q)} = \mathbf{P}_{k,n\pm 1,p}^{(q)}$ $\mathbf{c}_{k,n,p}^{(q)} = \mathbf{c}_{k,n\pm 1,p}^{(q)}$
END

**Table 6.2:** The simplified RLS algorithm

We notice that a similar approach is adopted in [97] though in a different context. In [94], the same simplified RLS is used but a motivation lacks.

**Adaptive Carrier Recovery** Following the derivations given in [98], the optimum  $\theta_{k,n,p}^{(q)}$  is achieved when

$$\text{Im}\{\hat{s}_{k,n,p}^{(q)} s_{k,n,p,\text{ref}}^*\} = 0. \quad (6.26)$$

Note that the CFO contained in (6.10) is caused by a mismatch between the actual channel scale and its estimate. Such a mismatch is distinctive for each branch of the receiver but common to all the subbands. This means that in the steady state,  $\theta_{k,n,p}^{(q)}$  should equal  $2\pi f_k n T \gamma_q / \alpha_q$  [c.f. (6.10)], which equivalently leads to  $\frac{\theta_{0,n,p}^{(q)}}{f_0} = \dots = \frac{\theta_{K-1,n,p}^{(q)}}{f_{K-1}}$ . For this reason, the second-order digital phase-locked loop (PLL) used in [92, 98, 99], can be adapted for the multi-band scheme in this work as

$$\Theta_{n,p}^{(q)} = \frac{1}{K} \sum_{k=0}^{K-1} \frac{\text{Im} \left\{ \hat{s}_{k,n,p}^{(q)} \left( s_{k,n,p,\text{ref}} - \sum_{q', q' \neq q} \hat{s}_{k,n,p}^{(q')} \right)^* \right\}}{f_k}, \quad (6.27)$$

$$\eta_{n\pm 1,p}^{(q)} = \eta_{n,p}^{(q)} + (-1)^p \Theta_{n,p}^{(q)}, \quad (6.28)$$

$$\beta_{n\pm 1,p}^{(q)} = \beta_{n,p}^{(q)} + K_1 \Theta_{n,p}^{(q)} + (-1)^p K_2 \eta_{n\pm 1,p}^{(q)}, \quad (6.29)$$

$$\theta_{k,n,p}^{(q)} = f_k \beta_{n,p}^{(q)}, \quad (6.30)$$

where  $K_1$  and  $K_2$  denote the proportional and integral phase-tracking constants, respectively. The initial values of  $\eta_{n,p}^{(q)}$  and  $\beta_{n,p}^{(q)}$  are set to zeros for  $n = p = 0$ . Compared to the adopted PLL in [92, 98, 99], another difference is the existence of  $(-1)^p$ , which is inserted here due to the existence of a backward sweep.

## 6.4 Experimental Results

We start from a noisy version of (6.4):

$$\bar{r}(t) = \sum_{r=0}^{Q-1} \bar{h}_q \alpha_q^{1/2} s(\alpha_q(t - \tau_q)) + \bar{n}(t), \quad (6.31)$$

where the scale  $\alpha_q$  is modeled to be uniformly distributed between  $[0.99, 1.01]$ ; the delay  $\tau_q$  is modeled to be uniformly distributed between  $[0, 200]$ ms and

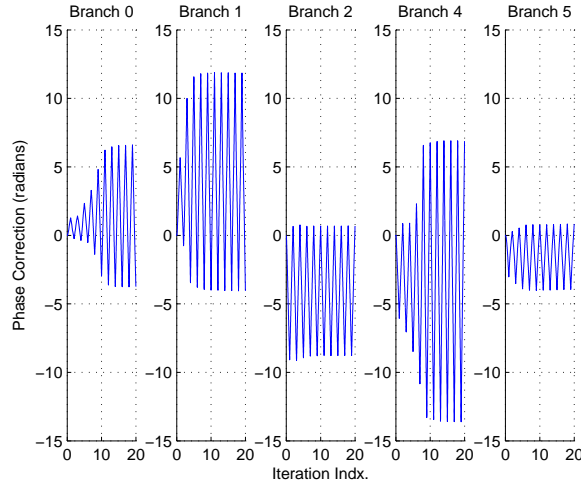


Figure 6.4: Phase corrections at each branch

the path gain  $\bar{h}_q$  is modeled as an i.i.d. Gaussian variable with mean zero and variance  $\sigma_q^2$ , where  $\sigma_q^2$  follows an exponential power delay profile as  $\sigma_q^2 = e^{-\tau_q/50}$ . The values of  $\bar{h}_q$ ,  $\tau_q$  and  $\alpha_q$  are assumed to stay constant during the transmission. In addition, the noise is assumed to be a white Gaussian process with mean zero and variance  $\sigma^2$ . The signal-to-noise ratio (SNR) in this chapter is defined as

$$\text{SNR} = \frac{\int |\bar{r}(t) - \bar{n}(t)|^2 dt}{\int |\bar{n}(t)|^2 dt}.$$

For the transmitted data signal, we choose  $K = 38$  subbands. Each subband has a bandwidth  $B = 60\text{Hz}$ , and the distance between the center frequencies of two adjacent subbands is  $\Delta_f = 100\text{Hz}$ . Therefore, the overall bandwidth is  $3790\text{ Hz}$ , which spans the spectrum  $[4105\text{Hz}, 7895\text{Hz}]$ .

In each subband, a sequence of  $N = 117$  symbols is transmitted: 70 data symbols are equally partitioned into four blocks, with pilot symbols inserted in between. The remaining 47 pilot symbols are arranged in such a fashion that the initial pilot block consists of 31 pilot symbols and each of the other four pilot blocks has 4 pilot symbols. We refer to Fig. 6.1 for the transmitter

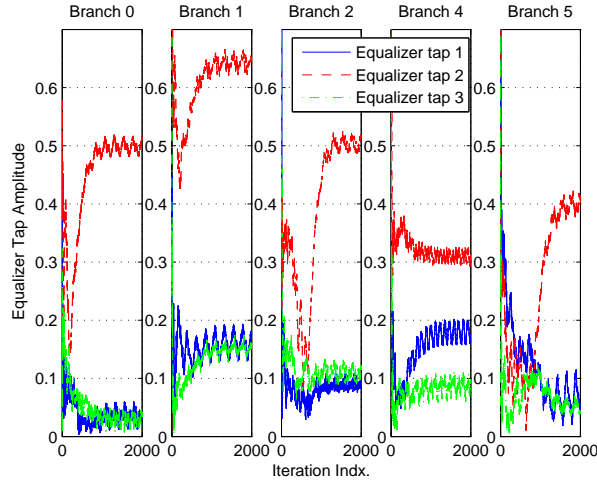


Figure 6.5: Convergence of equalizer taps (subband 0)

structure. The data symbols are based on BPSK modulation and generated in the following way: 1330 information bits are encoded by a standard 1/2-rate convolutional encoder with the generator polynomial (5, 7). The resulting bits are randomly interleaved and then allocated to each subband.

The transmit pulse is defined in (6.3), which uses a symbol rate of  $1/T = 60\text{Hz}$  and a rolloff factor  $\kappa = 1/2$ . It can be shown that with parameters chosen as such, the inequality in (6.8), which is crucial to the validity of Proposition 6.1, is satisfied.

For the receiver, we let the equalizer on each branch have  $L_{\text{tap}} = 3$  taps; the forgetting factor of the RLS filter is  $\lambda = 0.99$ ; the probability threshold is  $\Gamma = 0.8$ , and the PLL parameters are chosen as  $K_1 = 2 \times 10^{-2}$  and  $K_2 = 4 \times 10^{-2}$ . The equalizer performs  $P = 20$  iterations sweeping over the received signal forward and backward.

For the sake of illustration, let us first look at one particular realization of such a channel for  $\text{SNR} = 5 \text{ dB}$ , which comprises  $Q = 20$  paths. The parameters of the 10 most significant paths are given in Table 6.3.

Out of the 20 paths, the channel estimator, which corresponds to a scale-lag filter-bank used as in [33], has only detected 5 paths whose delay and

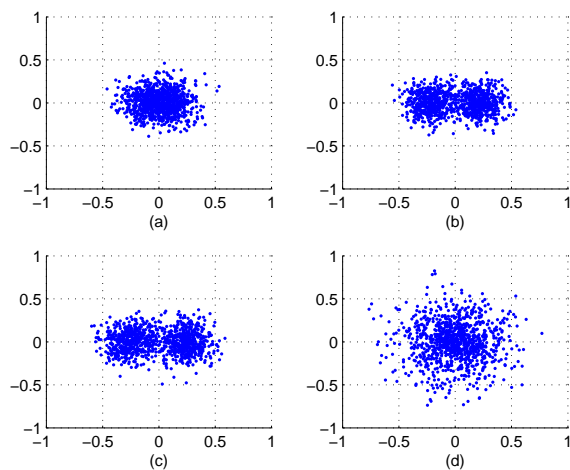


**Figure 6.6:** Constellation of equalized BPSK symbols: (a) after the 1st sweep; (b) after the 10th sweep; (c) after the 20th sweep; (d) using a single-branch receiver and after the 20th sweep.

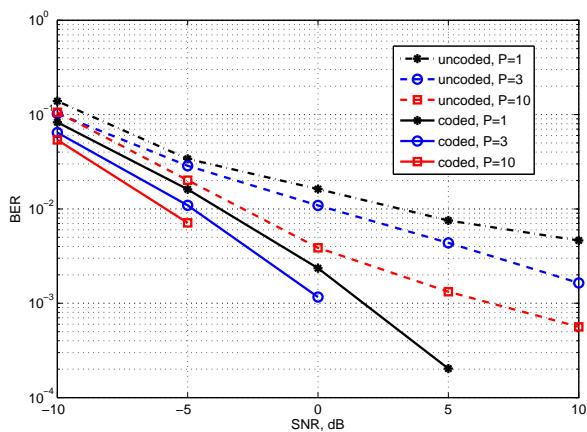


**Figure 6.7:** Uncoded and coded BER performance of our proposed equalizer v.s. SNR.

**Table 6.3:** A channel example

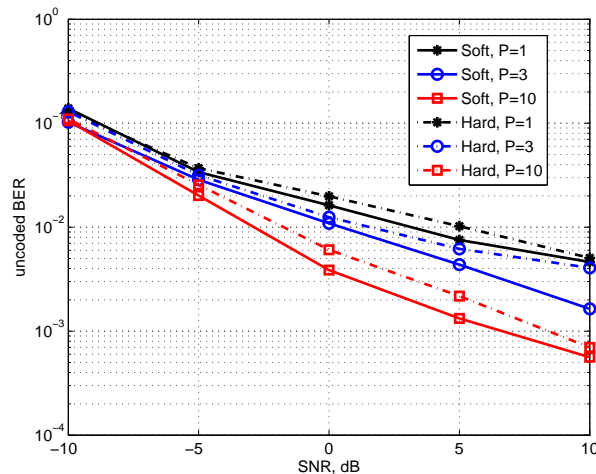
Channel State Information					Estimation	
	path	gain	scale	delay (ms)	scale	delay (ms)
SNR: 5dB	$q = 0$	0.4422	0.9968	162.1	0.9965	162.5
	$q = 1$	0.4267	0.9991	78.8	0.9995	78.8
	$q = 2$	0.4252	1.0048	0	1.0050	0.02
	$q = 3$	0.3968	0.9963	80.2		
	$q = 4$	0.2916	1.0004	27.7	1.0005	27.7
	$q = 5$	-0.2707	0.9987	111.6	0.9985	111.6
	$q = 6$	-0.1964	0.9977	73.5		
	$q = 7$	-0.1767	0.9991	32.2		
	$q = 8$	0.1234	0.9967	105.4		
	$q = 9$	-0.1109	1.0029	87.3		

**Table 6.4:** Performance

BER prior to decoding	$P = 1$	$P = 5$	$P = 10$	$P = 15$	$P = 20$
	0.25	0.093	0.0417	0.0368	0.0281
BER after decoding	$P = 1$	$P = 5$	$P = 10$	$P = 15$	$P = 20$
	0.3516	0.0039	0	0	0

scale estimates are given in the corresponding rows in Table 6.3 (note that the 3rd path is not detected). Accordingly, five branches are established at the receiver corresponding to each detected path. Fig. 6.4 illustrates the phase correction in radians generated by the PLL for these 5 branches, respectively during the  $P = 20$  sweeps, from which we can make the following observations: 1) the slope of the phase correction in the forward sweeps is opposite to that in the downward sweeps because the order of the input samples is reversed; 2) for each branch, the larger the scale mismatch of the  $q$ th path, the steeper the slope of the phase correction curve at the  $q$ th receiver branch. This could suggest that the  $q$ th path has the most significant contribution to the signal obtained at the  $q$ th receiver branch.

In Fig. 6.5, the amplitude of the equalizer taps for subband 0 obtained during different iterations is plotted. One can see that when convergence is reached, the equalizer taps only have a small oscillation. This, together with



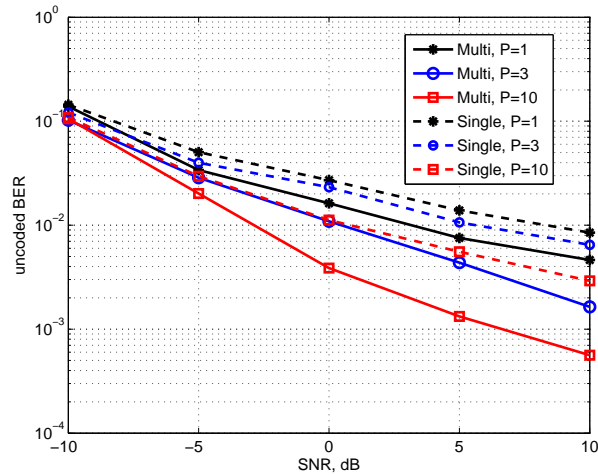
**Figure 6.8:** *Uncoded BER performance v.s. SNR, using soft-guided RLS updating and unconditional RLS updating.*

Fig. 6.4, indicates that the effective channel at each receiver branch is approximately a time-invariant FIR subject to a CFO as Proposition 6.1 suggests.

The bit-error rate (BER) after a certain number of iterations is given in Table 6.4 where we can see, especially from the BER prior to decoding, that multiple (forward and backward) sweeps allow for more time for the equalizer to converge. This is also corroborated by Fig. 6.6(a) through Fig. 6.6(c), which show a compacter constellation cloud with more sweeps.

In Fig. 6.6(d), we show the constellation of the equalized symbols, which are obtained by a single-branch receiver. In this case, the receiver is aligned with path 0, which has the strongest gain, and which uses  $\hat{\alpha}_0$  to resample the received signal. Such a receiver is commonly used in the field, e.g., in [94] or in [92] with a single receive antenna. It is obvious from Fig. 6.6(d) that when the multi-scale effect of the channel is very pronounced as in the example, such a single-branch receiver will become inferior of symbol detection.

We generalize the above observations by running a Monte Carlo simulation. During each run, a different realization of the channel, data symbols and noise is created at random. Fig. 6.7 illustrates the BER performance



**Figure 6.9:** *Uncoded BER performance v.s. SNR, using our multi-layer equalizer and a single-layer equalizer.*

against the SNR both prior to and after decoding, for the 1st, 3rd and 10th sweeps. It is clear that the BER performance improves with the number of iterations as well as the SNR.

As discussed in the previous section, the proposed receiver uses soft information not only for decoding purposes but also in the decision-directed mode the updating stage of the equalizer taps : the soft information determines which reference symbol is to be used as well as whether or not to update the equalizer taps. As shown in Fig. 6.8, which depicts the BER prior to decoding, utilizing soft information makes the adaptive equalizer converge much faster than utilizing just hard information.

The great performance improvement of our multi-branch equalizer with respect to that of a single-branch equalizer is quantitatively illustrated by Fig. 6.9.



## 6.5 Summary

A multi-band transmitter combined with an adaptive multi-branch equalizer is proposed for communications over an MSML channel. The multi-band transmission is designed to reduce the equalization complexity, while maintaining a high data rate. Thanks to a carefully designed transmit/receive pulse, the signal obtained at each receiver branch can be described by a time-invariant FIR subject to a CFO. A semi-blind equalizer is applied for such a channel, which comprises a PLL, followed by a time-invariant FIR filter. The updating of both the PLL and the filter taps are achieved by means of a SISO turbo decoder. Simulation results show that the proposed transceiver yields a robust performance for the MSML channels.

## Appendix 6.A Proof of Proposition 6.1

Because we assume that the guard bands between adjacent subbands are large enough such that the inter-band interference due to Doppler can be neglected, it suffices therefore to just focus on a single-band case ( $K = 0$ ) in the proof, i.e.,  $\bar{s}(t) = s_0(t)e^{j2\pi f_0 t}$ .

For analytical purposes, let us use rewrite (6.4) in a more generalized way as

$$\bar{r}(t) = \int_1^{\alpha_{\max}} \int_0^{\tau_{\max}} \bar{h}(\alpha, \tau) \sqrt{\alpha} \bar{s}(\alpha(t - \tau)) d\alpha d\tau, \quad (6.32)$$

where  $\bar{h}(\alpha, \tau)$  is also known as the wideband spread function (WSF) of the channel [20], which has a support for  $\alpha \in [1, \alpha_{\max}]$  and  $\tau \in [0, \tau_{\max}]$ . Actually, (6.4) can be viewed as a special case of (6.32) as  $\bar{h}(\alpha, \tau) = \sum_q \bar{g}_q \delta(\alpha - \alpha_q) \delta(\tau - \tau_q)$ .

We first introduce two parameters  $a_*$  and  $T_*$ , which are called as the *dilation spacing* and *translation spacing*, respectively. These two parameters are uniquely determined by the transmit pulse  $p(t)$ . With the bandwidth of  $p(t)$  being  $B$ , we have  $T_* = 1/B = T$ ; further, if the Mellin support<sup>2</sup> of  $p(t)e^{j2\pi f_0 t}$  being  $M_*$ , then  $a_* = e^{1/M_*}$ . With aid of  $a_*$  and  $T_*$ , it is shown in [85] that the continuous WSF  $\bar{h}(\alpha, \tau)$  can be approximated by a smoothed version of discrete samples, and accordingly, the integrals in (6.32) be replaced by finite summations such that

$$\bar{r}(t) \approx \sum_{r=0}^{R_*} e^{j2\pi f_0 a_*^r t} \sum_{l=0}^{L_*(r)} g_{r,l} a_*^{r/2} s(a_*^r t - lT_*), \quad (6.33)$$

where

$$g_{r,l} = \int_0^{\tau_{\max}} \int_1^{\alpha_{\max}} \bar{h}(\alpha, \tau) e^{-j2\pi f_0 a_*^r \tau} \operatorname{sinc}\left(r - \frac{\ln \alpha}{\ln a_*}\right) \operatorname{sinc}\left(l - \frac{a_*^r \tau}{T_*}\right) d\alpha d\tau, \quad (6.34)$$

and  $R_* = \lceil \ln \alpha_{\max} / \ln a_* \rceil$  and  $L_*(r) = \lceil a_*^r \tau_{\max} / T_* \rceil$ .

The expression in (6.33) suggests that the continuous channel  $\bar{h}(\alpha, \tau)$  is approximated by a series of discrete coefficients  $g_{r,l}$ 's, which are obtained by sampling the channel in the scale (frequency) direction at positions

$$\{f_0, a_* f_0, \dots, a_*^{R_*} f_0\}$$

<sup>2</sup>See [34] for the definition of the Mellin support.

and sample in the lag (time) direction at positions

$$\{0, T_*/a_*^r, \dots, L_*T_*/a_*^r\}.$$

Actually, we can sample the channel on a different set of grids. To realize this, let us consider an auxiliary signal

$$\tilde{r}^{(q)}(t) = \sqrt{a_*^{-\frac{d}{D}}} \bar{r} \left( a_*^{-\frac{d}{D}} \left( t + \frac{d'}{D'} T_* \right) \right), \quad (6.35)$$

which is obtained by time-shifting the original received signal  $\bar{r}(t)$  with a factor of  $-\frac{d'}{D'} T_*$ , and then scaling with a factor of  $a_*^{-\frac{d}{D}}$ . Here,  $d, D, d'$  and  $D'$  are such chosen integers that

$$\alpha_q = a_*^{\frac{d}{D}} \text{ and } \tau_q = \frac{d'}{D'} T_*, \quad (6.36)$$

for  $q = 0, \dots, Q$ . For this auxiliary signal, we can find an expression by adapting (6.32) to

$$\tilde{r}^{(q)}(t) = \sqrt{a_*^{-\frac{d}{D}}} \int \int \bar{h}(\alpha, \tau) \sqrt{\alpha} \left( \alpha a_*^{-\frac{d}{D}} s \left( t - \frac{\tau - a_*^{-\frac{d}{D}} \frac{d'}{D'} T_*}{a_*^{-\frac{d}{D}}} \right) \right) d\alpha d\tau.$$

By letting  $\alpha' = \alpha a_*^{-\frac{d}{D}}$  and  $\tau' = \tau a_*^{\frac{d}{D}} - \frac{d'}{D'} T_*$ , we obtain that

$$\tilde{r}^{(q)}(t) = \int \int \bar{h} \left( \alpha' a_*^{\frac{d}{D}}, \frac{\tau' + \frac{d'}{D'} T_*}{a_*^{\frac{d}{D}}} \right) \sqrt{\alpha'} s(\alpha'(t - \tau')) d\alpha' d\tau'. \quad (6.37)$$

Obviously, the function

$$\tilde{h}^{(q)}(\alpha, \tau) = \bar{h} \left( \alpha a_*^{\frac{d}{D}}, \frac{\tau + \frac{d'}{D'} T_*}{a_*^{\frac{d}{D}}} \right) \quad (6.38)$$

defines the WSF corresponding this scaled/delayed version  $\tilde{r}^{(q)}(t)$ , on which we can apply the same smoothing operation just like in (6.33) leading to the following approximation

$$\tilde{r}^{(q)}(t) \approx \sum_{r=0}^{R_*} e^{j2\pi f_0 a_*^r t} \sum_{l=0}^{L_*(r)} \tilde{g}_{r,l}^{(q)} a_*^{r/2} s(a_*^r t - lT_*), \quad (6.39)$$

where we can show that

$$\begin{aligned}
\tilde{g}_{r,l}^{(q)} &= \int \int \tilde{g}^{(q)}(\alpha, \tau) e^{-j2\pi f_0 a_\star^r \tau} \operatorname{sinc}\left(r - \frac{\ln \alpha}{\ln a_\star}\right) \operatorname{sinc}\left(l - \frac{a_\star^r \tau}{T_\star}\right) d\alpha d\tau, \\
&= \int \int \bar{h}\left(\alpha a_\star^{\frac{d}{D}}, \frac{\tau + \frac{d'}{D'} T_\star}{a_\star^{\frac{d}{D}}}\right) e^{-j2\pi f_0 a_\star^r \tau} \\
&\quad \times \operatorname{sinc}\left(r - \frac{\ln \alpha}{\ln a_\star}\right) \operatorname{sinc}\left(l - \frac{a_\star^r \tau}{T_\star}\right) d\alpha d\tau, \\
&= e^{j2\pi f_0 a_\star^r \frac{d'}{D'} T_\star} g_{r+\frac{d}{D}, l+\frac{d'}{D'}} = e^{j2\pi f_0 a_\star^r \frac{d'}{D'} T_\star} g_{r,l}^{(q)},
\end{aligned}$$

where [c.f. (6.34) and (6.36)]

$$\begin{aligned}
g_{r,l}^{(q)} &= g_{r+\frac{d}{D}, l+\frac{d'}{D'}} \\
&= \int \int \bar{h}(\alpha, \tau) e^{-j2\pi f_0 a_\star^{r+\frac{d}{D}} \tau} \\
&\quad \times \operatorname{sinc}\left(r + \frac{d}{D} - \frac{\ln \alpha}{\ln a_\star}\right) \operatorname{sinc}\left(l + \frac{d'}{D'} a_\star^r - \frac{a_\star^{r+\frac{d}{D}} \tau}{T_\star}\right) d\alpha d\tau.
\end{aligned}$$

The above relationship will be important when we realize that

$$\bar{r}(t) = \sqrt{a_\star^{\frac{d}{D}}} \tilde{r}^{(q)}\left(a_\star^{\frac{d}{D}} t - \frac{d'}{D'} T_\star\right), \quad (6.40)$$

and by substituting (6.39) we have

$$\begin{aligned}
\bar{r}(t) &\approx \sum_{r=0}^{R_\star} e^{j2\pi f_0 a_\star^r \left(a_\star^{\frac{d}{D}} t - \frac{d'}{D'} T_\star\right)} \sum_{l=0}^{L_\star(r)} \tilde{g}_{r,l}^{(q)} \sqrt{a_\star^{r+\frac{d}{D}}} s\left(a_\star^r \left(a_\star^{\frac{d}{D}} t - \frac{d'}{D'} T_\star\right) - l T_\star\right), \\
&= \sum_{r=0}^{R_\star} e^{j2\pi f_0 a_\star^{r+\frac{d}{D}} t} \sum_{l=0}^{L_\star(r)} g_{r+\frac{d}{D}, l+\frac{d'}{D'}} \sqrt{a_\star^{r+\frac{d}{D}}} s\left(a_\star^{r+\frac{d}{D}} t - \left(l + \frac{d'}{D'} a_\star^r\right) T_\star\right).
\end{aligned} \quad (6.41)$$

Compared with (6.33), we understand that the continuous channel  $\bar{h}(\alpha, \tau)$  can also be sampled in a different set of grids. To realize this, we can rewrite (6.41) further as

$$\bar{r}(t) \approx \sum_{r=\frac{d}{D}, 1+\frac{d}{D}, \dots} e^{j2\pi f_0 a_\star^r t} \sum_{l=\frac{d'}{D'} a_\star^r, 1+\frac{d'}{D'} a_\star^r, \dots} g_{r,l}^{(q)} \sqrt{a_\star^r} s(a_\star^r t - l T_\star).$$

In light of (6.36), the above suggests that the channel is sample at the scale (frequency) direction at positions

$$\{\alpha_q f_0, \alpha_q a_* f_0, \dots\}$$

and sampled in the lag (time) direction at positions

$$\left\{ \frac{0 \cdot T_*}{\alpha_q a_*^r} + \frac{\tau_q}{\alpha_q}, \frac{1 \cdot T_*}{\alpha_q a_*^r} + \frac{\tau_q}{\alpha_q}, \dots \right\}.$$

Obviously, the beginning of the sampling position is aligned with the scale/lag of the  $q$  path if we use a discrete path model in (6.32) to define the channel.

We resume from (6.41), and find one baseband counterpart of  $\bar{r}(t)$  as

$$\bar{r}\left(t + \frac{\tau_q}{\alpha_q}\right) e^{-j2\pi f_0 \alpha_q t} = r^{(q)}(t) + \Delta_r^{(q)}(t), \quad (6.42)$$

with

$$r^{(q)}(t) = \sum_l g_{0,l}^{(q)} \sqrt{\alpha_q} s(\alpha_q t - lT_*), \quad (6.43)$$

and

$$\Delta_r^{(q)}(t) = \sum_{r \neq 0} e^{j2\pi f_0 \alpha_q (a_*^r - 1)t} \sum_l g_{r,l}^{(q)} \sqrt{\alpha_q a_*^r} s(\alpha_q a_*^r t - lT_*), \quad (6.44)$$

where we have used a new symbol  $g_{r,l}^{(q)} := g_{r+\frac{d}{D}, l+\frac{d'}{D}}$  not only to simplify the notation, but also underline its relationship with the  $q$ th path.

Due to (??) and the fact  $T = T_*$ , it follows that

$$\Delta_r^{(q)}(t) = \sum_{r \neq 0} e^{j2\pi f_0 \alpha_q (a_*^r - 1)t} \sum_l g_{r,l}^{(q)} \sqrt{\alpha_q a_*^r} \sum_n s_{0,n} p(\alpha_q a_*^r t - lT_* - nT_*).$$

Now that the bandwidth of  $p(\alpha_q a_*^r t)$  equals  $\alpha_q a_*^r B$ , the above implies that the lower-bound of  $\Delta_r^{(q)}(t)$  in the frequency domain is  $\alpha_q (a_* - 1) f_0 - \alpha_q a_* B/2$ . As a result, by apply a matched filter  $p_q(t)$  on  $\bar{r}\left(t + \frac{\tau_q}{\alpha_q}\right) e^{-j2\pi f_0 \alpha_q t}$ , we are able to remove the nuisance term  $\Delta_r^{(q)}(t)$  if the higher-bound of  $p_q(t)$  in the frequency domain, equal to  $\alpha_q B/2$ , is smaller than the lower-bound of  $\Delta_r^{(q)}(t)$ , or equivalently,

$$a_* \geq \frac{2f_0 + B}{2f_0 - B}. \quad (6.45)$$

In that case, the output of the matched filter becomes

$$\begin{aligned} y_0^{(q)}(t) &= \int p_q^*(t-t')\bar{r}(t'+\frac{\tau_q}{\alpha_q})e^{-j2\pi f_0\alpha_q t'} dt', \\ &= \int p_q(t'-t) \sum_l g_{0,l}^{(q)} \sqrt{\alpha_q} s(\alpha_q t' - lT_\star) dt', \end{aligned} \quad (6.46)$$

where the last equality is obtained by substituting (??) and using the property that  $p(t)$  as defined in (6.3) is real and symmetric. If we sample  $y_0^{(q)}(t)$  with a sampling rate  $\alpha_q/T$ , the resulting sample obtained at the  $m$ th sampling instant can be expressed as

$$\begin{aligned} y_0^{(q)}[m] &= \int p_q^*(t - \frac{mT_\star}{\alpha_q}) \sum_l g_{0,l}^{(q)} \sqrt{\alpha_q} \sum_n s_{0,n} p(\alpha_q t - lT_\star - nT_\star) dt, \\ &= \sum_l h_{0,l}^{(q)} \sum_n s_{0,n} \int \alpha_q p(\alpha_q t - mT_\star) p(\alpha_q t - lT_\star - nT_\star) dt \\ &\stackrel{a}{=} \sum_l g_{0,l}^{(q)} \sum_n s_{0,n} \delta_{m-n-l} \\ &= \sum_l g_{0,l}^{(q)} s_{0,m-l}, \end{aligned} \quad (6.47)$$

where in  $\stackrel{a}{=}$ , we have made use of the property that for a root raised cosine function  $p(t)$  as given in (6.3), it holds that  $\int \alpha_q p(\alpha_q t - mT) p(\alpha_q t - nT) dt = \delta_{m-n}$ . By (6.47), we conclude the proof of Proposition 6.1.

## Appendix 6.B Proof of Proposition 6.2

We follow (6.41) in Proposition 6.1 to provide the proof for Proposition 6.2. We only focus on the mismatch of the scale parameters. Instead of  $\alpha_q = a_\star^{\frac{d}{D}}$  in (6.36), the scale estimate gives  $\hat{\alpha}_q = \alpha_q - \gamma_{q'}$ , for  $q = 0, \dots, Q-1$ . In this case we build (6.42) in practice as

$$\bar{r}(t + \hat{\tau}_q/\hat{\alpha}_q) e^{-j2\pi f_0 \hat{\alpha}_q t} = \bar{r}(t + \tau_q/\alpha_q + \Delta_t) e^{-j2\pi f_0 \hat{\alpha}_q t},$$

where  $\Delta_t = \hat{\tau}_q/\hat{\alpha}_q - \tau_q/\alpha_q$ . We ignore the timing shifts for analysis simplicity reasons, and thus consider the following equation alternatively as

$$\begin{aligned}
& \bar{r}(t + \tau_q/\alpha_q) e^{-j2\pi f_0 \hat{\alpha}_q t} \\
&= e^{-j2\pi f_0 (\alpha_q - \gamma_q) t} \sum_{r=0}^{R_\star} e^{j2\pi f_0 a_\star^{r+\frac{d}{D}} t} \\
&\quad \times \sum_{l=0}^{L_\star(r)} g_{r+\frac{d}{D}, l+\frac{d'}{D'}} \sqrt{a_\star^{r+\frac{d}{D}}} s \left( a_\star^{r+\frac{d}{D}} t - \left( l + \frac{d'}{D'} a_\star^r \right) T_\star \right) \\
&= \sum_{r=0}^{R_\star} e^{j2\pi f_0 a_\star^r \gamma_q t} e^{j2\pi f_0 \alpha_q (a_\star^r - 1) t} \sum_{l=0}^{L_\star(r)} g_{r,l}^{(q)} \sqrt{\alpha_q a_\star^r} s \left( \alpha_q a_\star^r t - \left( l + \frac{d'}{D'} a_\star^r \right) T_\star \right) \\
&= \hat{r}^{(q)}(t) + \hat{\Delta}_r^{(q)}(t) \tag{6.48}
\end{aligned}$$

where

$$\hat{r}^{(q)}(t) = e^{j2\pi f_0 \gamma_q t} \sum_l g_{0,l}^{(q)} \sqrt{\alpha_q} s(\alpha_q t - l T_\star)$$

and

$$\hat{\Delta}_r^{(q)}(t) = \sum_{r \neq 0} e^{j2\pi f_0 a_\star^r \gamma_q t} e^{j2\pi f_0 \alpha_q (a_\star^r - 1) t} \sum_l g_{r,l}^{(q)} \sqrt{\alpha_q a_\star^r} s(\alpha_q a_\star^r t - l T_\star).$$

Similarly as clarified in Proposition 6.1, to eliminate the term  $\hat{\Delta}_r^{(q)}(t)$ . Specifically,  $\hat{r}^{(q)}(t)$  is higher-bounded by the frequency component  $\alpha_q B/2 + f_0 \gamma_q$ , while  $\hat{\Delta}_r^{(q)}(t)$  is lower-bounded by the frequency component  $f_0 \hat{\alpha}_q (a_\star - 1) + f_0 a_\star \gamma_q - \alpha_q a_\star B/2$ . Thus, we herein require in the frequency domain that

$$\begin{aligned}
\alpha_q B/2 + f_0 \gamma_q &\leq f_0 \hat{\alpha}_q (a_\star - 1) + f_0 a_\star \gamma_q - \alpha_q a_\star B/2 \\
&= f_0 \alpha_q (a_\star - 1) + f_0 \gamma_q - \alpha_q a_\star B/2,
\end{aligned}$$

and in this manner, we have the same condition given by (6.45).

It indicates that the output of the matched filter becomes

$$\begin{aligned}
y_0^{(q)}(t) &= \int \sqrt{\hat{\alpha}_q} p^*(\hat{\alpha}_q(t-t')) \bar{r}(t') e^{-j2\pi f_0 \hat{\alpha}_q t'} dt', \\
&= \int \sqrt{\hat{\alpha}_q} p^*(\hat{\alpha}_q(t-t')) \hat{r}^{(q)}(t) dt', \\
&= \int \sqrt{\hat{\alpha}_q \alpha_q} p^*(\hat{\alpha}_q(t-t)) e^{j2\pi f_0 \gamma_q t'} \sum_l g_{0,l}^{(q)} s(\alpha_q t' - l T_\star) dt',
\end{aligned}$$

which is an adapted version of (6.46). If we sample  $y_0^{(q)}(t)$  with a sampling rate  $\hat{\alpha}_q/T$  by assuming  $T_\star = T$ , the resulting sample obtained at the  $m$ th sampling instant can be expressed as

$$\begin{aligned}
y_0^{(q)}[m] &= \int p^*(\hat{\alpha}_q t - mT_\star) \sum_l g_{0,l}^{(q)} \sqrt{\hat{\alpha}_q \alpha_q} \sum_n s_{0,n} p(\alpha_q t - lT_\star - nT_\star) dt, \\
&= \sum_l h_{0,l}^{(q)} \sum_n s_{0,n} \int \sqrt{\hat{\alpha}_q \alpha_q} e^{j2\pi f_0 \gamma_q t} \\
&\quad \times p((\alpha_q - \gamma_q)t - mT) p(\alpha_q t - lT - nT) dt \\
&\approx \sum_l h_{0,l}^{(q)} \sum_n s_{0,n} \int \alpha_q e^{j2\pi f_0 \gamma_q t} p(\alpha_q t - mT) p(\alpha_q t - lT - nT) dt \\
&= \sum_l h_{0,l}^{(q)} \sum_n s_{0,n} \int e^{j2\pi f_0 (t-mT) \gamma_q / \alpha_q} p(t) p(t - (l+n-m)T) dt \\
&= e^{-j2\pi f_0 m T \gamma_q / \alpha_q} \sum_l h_{0,l}^{(q)} \sum_n s_{0,n} \\
&\quad \times \int e^{j2\pi f_0 t \gamma_q / \alpha_q} p(t) p(t - (l+n-m)T) dt
\end{aligned}$$

where we argue that the scale estimate error  $\gamma_q$  is sufficiently small such that  $\gamma_q / \alpha_q \ll 1$ . Similarly due to the fact that  $\gamma_q$  is sufficiently small such that

$$\int e^{j2\pi f_0 t \gamma_q / \alpha_q} p(t) p(t - (l+n-m)T) dt \approx \int p(t) p(t - (l+n-m)T) dt,$$

we are allowed to proceed with

$$\begin{aligned}
y_0^{(q)}[m] &\approx e^{-j2\pi f_0 m T \gamma_q / \alpha_q} \sum_l h_{0,l}^{(q)} \sum_n s_{0,n} \int p(t) p(t - (l+n-m)T) dt \\
&= e^{-j2\pi f_0 m T \gamma_q / \alpha_q} \sum_l h_{0,l}^{(q)} \sum_n s_{0,n} \delta_{m-l-n} \\
&= e^{-j2\pi f_0 m T \gamma_q / \alpha_q} \sum_l h_{0,l}^{(q)} s_{0,m-l}
\end{aligned} \tag{6.49}$$

In other words, if we consider a generalization of (6.49) on the  $k$ th subband, we have

$$y_k^{(q)}[n] \approx e^{-j2\pi f_k n T \gamma_q / \alpha_q} \sum_l h_{k,l}^{(q)} s_{k,n-l},$$

which concludes the proof of Proposition 6.2.



## Chapter 7

---

# Conclusions and Future Work

*To acknowledge what is the known and the unknown is knowledge.*

Confucius

## 7.1 Conclusions

Future wireless communication systems are required to offer a high data transfer rate between fast moving terminals. The resulting time-varying channels will bring great challenges to transceiver designs. Especially when a wideband transmission is introduced in, e.g., underwater acoustic communications and ultra wideband radar systems, the Doppler scaling factors can severely deteriorate the performance of the communication system.

Corresponding to the research questions raised in Chapter 1, this thesis proposed the following answers:

- For an orthogonal frequency-division multiplexing (OFDM) transmission over a narrowband time-varying channel, we investigated efficient architectures to implement channel estimation and equalization based on a basis expansion model (BEM) employed to model the time-varying channel. Among several BEM options, we found in particular that the critically-sampled complex exponential BEM (CCE-BEM) allows for a more efficient hardware architecture than other choices, while still maintaining a high modeling accuracy. Moreover, a small BEM order is appealing since it can provide a sufficiently high accuracy for the symbol detection while avoiding costly hardware utilization.
- The amount of interference resulting from wideband channels, which we have assumed to follow the multi-scale/multi-lag (MSML) model,

has been analyzed in the frequency domain and the time domain, respectively. The wideband channels result in full channel matrices in both domains. However, banded approximations are still possible, leading to a significant reduction in the equalization complexity. We found that optimal resampling is indispensable for wideband OFDM communications, and then proposed to use the conjugate gradient (CG) algorithm to equalize the channel iteratively which allows to further reduce the overall complexity by using a truncated CG in practice. The suitability of the CG equalization with a diagonal preconditioner has also been discussed. Measures for determining whether time-domain or frequency-domain equalization should be undertaken were provided to obtain the best BER performance with the same complexity.

- The traditional single-rate transmission scheme, e.g., OFDM, has an inherent match with the uniform time-frequency (T-F) lattice of narrowband time-varying channels. When multiple Doppler scales emerge in a wideband channel, a non-uniform T-F lattice is introduced and thus novel transmission schemes can be developed. A new parameterized data model was first proposed, where the continuous MSML channel is approximated by discrete channel coefficients. We have proposed a novel multi-layer transceiver for such MSML channels. At the transmitter, the information symbols are placed at different non-overlapping sub-bands or layers to enhance the spectral efficiency, where each layer has a distinctive bandwidth, and therefore, the transmission in each layer is characterized by a different data rate. To combat the multiscale multi-lag effect of the channel, a filterbank is deployed at the receiver, where each branch of the filterbank resamples the received signal in a different way. By selecting a proper transmitter pulse, we have shown that the effective input/output (I/O) relationship in the discrete domain can be captured by a block-diagonal channel, with each diagonal block being a banded matrix. As a result, the low-complexity equalizers that have been intensively used for narrowband systems become also applicable here. This novel multi-layer transmission scheme can achieve the same bandwidth efficiency as a traditional transmission scheme, e.g., OFDM, while allowing for

an improved bit-error-ratio (BER) performance especially when a large scale spread is present.

- To bypass the exact estimation of wideband channel coefficients, a multi-band transmitter combined with an adaptive multi-branch equalizer has been proposed for communications over a wideband MSML channel. At the transmitter, a multi-band transmission is used, which reduces the receiver complexity while still maintaining a high data rate. At the receiver, a multi-branch framework is adopted, where each branch is aligned with the scale and delay of one path in the propagation channel. By intelligently designing the transmit and receive filter, the discrete signal at each branch can be characterized by a time-invariant finite impulse response (FIR) system subject to a carrier frequency offset (CFO). This enables a simple equalizer design: a phase-locked loop (PLL), which aims to eliminate the CFO is followed by a time-invariant FIR filter. The updating of both the PLL and the filter taps is achieved by leveraging the soft-input soft-output (SISO) information yielded by a turbo decoder. The proposed transceiver has been validated to render a more robust performance for the MSML channels than conventional methods.

Consequently, we can conclude the thesis as follows. For a narrowband time-varying OFDM system, an OFDM receiver using a simple BEM design (i.e., the CCE-BEM) and a small BEM order is sufficient to support mobile users at a realistic velocity as discussed in Chapter 3. If wideband transmissions are adopted, Doppler scales emerge when communication terminals are moving rapidly and thus the channel is time-varying. When a large Doppler scale spread is present, a single-scale assumption at the receiver introduces a remarkable performance penalty, and thus the multi-scale behavior of the channel should be considered. In this case, previous methods of designing narrowband OFDM receivers are not viable. In addition to an optimum resampling operation, many extra efforts are needed to be taken to reduce the complexity of equalizing a wideband time-varying channel, compared with a narrowband OFDM receiver. This part has been discussed in Chapter 4. As an alternative, in Chapter 5, a novel block transmission scheme, which supports multiple data rates on different frequency subbands

or layers, has been proposed instead of the traditional OFDM transmission that adopts a single data rate at all subcarriers. The benefits of this multi-layer transmission scheme include the re-use of previous equalization structures designed for narrowband time-varying channel, as well as a performance improvement for the wideband time-varying channels. However, if the exact channel information is not available which is usually the case in the wideband regime, an adaptive equalization approach is required. Using a multi-band transmission and a multi-branch receiver structure, the multi-layer turbo equalization proposed in Chapter 6 bypasses the precise channel estimation and provides a robust performance for the wideband MSML channels.

## 7.2 Future Work

**Filed Testing** In this thesis, we did not mention any experiment based on realistic data. However, we have already examined our transceiver described in Chapter 6 using some sea trial data, and the tested results validate our proposed scheme. In the future, more sea trials can be carried out, e.g., within an European research project called “RACUN” (i.e., Robust Acoustic Communications in Underwater Networks), and the results from these experiments may be included in our future paper which is currently being prepared. For a real-time testing in practice, we have already initialized the conversion from the Matlab<sup>®</sup> codes into suitable C/C++ codes to run our signal-processing algorithm on a specific digital signal processor (DSP) embedded in the hardware platform. This part of work also needs to be finalized in the future.

**Hardware Prototyping** In most existing works on time-varying communication systems, how to prototype the transceiver in hardware is rarely studied. We have discussed an efficient hardware architecture for the channel estimator and channel equalizer of OFDM systems over narrowband time-varying channels. However, this is still far from a hardware prototype design of the whole system. For wideband time-varying systems, researches on the hardware prototyping are even more scarce.

**Compressive Sensing** Compressive sensing allows for an efficient reconstruction of sparse signals from sub-Nyquist-rate samples. Compared to the conventional approach based on the Nyquist sampling theory, this technique can exploit the sparsity of the channel in the time and frequency domain, thereby significantly reducing the power consumption of analog-to-digital converters. Hence it is particularly useful for wideband signals, which are usually sparse in nature and the corresponding Nyquist sampling rate can be too high to be practical. It could be interesting to combine compressive sensing techniques with our proposed processing procedures for MSML channels, which may further simplify the receiver designs proposed in this thesis.

**Cooperative Networks** In this thesis, we focus on a point-to-point communication link instead of cooperative networking. In fact, a future wireless communication terminal will likely not operate alone but jointly work with many other users. Therefore, how to efficiently cooperate with each other, particularly in wideband MSML channels, and how to build a reliable communication network could be a worthwhile research topic.



---

## Bibliography

- [1] R. Mailloux, A. Oliner, M. Salazar-Palma, T. Sarkar, and D. Sengupta. *History of Wireless*. Wiley-IEEE Press, 2006.
- [2] P. Schniter. Low-complexity equalization of OFDM in doubly selective channels. *IEEE Transactions on Signal Processing*, 52(4):1002–1011, 2004.
- [3] L. Rugini, P. Banelli, and G. Leus. Simple equalization of time-varying channels for OFDM. *IEEE Communications Letters*, 9(7):619–621, 2005.
- [4] Z. Tang, R. C. Cannizzaro, G. Leus, and P. Banelli. Pilot-assisted time-varying channel estimation for OFDM systems. *IEEE Transactions on Signal Processing*, 55(5):2226–2238, 2007.
- [5] K. Fang, L. Rugini, and G. Leus. Low-complexity block turbo equalization for OFDM systems in time-varying channels. *IEEE Transactions on Signal Processing*, 56(11):5555–5566, 2008.
- [6] X. Ma and W. Zhang. Fundamental limits of linear equalizers: Diversity, capacity, and complexity. *IEEE Transactions on Information Theory*, 54(8):3442–3456, 2008.
- [7] H.-C. Wu. Analysis and characterization of intercarrier and interblock interferences for wireless Mobile OFDM systems. *IEEE Transactions on Broadcasting*, 52(2):203–210, 2006.
- [8] X. Ma and G. B. Giannakis. Maximum-diversity transmissions over doubly selective wireless channels. *IEEE Transactions on Information Theory*, 49(7):1832–1840, 2003.
- [9] I. Barhumi, G. Leus, and M. Moonen. Equalization for OFDM over doubly-selective channels. *IEEE Transactions on Signal Processing*, 54(4):1445–1458, April 2006.

- 
- [10] T. Strohmer and S. Beaver. Optimal OFDM design for time-frequency dispersive channels. *IEEE Transactions on Communications*, 51(7):1111–1122, 2003.
- [11] I. Barhumi, G. Leus, and M. Moonen. Time-domain and frequency-domain per-tone equalization for OFDM in doubly-selective channels. *Elsevier Signal Processing*, 84(11):2055–2066, November 2004.
- [12] T. H. Glisson, C. I. Black, and A. P. Sage. On sonar signal analysis. *IEEE Transactions on Aerospace and Electronic Systems*, 6:37 – 50, 1970.
- [13] P. Bello. Characterization of randomly time-variant linear channels. *IEEE Transactions on Communications Systems*, 11(4):360–393, 1963.
- [14] W. C. Jakes. *Microwave Mobile Communications*. Wiley, 1974.
- [15] L. G. Weiss. Wavelets and wideband correlation processing. *IEEE Signal Processing Magazine*, 11(1):13–32, 1994.
- [16] D. W. Ricker. The Doppler sensitivity of large TW phase modulated waveforms. *IEEE Transactions on Signal Processing*, 40(10):2406–2413, 1992.
- [17] A. B. Carlson. *Communication systems*. McGraw-Hill Inc, 2nd edition, 1981.
- [18] M. Speth, S.A. Fechtel, G. Fock, and H. Meyr. Optimum receiver design for wireless broad-band systems using OFDM. *IEEE Transactions on Communications*, 11:1668–1677, 1999.
- [19] E. J. Kelly and R. P. Wishner. Matched-filter theory for high-velocity accelerating targets. *IEEE Transactions on Military Electronics*, 0:56 – 69, 1965.
- [20] L. H. Sibul, L. G. Weiss, and T. L. Dixon. Characterization of stochastic propagation and scattering via Gabor and wavelet transforms. *Journal of Computational Acoustics*, 2(1):345–369, Jan. 1994.
- [21] Y. Jiang and A. Papandreou-Suppappola. Discrete time-scale characterization of wideband time-varying systems. *IEEE Transactions on Signal Processing*, 54(4):1364–1375, 2006.
- [22] S. Rickard, R. Balan, V. Poor, and S. Verdu. Canonical time-frequency, time-scale, and frequency-scale representations of time-varying channels. *Journal of Communication and Information Systems*, 5(5):1–30, 2005.
- [23] R. K. Young. *Wavelet theory and its applications*. Kluwer Academic Publishers, 1995.
- [24] A. Bircan, S. Tekinay, and A. N. Akansu. Time-frequency and time-scale representation of wireless communication channels. In *Proc. IEEE-SP Int Time-Frequency and Time-Scale Analysis Symp*, volume 1, pages 373–376, 1998.



- [25] U. Mitra and G. Leus. Equalizers for multi-scale/multi-lag wireless channels. In *Proc. IEEE Global Commun. Conf. (GLOBECOM)*, pages 1–5, 2010.
- [26] T. Rappaport. *Wireless Communications Principles and Practice*. Prentice Hall, 2nd edition, 2002.
- [27] J. G. Proakis. *Digital Communications*. New York: McGraw-Hill, 4rd edition, 2001.
- [28] B. Li, S. Zhou, M. Stojanovic, L. Freitag, and P. Willett. Multicarrier communication over underwater acoustic channels with nonuniform Doppler shifts. *IEEE Journal of Oceanic Engineering*, 33(2):198–209, 2008.
- [29] S. Yerramalli and U. Mitra. Optimal resampling of OFDM signals for multiscale-multilag underwater acoustic channels. *IEEE Journal of Oceanic Engineering*, 36(1):126–138, 2011.
- [30] A.-B. Salberg and A. Swami. Doppler and frequency-offset synchronization in wideband OFDM. *IEEE Transactions on Wireless Communications*, 4(6):2870–2881, 2005.
- [31] G. Kaiser. *A Friendly Guide to Wavelets*. Birkhauser, Boston, 1994.
- [32] B.-G. Iem, A. Papandreou-Suppappola, and G. F. Boudreaux-Bartels. Wideband Weyl symbols for dispersive time-varying processing of systems and random signals. *IEEE Transactions on Signal Processing*, 50(5):1077–1090, 2002.
- [33] A. R. Margetts, P. Schniter, and A. Swami. Joint scale-lag diversity in wideband mobile direct sequence spread spectrum systems. *IEEE Transactions on Wireless Communications*, 6(12):4308–4319, 2007.
- [34] J. Bertrand, P. Bertrand, and J. P. Ovarlez. The Mellin transform. In A. D. Poularikas, editor, *The Transforms and Applications Handbook*, chapter 11, pages 829–885. CRC Press LLC, Boca Raton, Fla, USA, 1996.
- [35] L. Cohen. The scale representation. *IEEE Transactions on Signal Processing*, 41(12):3275–3292, 1993.
- [36] A. M. Sayeed and B. Aazhang. Joint multipath-Doppler diversity in mobile wireless communications. *IEEE Transactions on Communications*, 47(1):123–132, 1999.
- [37] G. B. Giannakis and C. Tepedelenlioglu. Basis expansion models and diversity techniques for blind identification and equalization of time-varying channels. *Proceedings of the IEEE*, 86(10):1969–1986, 1998.

- [38] X. Ma, G. B. Giannakis, and S. Ohno. Optimal training for block transmissions over doubly selective wireless fading channels. *IEEE Transactions on Signal Processing*, 51(5):1351–1366, 2003.
- [39] T. Zemen and C. F. Mecklenbrauker. Time-variant channel estimation using discrete prolate spheroidal sequences. *IEEE Transactions on Signal Processing*, 53(9):3597–3607, 2005.
- [40] K. Fang, G. Leus, and L. Rugini. Block transmissions over doubly-selective channels: Iterative channel estimation and turbo equalization. *EURASIP Journal on Advances in Signal Processing*, 2010:13, 2010.
- [41] T. Hrycak, S. Das, G. Matz, and H. G. Feichtinger. Low complexity equalization for doubly selective channels modeled by a basis expansion. *IEEE Transactions on Signal Processing*, 58(11):5706–5719, 2010.
- [42] M. Visintin. Karhunen-Loève expansion of a fast Rayleigh fading process. *IET Electronics Letters*, 32(18):1712–1713, Aug 1996.
- [43] M. Dong, L. Tong, and B.M. Sadler. Optimal insertion of pilot symbols for transmissions over time-varying flat fading channels. *IEEE Transactions on Signal Processing*, 52(5):1403–1418, May 2004.
- [44] M. K. Tsatsanis and G. B. Giannakis. Time-varying system identification and model validation using wavelets. *IEEE Transactions on Signal Processing*, 41(12):3512–3523, 1993.
- [45] M. I. Doroslovacki and H. Fan. Wavelet-based linear system modeling and adaptive filtering. *IEEE Transactions on Signal Processing*, 44(5):1156–1167, 1996.
- [46] M. Martone. Wavelet-based separating kernels for array processing of cellular DS/CDMA signals in fast fading. *IEEE Transactions on Communications*, 48(6):979–995, 2000.
- [47] J. A. C. Bingham. Multicarrier modulation for data transmission: an idea whose time has come. *IEEE Communications Magazine*, 28(5):5–14, 1990.
- [48] Z. Wang and G. B. Giannakis. Wireless multicarrier communications: where Fourier meets Shannon. *IEEE Signal Processing Magazine*, 17(3):29–48, 2000.
- [49] B. Muquet, Z. Wang, G. B. Giannakis, M. de Courville, and P. Duhamel. Cyclic prefixing or zero padding for wireless multicarrier transmissions? *IEEE Transactions on Communications*, 50(12):2136–2148, 2002.
- [50] G. H. Golub and C. F. van Loan. *Matrix Computations*. Johns Hopkins Univ. Press, 3rd edition, 1996.

- [51] I. Daubechies. *Ten lectures on wavelets*. Society for Industrial and Applied Mathematics, Philadelphia, PA, USA, 1992.
- [52] S. Galli and O. Logvinov. Recent developments in the standardization of power line communications within the IEEE. *IEEE Communications Magazine*, 46(7):64–71, July 2008.
- [53] F. Xiong. *Digital Modulation Techniques*. Artech House, Inc., Norwood, MA, USA, 2nd edition, 2006.
- [54] S. L. Linfoot, M. K. Ibrahim, and M. M. Al-Akaidi. Orthogonal wavelet division multiplex: An alternative to OFDM. *IEEE Transactions on Consumer Electronics*, 53(2):278–284, 2007.
- [55] K. M. Wong, J. Wu, T. N. Davidson, Q. Jin, and P.-C. Ching. Performance of wavelet packet-division multiplexing in impulsive and gaussian noise. *IEEE Transactions on Communications*, 48(7):1083–1086, 2000.
- [56] A. R. Lindsey. Wavelet packet modulation for orthogonally multiplexed communication. *IEEE Transactions on Signal Processing*, 45(5):1336–1339, 1997.
- [57] G. W. Wornell. Emerging applications of multirate signal processing and wavelets in digital communications. *Proceedings of the IEEE*, 84(4):586–603, 1996.
- [58] W. W. Jones. Multi-scale wavelet modulation. In *Proc. Southeastern Symp. System Theory*, pages 576–580, 1994.
- [59] X. Cai and G. B. Giannakis. Bounding performance and suppressing intercarrier interference in wireless mobile OFDM. *IEEE Transactions on Communications*, 51(12):2047–2056, 2003.
- [60] G. Leus. On the estimation of rapidly time-varying channels. In *Proc. Europ. Signal Process. Conf. (EUSIPCO)*, Vienna, Austria, Sept. 2004.
- [61] L. Rugini, P. Banelli, and G. Leus. Low-complexity banded equalizers for OFDM systems in doppler spread channels. *EURASIP Journal on Applied Signal Processing*, 2006(Article ID 67404):248 – 248, 2006.
- [62] D. K. Borah and B. D. Hart. Frequency-selective fading channel estimation with a polynomial time-varying channel model. *IEEE Transactions on Communications*, 47(6):862–873, June 1999.
- [63] S. Tomasin, A. Gorokhov, H. Yang, and J.-P. Linnartz. Iterative interference cancellation and channel estimation for mobile OFDM. *IEEE Transactions on Wireless Communications*, 4(1):238–245, Jan. 2005.

- [64] C. Dick and F. Harris. FPGA implementation of an OFDM PHY. In *Proc. Asilomar Conference on Signals, Systems, and Computers*, volume 1, pages 905–909, 2003.
- [65] Y. Tang, L. Qian, and Y. Wang. Optimized software implementation of a full-rate IEEE 802.11a compliant digital baseband transmitter on a digital signal processor. In *Proc. IEEE Global Commun. Conf. (GLOBECOM)*, volume 4, 2005.
- [66] Z. Tang, R. Remis, and M. L. Norderwaard. On preconditioned conjugate gradient method for time-varying OFDM channel equalization. In *Proc. IEEE Int. Conf. Acoust., Speech, Signal Process. (ICASSP)*, volume 5, pages 2119–2122, Kyoto, Japan, 2012.
- [67] Z. Tang and G. Leus. Time-varying MIMO-OFDM channel estimation with aid of pilots. *EURASIP Journal on Advances in Signal Processing*, 1:74, 2011.
- [68] E.-J. Im. *Optimizing the performance of sparse matrix-vector multiplication*. PhD thesis, University of California Berkeley, May 2000.
- [69] High rate ultra wideband PHY and MAC standard, 2008.
- [70] A. Takach, B. Bowyer, and T. Bollaert. C based hardware design for wireless applications. In *Proc. Design, Auto. and Test in Europe (DATE)*, pages 124–129, 2005.
- [71] E. M. Sozer, J. G. Proakis, R. Stojanovic, J. A. Rice, A. Benson, and M. Hatch. Direct sequence spread spectrum based modem for under water acoustic communication and channel measurements. In *Proc. IEEE/MTS OCEANS*, volume 1, pages 228–233, Monticello, IL, USA, 1999.
- [72] G. Leus and P. van Walree. Multiband OFDM for covert acoustic communications. *IEEE Journal on Selected Areas in Communications*, 26(9):1662–1673, 2008.
- [73] J. R. Shewchuk. An introduction to the conjugate gradient method without the agonizing pain. Technical report, Carnegie Mellon University,, 1994.
- [74] M. Benzi. Preconditioning techniques for large linear systems: A survey. *Journal of Computational Physics*, 182:418–477, 2002.
- [75] M. J. Groote and T. Huckle. Parallel preconditioning with sparse approximate inverses. *SIAM Journal on Scientific Computing*, 18:838–853, 1997.
- [76] Z. Tang, R. Remis, G. Leus, T. Xu, and M. L. Norderwaard. Equalization for multi-scale/multi-lag OFDM channels. In *Proc. Allerton Conf. Comm., Control, and Comput.*, volume 1, pages 654–661, Illinois, USA, 2011.

- [77] T. Xu, Z. Tang, G. Leus, and U. Mitra. Time- or frequency-domain equalization for wideband ofdm channels? In *Proc. IEEE Int. Conf. Acoust., Speech, Signal Process. (ICASSP)*, volume 5, pages 3029–3032, Kyoto, Japan, 2012. accepted by ICSSAP 2012.
- [78] C. C. Paige and M. A. Saunders. LSQR: An algorithm for sparse linear equations and sparse least square problems. *ACM Transactions on Mathematical Software*, 8:43–71, 1982.
- [79] M. Hanke. *Conjugate Gradient Type Methods for ill-Posed Problems*. Longman Scientific & Technical, 1992.
- [80] D. Falconer, S. L. Ariyavisitakul, A. Benyamin-Seeyar, and B. Eidson. Frequency domain equalization for single-carrier broadband wireless systems. *IEEE Communications Magazine*, 40(4):58–66, 2002.
- [81] K. Tu, D. Fertonani, T. M. Duman, M. Stojanovic, J. G. Proakis, and P. Hursky. Mitigation of intercarrier interference for OFDM over time-varying underwater acoustic channels. *IEEE Journal of Oceanic Engineering*, 36(2):156–171, 2011.
- [82] G. Leus, T. Xu, and U. Mitra. Block transmission over multi-scale multi-lag wireless channels. In *Proc. Asilomar Conference on Signals, Systems, and Computers*, pages 1050–1054, 2010.
- [83] G. W. Wornell and A. V. Oppenheim. Wavelet-based representations for a class of self-similar signals with application to fractal modulation. *IEEE Transactions on Information Theory*, 38(2):785–800, 1992.
- [84] W. W. Jones. *A unified approach to orthogonally multiplexed communication using wavelet bases and digital filter banks*. Ph.d. dissertation, Ohio University, Athens, OH, U.S., August 1994.
- [85] T. Xu, G. Leus, and U. Mitra. Orthogonal wavelet division multiplexing for wideband time-varying channels. In *Proc. IEEE Int. Conf. Acoust., Speech, Signal Process. (ICASSP)*, volume 5, pages 3556–3559, Prague, Czech, 2011.
- [86] C. Cattani. Shannon wavelets theory. *Mathematical Problems in Engineering*, page doi:10.1155/2008/164808, 2008.
- [87] W. Kozek and A. F. Molisch. Nonorthogonal pulseshapes for multicarrier communications in doubly dispersive channels. *IEEE Journal on Selected Areas in Communications*, 16(8):1579–1589, 1998.
- [88] A. Barbieri, G. Caire, and U. Mitra. An approximate eigenmode decomposition for doubly-selective wireless channels. In *Proc. IEEE Int. Conf. Acoust., Speech, Signal Process. (ICASSP)*, pages 2857 – 2860, March 2008.

- [89] E. J. Zalubas and W. J. Williams. Discrete scale transform for signal analysis. In *Proc. IEEE Int. Conf. Acoust., Speech, Signal Process. (ICASSP)*, volume 3, pages 1557–1560, 1995.
- [90] K. Tu, T.M. Duman, J.G. Proakis, and M. Stojanovic. Cooperative MIMO-OFDM communications: Receiver design for Doppler-distorted underwater acoustic channels. In *Proc. Asilomar Conference on Signals, Systems, and Computers*, pages 1335–1339, 2010.
- [91] M. K. Tsatsanis and G. B. Giannakis. Optimal decorrelating receivers for DS-CDMA systems: A signal processing framework. *IEEE Transactions on Signal Processing*, 44(12):3044–3055, December 1996.
- [92] M. Stojanovic, J. Catipovic, and J. G. Proakis. adaptive multichannel combining and equalization for underwater acoustic communications. *Journal of the Acoustical Society of America*, 94(3):1621–1631, 1993.
- [93] Z. Tang and G. Leus. RLS direct equalizer estimation with assistance of pilots for time-varying channels. *Proc. Europ. Signal Process. Conf. (EUSIPCO)*, September 2005.
- [94] P. A. van Walree and G. Leus. Robust underwater telemetry with adaptive turbo multiband equalization. *IEEE Journal of Oceanic Engineering.*, 34(4):645–655, 2009.
- [95] R. Koetter, A. C. Singer, and M. Tuchler. Turbo equalization. *IEEE Signal Processing Magazine*, 21(1):67–80, 2004.
- [96] H. V. Poor and S. Verdú. Probability of error in MMSE multiuser detection. *IEEE Transactions on Information Theory*, 43(3):858–871, 1997.
- [97] R. Otnes and M. Tuchler. Iterative channel estimation for turbo equalization of time-varying frequency-selective channels. *IEEE Transactions on Wireless Communications*, 3(6):1918–1923, 2004.
- [98] M. Stojanovic, J. A. Catipovic, and J. G. Proakis. Phase-coherent digital communications for underwater acoustic channels. *IEEE Journal of Oceanic Engineering*, 19(1):100–111, 1994.
- [99] A. Weinberg and B. Liu. Discrete time analyses of nonuniform sampling first- and second-order digital phase lock loops. *IEEE Transactions on Communications*, 22(2):123–137, 1974.

---

## Samenvatting

Dit proefschrift is gewijd aan transceiver ontwerpen voor draadloze communicatiesystemen met hoge transmissiesnelheden en snel bewegende zenders of ontvangers. De uitdagingen zijn tweeledig. Enerzijds hebben toekomstige draadloze systemen meer spectrale bandbreedte nodig om hogere datasnelheden te halen, hetgeen kan resulteren in frequentie-selectiviteit van het communicatiekanaal. Anderzijds ontstaan bij hoge mobiele snelheden Doppler-effecten, hetgeen kan resulteren in tijd-selectiviteit van de communicatiekanalen. Daarom is het waarschijnlijk dat toekomstige draadloze communicatiesystemen moeten werken met dubbel-selectieve kanalen. Dit veroorzaakt velerlei problemen in het ontwerp van transceivers. In dit proefschrift onderzoeken we deze uitdagingen in de volgende vier scenario's, en stellen een aantal bijbehorende oplossingen voor.

### **OFDM voor smalbandige kanalen:**

Orthogonale frequentie-division multiplexing (OFDM) is een transmissietechniek die gebruik maakt van een reeks draaggolven. In een smalband scenario worden Doppler-effecten goed benaderd door frequentieverschuivingen. Hierdoor kan een smalband dubbel-selectief kanaal voor OFDM systemen bij benadering gekarakteriseerd worden als een bandmatrix, vooral wanneer een basis-expansie model (BEM) wordt benut om het kanaal te modelleren. Dit laat een lagere complexiteit van de kanaalegalisatie toe. Er zijn echter verschillende BEMs beschikbaar. We kiezen een bepaalde BEM die leidt tot een efficiëntere hardware ar-

chitectuur dan andere keuzes, met behoud van een hoge nauwkeurigheid van het model.

#### **OFDM voor breedband kanalen:**

Het Doppler effect manifesteert zich als een iets ander verschijnsel voor breedband kanalen in vergelijking met smalbandige kanalen. In het bijzonder wordt de golfvorm voor breedband signalen meetbaar verbreed of gecompriëerd wanneer Doppler aanwezig is, en niet alleen verschoven in frequentie. Dit gedrag vraagt om nieuwe ontwerpen voor breedband OFDM systemen. Eerst kwantificeren we de verstoring als gevolg van breedband dubbel-selectieve kanalen die volgt uit het multi-scale/multi-lag (MSML) model. Daarna bespreken we een egalisatiemethode voor breedband kanalen zowel in het frequentiedomein als in het tijdsdomein. Een nieuw optimaal herbemonsteringsproces wordt ook geïntroduceerd, welke gewoonlijk niet nodig is voor smalbandige systemen.

#### **Multi-Rate transmissie over breedband kanalen:**

Traditionele transmissie met meerdere draaggolven, zoals OFDM, gebruiken een uniforme datarate voor elke hulpdraaggolf, die inherent niet goed aansluit op breedband tijdsafhankelijke kanalen. In feite suggereert de tijdvariatie van breedband kanalen, dat wil zeggen de Doppler schalen, het gebruik van een niet-uniform bemonsteringsmechanisme. Om dit te beperken stellen we een nieuwe multi-rate transmissiemethode voor waarin informatie-symbolen op verschillende niet-overlappende subbanden geplaatst worden, met voor elke subband een andere bandbreedte. Om het MSML effect van het kanaal te bestrijden wordt een filterbank ingezet bij de ontvanger, waarbij elke tak van de filterbank het ontvangen signaal op een corresponderende snelheid bemonstert. Door het selecteren van een goede zend/ontvangst-puls kan de effectieve ingangs-uitgangsrelatie worden gekarakteriseerd door een blok-diagonale matrix, waarbij elk diagonale blok een bandmatrix is, net als voor smalband OFDM systemen. Het voordeel hiervan is dat de bestaande lage-complexiteit egalisators ook kunnen worden gebruikt voor breedband communicatie.



**Robuuste multi-band transmissie over breedband kanalen:**

Nauwkeurige kanaalschatting is voor breedband dubbel-selectieve kanalen uitdagend en lastig. Adaptieve kanaalegalisatie is dus aantrekkelijk omdat precieze kanaalinformatie niet nodig is, en omdat het robuust is in verschillende omgevingen. Wanneer het MSML effect ontstaat in breedband kanalen is het niet verstandig om bestaande adaptieve egalisatiemethoden te gebruiken die ontworpen zijn voor andere scenario's, bijvoorbeeld smalbandige kanalen. Wij kiezen voor een multi-band frequentie-division multiplexing (FDM) modulatie bij de zender om de egalisatiecomplexiteit te verminderen, en tegelijkertijd een hoge data rate mogelijk te maken. Door een zorgvuldig ontwerp van de zendpuls is onze voorgestelde meerlaags turbo-egalisatiemethode, bestaand uit een fasevergrendelde regeling (PLL) gevolgd door een time-invariant eindige impulsresponsie (FIR) filter, in staat dergelijke MSML kanalen te egaliseren.



---

## Acknowledgements

### 为中华之崛起而读书

This thesis partially presents the research work during my study towards a Ph.D degree at the Circuits and Systems (CAS) Group, the Delft University of Technology (TU Delft), The Netherlands. Prior to joining the TU Delft, I was selected by the National University of Defense Technology in China as a candidate and finally won a four-year scholarship from the China Scholarship Council (CSC) in 2008. Over these four years, it has been my great fortune to encounter many people who have given me their professional helps, generous supports, companionship and encouragements.

I would first like to thank my promotor, Prof. Alle-Jan van der Veen, who shows me an great example how to be a researcher. It was his course “Signal Processing for Communications” that opened for me the door to the world of linear algebra and motivated me to start my Ph.D research here.

Special thanks to my second promotor, Prof. Geert Leus, the person who delivered to me the beauty and elegance of signal processing, and also guided me throughout my study at TU Delft. Without his supervision, I would have hardly gone through so many difficulties in my Ph.D research. He is a good listener and a smart advisor, even when I find myself difficult in explaining things to him. Almost every discussion about my research with him was inspiring, and I want to say that it is really cheerful to work with him.

Many thanks to my co-supervisor, Dr. Rene van Leuken, for giving me the opportunity to start my Ph.D study at Delft. He is a good leader to me, who gives me the freedom to explore research topics that interested me and generously offers me encouragements to proceed when I am puzzled.

Dr. Zijian Tang, who is a colleague, a friend and also a teacher to me, deserves my biggest applause. The cooperation with him not only has led us to a fruitful research, but also has taught me how to think as a Ph.D researcher.

Without him, I might have to struggle for more years to finish my study at TU Delft. He is also like a big brother to me, who kindly offered to be my referral when I was stuck in trouble during my last two years at Delft.

I also want to thank Prof. Urbashi Mitra, from the Ming Hsieh Department of Electrical Engineering, the University of Southern California, U.S., for insights, inspirations, discussions and suggestions during her visit to the CAS group. It is my honor to cooperate with her to publish several papers in the past years.

It has been a great pleasure working with so many helpful and nice colleagues in the CAS group: Minaksie, Laura, Rosario, Antoon, Alexander, Huib, Rob, Edoardo, Nick, Wim, Kun Fang, Qin Tang, Yiyin Wang, Yu Bi, Mu Zhou, Toon, Claud, Vijay, Seyran, Millad, Sina, Sharzard, Dony, Venkat, Sundeeep, Hadi, Hamid, Raj, Amir, Yuki, Mohammad, Sumeet, Matthew, Shingo, Chock, ... Thank you for the time being together. Additionally, I would like to thank Prof. Kees Beenakker for introducing TU Delft to me for the first time, Dr. Homayoun Nikookar for teaching me knowledge about wavelet techniques, and also Cees Timmers and Franca Post from the CICAT of TU Delft for the visa assistance.

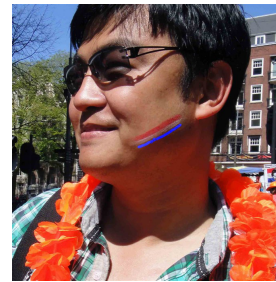
During my studies at Delft, I feel so lucky that I have so many good friends. Please allow me to only randomly list a small part of them, in no particular order: Hao Lu, Jia Wei, Manyi Qian, Dajie Liu, Song Yang, Yao Wang, Qing Wang, Yuan He, Chang Wang, Hui Yu, Yiyi Yang, Zeying Song, Jie Li, Gang Liu, Ke Liang, Xu Jiang, Jitang Fan, Zongbo Wang, Hao Cui, ... and too many others to list them all here. Thank you all for lighting up my life here. Especially to Yu Zhao, my sincere gratitude for your company in all those many years. Thank you.

Moreover, I thank all the committee members for kindly agreeing to devote time and effort in judging and giving precious opinions to this thesis.

Finally, this thesis is specially dedicated to my parents for their unconditional love. Without their support, I cannot go this far.

---

## Curriculum Vitae



Tao Xu was born in Jinzhou, Liaoning, China, in September 1982. He received the Bachelor degree in electrical engineering (profile: telecommunication engineering) and the Master degree in electronic science and technology (profile: microelectronics and solid state electronics), in 2005 and 2007, respectively, from the National University of Defense Technology (NUDT), Changsha, China. In 2008, he became a Ph.D student in the same university, and then he won a four-year scholarship from the China Scholarship Council (CSC) as the financial support for overseas studies. Since December 2008, he has been working towards to the Ph.D degree in the Circuits and Systems (CAS) group at the Faculty of Electrical Engineering, Mathematics and Computer Science (EEMCS) of the Delft University of Technology (TU Delft), The Netherlands. During his bachelor and master studies, he used to work on the fields of hardware system designs, employing FPGAs and VLSI circuits. His research work in TU Delft lied in the area of signal processing for communications (SP-COM) and also electronic system level (ESL) design, employing tools from linear algebra and statistical signal processing as well as high-level synthesis techniques.



---

## List of Publications

### Journal Papers:

1. T. Xu, Z. Tang, G. Leus, and U. Mitra. Robust Transceiver Design with Multi-layer Adaptive Turbo Equalization for Doppler-Distorted Wideband Channels. *IEEE Transactions on Wireless Communications*, submitted.
2. T. Xu, Z. Tang, G. Leus, and U. Mitra. Multi-Rate Block Transmissions over Wideband Multi-Scale Multi-Lag Channels. *IEEE Transactions on Signal Processing*, 2012.
3. T. Xu, Z. Tang, R. Remis, and G. Leus. Iterative Equalization for OFDM Systems over Wideband Multi-scale Multi-lag Channels. *EURASIP Journal on Wireless Communications and Networking*, DOI:10.1186/1687-1499-2012-280, August 2012.
4. H. Lu, T. Xu, H. Nikookar, and L.P. Ligthart. Performance Analysis of the Cooperative ZP-OFDM: Diversity, Capacity and Complexity. *International Journal on Wireless Personal Communications*, DOI:10.1007/s11277-011-0470-9, December 2011.

### Book Chapter:

1. H. Lu, T. Xu and H. Nikookar. Cooperative Communication over Multi-scale and Multi-lag Wireless Channels. In *Ultra Wideband*, ISBN:978-953-307-809-9, InTech, March 2012.
2. H. Lu, H. Nikookar, and T. Xu. OFDM Communications with Cooperative relays. In *Communications and Networking*, ISBN:978-953-307-114-5, InTech, September 2010.

**Conference Papers:**

1. T. Xu, Z. Tang, G. Leus, and U. Mitra. Robust Multiband Receiver with Adaptive Turbo Multi-layer Equalization for Underwater Acoustic Communications. accepted by *MTS/IEEE OCEANS*, Virginia, USA, October 2012.
2. T. Xu, Z. Tang, G. Leus, and U. Mitra. Time- or Frequency-Domain Equalization for Wideband OFDM Channels?. In *Proc. International Conference on Acoustics, Speech, and Signal Processing (ICASSP)*, pages 3556–3559, Kyoto, Japan, March 2012.
3. T. Xu; Z. Tang; H. Lu; R. van Leuken. Memory and Computation Reduction for Least-Square Channel Estimation of Mobile OFDM Systems. In *Proc. IEEE International Symposium on Circuits and Systems (ISCAS)*, pages 3556–3559, Seoul, Korea, May 2012.
4. T. Xu, M. Qian, and R. van Leuken. Parallel Channel Equalizer for Mobile OFDM Systems. In *Proc. International Workshop on Circuits, Systems and Signal Processing (ProRISC)*, pages 200–203, Rotterdam, Netherlands, October 2012.
5. T. Xu, G. Leus, and U. Mitra. Orthogonal Wavelet Division Multiplexing for Wideband Time-Varying Channels. In *Proc. International Conference on Acoustics, Speech, and Signal Processing (ICASSP)*, pages 3556–3559, Prague, Czech, May 2011.
6. Z. Tang, R. Remis, T. Xu, G. Leus and M.L. Nordenvaad. Equalization for multi-scale multi-lag OFDM channels . In *Proc. Allerton Conference on Communication, Control, and Computing (Allerton)*, pages 654–661 , Monticello, IL, USA, September 2011.
7. H. Lu, T. Xu, M. Lakshmanan, and H. Nikookar. Cooperative Wavelet Communication for Multi-relay, Multi-scale and Multi-lag Wireless Channels. In *Proc. IEEE Vehicular Technology Conference (VTC)*, pages 1–5 , Budapest, Hungary, May 2011.
8. H. Lu, T. Xu, and H. Nikookar. Cooperative Scheme for ZP-OFDM with Multiple Carrier Frequency Offsets over Multipath Channel. In



- 
- Proc. IEEE Vehicular Technology Conference (VTC)*, pages 11–15, Budapest, Hungary, May 2011.
9. T. Xu, H. Lu, H. Nikookar, and R. van Leuken. Cooperative Communication with Grouped Relays for Zero-Padding MB-OFDM. In *Proc. IEEE International Conference on Information Theory and Information Security (ICITIS)*, pages 11–15, Beijing, China, December 2010.
  10. G. Leus, T. Xu, and U. Mitra. Block Transmission over Multi-Scale Multi-Lag Wireless Channels. In *Proc. Asilomar Conference on Signals, Systems, and Computers (Asilomar)*, pages 1050–1054, Pacific Grove, CA, USA, November 2010.
  11. H. Lu, T. Xu, and H. Nikookar. Performance Analysis of the STFC for Cooperative ZP-OFDM Diversity, Capacity, and Complexity. In *Proc. International Symposium on Wireless Personal Multimedia Communications (WPMC)*, pages 11–14, Recife, Brazil, October 2010.
  12. T. Xu, M. Qian, and R. van Leuken. Low-Complexity Channel Equalization for MIMO OFDM and its FPGA Implementation. In *Proc. International Workshop on Circuits, Systems and Signal Processing (ProRISC)*, pages 500–503, Veldhoven, Netherlands, November 2010.
  13. T. Xu, H.L. Arriens, R. van Leuken and A. de Graaf. Precise SystemC-AMS Model for Charge-Pump Phase Lock Loop with Multiphase Outputs. In *Proc. IEEE International Conference on ASIC (ASICON)*, pages 50–53, Changsha, China, October 2009.
  14. T. Xu, H.L. Arriens, R. van Leuken and A. de Graaf. A Precise SystemC-AMS model for charge pump phase lock loop verified by its CMOS circuit. In *Proc. International Workshop on Circuits, Systems and Signal Processing (ProRISC)*, pages 412–417, Veldhoven, Netherlands, November 2009.

